Design, Synthesis and Biological Evaluation of Bioorganometallic Metallarectangles

A dissertation submitted to the University of Cape Town in fulfilment of the requirements for the degree of

Master of Science

by

Taryn Golding

Supervisor: **Associate Professor Gregory Smith**

Department of Chemistry
University of Cape Town
Rondebosch
7701

February 2021

Plagiarism Declaration

I know the meaning of plagiarism and declare that all of the work in the document, "**Design, Synthesis and Biological Evaluation of Bioorganometallic Metallarectangles**", is my own work and to the best of my knowledge has not been previously submitted for examination for any degree, at any university. All sources of information are cited and fully referenced at the end of each chapter.

Signature: Signed by candidate

Date: 01 February 2021

Acknowledgments

Above all, I thank God for His continued grace and blessings, as without Him, I would not have been able to complete this degree.

Secondly, to my supervisor, Assoc. Prof. Gregory Smith, I would like to extend my sincerest appreciation and gratitude. Thank you for your invaluable support and guidance, and most importantly, for believing in me and always pushing me to do better. You have helped me develop in all aspects as a researcher, so thank you for that!

To Nozuko, Sinethemba, and Thato, thank you for all of the laughs and UNO™ games. To Mr. Stephen de Doncker, I'm thankful for our chats, and of course, your constant assistance, not only in the lab but outside as well. To Mr. Athi Welsh, thank you for taking the time to read through my chapters and provide me with critical feedback and suggestions. And finally, to all the members of the Organometallic Research Group, thank you for all the insightful discussions and your encouragement.

A special thank you to Mr. Virgil Verhoog from the Department of Clinical Pharmacology. I appreciate your advice and support while I was working in the tissue culture lab. Thank you for always taking the time to show me the tips and tricks that you have learnt over the years. I would also like to thank Dr. Roxanne Mohunlal for conducting the β-haematin inhibition assays and for helping me analyse the data. Also, Dr. Supratim Biwas for conducting the anticancer screening of my compounds.

I would also like to acknowledge Mr. Pete Roberts and Dr. Marwaan Rylands for recording all of my NMR spectra. To Dr. Marwaan Rylands, thank you for your efforts, particularly with the DOSY experiments and also for helping me better understand certain aspects of my work. Further thanks are extended to Dr. Hong Su for the single-crystal X-ray diffraction analysis, Mr. Alexios Vicatos for the PXRD studies, and Dr. Mziyanda Mbaba for the computational studies.

I am truly grateful for the financial support provided by the NRF, UCT, and WEFT.

To my mother, Ms. Colleen Golding, thank you for constantly reminding me that it is OK to take a break, but most importantly, reminding me to always have faith. A special thank you to my brother, Mr. Michael Golding, for your constant motivation and words of encouragement, it is always appreciated. And finally, Mr. Aldo Damon, words cannot describe how grateful I am for your unwavering support, motivation, and unmatched patience throughout my degree. I love you all!

Publications

Journal articles:

Recent Advances in the Biological Investigation of Organometallic Platinum-Group Metal (Ir, Ru, Rh, Os, Pd, Pt) Complexes as Antimalarial Agents.

M. Mbaba, **T. M. Golding** and G. S. Smith, *Molecules*, 2020, **25**, 5276.

Abstract

Malaria is a devastating mosquito-borne disease, characterized by high levels of morbidity and mortality. The absence of a suitable vaccine to offer protection and the emergence of drug-resistant parasite strains continues to be the driving force behind the development of new antimalarial agents. Cancer, which is the second leading cause of deaths globally, accounted for a estimated 9.6 million deaths in 2018. Despite tremendous advances made within the field of drug discovery, the past four decades of cancer chemotherapeutic treatment has largely depended on platinum-based drugs (e.g. cisplatin and its derivatives). Unfortunately, the use of these metallodrugs are accompanied by severe adverse side-effects. Additionally, the evolution of resistant cancer cell sub-types has rendered many of these highly efficacious platinum drugs, ineffective. Utilizing alternative platinum-group metals (PGMs), such as iridium and ruthenium, and incorporating known pharmacophoric scaffolds within the framework of a target compound, has been a favourable approach toward combating these obstacles, while further enhancing the pharmacological activity of potential drug candidates.

The increased popularity and success of metal-containing compounds as pharmaceutical agents has prompted investigations into the pharmacological activity of a different class of metal-based compounds, supramolecular coordination complexes (SCCs). Such complexes have been extensively investigated for their anticancer activity, with many PGM SCCs displaying activity greater than or comparable to available clinical chemotherapeutic drugs. Interestingly, however, no studies have investigated the antiplasmodial activity of SCCs, a field that warrants further exploration.

Due to the pharmacological activity associated with the quinoline scaffold, this pharmacophore was incorporated into a newly designed *N*,*N*'-ditopic ligand (**L**). The quinoline-containing ligand (**L**), synthesized *via* a Suzuki cross-coupling reaction, was reacted with either [Ir(Cp*)(μ-Cl)Cl]$_2$ or [Ru(*p*-cymene)(μ-Cl)Cl]$_2$, *via* a bridge splitting reaction, to yield the corresponding precursor binuclear complexes. The subsequent iridium(III) and ruthenium(II) metallarectangles were synthesized, as their triflate salts, *via* coordination-driven self-assembly. All of the compounds were fully characterised using an array of spectroscopic (^{1}H, ^{13}C, DOSY NMR, and FT-IR spectroscopy) and analytical (ESI-MS and melting point analysis) techniques. The known, corresponding 4,4'-bipyridine analogues were also synthesized to evaluate the pharmacological effects of incorporating the quinoline pharmacophore into the framework. Single crystal X-ray diffraction confirmed the

proposed molecular structure of the iridium binuclear complex, [{$IrCl_2$(Cp*)}$_2$(μ-**L**)], and DFT calculations support the proposed structure of metallarectangle [{Ir(μ-Cl)(Cp*)}$_4$(μ-**L**)$_2$](OTf)$_4$.

All of the synthesized compounds were evaluated for their *in vitro* antiplasmodial activity against the chloroquine-sensitive (NF54) and multidrug-resistant (K1) strains of the malaria parasite, *Plasmodium falciparum*, which is the most virulent species within the genus *Plasmodium*. In general, incorporation of the quinoline scaffold enhanced the activity at least two-fold, compared to the corresponding 4,4'-bipyridyl analogues. Metal complexation increased the *in vitro* antiplasmodial activity of the uncoordinated ligands (both **L** and 4,4'-bipyridine) up to 50-fold, in both the NF54 and K1 strains of the parasite. An increase in the nuclearity of the system resulted in a further increase in activity of up to 12-fold. Furthermore, the resistance indices of the synthesized compounds suggest that they largely retain their activity in the resistant strain of the parasite.

Considering that quinoline-containing compounds are generally known to inhibit haemozoin formation, to gain insight into a possible mechanism of action, the quinoline-containing ligand **L** and selected metallarectangles, [{Ir(Cp*)}$_4$(μ-η^2-η^2-C_2O_4)$_2$(μ-**L**)$_2$](OTf)$_4$ and [{Ru(*p*-cymene)}$_4$(μ-η^2-η^2-C_2O_4)$_2$(μ-**L**)$_2$](OTf)$_4$, were tested for their β-haematin inhibitory activity. Both of the tested metallarectangles displayed promising β-haematin inhibitory activity, with the iridium metallarectangle inhibiting β-haematin formation to almost the same extent as CQ.

Furthermore, the new quinoline-containing compounds were evaluated for their *in vitro* anticancer activity in MCF-7 and MDA-MB-231 breast cancer cell lines. The preliminary cytotoxic screen, in the MCF-7 cell line, revealed that ligand **L** and metallarectangle [{Ir(μ-Cl)(Cp*)}$_4$(μ-**L**)$_2$](OTf)$_4$ displayed superior activity to cisplatin. Interestingly, despite being near inactive in the MCF-7 cell line, [{Ru(*p*-cymene)}$_4$(μ-η^2-η^2-C_2O_4)$_2$(μ-**L**)$_2$](OTf)$_4$ displayed the greatest activity in the triple-negative MDA-MD-231 cell line, at 10 µM, exceeding the 45% reduction in cell viability caused by cisplatin at the same concentration. Upon evaluation in a multidose screen, ligand **L** and metallarectangle [{Ir(μ-Cl)(Cp*)}$_4$(μ-**L**)$_2$](OTf)$_4$ displayed antiproliferative activity almost two-fold greater than cisplatin, in the MCF-7 cell line, while [{Ru(*p*-cymene)}$_4$(μ-η^2-η^2-C_2O_4)$_2$(μ-**L**)$_2$](OTf)$_4$ was over two-times more active than cisplatin in the MDA-MB-231 cell line. Finally, the aforementioned compounds were evaluated for their cytotoxicity against the non-tumorigenic MCF-12A cell line. The selectivity indices of these compounds suggest that they demonstrate increased selectivity toward cancerous cells, over healthy cells.

List of Symbols and Abbreviations

°	Degree
δ	Chemical shift
ν	Wavenumber
µM	Micro molar (10^{-6} M)
ACT	Artemisinin-based combination therapy
ATP	Adenosine triphosphate
ATR	Attenuated total reflection (IR)
br	Broad signal
bpy	4,4'-Bipyridine
Cp	Cyclopentadienyl
Cp*	1,2,3,4,5-pentamethylcyclopentadienyl
CQ	Chloroquine
CQDP	Chloroquine diphosphate
d	Doublet (NMR)
DCM	Dichloromethane
dd	Doublet-of-doublets (NMR)
DMSO	Dimethylsulfoxide
DNA	Deoxyribonucleic acid
DOSY	Diffusion-ordered spectroscopy
EPR	Enhanced permeability and retention
ESI-MS	Electrospray ionization mass spectrometry
EtOAc	Ethyl acetate
Et_2O	Diethyl ether
EtOH	Ethanol
eq.	Equivalent(s)
FT-IR	Fourier transform infrared spectroscopy
FQ	Ferroquine
Hb	Haemoglobin
HOMO	Highest occupied molecular orbital

HSQC	Heteronuclear single quantum correlation spectroscopy
Hz	Hertz
IC_{50}	50% cell viability concentration
IR	Infrared
J	Coupling constant
K1	Resistant strain *P. falciparum*
LC	Liquid chromatography
Lit.	Literature
LUMO	Lowest unoccupied molecular orbital
m	Multiplet (NMR)
MeOH	Methanol
MHz	MegaHertz
min	Minutes
MOF	Metal-organic framework
MOM	Metal-organic materials
M.P.	Melting point
MTT	1-(4,5-Dimethylthiazol-2-yl)-2,5-diphenyltetrazolium bromide
m/z	Mass to charge ratio
NADH	Nicotinamide adenine dinucleotide
NF54	Sensitive strain *P. falciparum*
NMR	Nuclear magnetic resonance spectroscopy
OA	Oxidative addition
p	Pentet (NMR)
PBS	Phosphate buffer saline
PES	Phenazine ethosulphate
P. falciparum	*Plasmodium falciparum*
PGM	Platinum group metal(s)
***p*LDH**	Plasmodium lactate dehydrogenase
ppm	Parts per million
PT	Proton transfer
PXRD	Powder X-ray diffraction

RBC	Red blood cell
R_f	Retention factor
ROS	Reactive oxygen species
r.t.	Room temperature
s	Singlet (NMR); strong (IR)
SCC	Supramolecular coordination complex
S.I.	Selectivity index
S_NAr	Nucleophilic aromatic substitution
t	Triplet (NMR)
TB	Tuberculosis
TFA	Trifluoroacetic acid
TLC	Thin layer chromatography
UV	Ultra-violet

Table of Contents

CHAPTER 1

Introduction

1.1 Malaria

1.1.1 History and prevalence

Malaria is a disease of devastating global impact and is characterized by high levels of morbidity and mortality in both adults and children, throughout tropical and subtropical regions of the world.[1-4] It is one of the world's most ancient diseases, with reports of symptoms matching those of malaria dating back to as early as 3000 B.C.[2,3] Malaria stems from the Italian word "mal-aria", meaning bad air, and is caused by an intra-erythrocytic protozoan parasite, initially identified by Alfonse Laveran in 1880.[5] In 1889, R. Ross discovered that mosquitoes were the transmitters (vectors) of these parasites.[6] This disease is caused by a protozoan parasite of the genus *Plasmodium*, which is transmitted through the bite of an infected female *Anopheles* mosquito.[2,3] Within the *Plasmodium* genus there are currently five malaria parasite species known to cause human malaria; *P. falciparum*, *P. vivax*, *P. knowlesi*, *P. malariae,* and *P. ovale*.[2,7] Compared to the latter species, *P. falciparum* is the most virulent and is responsible for the most malaria-related deaths globally.[2,3,6,7] Characteristics of *P. falciparum* that make it so dangerous include its unique pathogenesis, which causes microvascular obstruction in vital organs, and its ability to readily develop drug resistance.[8]

Despite the number of estimated cases declining between 2010 to 2014, the subsequent years have seen a resurgence in the number of malaria cases globally.[1] The 2019 World Health Organisation (WHO) report estimated that in 2018 alone, there were approximately 228 million cases of malaria worldwide.[1] Unfortunately, the African region bore the largest burden, accounting for 93% (213 million) of these cases (Figure 1.1).[1] However, the true number of cases may be higher, as underdeveloped countries may not possess the correct resources required to record or report malaria related incidents. This disease remains entrenched in the poorest areas of the world, within the warm tropical and sub-tropical countries of Africa, where the climates are suitable for the reproduction and proliferation of the *Anopheles* mosquito.[3, 9,10] Unfortunately, this disease continues to contribute to the cycle of poverty faced by people in these underdeveloped areas, where there is insufficient health care funding, poor infrastructure, and densely populated regions.[11,12]

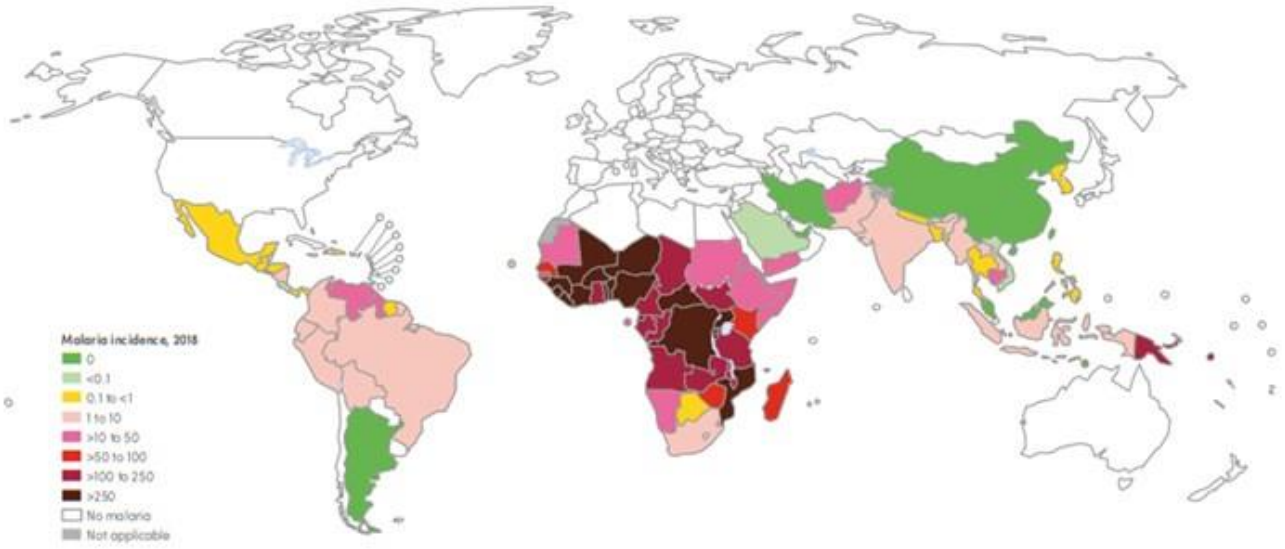

Figure 1.1: *A map showing the geographical distribution of the malaria case incidence rate (cases per 1000 people) for 2018.*[1]

Drug discovery within this field has thus become increasingly challenging, due to the wide diffusion of the disease, the frequent emergence of drug-resistant parasite strains, and the limited arsenal of effective antimalarial agents. This has consequently prompted research into better understanding the biology of the parasite, which can aid in the development of new strategies to successfully treat and/or prevent this uncontrollable and devastating disease.

1.1.2 Life-cycle and biology of the Plasmodium parasite

There are three main phases within the life-cycle of the *Plasmodium* parasite; the liver, the erythrocytic (blood cell), and the vector (mosquito) stage (Figure 1.2).[13] Human infection begins with an infective bite by a female *Anopheles* mosquito, inoculating the individual with sporozoites of the *Plasmodium* parasite that are transferred from the salivary glands of the mosquito into the bloodstream of the human host (Figure 1.2 **A**).[2,7,14] The sporozoites are then transported in the bloodstream to the mammalian liver, where they invade hepatocytes.[7,14] These parasites can either remain dormant as hypnozoites (which can cause clinical relapses at regular intervals but are only observed upon infection with *P. vivax or P.ovale*) or can continue to replicate and develop within the liver.[2,13-15] The infected hepatocytes eventually rupture, releasing merozoites into the bloodstream, which invade and proliferate within the erythrocytes (Figure 1.2 **B**).[2,14]

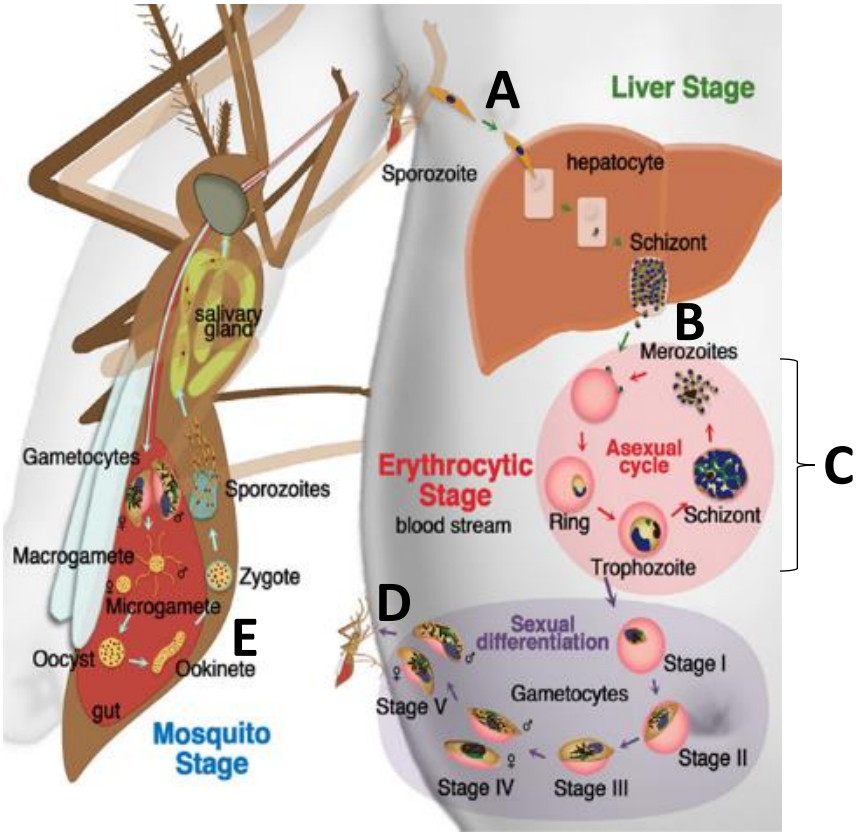

Figure 1.2: *The life-cycle of the Plasmodium parasite.*[14]

The merozoites develop asexually within the red blood cells through its three developmental stages, namely the ring, trophozoite, and schizont stages (Figure 1.2 **C**).[2,14] It is during this asexual erythrocytic stage, within the human host, that the parasite is most pathogenic, causing the patient to be symptomatic.[7,14,16] Clinical symptoms associated with uncomplicated malaria include high fever, nausea, vomiting, diarrhoea, and abdominal pain.[2] During the schizont stage, schizogony gives rise to merozoites, which are released upon the rupturing of infected red blood cells and immediately invade new erythrocytes.[2,14] During each round of schizogony, approximately 1% of the merozoites differentiate into male and female gametocytes, which are ingested by an uninfected *Anopheles* mosquito during its next blood meal (Figure 1.2 **D**).[2,13-15] The sexual phase, which is non-pathogenic, then commences within the midgut of the mosquito, as the male and female gametocytes fuse to form a zygote (Figure 1.2 **E**).[2,14] This process occurs within an environment almost totally derived from host blood.[13] Development and consequent rupturing of the zygote releases thousands of daughter sporozoites, which migrate to the salivary glands of the mosquito, where they may be injected into an uninfected human host, completing the parasites' life cycle.[2,14]

During the trophozoite stage, while in the erythrocytes of the human host, the parasite utilizes hemoglobin (Hb) as the main source of nutrition during proliferation.[2,17-20] The Hb is ingested *via* phagocytosis and is transported to the acidic digestive vacuole (DV) of the parasite, where it is degraded through a series of sequential metabolic processes.[2,18-21] Extensive degradation of hemoglobin generates a large amount of "free" heme (Figure 1.3) as a by-product.[2,17,18,20,22] Many studies have shown that heme is toxic to the parasite as it can generate oxygen free radicals.[2,19,20,23] These reactive oxygen species (ROS), among other things, can cause lipid peroxidation, which involves degradation of the lipids within the parasitic membrane, and eventual cell lysis.[19,20,24] To alleviate this problem, malaria parasites have evolved a distinct detoxification mechanism.[2,20] The Fe(II) in the toxic heme is rapidly oxidized to Fe(III), generating hematin, which is biocrystallized into an insoluble, chemically inert pigment known as hemozoin, which is non-toxic toward the parasite (Figure 1.3).[2,18-20]

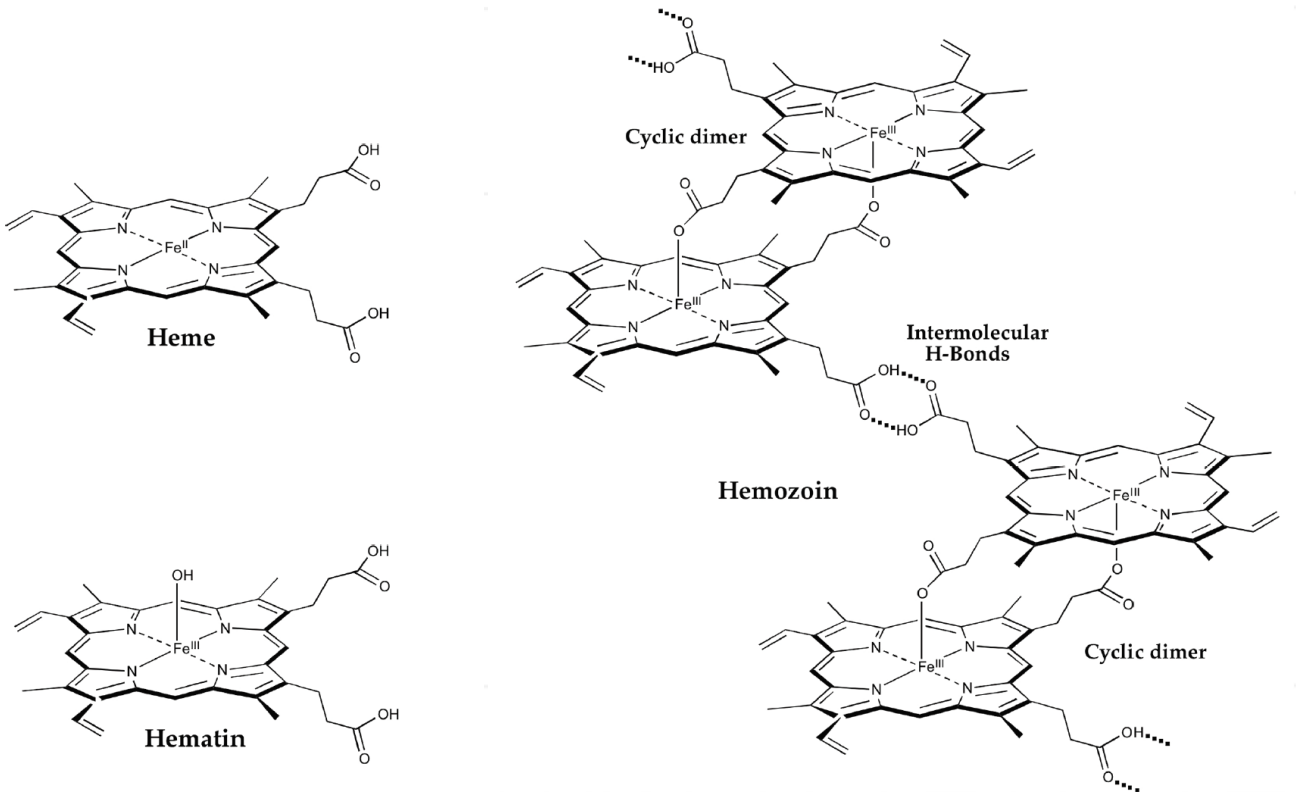

Figure 1.3: *Structures of heme, hematin, and hemozoin.* [20]

Various classes of antimalarial drugs are continuously being developed and are aimed at targeting pathways that are crucial for not only the survival but the proliferation of the parasite. To ensure the success of antimalarial drugs, pathways that are unique to the parasite and/or pathways that greatly differ from those performed within the host are targeted, as this ensures minimal unwanted side-effects. The continuous degradation of hemoglobin and the concomitant detoxification of the generated free heme are necessary for the successful growth and proliferation of the parasite.[18] Consequently, this unique process of heme detoxification has been exploited by many researchers and is one of the primary potential targets for new antimalarial drugs.[17]

1.1.3 Antimalarial treatments and drug resistance

Malaria is a major cause of human suffering and despite the scientific advances made over the years to better understand this disease, efforts to successfully treat and eradicate malaria have been to no avail. The first record of malaria treatment dates back to the 1600s when the bark of the *Cinchona* tree was used to treat malarial symptoms.[17] However, this was prior to the identification of the malaria parasite and the knowledge that mosquitoes are the vectors.[17] Upon these discoveries, a combined action of DDT (dichlorodiphenyltrichloroethane) pesticide, utilized for vector control, and effective antimalarial treatments nearly eradicated this disease by the mid-20th century.[2,3]

1.1.3.1 Quinoline and non-quinoline based drugs

Quinine (Figure 1.4a), which was purified from the bark of the *Cinchona* tree in 1820, was the first antimalarial agent to be isolated and chemically characterized.[17] Despite quinine still playing its role within malaria treatment, quinoline derivatives have become more widely used, as it is the quinoline scaffold that is responsible for the antimalarial properties of quinine.[25] The eventual recognition of chloroquine (CQ) (Figure 1.4b), which is structurally derived from quinine, was later synthesized in 1934.[17] CQ was the most effective and widely used antimalarial during the mid-20th century WHO Global Eradication Programme.[17] For years, CQ remained the leading first-line antimalarial due to it being relatively non-toxic (compared to its predecessor quinine), inexpensive, and highly efficacious.[2,4,26]

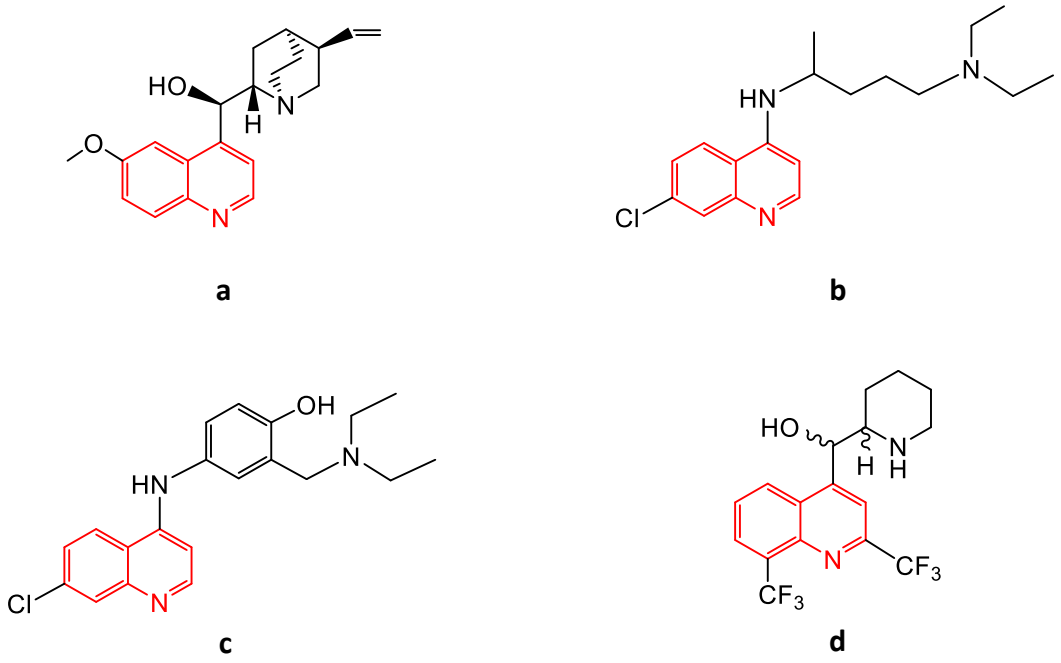

Figure 1.4: *Structures of a) quinine, b) chloroquine, c) amodiaquine and d) mefloquine, highlighting the quinoline scaffold in each drug.*

Despite being used as an antimalarial agent for decades, the exact mechanism of action of CQ is still not completely understood. However, it is widely accepted that CQ interferes with heme detoxification, as shown in Figure 1.5.[2,19,21,27,28] CQ is a diprotic weak base and can pass through the membranes of the erythrocyte and parasite in its unprotonated form, and accumulate within the acidic DV.[2,21,25-28] The acidic nature of the vacuole protonates the drug, which is unable to diffuse back through the membrane and thus remains trapped inside the DV.[2,26,27] Once the parasite degrades the hosts' Hb, the protonated form of the drug forms a complex with the hydroxy or aqua complex of ferriprotoporphyrin IX (hematin), inhibiting crystallization to hemozoin and hence detoxification.[2,21,27,28] This results in a build-up of significant quantities of toxic heme, leading to membrane and electronic stress, and eventual cell death.[2,19,26]

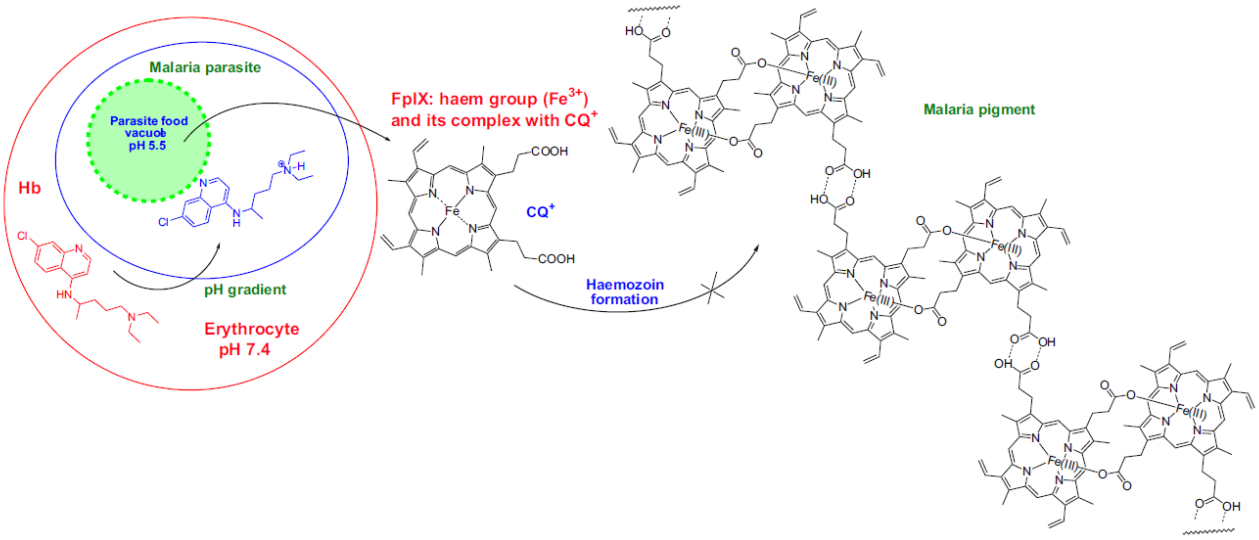

Figure 1.5: *Proposed mechanism of action of CQ.*[21]

The efficacy of CQ has however been greatly compromised by the advent of drug-resistant parasite strains of *P. falciparum*, with the first reported cases of CQ resistance appearing in the late 1950s.[2,17] Within CQ-resistant strains there is reduced uptake and/or accumulation of the drug within the DV of the parasite, which is possibly due to changes in genes that encode membrane transport proteins.[26] However, despite the development of CQ-resistant *P. falciparum* strains, the quinoline moiety continues to be an attractive scaffold for the design and synthesis of new antimalarial agents. Furthermore, its limited host toxicity, cost-effective synthesis, ease of use, and excellent clinical efficiency[25] have prompted efforts to develop new antimalarial drugs based on the quinoline scaffold.[2] Synthetic derivatives include 4-amino-quinolines, such as amodiaquine (Figure 1.4c), and quinoline-methanols such as mefloquine (Figure 1.4d).[2] Unfortunately, the increasing emergence of drug-resistant parasite strains[29,30] has prompted further investigations into alternative scaffolds to treat this disease.[2]

Artemisinin, which was isolated from *Artemisia annua* (sweet wormwood) by Chinese scientists in the 1970s, is better known to Chinese herbalists as Qinghao and is responsible for the reputed medicinal action of the herb *Artemisia annua*, which had been used for centuries to treat fever.[2,31] Artemisinin and its derivatives (e.g. dihydroartemisinin, artesunate, and artemether) (Figure 1.6), which are the latest class of antimalarials, are fast-acting and highly effective, and have shown to provide the most rapid parasite clearance among known antimalarials.[2,8,32,33] Furthermore, these compounds display relatively low toxicity and nanomolar potency *in vitro* against *P. falciparum*,[34-36]

and became the new hope during the 1990s when parasite resistance to available major antimalarial drugs, such as CQ, worsened across malaria-endemic areas globally.[8,33]

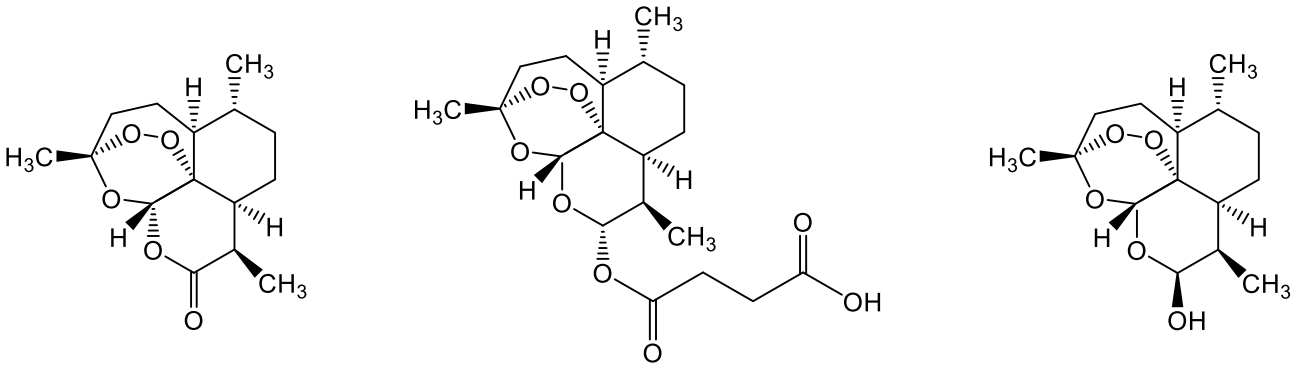

Figure 1.6: *Structures of a) artemisinin and examples of its derivatives, b) artesunate and c) dihydroartemisinin.*

Initially, the aforementioned drugs were administered as a monotherapeutic treatment. [37] However, to improve treatment outcomes and counter the threat of resistance, in 2006 the WHO recommended that combinations of antimalarials be used.[37] The concept was based on the potential to improve the therapeutic efficacy upon simultaneous administration of two or more drugs, with independent modes of action.[37] Furthermore, simultaneous administration could delay resistance to the individual components of the combination, by limiting the exposure of the parasite to the individual drugs and thus reducing the time available for the parasite to adapt.[37] The rationale behind combining antimalarials with different modes of action include 1) the combination of antimalarials is often more effective and 2) should resistance arise to one of the drugs in combination, during treatment, the parasite could still be killed by the other drug.[37] To realize these advantages, these partner drugs must be independently effective, as the mutual protection is thought to prevent or delay resistance.[37]

Artemisinin and its derivatives are an extremely potent and effective class of antimalarial agents, particularly when used in combination with a second antimalarial. This is known as artemisinin-based combination therapy (ACT).[37] The administration of artemisinin, or a derivative thereof, will kill the majority of the parasites due to its potent activity.[37,38] However, it is absorbed and eliminated rather rapidly from the hosts' bloodstream and therefore complete parasite clearance is dependent on the partner drug.[37,38] A second drug, which has a longer retention time within the body, is then administered, killing the remaining parasites within the host.[37,38] Some of the slow-acting antimalarial

drugs used in ACT include lumefantrine, amodiaquine, mefloquine, and piperaquine, many of which are based on the quinoline scaffold.[38] Today, ACT is the recommended and standard first-line therapy for uncomplicated *P. falciparum* malaria, across various regions in the world.[1]

Despite the proven effectiveness of ACT, disadvantages associated with this treatment regimen include poor patient compliance, increased risk of adverse effects which may be caused by drug-drug interactions, and increased cost.[37-39] And, even when used in combination, the individual drugs are still susceptible to the development of resistance, which has been emerging.[2,33] Due to most of the drugs currently in the developmental pipeline being derivatives of artemisinin, should the current generation of ACTs fail, there would be no alternative treatment available on the market.

Despite emerging resistance, quinoline-containing compounds have proven to be a promising class of bioactive molecules, within the field of drugs and pharmaceuticals, and have shown to possess a spectrum of pharmacological activities. Apart from being potent antiplasmodial agents,[25,40-42] this scaffold has further proven to have pharmacological importance within cancer treatment.[43-48]

1.2 Cancer

1.2.1 Cancer prevalence and mortality

Cancer, which is defined as an abnormal growth of cells within a particular part of the body,[49] is the second leading cause of death globally.[50] In 2018, it accounted for an estimated 9.6 million deaths, with approximately 70% of these deaths occurring in low- and middle-income countries.[50] Putting that into perspective, globally, about 1 in 6 deaths are due to cancer.[50] The growth of this disease exerts tremendous financial, physical, and emotional strain on individuals, families, and health care systems.[50]

Cancer is a group of diseases that can vary in their state of cellular differentiation, rate of growth, response to treatment, metastatic potential, diagnostic detectability, and prognosis.[49] The exact causes of cancer are not clearly defined, but it is known that both internal and external factors have a role to play.[49,51] External factors, such as exposure to carcinogens, including chemicals and ultraviolet (UV) radiation, and internal factors, including genetic predisposition and defects within the immune system, have all been shown to play a role within the onset of cancer.[49,51] Ultimately, this interplay between the environment and genetics can lead to genetic mutations and subsequent tumourigenesis.[49,51]

1.2.2 Cell-cycle and biology of cancer

Cancer is characterized by abnormal gene expression, which can lead to a dysregulated balance between cell division and cell death.[49,51] This imbalance favours the abnormal growth of a tumour cell population.[49] Tumour development arises due to repeating rounds of mutation and proliferation.[52,53] At each step, a single cell is mutated, enhancing its proliferation so that its progeny is the dominant clone in the tumour (Figure 1.7).[52,53] Rarely, however, does a single gene mutation lead to the onset of cancer.[51] Instead more typically, proliferation continues creating an opportunity for multiple genes to undergo a series of mutations.[52] This creates a more rapidly proliferating cell type, that escapes normal growth restraints, allowing for further mutations and an increase in the size of the tumour cell population.[51,53]

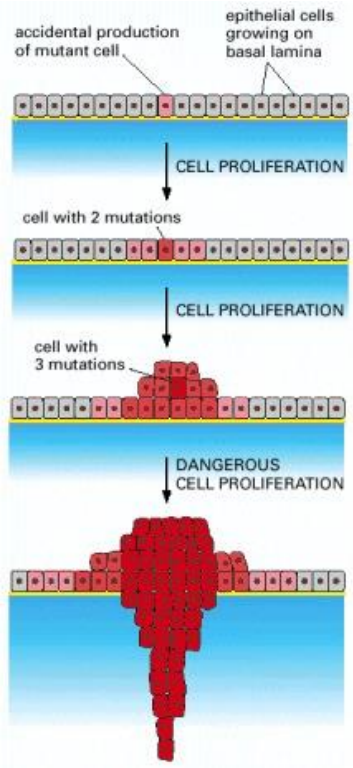

Figure 1.7: *Image depicting the clonal evolution of cancer cells.*[52]

Mutations in two classes of genes, proto-oncogenes, and tumour-suppressor genes, have been linked to the onset of cancer.[51] Proto-oncogenes can be activated by mutations to become oncogenes.[51] When activated, these genes lead to a dysregulation of cell processes as they become excessively active in growth promotion.[49,51] Furthermore, inactivation or deletion of tumour-suppressor genes, which generally restrain growth, can promote the abnormal growth of cells.[49,51,53]

There is more than one mechanism by which alterations in gene expression (mutations) may occur. The first mechanism directly involves DNA, which includes gene mutation, amplification, translocation, or deletion.[49] The second mechanism is a result of abnormal gene translation or transcription.[49] However, both cases yield the same result; an imbalance between cell replication and cell death, leading to the extensive growth of the tumour tissue, with a growth rate often exceeding that of the surrounding normal tissue, where there is a state of equilibrium between proliferation and death.[49,53] This is a disease of multicellular organisms, implying that there is something inherent in processes such as cell proliferation, differentiation, and motility that is crucial to the process of tumorigenesis.[49]

A tumour can either be benign or malignant. Benign tumours, although they expand, remain localized and do not invade the surrounding tissue.[49,53] The cells comprising these tumours closely resemble normal cells and thus may function as such.[51] In contrast, malignant tumours are capable of invading and destroying adjacent healthy tissues and can metastasize.[49,53] Metastasis is the spread of cancer cells from a primary tumour, through lymphatic channels or blood vessels, to seed secondary tumours in distant sites of the body (Figure 1.8).[49,53,54] Invasion of surrounding tissues, by malignant tumours, can interfere with vital functions, with the severity increasing should they metastasize to vital organs such as the brain.[49]

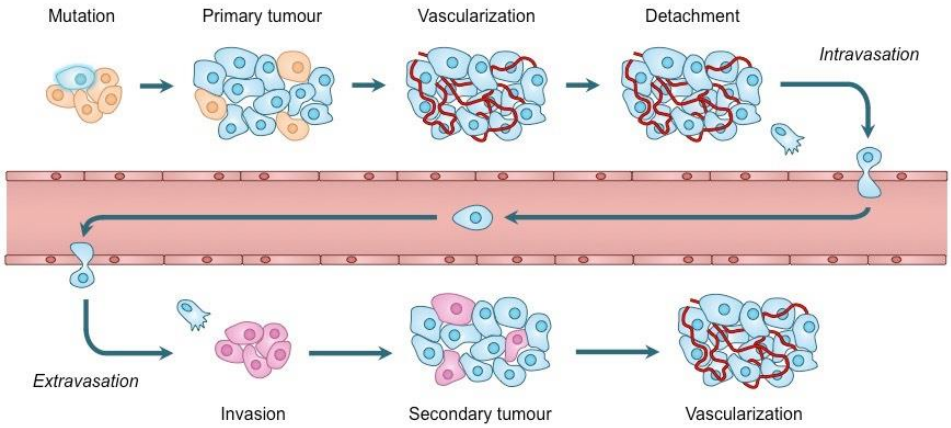

Figure 1.8: *Formation of secondary tumours via metastasis.*[55]

Metastasis is a key characteristic of malignant tumours and is, unfortunately, one of the greatest challenges in cancer treatment today.[54] Furthermore, the progression of a cancerous growth leads to cell heterogeneity in characteristics such as metastatic potential, differentiation state, cell antigenicity, rate of cell proliferation, and the relative response to chemotherapeutic agents.[49]

Consequently, an understanding of the pharmacological principles, tumour biology, and cell kinetics of this disease is imperative to the design of successful treatments.[56]

1.2.3 Cancer therapies and chemoresistance

Today, various forms of therapy are available to manage and treat cancer. "Local" forms of treatment, such as radiation and surgery, are used to treat localized tumours.[57] Drug treatments, often called "systemic" treatments, such as immunotherapy, targeted therapy, and chemotherapy, can affect the entire body.[57] Often, these therapies are used in combination. For example, chemotherapy, as an adjunct to surgery, is the routinely offered treatment upon the detection of primary (early) cancers.[58] The principal modalities used to treat advanced and localized solid tumours include radiotherapy and surgery.[58] However, for patients that present with metastatic spread, cytotoxic chemotherapy is the adopted treatment.[58] Unfortunately, each form of therapy is accompanied by adverse side-effects.[58]

Cytotoxic chemotherapeutic agents primarily damage proliferating cells.[58] However, the processes governing proliferation are common to both cancer and normal cells.[58] Consequently, both cell populations are susceptible to chemotherapeutic damage, due to the poor specificity of these cytotoxic agents.[58] This leads to a subsequent trade-off, as toxicity is experienced by normal tissues as the chemotherapeutic agents aim to achieve maximum tumour cell death.[58] Furthermore, acute complications experienced during the treatment period include necrosis, myelosuppression, reduced fertility, hair loss, vomiting, and nausea.[58] There have also been reports of side-effects developing months after treatment, such as cardiomyopathy and pulmonary fibrosis.[58]

Available chemotherapeutic agents can be classified according to their mechanism of action.[56] For example, alkylating agents impair cellular function upon the formation of covalent bonds with DNA and/or RNA.[56] Furthermore, antimetabolites and platinum agents both interfere with DNA synthesis.[56]

Unfortunately, the intrinsic or acquired mutations that occur during tumorigenesis protect cancer cells from cytotoxic agents.[58-60] This ultimately leads to drug resistance, which is the most common cause of treatment failure.[58-60] The most common drug resistance mechanism involves altered gene expression.[56] Repeated exposure of a tumour to a single anti-cancer agent can lead to the overexpression of the MDR-1 gene.[56] This overexpression is directly correlated with rising resistance to anti-neoplastic agents and can induce cross-resistance, not only to that particular drug but other

agents within the same drug class.[56,60] One approach to circumvent this rising resistance includes combination chemotherapy, whereby chemotherapeutic agents from different drug classes are used in combination. This treatment regimen provides maximum cell kill, with toxicity in the range tolerated by the host for each drug.[56] Utilizing drugs with different dose-limiting toxicities and different mechanisms of action can allow for synergistic or additive effects, increasing the coverage of resistant cell lines within heterogeneous tumour populations, while further preventing the development of new drug-resistant cells.[56]

Consequently, new drugs, with novel mechanisms of action, which are not subject to the same resistance mechanisms, as well as new strategies for the use of existing drugs, are urgently needed to allow for the successful treatment of drug-resistant cancers. The quinoline pharmacophore, which was previously discussed to be a potent antiplasmodial agent, has also been extensively investigated and has shown promise as a potential anti-cancer agent.[44,45,61-64]

1.2.3.1 Quinoline-based drugs

Various quinoline derivatives have been reported to display potent antiproliferative activity. An example includes 1-(4-(1*H*-imidazol-1-yl)-3-cyanopyrrolo[1,2-*a*]quinoline (Figure 1.9a), which was synthesized by Kemnitzer *et al*.[62] This quinoline-containing compound displayed EC_{50} values in the low nanomolar range against T47D human breast cancer cells, HCT116 human colon cancer cells, and SNU398 hepatocellular carcinoma cancer cells.[62] Kohn *et al*. studied the *in vitro* antiproliferative activity of a series of Baylis-Hillman adducts and derivatives.[65] Of the synthesized compounds, a quinoline-phthalide derivative (Figure 1.9b) displayed the most potent activity across all the tested cell lines, most notably against the NCI-ADR cell line, which expresses a multiple drugs resistance phenotype.[65] Lastly, compounds **c** and **d** (Figure 1.9), which were synthesized by Mikata *et al*.[66] and Sharples *et al*.[67] respectively, both show strong binding to DNA, which is a well-known target of chemotherapeutic agents[43] such as cisplatin. These are but a few examples, however, there are a plethora of articles depicting the potential, and in many cases the success, of quinoline-containing compounds within pharmacology.[43-48,62,65]

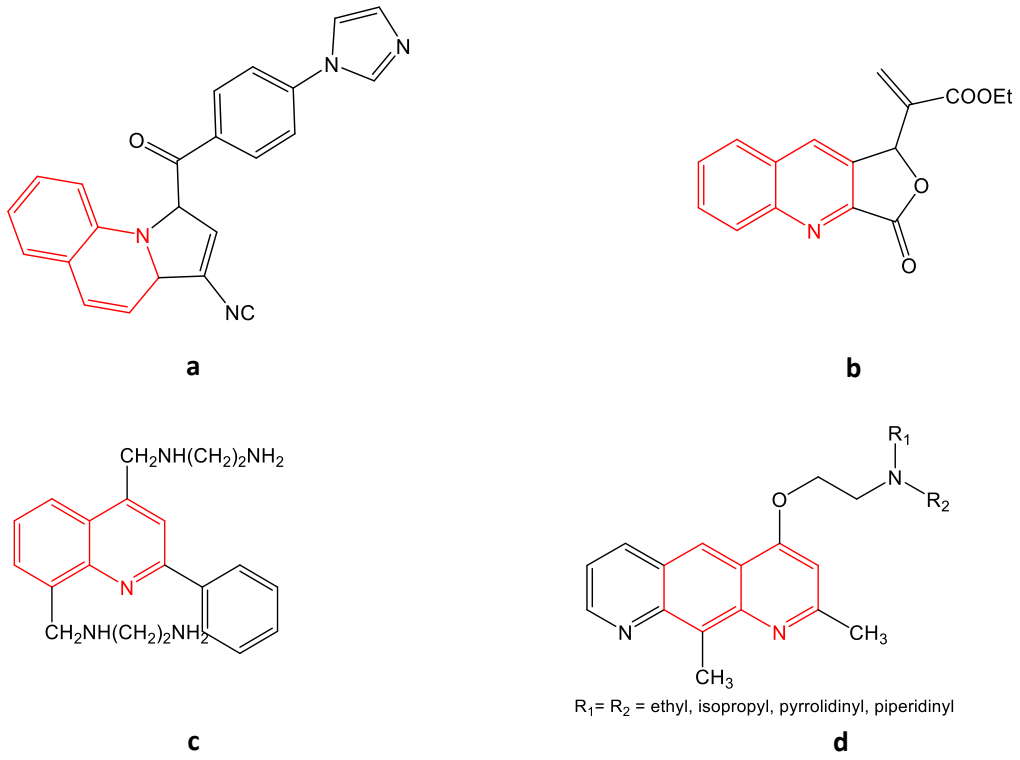

Figure 1.9: *Examples of quinoline-containing compounds that display promising anti-cancer activity.*

However, for both cancer and malaria, the intrinsic and acquired resistance to several chemotherapeutic agents is yielding drugs that were once highly efficacious, fruitless, hampering the drug development progress made thus far. This has prompted research into alternative approaches. To continue the battle against resistance, one approach, the incorporation of metals, has recently taken wind and has proven to be invaluable, as some of the most effective antimalarial and anticancer agents are metal-based compounds.

1.3 Metals in medicine

1.3.1 History of metal-based drugs

Within the field of medicinal chemistry, many organic compounds have shown to not have a purely organic mode of action.[68-70] Metal ions can play a significant role in the mechanism of action of organic drugs. Organic compounds can directly or indirectly affect metal ion metabolism or they can be bio-transformed and activated by metal ions, all of which display the necessity of inorganic elements within biological and biomedical processes.[68-70] Despite nature being greatly limited to the use of bioavailable metal ions, there are many rarer transition metals that may provoke novel biological responses upon interaction with biomolecules.[71] It is for this particular reason that metal-

biomolecule complexes are of interest in medicinal applications, where the incorporation of metals into medicines dates back centuries.[2,71]

Metal-based drugs have served as therapeutic agents in the ancient history of medicine and during the pioneering times of modern pharmacology.[4] Precious metals have been used for approximately 3500 years for medicinal purposes.[72] Records show that in China and Arabia, gold was included in a vast number of medicines, and during that period these metals were believed to provide health benefits purely because of their rarity.[72] However, over time they were largely abandoned due to rather valid concerns regarding their systemic toxicity and the rapid evolution of modern organic medicinal chemistry.[4] Exceptions included the use of platinum-based drugs in cancer chemotherapy and a few success stories such as auranofin, which is used in the treatment of rheumatoid arthritis.[4] This situation has however substantially changed over the past few decades as researchers have linked the medicinal properties of inorganic drugs to specific biological properties, resulting in a resurgence of interest in metal-based drugs possessing therapeutic properties.[4,72]

There is no question about the success of metal-containing compounds within the pharmaceutical industry today.[73-76] This field was however stimulated by the success of the metal-based anticancer drug cisplatin (Figure 1.10a).[68,77] The biological activity of cisplatin was first discovered by Rosenberg and co-workers.[78,79] This group of researchers noticed the unusual growth-limiting behaviour of *Escherichia coli* (*E. coli*) incubated in an ammonium chloride growth medium, inside a chamber with platinum electrodes.[78,79] The compound responsible for this limited growth was isolated[79] and identified as cisplatin, which interestingly enough was already known as Peyrone's chloride, a complex first synthesized by Michele Peyrone in 1845.[80] This complex was later tested for its antitumor activity[81] and today, cisplatin, whose anticancer properties were discovered in the 1960s, is still one of the most widely clinically used metal-based anticancer drugs.[68,72,76,81,82]

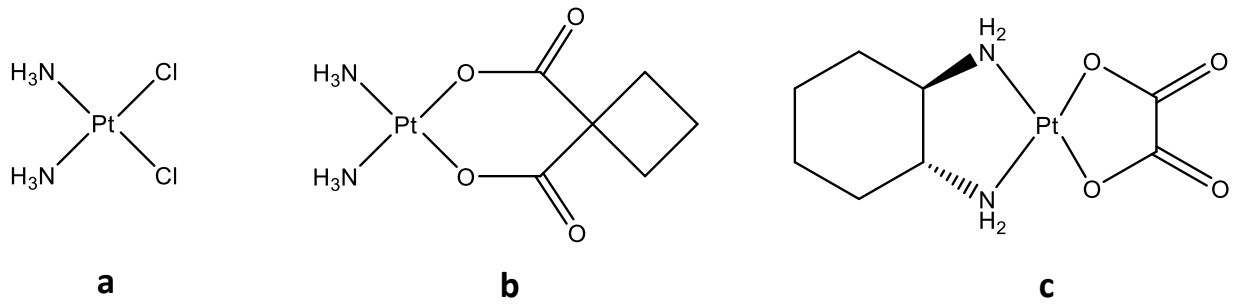

Figure 1.10: *Chemical structures of the clinically used platinum drugs a) cisplatin, b) carboplatin, and c) oxaliplatin*.

Unfortunately, cisplatin has shown to be notoriously toxic to the gastrointestinal tract and the kidneys,[83,84] prompting research into the synthesis and biological evaluation of several cisplatin analogues,[85] with the aim to reduce the severe nephrotoxicity while retaining the anticancer efficacy.[77] The first breakthrough was the discovery of carboplatin (Figure 1.10b), which contains a more stable leaving group than the chlorides in cisplatin, lowering its toxicity without affecting its antitumor activity.[77,86] Clinical evaluation of carboplatin did not reveal significant evidence of nephrotoxicity and was shown to be less emetic than cisplatin.[87] Today, several platinum-based drugs, some of which are shown in Figure 1.10, are widely used in the treatment of various neoplasms.[76] However, despite the tremendous advances made within the field of oncology, the associated toxicity, resultant side-effects, and intrinsic or acquired resistance upon treatment with these platinum-based drugs are an endless struggle, and yet, they continue to be the most sought after chemotherapeutic agents.[76,82,88]

Currently, the largest research area of medicinal organometallic chemistry is the development of anticancer agents.[89] However, organometallic complexes as antimalarial agents have also generated significant scientific interest.[89] The use of metal compounds for the treatment of parasitic diseases has been prompted by several considerations. Firstly, various inorganic salts were administered for the treatment of tropical diseases during the pioneering times of modern pharmacology,[90] some of which displayed very good activity.[4] Secondly, metal complexes seem to be suited for the treatment of parasitic diseases as they have shown noticeable selectivity for biomolecules within the parasite over that of the hosts' biomolecules.[4] Finally, metals can contribute to the novelty of antiparasitic agents (metal-drug synergism), as the insertion of metals into the framework of an already established antiparasitic drug can enhance its pharmacological activity (e.g. ferroquine).[91,92] Furthermore, the complexation of classic antiparasitic drugs can modulate their activity and pharmacokinetic parameters (e.g. gold-CQ).[4,93]

This possible metal-drug synergism, achieved upon the incorporation of a metal into an organic compound that possesses some level of biological activity, offers the opportunity to fine-tune the metal and/or ligands to achieve or enhance the desired efficacy. [2,94] This can allow for the discovery of new drugs with novel mechanisms of action.[2,94] Metal-drug synergism can further enhance the biological activity of the parental organic drug by masking it upon coordination, possibly stabilizing it, and thus ensuring that the biological targets are reached more efficiently, by extending the residence time of the drug within the organism.[94] Furthermore, metal-complexation can decrease

metal-associated toxicity, as complexation to the organic drug limits the availability of the metal for undesirable reactions, which could lead to toxicity and possible side-effects.[94]

Ferroquine (FQ) (Figure 1.11), which was the first reported derivative of CQ, to contain a ferrocene molecule, has become the most successfully synthesized and tested metalloantimalarial to date and has completed phase IIb clinical trials.[2,95] First synthesized in 1997, FQ, despite sharing structural and biological similarities with CQ, showed high activity in both CQ-sensitive and -resistant strains of *P. falciparum in vitro,* with activity exceeding that of CQ by 22-fold in the CQ-resistant strains.[91,96] The antimalarial activity of this drug was a remarkable discovery, as it not only presents activity at nanomolar concentrations,[97] but has a potency comparable to that of artemisinins, with a high selectivity index.[2] The activity of FQ is attributed to its dual action mechanism.[4,25] Firstly, this compound inhibits β-hematin formation to a greater extent than CQ.[4,25,98] Secondly, redox activation from ferrocene [Fe(II)] to ferrocenium [Fe(III)] results in the generation of reactive oxygen species (ROS) that can cause irreversible damage to the parasite.[4,25,98]

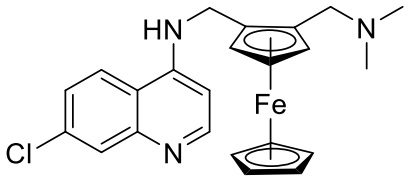

Figure 1.11: *Structure of ferroquine (FQ).*

The biological activity of metallodrugs is dependent on the oxidation state of the metal centre, which varies depending on the nature of the ligands used, and the rate of ligand exchange.[72,89] These characteristics impact not only the biological transformations that occur en-route, but the interactions between the drug and the biological target and thus the resultant therapeutic activity.[72] Manipulation of these features can fine-tune the activity of the drug, maximizing its potency while minimizing its overall toxicity.[72] The diverse structural types of organometallic complexes, their redox properties, and variations in ligand bonding modes, make them attractive within the field of medicinal chemistry.[99] The unique properties associated with organometallic molecules are somewhat intermediate between those of inorganic and classical organic compounds, integrating the best features of both, providing new opportunities within medicinal chemistry.[99,100] The versatility of platinum group metal (PGM) metallodrugs, in particular, are illustrated by their array of medicinal applications.[72,76,101-103]

1.3.2 PGM metalloantimalarials

Due to the increasing appearance of chemoresistance and the limited arsenal of effective antimalarial agents, metal complexes offer an excellent opportunity to find new leads against this infectious disease. A review released in 2004 by Sánchez-Delgado *et al*. provides a rather extensive and in-depth account of the history of standard antimalarial drugs and the evolution of metal-based compounds as antimalarials.[94] Furthermore, progress in the identification of new biomolecular targets and the increased knowledge of parasite genomics provides promise for the discovery of new antiparasitic metallodrugs with new mechanisms of action.[4]

Chellan *et al*. synthesized a suite of bi- and trinuclear pyridyl aromatic ethers and studied their *in vitro* antiplasmodial activity against NF54 and Dd2 strains of *P. falciparum*, as well as the β-hematin inhibition ability of these complexes.[104] All of the complexes showed enhanced activity compared to the corresponding metal-free ligands. Furthermore, the trinuclear complexes displayed significantly higher activities than their binuclear counterparts.[104] This suggested that an increase in the number of metal centres (multinuclearity) leads to an increase in the pharmacological activity,[104] a phenomenon supported by several other studies.[105-107] The triruthenium complex shown in Figure 1.12 displayed the most promising antimalarial activity, with IC_{50} values in the low micromolar range, and a β-hematin inhibitory activity (IC_{50} = 20.72 μM) comparable to that of CQ (IC_{50} = 18.43 μM).[104]

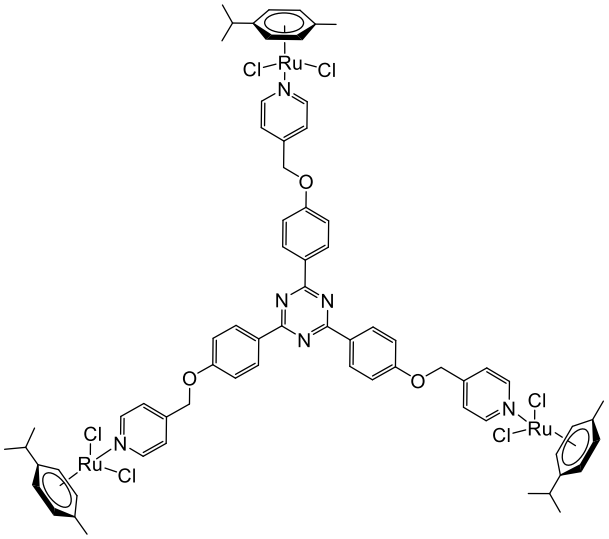

Figure 1.12: *Structure of a trinuclear ruthenium functionalized pyridyl aromatic ether displaying IC_{50} values comparable to chloroquine.*[104]

Due to the complex being polyaryl in nature it is capable of intermolecular π-π interactions and it is therefore possible that hemozoin formation is inhibited due to π-π stacking with hematin.[104] Furthermore, this complex displayed a lower resistance index (RI) compared to CQ, suggesting increased activity against the CQ-resistant strain relative to the CQ-sensitive strain of the parasite.[104] RI values are useful in the analysis of potential drug candidates and provide essential information on whether or not this drug candidate is susceptible to the same resistance mechanism as established drugs; where a low RI value (i.e. ≤ 1) is desired.[104]

Furthermore, a series of 2-phenylbenzimidazole Ir(III), Rh(III), and Ru(II) cyclometallated complexes were synthesized by Rylands *et al*. and evaluated for their antiplasmodial activity against both CQ-sensitive (NF54) and CQ-resistant (K1) strains of *P. falciparum.*[108] An example is the trifluoromethyl iridium(III) cyclometallated complex (Figure 1.13), which displays IC_{50} values of 1.62 ± 0.04 µM and 1.20 ± 0.23 µM in the NF54 and K1 strains respectively.[108] Despite not being comparable to CQ (IC_{50} = 0.044 and 0.29 ± 0.04 µM in the NF54 and K1 strains respectively), the RI value of this complex (0.74) is significantly lower than the RI of CQ (6.59), suggesting that this complex maintains its activity in the resistant strain, showing no cross-resistance.[108]

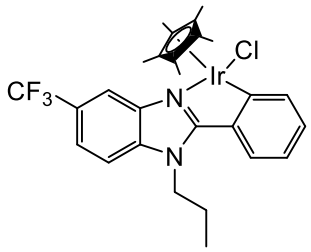

Figure 1.13: *Benzimidazole-containing iridium(III) cyclometallated complex.*[108]

1.3.2.1 Quinoline-based PGM metalloantimalarials

Despite there being a limited number of effective PGM complexes displaying antimalarial activity, there are significantly more PGM complexes, containing quinoline scaffolds, that display promising to excellent antiplasmodial activity, some far exceeding that of CQ.[109-113] As discussed in Section 1.1.3, several organic compounds have been used in the treatment of malaria, many of which contain a quinoline scaffold, emphasizing the importance of this pharmacophore.

One of the most successful approaches thus far, within the field of metalloantimalarials, has been the modification of CQ with metal-containing fragments (e.g. FQ).[2] The complexation of CQ can alter not only the electronic properties but the transport, bioavailability, and other pharmaceutically

relevant properties of this parent compound.[2,114] Incorporating a metal also introduces several alternative chemical and biochemical pathways, providing potentially new mechanisms of antimalarial action e.g. DNA-metal binding.[114] Compared to their organic counterparts, several complexes of both CQ and its derivatives have shown increased efficacy in CQ-sensitive, and most notably, in CQ-resistant strains of *P. falciparum*,.[2,109,110]

An early study on a first-generation $[RuCQCl_2]_2$ complex (Figure 1.14) reported a significant enhancement of the parent drug (CQ) against CQ-resistant (FcB1 and FcB2) strains of *P. falciparum* (2 – 5 fold more effective), following complexation.[109] The mechanism by which *Plasmodium* parasites become resistant to CQ involves reduced uptake of the drug.[115] It has been reported that the principal target of $[RuCQCl_2]_2$ is heme aggregation.[114] Since the activity of this compound exceeds that of CQ in the resistant strains (when measurements were taken at the interface of *n*-octanol/aqueous acetate buffer mixtures, pH < 5), it suggests an alternative uptake mechanism, allowing it to overcome CQ-resistance.[114]

Later, Ru(II)-CQ complexes of the general formula $[Ru(\eta^6\text{-arene})(CQ)Cl_2]$ were synthesized, which displayed activity against both CQ-sensitive (PFB, FcB1, 3D7, and F32) and -resistant (W2, K1, and Dd2) strains of *P. falciparum.*[110] Ruthenium complexation, in particular, offers the chance to counteract some of the biochemical mechanisms that are responsible for CQ-resistance,[72,114,116] with the potency of the complexes synthesized exceeding that of chloroquine diphosphate (CQDP) in the resistant strains of the parasite.[110]

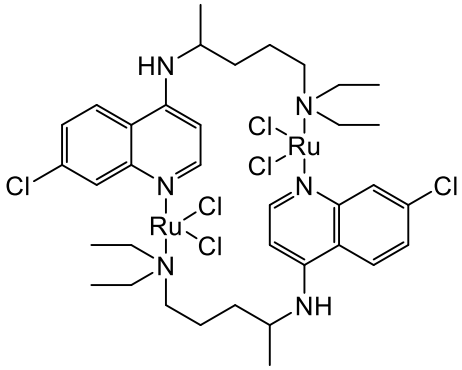

Figure 1.14: *Structure of* $[RuCQCl_2]_2$.[109]

Driven by the success of FQ and the similarity between the chemistry of ferrocene and ruthenocene, ruthenoquine (RQ) (Figure 1.15) (a ferroquine analogue) and its structural derivatives were synthesized by Chibale and co-workers.[111-113] These complexes displayed high *in vitro* efficacy against both CQ-sensitive and -resistant strains of *P. falciparum*, showing potency comparable to those obtained for analogous ferrocene compounds.[111-113] Similarly, as observed for FQ, the addition of the ruthenocene moiety was essential for overcoming CQ-resistance.[117]

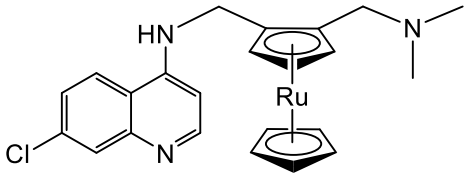

Figure 1.15: *Structure of ruthenoquine synthesized by Chibale et al.*[111]

There is the potential for these complexes to develop cross-resistance, given the resemblance to their parent drug.[2,116] Despite this, metal coordination to antimalarial drugs, in most cases, offers improved activity compared to the parental organic drug, against both CQ-sensitive and -resistant strains of the parasite.[2,116] The possible metal-drug synergism between the active, organic, antimalarial portion of the molecule, and the metal, is thus beneficial for the overall activity.[2,4,118] Direct interaction between the metal centre and specific parasitic biomolecular targets can also potentially inhibit parasite growth, with metal ion toxicity possibly inducing electronic stress and oxidative damage within the parasite.[2] Furthermore, the discovered ability of the metal to avoid detection by the transmembrane proteins, which is a cause of resistance, leads to increased accumulation of the drug inside the food vacuole of the parasite.[2] Although further studies are needed on the potential long term effects of metal ion accumulation and metabolism, for the most part, metal coordination compounds have proven to be advantageous over their organic counterparts in combatting the rising resistance against known antimalarials.

1.3.3 PGM anticancer agents

Resistance, however, is not a problem exclusive to malaria but is experienced within cancer therapy as well. The clinical success of the anticancer drug cisplatin (and related Pt complexes), the side-effects associated with Pt-based drugs, and the emerging drug resistance, has fuelled the search for new and active complexes, containing alternative transition metals, with improved properties.[119]

A study by Liu *et al.* involved synthesizing a series of functionalized cyclopentadienyl Ir(III) complexes, which were investigated for their cytotoxicity toward A2780 human ovarian cancer cell lines.[119] Complexes **a** and **b**, shown in Figure 1.16, exhibit potent cytotoxicity (IC_{50} = 0.72 ± 0.01 and 0.57 ± 0.09 μM respectively) with activity approximately two-fold greater than cisplatin (IC_{50} = 1.22 ± 0.12 μM) in the A2780 cancer cell line.

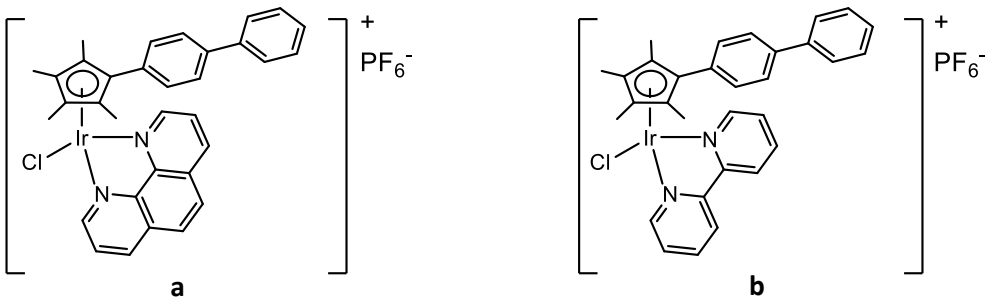

a **b**

Figure 1.16: *Structures of **a**) [(η^5-$C_5Me_4C_6H_4C_6H_5$)Ir(phen)Cl]PF_6 and **b**) [(η^5-$C_5Me_4C_6H_4C_6H_5$)Ir(bpy)Cl]PF_6 which displayed cytotoxicities in the low micromolar range.[119]*

Moving away from the traditional idea that ligands are merely metal binders, various multifunctional ligands are being developed and tailored to improve the applicability of metal-based compounds as medicinal agents.[120] Hartinger and co-workers[121] utilized the knowledge that nonsteroidal anti-inflammatory drugs, such as aspirin and meloxicam, have chemotherapeutic effects, playing a role in not only the prevention but inhibition of tumors.[122-124] The group thus synthesized a series of novel oxicam ligands which they coordinated to bioactive ruthenium and osmium metal centres.[121] Bidentate coordination of these ligands, particularly to osmium, resulted in enhanced biological activity compared to the parent organic compound, against a range of cancer cell lines.[121] The most active complex is shown in Figure 1.17, with cytotoxicity exceeding that of NAMI-A against human colorectal (HCT116), non-small-cell lung (NCI-H460), colon (SW480), and cervical (SiHa) cancer cell lines.[121]

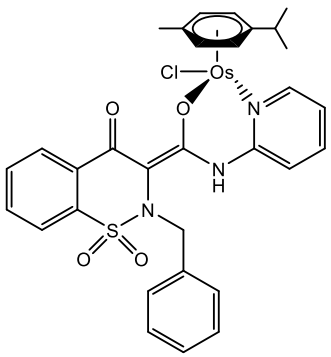

Figure 1.17: *Structure of chlorido(2-benzyl-4-oxido-N-(pyridin-2-yl)-2H-benzo[e][1,2]thiazine-3-carboxamide 1,1-dioxide)(cym)osmium(II), with a cytotoxicity exceeding NAMI-A in various cancer cell lines.[121]*

Due to their relatively low toxicity and preferential accumulation within cancer cells, Ru(II)-arene complexes have attracted increasing attention as potential bioorganometallic anticancer agents.[99,100,125,126] Excellent examples include NAMI-A[127,128] and KP1019 (Figure 1.18) which have both reached the stage of clinical evaluation in humans.[129] Particular interest in NAMI-A stems from its anti-metastatic activity and relatively low host toxicity.[101] The effects on tumour metastases by NAMI-A involves modulating biological processes rather than being destructive toward DNA or other biological targets of the cell replicative mechanism.[130] This is the key distinguishing feature of NAMI-A compared to other platinum anticancer drugs; despite the uncertainty in the exact mechanism of anti-metastasis, DNA is not the major target.[131] On the other hand, KP1019 proved to be an effective cytotoxic agent in the treatment of platinum-resistant colorectal cancers.[132] In a pilot clinical phase I study, patients treated with this compound experienced no serious side-effects and disease stability of up to 10 weeks was achieved in five of the six treated patients.[133] Unfortunately, poor solubility delayed further clinical testing. This was overcome by replacing KP1019 with its more soluble analogue NKP-1339, with a sodium counterion (Figure 1.18).[134] Several reviews provide further detail on these complexes, including their development, *in vitro* and *in vivo* activities, biomolecular interactions, and possible mechanisms of action.[129,135-139]

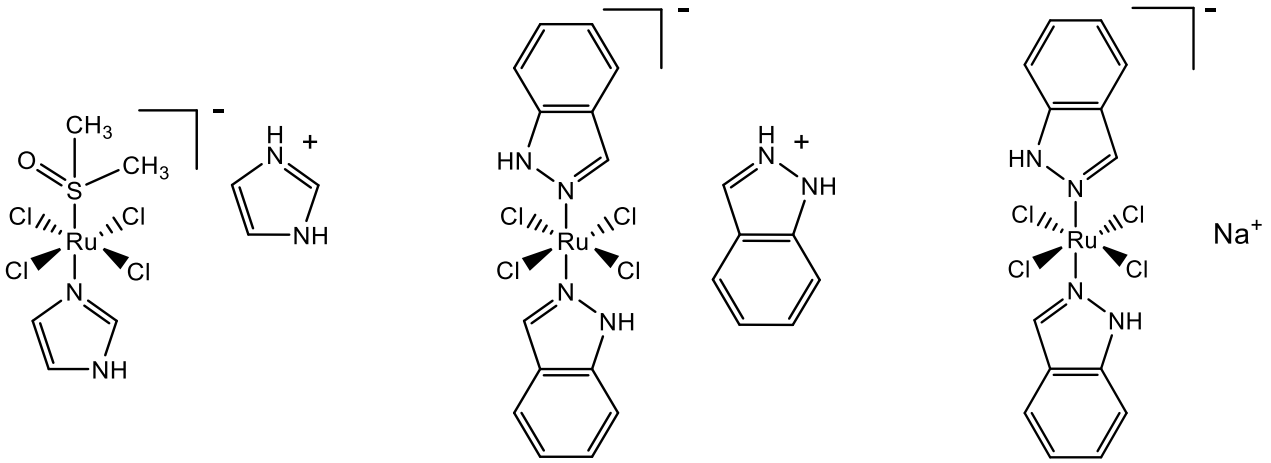

Figure 1.18: *Structures of NAMI-A, KP1019, and NKP-1339.*

Another example is the water-soluble organometallic species [Ru(η^6-toluene)Cl_2(pta)] (pta = 1,3,5-triaza-7-phosphatricyclo-[3.3.1.1]decane) synthesized by C. S. Allardyce *et al.*,[140] that shows high selective antimetastatic activity *in vivo* but rather weak cytotoxicity *in vitro*, a trend similarly observed for the *in vitro* and *in vivo* effects of NAMI-A.[141,142] Despite neither compounds showing activity

against primary tumours, both reduce the number and weight of metastases cells, with [Ru(η^6-toluene)Cl_2(pta)] having a clearance rate slightly superior to NAMI-A.[141,142]

1.3.3.1 Quinoline-based PGM anticancer agents

As mentioned, the quinoline scaffold is a widely recognized and used pharmacophore. Considering that the well-known antimalarial drug CQ showed anticancer activity,[46,47] it is not surprising that newly synthesized quinoline-containing complexes are tested for both their antimalarial and anticancer activity. The ruthenium-CQ antimalarial shown in Figure 1.14, synthesized by Rajapakse *et al*., was also tested for its antitumor activity.[110] This complex showed promising activity, inhibiting the growth of both colon and liposarcoma cancer cell lines.[110] There are currently no effective therapies for the treatment of liposarcoma and as a result, this complex serves as a potential drug candidate for its treatment.[110]

Moreover, Paitandi *et al.* synthesized two iridium complexes based on a pyrazole-appended quinoline-based BODIPY (Figure 1.19).[143] The cytotoxicity of these complexes were studied against the human cervical cancer cell line (HeLa) and showed increased potency compared to the corresponding free ligand,[143] highlighting the benefits of metal incorporation. Furthermore, the IC_{50} values of complexes **1** and **2**, at 24 h, were comparable to cisplatin under analogous conditions.[143] Finally, the selectivity of these complexes toward cancer cells over normal cells (HEK293) were evaluated.[143] Both complexes showed less toxicity toward the HEK293 cells, with IC_{50} values exceeding that of cisplatin.[143]

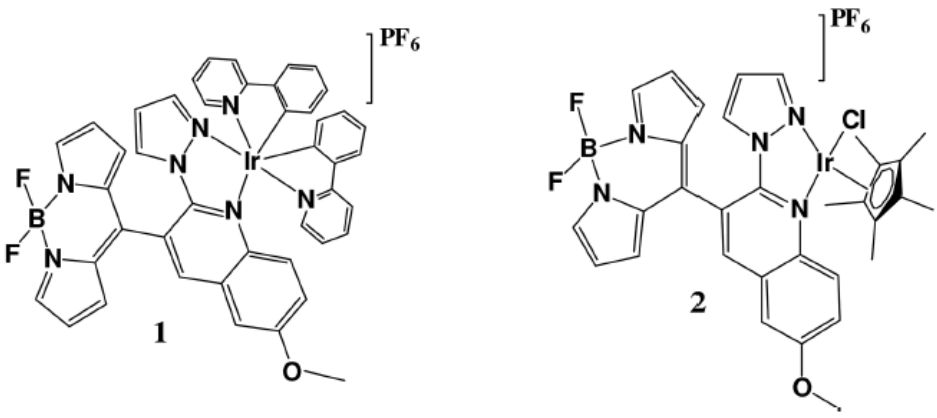

Figure 1.19: *Structures pyrazole-appended quinoline-based BODIPY Ir(III) complexes.*[143]

It is evident that a cooperative effect between the active, organic portion of the compound and the metal, are beneficial for the overall activity of potential drug candidates. This is supported by a plethora of studies reporting on the enhanced pharmacological activity of organic compounds upon metal complexation.[94,104,108,110,121,143] The widespread application of the aforementioned drugs and the various other biologically active metal complexes that are being designed are a testament to the importance of transition metal ions within various fields in biology. Despite extensive research into the pharmacological activity of metal-based compounds, investigations into the pharmacological activity of metallosupramolecular coordination compounds have only centred on their potential anticancer activity. The exploration into the use of such complexes for the treatment of additional diseases is limited, however, due to their intrinsic properties, this warrants further exploration.

1.4 Metallamacrocycles

1.4.1 Supramolecular Chemistry

It is well-known that nature has the ability to assemble extremely complex biomolecules from rather simple molecular precursors.[144] These precursor building units possess functionalities, in specific configurations, allowing them to interact with each other in a deliberate manner.[144] Nature further makes use of various weak, non-covalent interactions such as donor-acceptor, hydrogen-bonding, π-π, and van der Waals interactions.[144,145] These intermolecular interactions allow for the self-assembly of complex architectures that are of critical importance for living organisms.[144] Self-assembly is defined as a spontaneous process in which organized structures are formed from an initially disordered state.[146] Examples of self-assembly in nature include nucleic acid assemblies, such as DNA, and protein folding.[144,145] The presence of these weak interactions are important for two reasons. Firstly, they maintain structural integrity while allowing for a large degree of flexibility.[145] This enables these self-assembled biomolecules to undergo conformational changes that are necessary for their function.[145] Secondly, due to the large number of weak interactions present, there is increased specificity through annealing processes.[145,147] This allows defect structures to be corrected, enabling the formation of the most thermodynamically favoured structure.[145,147] Consequently, such structures inspired chemists, seeking to exploit the aforementioned weak interactions, to design and synthesize scaffolds that can rival the complexity of natural systems.[144,145]

Supramolecular chemistry, also known as the chemistry of the intermolecular bond, results from the association of two or more chemical species that are held together by intermolecular forces, such as non-covalent interactions.[148,149] This field is highly interdisciplinary, crossing boundaries in and between the fields of chemistry, biology, and physics.[144] For synthetic chemists, increasing interest in this field is partly due to the complex and variously aesthetically pleasing structures of supramolecules and their resultant novel, physical and chemical properties.[144] The discovery of "crown ethers"[150], "spherands",[151] and "cryptands"[148], in the 1960s, was the first step toward realizing that complementary molecules can recognize each other *via* non-covalent interactions.[144] Furthermore, the physicochemical properties of these resultant large supramolecules differed from those of the precursor units.[144]

It should also be further noted that macrocycles themselves, such as crown ethers, have several features that make them ideal to tackle "difficult" targets. Due to their complexity and size, macrocycles can engage with targets through numerous binding sites, across a wide spatial distribution, resulting in increased affinity and selectivity.[152,153] Furthermore, cyclization provides a degree of structural pre-organization, which compared to linear analogues, may increase the strength of intermolecular interactions.[152-154] However, it is important to note that macrocycles are not entirely rigid, but rather offer a suitable compromise between structural pre-organization and flexibility, which can facilitate interactions with dynamic targets.[152-154] Some reports have also suggested that cyclization has a desirable impact on other essential properties necessary for drugs, such as metabolic stability, cell permeability, and overall pharmacokinetics.[152-154]

Supramolecular chemistry, which governs the host capabilities of the aforementioned macrocycles, can be broadly divided into three main branches, depending on the driving force of the assembly process.[144] These include i) supramolecular assemblies that utilize H-bonding motifs, ii) supramolecular assemblies that form primarily as a result of non-covalent interactions, such as van der Waals, π-π stacking, ion-dipole, and ion-ion interactions and finally iii) assembly processes that employ directional metal-ligand bonds (coordination-driven self-assembly).[144] Organic assemblies can take on a multitude of arrangements due to an almost infinite array of covalent links.[155] On the other hand, the inherent preferences of metals for particular geometries and metal-ligand orientations allow coordination assemblies to be highly directional, and thus the latter approach affords greater control.[144,155] Consequently, these building units assemble in a predictable nature to form well-defined and discrete supramolecules.[144]

1.4.2 Coordination-driven self-assembly

A critical feature of coordination-driven self-assembly is the directional and thus highly predictable nature of metal-ligand bonds.[144,149,155] The organic ligands serve as the donor building blocks and generally have two or more binding sites, at specific angular orientations. The metal-containing units, the acceptors, possess available coordination sites that are at a fixed angle relative to each other and allow for binding of the incoming ligands.[144] The number of binding sites available on the ligand and the number of available coordination sites on the metal, as well as the angles between them, guide the shape of the target assembly (Figure 1.20).[144] The spontaneous formation of metal-ligand bonds within a solution, in mixtures that contain both metal (donor) and ligand (acceptor) precursors, is defined as coordination-driven self-assembly.[71,149] This process has proven to be a powerful tool to synthesize unique and discrete supramolecular architectures with controlled sizes and shapes,[144,149,156] where the generated product is thermodynamically-favoured.[149] Despite macrocyclization being a kinetically unfavoured process, the formation of metallacycles are favoured under thermodynamic conditions.[144] This is due, in part, to the fact that entropy favours closed structures that are formed from a minimum number of components, rather than polymeric structures formed from a larger number of components.[144]

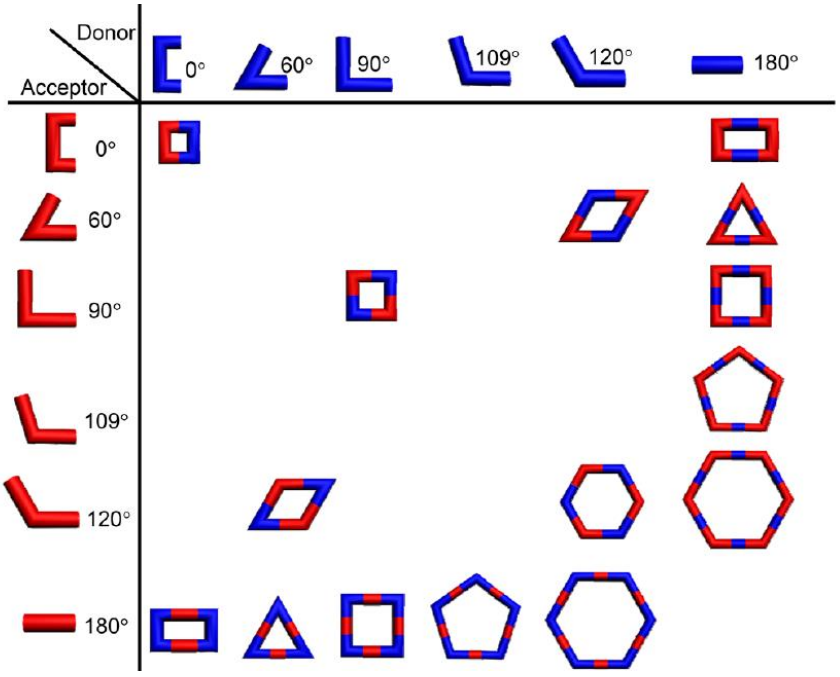

Figure 1.20: *Image showing the ditopic building units required to generate a suite of 2D convex polygons, via self-assembly.*[146]

The energy of metal-ligand bonds (15 – 50 kcal/mol) is of intermediate strength.[144-146] Compared to the weak non-covalent interactions discussed previously and the strong covalent carbon-carbon bonds in organic compounds, heteroatom-metal bonds are substantially labile.[144,145,149] This allows for kinetic reversibility within the self-assembly process.[144,149] This kinetic reversibility between the precursor building units, the intermediates, and the self-assembled architectures allow the system to self-correct and automatically rectify structural defects en-route to the most thermodynamically stable assembly.[144,145,149] This is achieved *via* several association and dissociation steps (Figure 1.21).[144,149] Consequently, this approach relies on thermodynamic control, to ensure the final assembly represents the thermodynamic minimum and is thus more thermodynamically stable than the precursor components and any kinetically formed intermediates.[144,149]

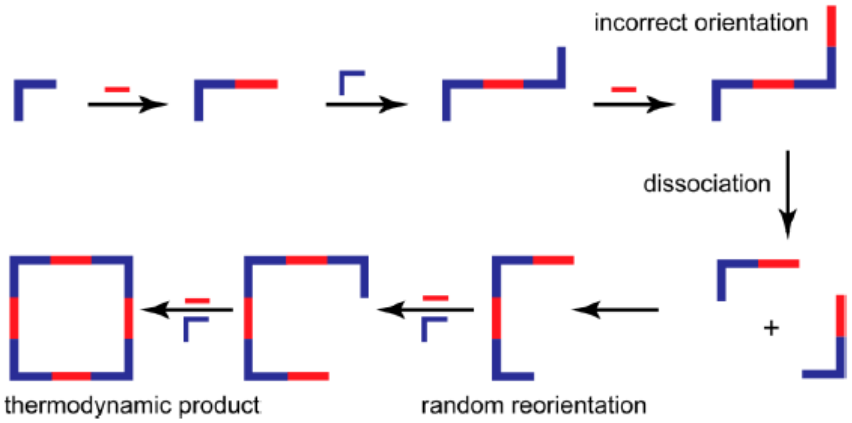

Figure 1.21: *Image taken from T. R. Cook and co-workers, showing the self-assembly process.[149] The image shows the continuous association and dissociation of fragments in solution until the most thermodynamically favoured (desired) structure is formed.*

There are two basic structural requirements when utilizing coordination-driven self-assembly to construct supramolecular architectures.[144] Firstly, the complementary precursor units need to have predefined bite angles and therefore be structurally rigid.[144] The fixed coordination geometries of transition metals allow them to self-assemble with various donors to form predictable architectures.[144] Furthermore, it is imperative that the correct stoichiometric ratios of the precursors are used.[144]

1.4.3 Supramolecular coordination complexes

Supramolecular coordination complexes (SCCs), formed *via* coordination-driven self-assembly, are *finite* systems that are stabilized by non-covalent intermolecular interactions, such as hydrogen bonding, π-π stacking, and van der Waals forces.[149] These constructs are formed, as mentioned, from selected metal centres that self-assemble with ligands that contain multiple binding sites.[149] These binding sites are orientated with a specific angularity, allowing for the generation of a closed structure.[149] It is important, however, to distinguish between metal-organic frameworks (MOFs) and SCCs, as both constructs are based on the same principle and are thus oftentimes confused.[149] For both systems, the geometry of the polyfunctional organic ligands (linker) and the coordination geometry of the metal ions (nodes), influence the final shape/structure of the resulting material.[157]

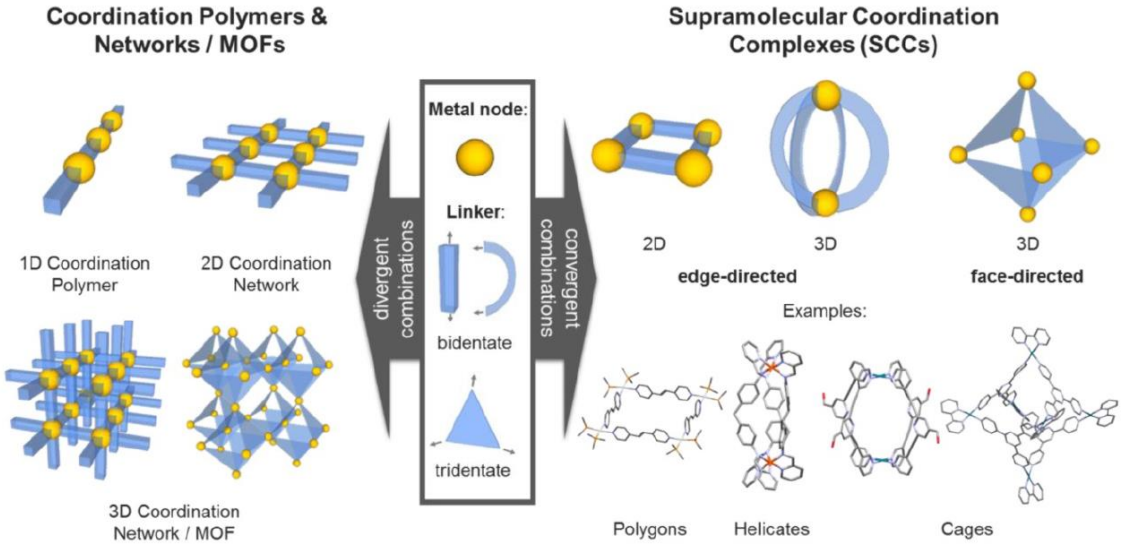

Figure 1.22: *Different types of metal-based assemblies formed from either a divergent or convergent arrangement of metal nodes and organic linkers.*[157]

However, the key distinguishing feature is in the arrangement of these linkers and nodes. Should the combination of the linker and node lead to a divergent arrangement, *infinite* networks or coordination polymers (e.g. MOFs) can be formed (Figure 1.22 – left).[149,157] Contrary to that, should a convergent arrangement occur, *discrete* or *finite* SCCs are formed (Figure 1.22 - right).[157] Therefore, by careful selection of the individual components, in the correct stoichiometric ratios, both the shape and size of the final structure can be controlled, enabling the synthesis of a library of compounds suited for specific requirements.

Due to the several promising organometallic fragments available for the construction of novel supramolecular materials, the design and synthesis of organometallic macrocyclic complexes is becoming a rapidly growing field of interest.[158] The self-assembly of pre-organized transition-metal complexes with polyfunctional ligands, to give discrete supramolecular complexes, has been studied by several groups,[144,159] with the final shape being dependent on the symmetry, type, and stoichiometry of the building units involved.[160,161]

1.4.4 Metallarectangles

In the 1900s, the Fujita group pioneered the construction of metallacycles *via* self-assembly.[162] This group utilized a stable cis-capped, square planar Pd(II) precursor and a rigid linear ligand (4,4'-bipyridine) to construct a square architecture (Figure 1.23).[162,163] Consequently, four $[enPd(II)]^{2+}$ (en = ethylenediamine) units were bridged by four linear ligands and due to the nature of the metal precursor used, there was no doubt about right angles at the corners.[162] The early adoption of 4,4'-bipyridine as a building block for SCCs can be attributed to its structural rigidity as a linear ditopic donor, its immediate availability from a range of commercial sources, and finally, its suitability as a ligand for an array of metals.[149] The bipyridine group has also been shown to be an important feature within some natural products, namely caerulomycins and collismycins, which have been shown to possess cytotoxic and antibiotic activity.[164-166] Furthermore, ^{1}H NMR spectroscopy confirmed that the resultant complex was formed under thermodynamic control.[162,163]

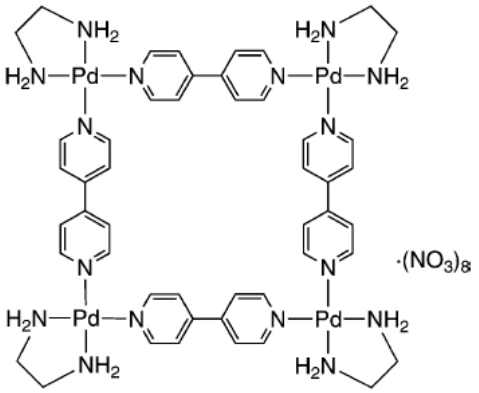

Figure 1.23: *Image of the first molecular square, synthesized via self-assembly, using a transition metal.*[162]

These initial investigations were prompted by the inability to incorporate 90° angles into organic frameworks without a level of framework or structural distortion.[163,167,168] The incorporation of a 90°

angle would allow for an array of new structures to be generated and this resulted in the exploitation of the 90° co-ordination angles present in some transition metals.[163]

As shown in Figure 1.24a, a molecular square can be formed by combining a 90° corner unit, in a 1:1 mole ratio, with a linear bridging ligand.[144] The synthetic strategy for the spontaneous assembly of a metallasquare involves a single step.[144,158] However, the one-step synthesis of a metallarectangle is not possible.[158,160] The combination of 90° corner units with two different rigid bifunctional ligands, does not yield the intended metallarectangle, instead, two metallasquares of different sizes (Figure 1.24b).[144,169] This is due to two reasons; (i) there is a strong enthalpic driving force that favours square formation and (ii) there is a lack of selective recognition by the two different ligands.[144] With metallarectangles being the focus of this study, it is important to note that a step-wise synthetic procedure is required for the synthesis of rectangular architectures.[158,160,170]

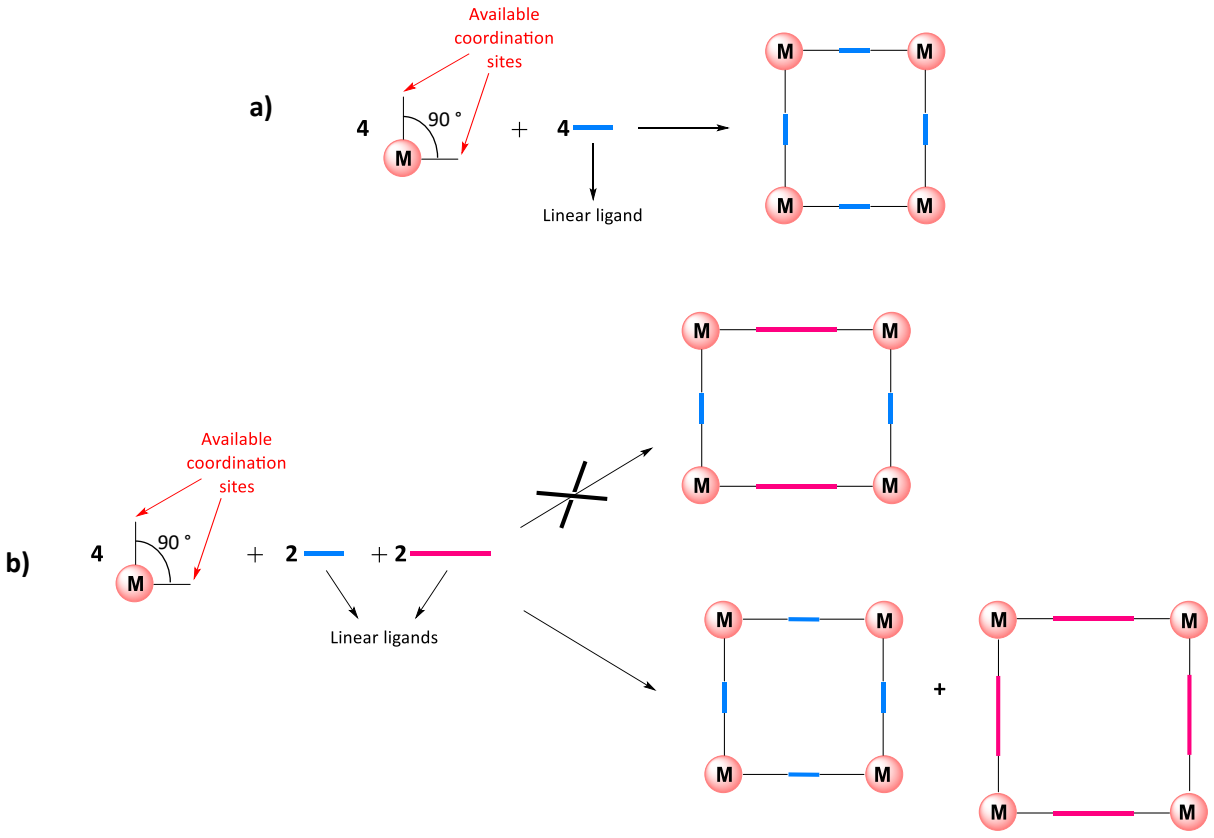

Figure 1.24: *(a) A 90° building unit and a rigid linear ligand lead to the formation of a metallasquare, (b) A 90° corner unit and two ligands, of different lengths, resulting in the formation of two metallasquares, instead of the desired metallarectangle.*

1.4.4.1 Design principles and structure

In most studies concerning rectangular architectures, the first step toward their synthesis requires synthesizing a stable pre-organized bimetallic molecular clip.[156,159,160,170-175] Transition metals are utilized due to their well-defined and predictable coordination geometries, compared to main group metals, which are unpredictable and thus less favoured.[144,145] To synthesize a discrete supramolecular architecture, as opposed to an extended coordination polymer, directing ligands are utilized to occupy concomitant coordination sites at the octahedral metal centre, for metals such as iridium and ruthenium.[145,149,161] Coordinatively inert directing ligands such as cyclopentadienyl (Cp), pentamethylcyclopentadienyl (Cp*), and arene-based ligands can be used to better control the accessibility of coordination sites at these metal centres.[149,158,160,161,176] These η^5 (Cp or Cp*) and η^6 (*p*-cymene) ligands occupy three of the six coordination sites, generating a "preorganized arrangement" (Figure 1.25).[158,160,161,176] Half-sandwich transition metal complexes are thus promising building blocks and have been extensively used to generate metallacycles,[71,144,159,161,177] as the incoming ligands are limited by the number of available coordination sites and their relative angularity.[145,149,158,160,161,176] Since the coordination sites are at a fixed angle relative to each other, a suitable bifunctional pyridyl-based donor, which acts as a bridging ligand, coordinates predictably to generate the [2+2] rectangular 2-D architecture (Figure 1.25). [156,159,160,170-175] SCCs synthesized from two components are often referred to as [m + n] self-assemblies, where m and n denote the number of acceptor and donor units respectively, in a single discrete ensemble.[149]

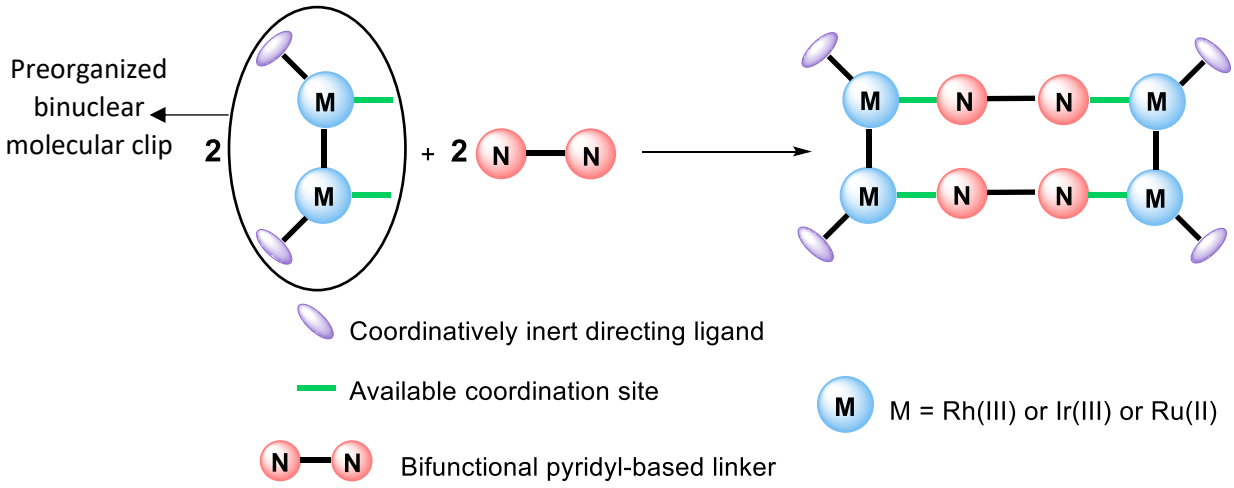

Figure 1.25: *Schematic representation of the [2+2] self-assembly of metallarectangles.*

It is important to understand how the building blocks, both the metals and ligands, can modulate the final shape and size of the discrete architecture.[159] The structure and size of the metallacycle can be easily fine-tuned by adjusting the shape and/or length of the bridging ligands and binuclear molecular clips.[156,159] Consequently, the final shape is dependent on and predetermined by the metal starting material, including its reactivity, coordination geometry, number of available coordination sites, and their relative orientation to each other. [144,145,149] It is further influenced by the coordinatively inert directing ligands such as Cp* or *p*-cymene, and the donor ligands used, including the number of donor sites and their mode of coordination. [144,145,149]

1.4.4.2 Synthesis

The self-assembly of molecular building blocks, containing various metals and polydentate ligands, can give rise to a plethora of discrete supramolecular 2-D metallacycles, such as squares and rectangles, or 3-D metallacages of different shapes and sizes. [144,159,160,170,171,173,178-181] Wang *et al*. synthesised the rectangular complex [{Ir(Cp*)}$_4$(μ-dhbq)$_2$(μ-N,N)$_2$](OTf)$_4$, *via* a [2+2] self-assembly, following a two-step strategy (Figure 1.26).[173] The first step involved synthesizing a preorganized, half-sandwich, binuclear molecular clip (Figure 1.26 – **1**), containing the bridging ligand 2,5-dihyroxy-1,4-benzoquinone (H_2dhbq).[173] The six-fold bridging capability of octahedral metal centres leads to diverse dimensionality within compounds, compared to those possessing a square planar geometry.[176] As mentioned, ligands such as Cp* occupy three coordination sites at the octahedral metal centre and thus control the accessibility of coordination sites to the incoming ligands, reducing the dimensionality.[158,160,161,176] Following chloride abstraction, the available coordination sites are at a fixed angle relative to each other. The subsequent step involved reacting the binuclear complex **1** with a suitable bifunctional ligand, which self-assembled, *via* a series of association and disassociation steps, until the most thermodynamically stable discrete construct was formed as its triflate salt (Figure 1.26 – **2** and **3**).[173] As mentioned, this step-wise strategy is necessary to synthesize metallarectangles and has been employed by several groups, utilizing various building units, to synthesize metallarectangles of varying sizes[159,160,170,174,175,182-188] and applications.[71,159,171,180,189]

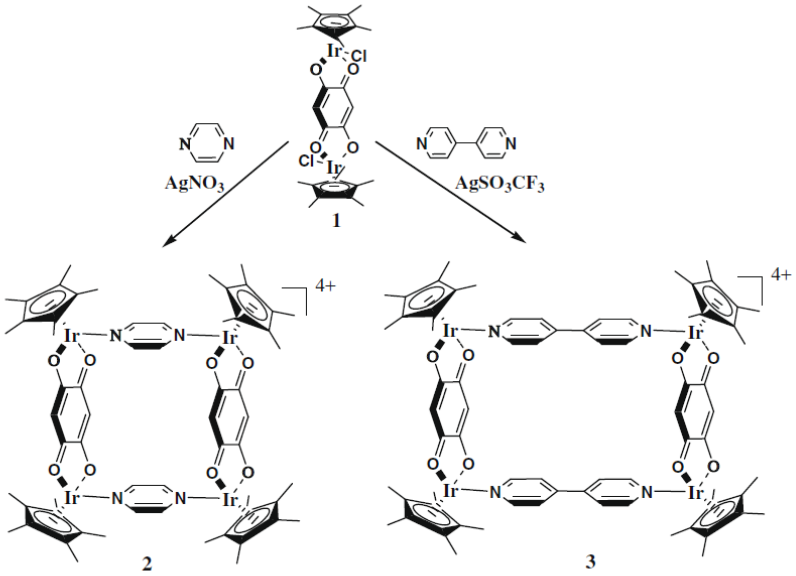

Figure 1.26: *Image taken from Wang et al., showing the step-wise synthesis of metallarectangles* ***2*** *and* ***3****.*[173]

1.4.4.3 Characterisation methods

The greatest challenge posed within the field of supramolecular chemistry is the characterization of the supramolecular complexes themselves, particularly the large, highly symmetrical, and discrete self-assembled entities.[190,191] Furthermore, small changes such as the solvent, the presence of a guest and slight modifications in the metals and/or ligands used, can have a huge impact on the characteristics of the resulting assembly.[191] Technological advancements in the characterization methods used to explain the structural phenomenon of these complexes have further spurred the growth of this field.[144] Since the formation of SCCs are driven by coordination-driven self-assembly, many of the commonly used characterization techniques in supramolecular chemistry can be applied to these complexes.[189] The more commonly used techniques, including various 1- and 2-D NMR spectroscopic techniques (^{1}H, COSY, NOESY), diffusion-order NMR spectroscopy (DOSY), mass spectrometry (MS), and X-ray diffraction,[189] will be discussed in this section.

1.4.4.3.1 Nuclear Magnetic Resonance Spectroscopy

Nuclear magnetic resonance (NMR) spectroscopy is one of the most commonly used techniques, not only within supramolecular chemistry but across all disciplines within chemistry. Despite not offering any structural information, ^{1}H NMR spectroscopy is oftentimes one of the first techniques used to determine whether a supramolecular architecture has formed.[190] The vast majority of metallamacrocycles, formed *via* coordination-driven self-assembly, are highly charged. This is due to the use of neutral nitrogen donor ligands with oxidized, electron-deficient metal ions. Therefore, an

evident displacement of peaks within the nuclear magnetic field is often indicative of the generation of a supramolecular assembly.[189-191] In most cases, in which pyridyl-based systems are used, an evident downfield shift of these proton signals are observed.[189,191] This is due to the loss of electron density upon coordination of the pyridine nitrogen atom to the electron-deficient metal centre (metal-ligand interactions). Although this technique can provide information about the composition and general features of the assembly, it is considered the most basic characterization method for such complexes.[189,190] Homonuclear 2D correlation NMR spectroscopic techniques, such as COSY and NOESY, provide through-bond and through-space connectivities and can further be used to aid in the assignment of signals and support the proposed structure.[189-191]

Diffusion ordered spectroscopy (DOSY) is a type of diffusion NMR experiment that provides a 2D map, similar to those in 2D NMR, in which the x-axis is the chemical shift and the y-axis is that of the diffusion coefficient. The key feature of this technique is its ability to separate the NMR signals of different compounds within a multicomponent system. This separation is based on the diffusion coefficients of the compounds within a solution, which is dependent on their shape and size.[192] Larger, linear compounds have shown to have smaller diffusion coefficients compared to smaller and more spherical compounds.[192] This technique has also been used to confirm that the complex spectra, often observed for supramolecular assemblies, are an intrinsic characteristic of such complexes, rather than contamination from lower molecular species.[193]

1.4.4.3.2 Mass Spectrometry

Mass spectrometry (MS) is one of the most extensively used characterization tools for supramolecular assemblies.[144,189] This technique can provide information about fragmentation pathways and the structure of the resultant supramolecular assembly.[192] Electrospray ionization (ESI), which is the ionization method used in this study, is known as a soft ionization technique.[189,190,192] Many other techniques are intrinsically harsh, causing dissociation, and are thus incompatible with compounds dominated by relatively weak non-covalent interactions.[144,192] ESI allows for intact ionization of weakly-bound non-covalent compounds, preventing the destruction of the ensemble, and suppresses extensive fragmentation.[144,189,192] This is achieved by keeping the internal energy of the ions low.[144,189] Furthermore, ESI is useful for analysing large, non-volatile, chargeable molecules, generating a broad charge distribution of multiply charged ions.[190,192] This allows for high molecular masses to be observed at relatively smaller *m/z* ratios.[192]

1.4.4.3.3 X-ray Diffraction

X-ray crystallography is currently the most reliable, powerful, and unambiguous method, allowing for the structural analysis of solid-state crystalline supramolecular assemblies and their intermolecular interactions.[189-192] The periodicity of the crystal lattice, in other words, the packing of the molecules, to gain sufficient diffraction power, is an essential property of a suitable crystal.[192] This periodicity is induced by crystal growth, which is a fairly spontaneous ordering/desolvation process that the molecules, ions and/or solvent molecules undergo.[192] Since supramolecular assemblies are held together by weak intermolecular interactions, such crystals are oftentimes sensitive to the environment and consequently unstable.[192] Solvent molecules often play a critical role in the growth of crystalline supramolecular systems and are needed for the construction of the periodical crystal lattice.[192] Therefore, the cavities within supramolecular assemblies are often filled with counter ions and/or volatile solvent molecules, making the crystals highly solvent dependent and thus fragile.[190] Furthermore, the conformational flexibility and structural complexity of self-assembled supramolecular assemblies oftentimes make them difficult to crystallize.[189] X-rays will not diffract and thus X-ray diffraction analysis cannot be performed on an amorphous material.[192] This includes single-crystal X-ray diffraction and powder diffraction.[192] Characterization by X-ray crystallography is sometimes hampered by difficulties in growing high-quality crystals suitable for structural analysis. However, in cases where a suitable crystal can be obtained, single-crystal X-ray diffraction provides the most reliable solid state-structural data, however with a risk of the solid-state structure differing from that in solution.

The intrinsic properties of such complexes, their size, and high symmetry make their characterization rather difficult compared to classical organic and inorganic compounds and instead more akin to the problems of larger biomolecules.[190] The best approach to properly and fully characterize such unique assemblies lies in combining as many of the aforementioned techniques as possible, including any additional techniques, and using them in conjunction to support the desired structure.[189,190] The accelerating interest in the synthesis and characterization of supramolecular assemblies has led to the exploration of these complexes as potential pharmacological agents, however, with a paucity of information on their antiparasitic activity.

1.5 Metallamacrocycles in medicine

Over the years metallamacrocyclic supramolecular complexes, bearing organometallic rhodium, ruthenium, and iridium half-sandwich fragments, have received a considerable amount of attention due to their myriad of potential applications, including as anticancer agents,[157,181,183] in catalysis,[188] and their host-guest,[194-196] and drug-delivery properties.[197-199]

As previously mentioned, metal ions have been exploited to enhance the biological activity of existing organic drugs. The inspiration for utilizing supramolecular species for biological applications stems from their various inherent properties.[71] Firstly, the dimensions of the metallacycle can be easily adjusted without significant synthetic changes (spatially tunable).[71] Secondly, since the coordination geometry is often predictable for a metal centre, having a controllable oxidation state, the metal ion used is versatile (electronically tunable).[71] Furthermore, coordination-driven self-assembly allows functional groups to be incorporated through pre- and/or post-self-assembly modifications.[71] And finally, SCCs generally have distinct internal cavities and thus possess guest/host capabilities, providing promise as drug-delivery scaffolds and cavity materials.[71,160] These intrinsic features of SCCs make them attractive for biological applications.

The biomedical applications of SCCs is still a growing field of study. However, in recent years, SCCs have been investigated as novel cytotoxic anticancer agents, with several studies demonstrating their potential.[184,200-203] These supramolecular compounds have mechanisms of action different from that of classical small-molecules, which is oftentimes related to their unique molecular recognition properties.[157]

1.5.1 In vitro cytotoxicity of SCCs

Biologically active ruthenium- and iridium-based small molecules (Section 1.3) prompted analogous studies of Ru(II) and Ir(III) SCCs.[172] As mentioned in Section 1.3.3, many ruthenium complexes have shown to be promising anticancer agents and have been evaluated both *in vivo* and *in vitro*.[99,100,125,126,128] With reports of Ru(III) complexes currently in clinical trials[133,204] and an arene-Ru(II) complex in an advanced stage of pre-clinical evaluation,[100] it is no surprise that several multinuclear ruthenium supramolecular assemblies have been evaluated as potential anticancer agents.[71,172,183,205-207]

Dubey *et al.* synthesized a tetranuclear ruthenium metallarectangle *via* the [2+2] self-assembly of *N,N'*-di-(4-pyridyl)-1,4,5,8-naphthalenetetracarbo-xydiimide and a binuclear arene ruthenium complex containing *O,O*-bridging 5,8-dihydroxy-1,4-naphthaquinonato (Figure 1.27).[172] Cytotoxicity studies of the complex showed that its potency exceeds that of cisplatin by approximately 7-fold within the AGC gastric cancer cell line.[172] Furthermore, this metallarectangle has shown to be active against the multidrug-resistant colon cancer cell line HCT15/CLO2 (IC_{50} = 16.5 μM), for which doxorubicin, a well-known anti-tumour drug, was ineffective.[172]

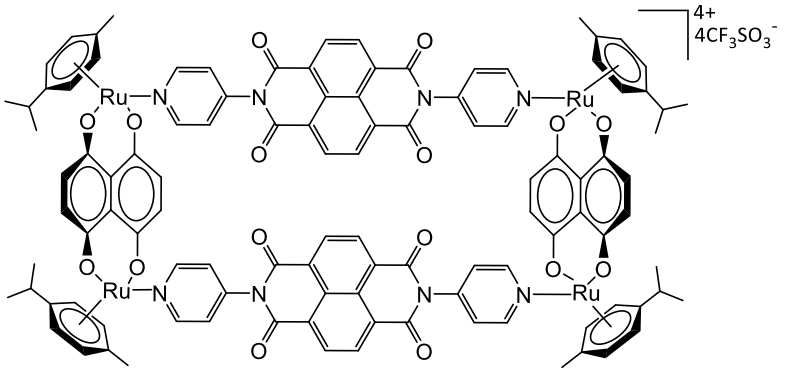

Figure 1.27: *Ruthenium metallarectangle possessing cytotoxicity that exceeds cisplatin in the AGC gastric cancer cell lines.*[172]

This suggests that the mechanism of cytotoxic action of this SCC differs from the classical anticancer drug doxorubicin. Furthermore, the metallacycle displayed antiproliferative effects that exceeded that of its metal precursor and organic ligand, suggesting that the intact metallacycle is responsible for the observed activity.

In another study, Vajpayee *et al*. synthesized a novel ruthenium nano-prismatic cage, with cytotoxicity exceeding that of cisplatin in SK-hep-1 (liver), HeLa (ovary), and HCT-15 (colon) cancer cell lines.[205] Based on previous literature findings this study suggested that the anticancer activity observed in the precursor binuclear complex (Figure 1.28) is enhanced in the metallacage, due to the increased nuclearity and the presence of an extended π-conjugated system.[205]

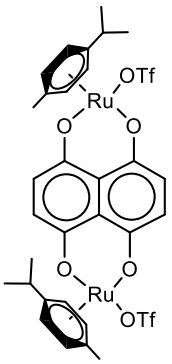

Figure 1.28: *Ruthenium precursor binuclear complex containing the cytotoxic ligand 5,8-dihydroxy-1,4-naphthoquinone, synthesized by Vajpayee et al.*[205]

Furthermore, many Ir(III) SCCs have been synthesized, with many displaying good to excellent biological properties.[182,208-210] Gupta and co-workers synthesized, *via* a [2+2] self-assembly, a benzimidazole-based iridium BODIPY metallarectangle (Figure 1.29) which possess a relatively high selectivity toward cancer cells, superior to that of cisplatin.[208] The cytotoxicity studies revealed that the complex is highly selective for human glioblastoma (U87) and cervical (HeLa) cancer cell lines over non-malignant lung fibroblast cells (WI38), with the activity being attributed to a possible synergistic effect of the iridium metal centre and the ligands used for the self-assembly.[208]

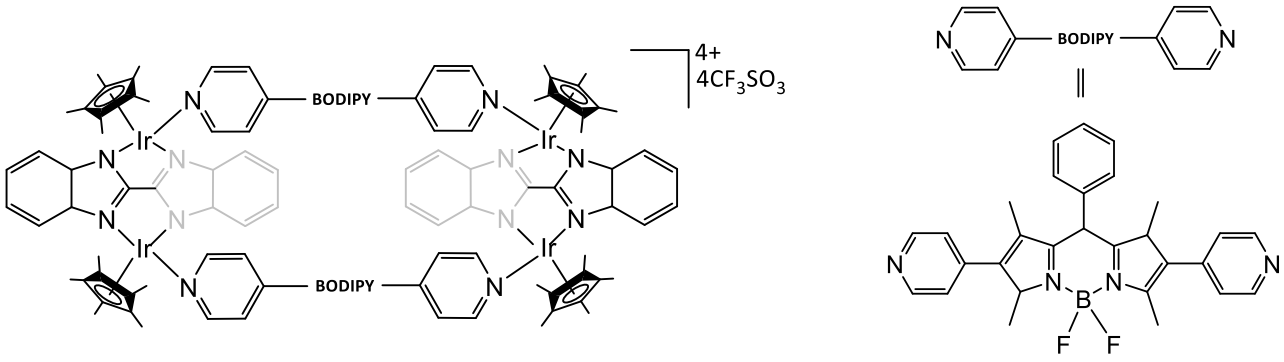

Figure 1.29: *Structure of the benzimidazole-based tetranuclear iridium metallarectangle.*[208]

Undoubtedly, there has been extensive research into the synthesis of SCCs and their resulting anticancer activity. However, it should be noted that this research is still in its infancy with regard to mechanisms of action and the treatment of alternative diseases. Based on research, no studies have analysed and reported on the antiparasitic activity of SCCs. The known antiparasitic activity of several multinuclear complexes (Section 1.3), the intrinsic properties of supramolecular assemblies (Section 1.5), and their potential to impart novel modes of action, lend them to the treatment of infectious diseases.

1.6 Motivation and rationale for the current study

The prevalence of both malaria and cancer, and the emerging drug resistance upon treatment of these illnesses, has hindered efforts to successfully treat and/or eradicate these diseases. The devastating morbidity and mortality statistics surrounding these diseases has prompted research into the discovery of novel drugs with alternative modes of action.

As previously discussed, quinoline-containing compounds have been extensively researched, and despite their initial recognition being in malaria treatment, this pharmacophoric scaffold has been repurposed and proven itself as an anticancer agent. Several quinoline-containing compounds have displayed promising antimalarial and anticancer activity and it is for this reason that the quinoline scaffold, a well-known pharmacophore, will be used in the synthesis of the ligand within this study.

Furthermore, metal incorporation into an organic scaffold has shown to not only enhance the biological activity of the uncoordinated organic ligand but alter the pharmacokinetic and physicochemical properties, potentially imposing novel mechanisms of action. These alternate modes of action can reduce the ability of these compounds to elicit resistance, relative to the parent drug, minimizing cross-resistance and potentially improving the selectivity. The field of bioorganometallic chemistry, therefore, provides promising alternatives to traditional organic drugs.

Literature has also reported on the number of potential applications of supramolecular coordination complexes (SCCs), with extensive research into their anticancer activity. The large and highly charged nature of these multinuclear systems makes them suitable for cancer treatment due to increased selectivity for cancer cells, based on the Enhanced Permeability and Retention (EPR) effect.[211,212] Despite the success of such complexes toward biomedical applications, during this study, no studies have explored the possible antimalarial properties of such complexes. Therefore, the antiplasmodial activity of discrete multinuclear SSCs, incorporating a biologically active pharmacophore into the framework, warrants further exploration. This study aims to explore the anticancer activity of Ir(III) and Ru(II) SCCs, as well as their potential as antiplasmodial agents, while examining possible cross-resistance against various tumour cell lines and parasitic strains.

1.7 Aims and objectives

1.7.1 General aims

As discussed in this chapter, there has been widespread research into the anticancer activity of supramolecular coordination complexes, but none into their potential antiplasmodial activity. Consequently, this research study offered an opportunity to shed some light on this less investigated area within research. As a result, this study aimed to:

- Synthesize a quinoline-containing ditopic ligand.
- Complex the ligand to $[IrCl_2(Cp^*)]_2$ and $[RuCl_2(p\text{-cymene})]_2$ to form the corresponding binuclear complexes.
- Utilize the precursor binuclear complexes, in the presence of $AgCF_3SO_3$, to synthesize the desired metallarectangles, *via* coordination-driven self-assembly.
- Evaluate the synthesized ligand and complexes for their biological activity as potential antiplasmodial and anticancer agents.

1.7.2 Specific objectives

The specific objectives of this study were to:

- Synthesize a quinoline-containing ditopic ligand *via* a Suzuki cross-coupling reaction (Figure 1.30).

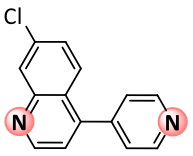

***Figure 1.30**: Structure of 7-chloro-4-(pyridin-4-yl)quinoline.*

- Synthesize Ir(III) and Ru(II) binuclear complexes containing *N,N'*-bidentate ligands (Figure 1.31).

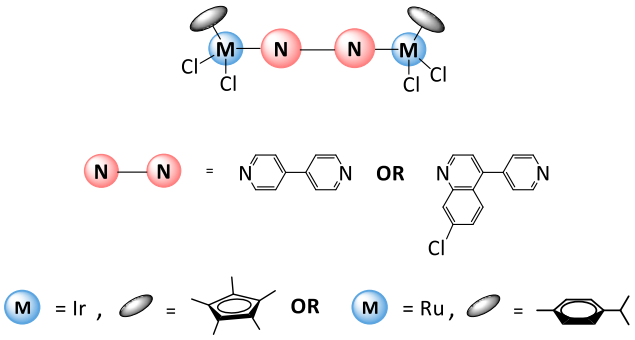

***Figure 1.31:** General structure of the precursor binuclear complex containing the bidentate ligands.*

❖ Utilize the precursor binuclear complexes to synthesize the corresponding cationic metallarectangles, as their triflate salts, *via* coordination-driven self-assembly (Figure 1.32).

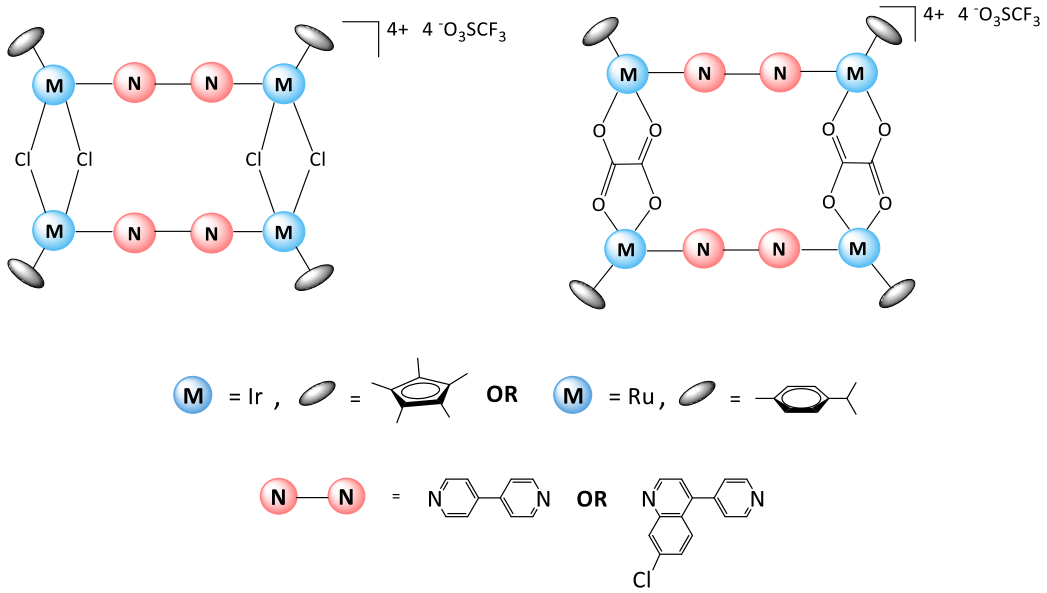

***Figure 1.32**: General structures of the cationic metallarectangles containing bidentate N,N'-ligands.*

❖ Characterize the synthesized compounds using various spectroscopic and analytical techniques including ^{1}H Nuclear Magnetic Resonance spectroscopy (NMR), ^{13}C NMR spectroscopy, DOSY spectroscopy, Fourier Transform-Infrared spectroscopy (FT-IR), high-resolution electrospray ionization (ESI) mass spectrometry, and melting point analysis.

❖ Investigate the *in vitro* antiplasmodial activity of the synthesized ligand and complexes against chloroquine-sensitive (NF54) and chloroquine-resistant (K1) strains of the malaria parasite, *Plasmodium falciparum*, using the *p*LDH assay.

❖ Investigate the *in vitro* anticancer activity of the newly synthesized ligand and complexes against the breast cancer MCF-7 and triple-negative MDA-MB-231 cell lines, using the MTT assay.

❖ Investigate the selectivity and cytotoxicity of the newly synthesized quinoline-based ligand and complexes, against the non-tumorigenic MCF-12A breast epithelial cell line.

1.8 References

1. https://www.who.int/news-room/feature-stories/detail/world-malaria-report-2019.
2. P. F. Salas, C. Herrmann and C. Orvig, *Chem. Rev.*, 2013, **113**, 3450-3492.
3. R. Carter and K. N. Mendis, *Clin. Microbiol. Rev.*, 2002, **15**, 564-594.
4. M. Navarro, C. Gabbiani, L. Messori and D. Gambino, *Drug Discov. Today*, 2010, **15**, 1070-1078.
5. N. J. White, *Science*, 2008, **320**, 330-334.
6. R. Nandal and A. Deep, *GJPER*, 2017, **6**, 22-27.
7. B. M. Greenwood, D. A. Fidock, D. E. Kyle, S. H. Kappe, P. L. Alonso, F. H. Collins and P. E. Duffy, *J Clin Invest*, 2008, **118**, 1266-1276.
8. B. Hanboonkunupakarn and N. J. White, *Trop. Dis. Travel Med. Vaccines*, 2016, **2**, 1-5.
9. R. W. Sutherst, *Clin. Microbiol. Rev.*, 2004, **17**, 136-173.
10. D. J. Rogers and S. E. Randolph, *Science*, 2000, **289**, 1763-1766.
11. N. Singh, A. Pandurangan, K. Rana, P. Anand, A. Ahmad and A. K. Tiwari, *Int. Curr. Pharm. J.*, 2012, **1**, 119-127.
12. R. W. Heidebrecht, Jr., C. Mulrooney, C. P. Austin, R. H. Barker, Jr., J. A. Beaudoin, K. C. Cheng, E. Comer, S. Dandapani, J. Dick, J. R. Duvall, E. H. Ekland, D. A. Fidock, M. E. Fitzgerald, M. Foley, R. Guha, P. Hinkson, M. Kramer, A. K. Lukens, D. Masi, L. A. Marcaurelle, X. Z. Su, C. J. Thomas, M. Weiwer, R. C. Wiegand, D. Wirth, M. Xia, J. Yuan, J. Zhao, M. Palmer, B. Munoz and S. Schreiber, *ACS Med. Chem. Lett.*, 2012, **3**, 112-117.
13. M. Delves, D. Plouffe, C. Scheurer, S. Meister, S. Wittlin, E. A. Winzeler, R. E. Sinden and D. Leroy, *PLoS Med.*, 2012, **9**, e1001169.
14. M. A. Biamonte, J. Wanner and K. G. Le Roch, *Bioorg. Med. Chem. Lett.*, 2013, **23**, 2829-2843.
15. L. Aravind, L. M. Lyer, T. E. Wellems and L. H. Miller, *Cell*, 2003, **115**, 771–785.
16. D. A. Baker, *Mol. Biochem. Parasitol.*, 2010, **172**, 57-65.
17. L. Tilley, P. Loria and M. Foley, *Antimalarial Chemotherapy*, Humana Press Inc., Totowa, New Jersey, 2001.
18. B. L. Tekwani and L. A. Walker, *Comb. Chem. High Throughput Screen.*, 2005, **8**, 63-79.
19. M. Navarro, W. Castro and C. Biot, *Organometallics*, 2012, **31**, 5715-5727.
20. R. Vanderesse, L. Colombeau, C. Frochot and S. Acherar, in *Current Topics in Malaria*, INTECH, 2016, ch. 11, pp. 205 - 233.
21. V. V. Kouznetsov and A. Gomez-Barrio, *Eur. J. Med. Chem.*, 2009, **44**, 3091-3113.
22. S. E. Francis, J. David J. Sullivan and D. E. Goldberg, *Annu. Rev. Microbiol.*, 1997, **51**, 97–123.
23. L. Tilley, P. Loria and M. Foley, in *Antimalarial Chemotherapy*, ed. P. J. Rosenthal, Humana Press Inc., Totowa, NJ, 2001, pp. 87-121.

24. C. Biot, W. Castro, C. Y. Botte and M. Navarro, *Dalton Trans.*, 2012, **41**, 6335-6349.
25. R. A. Jones, S. S. Panda and C. D. Hall, *Eur. J. Med. Chem.*, 2015, **97**, 335-355.
26. R. L. Summers, M. N. Nash and R. E. Martin, *Cell. Mol. Life Sci.*, 2012, **69**, 1967-1995.
27. L. M. Coronado, C. T. Nadovich and C. Spadafora, *Biochim Biophys Acta.*, 2014, **1840**, 2032-2041.
28. T. J. Egan, R. Hunter, C. H. Kaschula, H. M. Marques, A. Misplon and J. Walden, *J. Med. Chem.*, 2000, **43**, 283-291.
29. N. J. White, *Br. Med. Bull.*, 1998, **54**, 703-715.
30. P. S. Callaghan and P. D. Roepe, in *Handbook of Antimicrobial Resistance*, Spring Science & Business Media, New York, 2017, ch. 16, pp. 289-311.
31. D. L. Klayman, *Science*, 1985, **228**, 1049-1055.
32. N. J. White, *Trans. R. Soc. Trop. Med. Hyg.*, 1994, **88**, 41-43.
33. E. A. Ashley, M. Dhorda, R. M. Fairhurst, C. Amaratunga, P. Lim, S. Suon, S. Sreng, J. M. Anderson, S. Mao, B. Sam, C. Sopha, C. M. Chuor, C. Nguon, S. Sovannaroth, S. Pukrittayakamee, P. Jittamala, K. Chotivanich, K. Chutasmit, C. Suchatsoonthorn, R. Runcharoen, T. T. Hien, N. T. Thuy-Nhien, N. V. Thanh, N. H. Phu, Y. Htut, K.-T. Han, K. H. Aye, O. A. Mokuolu, R. R. Olaosebikan, O. O. Folaranmi, M. Mayxay, M. Khanthavong, B. Hongvanthong, P. N. Newton, M. A. Onyamboko, C. I. Fanello, A. K. Tshefu, N. Mishra, N. Valecha, A. P. Phyo, F. Nosten, P. Yi, R. Tripura, S. Borrmann, M. Bashraheil, J. Peshu, M. A. Faiz, A. Ghose, M. A. Hossain, R. Samad, M. R. Rahman, M. M. Hasan, A. Islam, O. Miotto, R. Amato, B. MacInnis, J. Stalker, D. P. Kwiatkowski, Z. Bozdech, A. Jeeyapant, P. Y. Cheah, T. Sakulthaew, J. Chalk, B. Intharabut, K. Silamut, S. J. Lee, B. Vihokhern, C. Kunasol, M. Imwong, J. Tarning, W. J. Taylor, S. Yeung, C. J. Woodrow, J. A. Flegg, D. Das, J. Smith, M. Venkatesan, C. V. Plowe, K. Stepniewska, P. J. Guerin, A. M. Dondorp, N. P. Day and N. J. White, *N. Engl. J. Med.*, 2014, **371**, 411-423.
34. A. J. Lin, D. L. Klayman and W. K. Milhous, *J. Med. Chem.*, 1987, **30**, 2147-2150.
35. A. Brossi, B. Venugopalan, L. D. Gerpe, H. J. C. Yeh, J. L. Flippen-Anderson, P. Buchs, X. D. Luo, W. Milhous and W. Peters, *J. Med. Chem.* , 1988, **31**, 645-650.
36. R. D. Slack, A. M. Jacobine and G. H. Posner, *Med. Chem. Comm*, 2012, **3**, 281-297.
37. http://helid.digicollection.org/pdf/s13418e/s13418e.pdf, *WHO: Guidelines for the treatment of malaria*, 2006.
38. https://www.who.int/docs/default-source/documents/publications/gmp/guidelines-for-the-treatment-of-malaria-eng.pdf?sfvrsn=a0138b77_2, *WHO: Guidelines for the treatment of malaria*, 2015.
39. Y. Bansal and O. Silakari, *Eur. J. Med. Chem.*, 2014, **76**, 31-42.

40. S. Manohar, U. C. Rajesh, S. I. Khan, B. L. Tekwani and D. S. Rawat, *ACS Med. Chem. Lett.*, 2012, **3**, 555-559.
41. S. Manohar, S. I. Khan and D. S. Rawat, *Chem. Biol. Drug Des.*, 2011, **78**, 124-136.
42. E. E. Gordey, P. N. Yadav, M. P. Merrin, J. Davies, S. A. Ward, G. M. J. Woodman, A. L. Sadowy, T. G. Smith and R. A. Gossage, *Bioorg. Med. Chem. Lett.*, 2011, **21**, 4512-4515.
43. S. Kumar, S. Bawa and H. Gupta, *Mini Rev. Med. Chem.*, 2009, **9**, 1648-1654.
44. V. R. Solomon and H. Lee, *Curr. Med. Chem.*, 2011, **18**, 1488-1508.
45. V. R. Solomon and H. Lee, *Eur. J. Pharmacol.*, 2009, **625**, 220-233.
46. A. R. Martirosyan, R. Rahim-Bata, A. B. Freeman, C. D. Clarke, R. L. Howard and J. S. Strobl, *Biochem. Pharmacol.*, 2004, **68**, 1729-1738.
47. C. Fan, W. Wang, B. Zhao, S. Zhang and J. Miao, *Bioorg. Med. Chem.*, 2006, **14**, 3218-3222.
48. A. Kondratskyi, K. Kondratska, F. Vanden Abeele, D. Gordienko, C. Dubois, R. A. Toillon, C. Slomianny, S. Lemiere, P. Delcourt, E. Dewailly, R. Skryma, C. Biot and N. Prevarskaya, *Sci. Rep.*, 2017, **7**, 15896.
49. R. W. Ruddon, *Cancer Biology*, Oxford University Press, Inc., USA, 4 edn., 2007.
50. WHO: Cancer, https://www.who.int/news-room/fact-sheets/detail/cancer, accessed 17 March 2020).
51. H. Lodish, A. Berk, P. Matsudaira, C. A. Kaiser, M. Krieger, M. P. Scott, L. Zipursky and J. Darnell, *Molecular Cell Biology*, W. H. Freeman, 5th edn., 2003.
52. B. Alberts, A. Johnson, J. Levis, M. Raff, K. Roberts and P. Walter, *Molecular Biology Of The Cell*, Garland Science, New York, 4th edn., 2002.
53. Nature, Cell Division and Cancer, **https://www.nature.com/scitable/topicpage/cell-division-and-cancer-14046590/**, accessed 09 July 2020.
54. A. Schroeder, D. A. Heller, M. M. Winslow, J. E. Dahlman, G. W. Pratt, R. Langer, T. Jacks and D. G. Anderson, *Nat. Rev.*, 2012, **12**, 39-50.
55. *Cancer Development*, https://ib.bioninja.com.au/standard-level/topic-1-cell-biology/16-cell-division/cancerdevelopment.html, accessed 09 July 2020.
56. V. Malhotra and M. C. Perry, *Cancer Biol. Ther.*, 2003, **2**, S2-S4.
57. *American Chemical Society*, https://www.cancer.org/treatment/treatments-and-side-effects/treatment-types.html, accessed 07 October 2020.
58. P. G. Corrie, *Medicine*, 2007, **36**, 24-28.
59. L. N. Abdullah and E. K.-H. Chow, *Clin. Transl. Med.*, 2013, **2**, 3.
60. D. B. Longley and P. G. Johnston, *J. Pathol.*, 2005, **205**, 275-292.
61. B. C. Pérez, I. Fernandes, N. Mateus, C. Teixeira and P. Gomes, *Bioorg. Med. Chem. Lett.*, 2013, **23**, 6769-6772.

62. W. Kemnitzer, J. Kuemmerle, S. Jiang, H. Z. Zhang, N. Sirisoma, S. Kasibhatla, C. Crogan-Grundy, B. Tseng, J. Drewe and S. X. Cai, *Bioorg. Med. Chem. Lett.*, 2008, **18**, 6259-6264.
63. C. Verbaanderd, H. Maes, M. B. Schaaf, V. P. Sukhatme, P. Pantziarka, V. Sukhatme, P. Agostinis and G. Bouche, *ecancer*, 2017, **11**, 1-35.
64. G. R. Mereddy and C. T. Ronayne, *J. Transl. Med.*, 2018, **8**.
65. L. K. Kohn, C. H. Pavam, D. Veronese, F. Coelho, J. E. De Carvalho and W. P. Almeida, *Eur. J. Med. Chem.*, 2006, **41**, 738-744.
66. Y. Mikata, M. Yokoyama, S.-i. Ogura, I. Okura, M. Kawasaki, M. Maeda and S. Yano, *Bioorg. Med. Chem. Lett.*, 1998, **8**, 1243-1248.
67. D. Sharples, G. Spengler, J. Molnar, Z. Antal, A. Molnar, J. T. Kiss, J. A. Szabo, A. Hilgeroth, S. Gallo, A. Mahamoud and J. Barbe, *Eur. J. Med. Chem.*, 2005, **40**, 195-202.
68. Z. Guo and P. J. Sadler, *Angew. Chem. Int. Ed.*, 1999, **38**, 1512-1531.
69. T. Latronico and G. M. Liuzzi, *Metalloproteinases In Medicine*, 2017, **4**, 1-13.
70. X. Yu, J. Shi, X. Wang and F. Zhang, *Pharmacol. Rep.*, 2020, **72**, 418-426.
71. T. R. Cook, V. Vajpayee, M. H. Lee, P. J. Stang and K. Chi, *Acc. Chem. Res.*, 2013, **46**, 2464-2474.
72. C. S. Allardyce and P. J. Dyson, *Platinum Metals Rev.*, 2001, **45**, 62-69.
73. W. Sim, R. T. Barnard, M. A. T. Blaskovich and Z. M. Ziora, *Antibiotics*, 2018, **7**, 1-15.
74. S. Medici, M. Peana, G. Crisponi, V. M. Nurchi, J. I. Lachowicz, M. Remelli and M. A. Zoroddu, *Coord. Chem. Rev.*, 2016, **327-328**, 349-359.
75. G. Faa, C. Gerosa, D. Fanni, J. I. Lachowicz and V. M. Nurchi, *Curr. Med. Chem.*, 2018, **25**, 75-84.
76. S. Dilruba and G. V. Kalayda, *Cancer Chemother. Pharmacol.*, 2016, **77**, 1103-1124.
77. L. Kelland, *Nat. Rev. Cancer*, 2007, **7**, 573-584.
78. B. Rosenberg, L. Van Camp and T. Krigas, *Nature*, 1965, **205**, 698-699.
79. B. Rosenberg, L. Van Camp, E. B. Grimley and A. J. Thomson, *J. Biol. Chem.*, 1967, **242**, 1347-1352.
80. A. W. Prestayko, S. T. Crooke and S. K. Carter, *Cisplatin: Current Status and New Developments*, Academic Press Inc., London, 1980.
81. B. Rosenberg, L. VanCamp, J. E. Trosko and V. H. Mansour, *Nature*, 1969, **222**, 385-386.
82. S. Manohar and N. Leung, *J. Nephrol.*, 2018, **31**, 15-25.
83. R. C. DeConti, B. R. Toftness, R. C. Lange and W. A. Creasey, *Cancer Res.*, 1973, **33**, 1310-1315.
84. B. J. Leonard, E. Eccleston, D. Jones, P. Todd and A. Walpole, *Nature*, 1971, **234**, 43-45.
85. R. Wilkinson, P. J. Cox, M. Jones and K. R. Harrap, *Biochimie*, 1978, **60**, 851-857.
86. K. R. Harrap, *Cancer Treat. Rev.*, 1985, **12**, 21-33.

87. A. H. Calvert, S. J. Harland, D. R. Newell, Z. H. Siddik, A. C. Jones, T. J. McElwain, S. Raju, E. Wiltshaw, I. E. Smith, J. M. Baker, M. J. Peckham and K. R. Harrap, *Cancer Chemother. Pharmacol.*, 1982, **9**, 140-147.
88. M. Galanski, *Recent Pat. Anti-Canc.*, 2006, **1**, 285-295.
89. U. Schatzschneider, in *Advances in Bioorganometallic Chemistry*, eds. T. Hirao and T. Moriuchi, Elsevier Inc., 1st edn., 2019, pp. 173-192.
90. H. Schmidt, *Ind. Med. Gaz.*, 1928, **63**, 643-650.
91. O. Domarle, G. Blampain, H. Agnaniet, T. Nzadiyabi, J. Lebibi, J. S. Brocard, L. A. Maciejewski, C. Biot, A. J. Georges and P. Millet, *Antimicrob. Agents. Chemother.*, 1998, **42**, 540–544.
92. V. Sharma, *Mini-Rev. Med. Chem.*, 2005, **5**, 337-351.
93. M. Navarro, *Coord. Chem. Rev.*, 2009, **253**, 1619-1626.
94. R. A. Sánchez-Dalgado, A. Anzellotti and L. Suarez, in *Metal Ions In Biological Systems. Metal Ions and Their Complexes in Medication.*, eds. A. Sigel and H. Sigel, Fontis Media S.A. and Marcel Dekker Inc., New York, 2004, vol. 41, ch. 12, pp. 429-469.
95. J. Held, C. Supan, C. L. O. Salazar, H. Tinto, L. N. Bonkian, A. Nahum, B. Moulero, A. Sié, B. Coulibaly, S. B. Sirima, M. Siribie, N. Otsyula, L. Otieno, A. M. Abdallah, R. Kimutai, M. Bouyou-Akotet, M. Kombila, K. Koiwai, C. Cantalloube, C. Din-Bell, E. Djeriou, J. Waitumbi, B. Mordmüller, D. Ter-Minassian, B. Lell and P. G. Kremsner, *Lancet Infect. Dis.*, 2015, **15**, 1409-1419.
96. C. Biot, G. Glorian, L. A. Maciejewski and J. S. Brocard, *J. Med. Chem.*, 1997, **40**, 3715-3718.
97. B. Pradines, T. Fusai, W. Daries, V. Laloge, C. Rogier, P. Millet, E. Panconi, M. Kombila and D. Parzy, *J. Antimicrob. Chemother.*, 2001, **48**, 179–184.
98. F. Dubar, C. Slomianny, J. Khalife, D. Dive, H. Kalamou, Y. Guerardel, P. Grellier and C. Biot, *Angew. Chem. Int. Ed.*, 2013, **52**, 7690-7693.
99. W. H. Ang, A. Casini, G. Sava and P. J. Dyson, *J. Organomet. Chem.*, 2011, **696**, 989-998.
100. P. J. Dyson, *CHIMIA*, 2007, **61**, 698-703.
101. S. Yuan, S. Chen, H. Wu, H. Jiang, S. Zheng, Q. Zhang and Y. Liu, *Chem. Commun.*, 2020, **56**, 1397-1400.
102. A. A. Holder, L. Lothar, W. R. Browne, M. A. W. Lawrence and J. L. Bullock, *Ruthenium complexes: Photochemical and biomedical applications*, Wiley-VCH, 2018.
103. V. Brabec and J. Kasparkova, *Coord. Chem. Rev.*, 2018, **376**, 75-94.
104. P. Chellan, K. M. Land, A. Shokar, A. Au, S. H. An, D. Taylor, P. J. Smith, K. Chibale and G. S. Smith, *Organometallics*, 2013, **32**, 4793-4804.
105. A. R. Burgoyne, C. H. Kaschula, M. I. Parker and G. S. Smith, *J. Organomet. Chem.*, 2017, **846**, 100-104.
106. C. Billecke, S. Finniss, L. Tahash, C. Miller, T. Mikkelsen, N. P. Farrell and O. Bogler, *Neuro Oncol.*, 2006, **8**, 215-226.

107. P. Govender, B. Therrien and G. S. Smith, *Eur. J. Inorg. Chem.*, 2012, **2012**, 2853-2862.

108. L. Rylands, A. Welsh, K. Maepa, T. Stringer, D. Taylor, K. Chibale and G. S. Smith, *Eur. J. Med. Chem.*, 2019, **161**, 11-21.

109. R. A. Sánchez-Delgado, M. Navarro, H. Pérez and J. A. Urbina, *J. Med. Chem.*, 1996, **39**, 1095-1099.

110. C. S. K. Rajapakse, A. Martínez, B. Naoulou, A. A. Jarzecki, L. Suárez, C. Deregnaucourt, V. Sinou, j. Schrével, E. Musi, G. Ambrosini, G. K. Schwartz and R. A. Sánchez-Delgado, *Inorg. Chem.*, 2009, **48**, 1122-1131.

111. P. Beagley, M. A. L. Blackie, K. Chibale, C. Clarkson and P. J. Smith, *J. Chem. Soc., Dalton Trans.*, 2002, 4426–4433.

112. P. Beagley, M. A. L. Blackie, K. Chibale, C. Clarkson, R. Meijboom, J. R. Moss, P. J. Smith and H. Su, *Dalton Trans.*, 2003, 3046–3051.

113. M. A. L. Blackie, P. Beagley, S. L. Croft, H. Kendrick, J. R. Moss and K. Chibale, *Bioorg. Med. Chem.*, 2007, **15**, 6510–6516.

114. A. Martinez, C. S. Rajapakse, B. Naoulou, Y. Kopkalli, L. Davenport and R. A. Sanchez-Delgado, *J. Biol. Inorg. Chem.*, 2008, **13**, 703-712.

115. B. S. Sekhon and N. Bimal, *J. Pharm. Educ. Res.*, 2012, **3**, 52-63.

116. A. Martinez, C. S. Rajapakse, D. Jalloh, C. Dautriche and R. A. Sanchez-Delgado, *J. Biol. Inorg. Chem.*, 2009, **14**, 863-871.

117. F. Dubar, T. J. Egan, B. Pradines, D. Kuter, K. K. Ncokazi, D. Forge, J. F. Paul, C. Pierrot, H. Kalamou, J. Khalife, E. Buisine, C. Rogier, H. Vezin, I. Forfar, C. Slomianny, X. Trivelli, S. Kapishnikov, L. Leiserowitz, D. Dive and C. Biot, *ACS Chem. Biol.*, 2010, **6**, 275-287.

118. R. Sanchez-Delgado, A. Anzellotti and L. Suarez, *Mini-Rev. Med. Chem.*, 2004, **4**, 159-165.

119. Z. Liu, A. Habtemariam, A. M. Pizarro, S. A. Fletcher, A. Kisova, O. Vrana, L. Salassa, P. C. A. Bruijnincx, G. J. Clarkson, V. Brabec and P. J. Sadler, *J. Med. Chem.*, 2011, **54**, 3011-3026.

120. K.-G. Liu, X.-Q. Cai, X.-C. Li, D.-A. Qin and M.-L. Hu, *Inorg. Chim. Acta*, 2012, **388**, 78-83.

121. A. Ashraf, F. Aman, S. Movassaghi, A. Zafar, M. Kubanik, W. A. Siddiqui, J. Reynisson, T. Söhnel, S. M. F. Jamieson, M. Hanif and C. G. Hartinger, *Organometallics*, 2019, **38**, 361-374.

122. J. Kaiser, *Science*, 2012, **337**, 1471-1473.

123. P. M. Rothwell, F. G. R. Fowkes, J. F. F. Belch, H. Ogawa, C. P. Warlow and T. W. Meade, *Lancet*, 2011, **377**, 31-41.

124. M. E. Barnard, E. M. Poole, G. C. Curhan, A. H. Eliassen, B. A. Rosner, K. L. Terry and S. S. Tworoger, *JAMA Oncol.*, 2018, **4**, 1675-1682.

125. M. Pongratz, P. Schluga, M. A. Jakupec, V. B. Arion, C. G. Hartinger, G. Allmaier and B. K. Keppler, *J. Anal. At. Spectrom.*, 2004, **19**, 46-51.

126. G. S. Smith and B. Therrien, *Dalton Trans.*, 2011, **40**, 10793-10800.
127. E. Alessio, G. Balducci, A. Lutman, G. Mestroni, M. Calligaris and W. M. Attia, *Inorg. Chim. Acta*, 1993, **203**, 205-217.
128. G. Sava, I. Capozzi, K. Clerici, G. Gagliardi, E. Alessio and G. Mestroni, *Clin. Exp. Metastasis*, 1998, **16**, 371–379.
129. E. Alessio and L. Messori, *Molecules*, 2019, **24**.
130. C. Pelillo, H. Mollica, J. A. Eble, J. Grosche, L. Herzog, B. Codan, G. Sava and A. Bergamo, *J. Inorg. Biochem.*, 2016, **160**, 225-235.
131. M. Bacac, A. C. Hotze, K. van der Schilden, J. G. Haasnoot, S. Pacor, E. Alessio, G. Sava and J. Reedijk, *J. Inorg. Biochem.*, 2004, **98**, 402-412.
132. M. R. Berger, F. T. Garzon, B. K. Keppler and D. Schmähl, *Anticancer Res.*, 1989, **9**, 761–766.
133. C. G. Hartinger, S. Zorbas-Seifried, M. A. Jakupec, B. Kynast, H. Zorbas and B. K. Keppler, *J. Inorg. Biochem.*, 2006, **100**, 891-904.
134. K. Śpiewak, S. Świątek, B. Jachimska and M. Brindell, *New J. Chem.*, 2019, **43**, 11296-11306.
135. R. Trondl, P. Heffeter, C. R. Kowol, M. A. Jakupec, W. Berger and B. K. Keppler, *Chem. Sci.*, 2014, **5**, 2925-2932.
136. A. Bergamo and G. Sava, *Chem. Soc. Rev.*, 2015, **44**, 8818-8835.
137. E. Alessio, *Eur. J. Inorg. Chem.*, 2017, **2017**, 1549-1560.
138. S. Thota, D. A. Rodrigues, D. C. Crans and E. J. Barreiro, *J. Med. Chem.*, 2018, **61**, 5805-5821.
139. S. M. Meier-Menches, C. Gerner, W. Berger, C. G. Hartinger and B. K. Keppler, *Chem. Soc. Rev.*, 2018, **47**, 909-928.
140. C. S. Allardyce, P. J. Dyson, D. J. Ellis and S. L. Heath, *Chem. Commun.*, 2001, 1396-1397.
141. C. Scolaro, A. Bergamo, L. Brescacin, R. Delfino, M. Cocchietto, L. G., T. j. Geldbach, G. Sava and P. J. Dyson, *J. Med. Chem.*, 2005, **48**, 4161-4171.
142. A. Bergamo, A. Masi, P. J. Dyson and G. Sava, *Int. J. Oncol.*, 2008, **33**, 1281-1289.
143. R. P. Paitandi, S. Mukhopadhyay, R. S. Singh, V. Sharma, S. M. Mobin and D. S. Pandey, *Inorg. Chem.*, 2017, **56**, 12232-12247.
144. R. Chakrabarty, P. S. Mukherjee and P. J. Stang, *Chem. Rev.*, 2011, **111**, 6810-6918.
145. B. J. Holliday and C. A. Mirkin, *Angew. Chem. Int. Ed.*, 2001, **40**, 2022 - 2043
146. W. Zheng, S.-T. Jiang, B. Jiang and H.-B. Yang, in *Metallomacrocycles: From Structures to Applications*, ed. H.-B. Yang, The Royal Society of Chemistry 2019, ch. 1, pp. 1-19.
147. D. S. Goodsell, *Am. Sc.*, 2000, **88**, 230-237.
148. J.-M. Lehn, *Angew. Chem. Int. Ed. Engl.*, 1988, **27**, 89-112.
149. T. R. Cook, Y. R. Zheng and P. J. Stang, *Chem. Rev.*, 2013, **113**, 734-777.

150. C. J. Pedersen, *Angew. Chem. Int. Ed. Engl.*, 1988, **27**, 1021-1027.
151. D. J. Cram, *Angew. Chem. Int. Ed. Engl.*, 1988, **27**, 1009 - 1112.
152. F. Giordanetto and J. Kihlberg, *J. Med. Chem.*, 2014, **57**, 278-295.
153. E. M. Driggers, S. P. Hale, J. Lee and N. K. Terrett, *Nat. Rev.*, 2008, **7**, 608-624.
154. J. Mallinson and I. Collins, *Future Med. Chem.*, 2012, **4**, 1409–1438.
155. S. L. Huang, G. X. Jin, H. K. Luo and T. S. Hor, *Chem. Asian J.*, 2015, **10**, 24-42.
156. L. L. Ma, J. Q. Han, W. G. Jia and Y. F. Han, *Beilstein J. Org. Chem.*, 2018, **14**, 2027-2034.
157. A. Pothig and A. Casini, *Theranostics*, 2019, **9**, 3150-3169.
158. J.-Q. Wang, C.-X. Ren and G.-X. Jin, *Organometallics*, 2006, **25**, 74-81.
159. Y. Han and G. Jin, *Acc. Chem. Res.*, 2014, **47**, 3571-3579.
160. Y. F. Han, W. G. Jia, W. B. Yu and G. X. Jin, *Chem. Soc. Rev.*, 2009, **38**, 3419-3434.
161. B. Therrien, *Eur. J. Inorg. Chem.*, 2009, **2009**, 2445-2453.
162. M. Fujita, J. Yazaki and K. Ogura, *J. Am. Chem. Soc.*, 1990, **112**, 5645-5647.
163. M. Fujita, M. Tominaga, A. Hori and B. Therrien, *Acc. Chem. Res.*, 2005, **38**, 371-380.
164. N. M. Simkovsky, M. Ermann, S. M. Roberts, D. M. Parry and A. D. Baxter, *J. Chem. Soc.*, 2002, **1**, 1847-1849.
165. F. Trecourt, B. Gervais, M. Mallet and G. Queguiner, *J. Org. Chem.*, 1996, **61**, 1673-1676.
166. F. Trécourt, B. Gervais, O. Mongin, C. L. Gal, F. Mongin and G. Quéguiner, *J. Org. Chem.*, 1998, **63**, 2892-2897.
167. P. R. Ashton, B. Odell, M. V. Reddington, A. M. Z. Slawin, J. F. Stoddart and D. J. Williams, *Angew. Chem. Int. Ed. Engl.*, 1988, **27**, 1550-1553.
168. B. Odell, M. V. Reddington, A. M. Z. Slawin, N. Spencer, J. F. Stoddart and D. J. Williams, *Angew. Chem. Int. Ed. Engl.*, 1988, **27**, 1547-1550.
169. R. V. Slone, K. D. Benkstein, S. Belanger, J. T. Hupp, I. A. Guzei and A. L. Rheingold, *Coord. Chem. Rev.*, 1998, **171**, 221-243.
170. Y. F. Han, W. G. Jia, Y. J. Lin and G. X. Jin, *Organometallics*, 2008, **27**, 5002-5008.
171. J. Mattsson, P. Govindaswamy, A. K. Renfrew, P. J. Dyson, P. Stepnicka, B. Suss-Fink and B. Therrien, *Organometallics*, 2009, **28**, 4350-4357.
172. A. Dubey, J. W. Min, H. J. Koo, H. Kim, T. R. Cook, S. C. Kang, P. J. Stang and K. W. Chi, *Chem. Eur. J.*, 2013, **19**, 11622-11628.
173. G. L. Wang, Y. J. Lin and G. X. Jin, *J. Organomet. Chem.*, 2010, **695**, 1225-1230.
174. Y. F. Han, Y. J. Lin, W. G. Jia and G. X. Jin, *Organometallics*, 2008, **27**, 4088–4097.
175. Y.-F. Han, Y.-J. Lin, W.-G. Jia, L.-H. Weng and G.-X. Jin, *Organometallics*, 2007, **26**, 5848-5853.
176. Y. Yamamotoa, H. Suzuki, N. Tajima and K. Tatsumi, *Chem. Eur. J.*, 2002, **8**, 372-379.

177. K. Severin, *Chem. Commun.*, 2006, 3859-3867.
178. P. Govindaswamy, G. Süss-Fink and B. Therrien, *Organometallics*, 2007, **26**, 915-924.
179. N. P. E. Barry, P. Govindaswamy, J. Furrer, G. Süss-Fink and B. Therrien, *Inorg. Chem. Commun.*, 2008, **11**, 1300-1303.
180. X. Chang, Z. Zhou, C. Shang, G. Wang, Z. Wang, Y. Qi, Z. Y. Li, H. Wang, L. Cao, X. Li, Y. Fang and P. J. Stang, *J. Am. Chem. Soc.*, 2019, **141**, 1757-1765.
181. Y. Zhao, L. Zhang, X. Li, Y. Shi, R. Ding, M. Teng, P. Zhang, C. Cao and P. J. Stang, *PNAS*, 2019, **116**, 4090-4098.
182. G. Gupta, B. S. Murray, P. J. Dyson and B. Therrien, *Materials*, 2013, **6**, 5352-5366.
183. N. P. Barry, F. Edafe and B. Therrien, *Dalton Trans.*, 2011, **40**, 7172-7180.
184. N. P. Barry, F. Edafe, P. J. Dyson and B. Therrien, *Dalton Trans.*, 2010, **39**, 2816-2820.
185. E. H. Wi, J. Y. Ryu, S. G. Lee, U. Farwa, M. Pait, S. Lee, S. Cho and J. Lee, *Inorg. Chem.*, 2019, **58**, 11493-11499.
186. H. Vardhan and F. Verpoort, *Polyhedron*, 2019, **157**, 262-266.
187. P. Li, Y.-M. Xu, W. Deng and Z.-J. Yao, *J. Organomet. Chem.*, 2019, **884**.
188. S. L. Huang, Y. J. Lin, T. S. Hor and G. X. Jin, *J. Am. Chem. Soc.*, 2013, **135**, 8125-8128.
189. H.-B. Yang, *Monographs in Supramolecular Chemistry, Metallomacrocycles: From Structures to Applications*, The Royal Society of Chemistry, 2018.
190. S. Leininger, B. Olenyuk and P. J. Stang, *Chem. Rev.*, 2000, **100**, 853−908.
191. A. Pastor and E. Martínez-Viviente, *Coord. Chem. Rev.*, 2008, **252**, 2314-2345.
192. C. A. Schalley, *Analytical Methods in Supramolecular Chemistry*, Wiley-VCH Verlag & Co. KGaA, Weinheim, Germany, 2012.
193. W. H. Otto, M. H. Keefe, K. E. Splan, J. T. Hupp and C. K. Larive, *Inorg. Chem.*, 2002, **41**, 6172−6174.
194. Y. F. Han, H. Li and G. X. Jin, *Chem. Commun. (Camb)*, 2010, **46**, 6879-6890.
195. J. Mattsson, P. Govindaswamy, J. Furrer, Y. Sei, K. Yamaguchi, B. Suss-Fink and B. Therrien, *Organomet.*, 2008, **27**, 4346-4356.
196. N. P. E. Barry and B. Therrien, *Eur. J. Inorg. Chem.*, 2009, **2009**, 4695-4700.
197. B. Therrien, G. Süss-Fink, P. Govindaswamy, A. K. Renfrew and P. J. Dyson, *Angew. Chem. Int. Ed.*, 2008, **47**, 3773-3776.
198. J. Mattsson, O. Zava, A. K. Renfrew, Y. Sei, K. Yamaguchi, P. J. Dyson and B. Therrien, *Dalton Trans.*, 2010, **39**, 8248-8255.
199. N. P. E. Barry, O. Zava, P. J. Dyson and B. Therrien, *Chem. Eur. J.*, 2011, **17**, 9669-9677.
200. A. Mishra, S. C. Lee, N. Kaushik, T. R. Cook, E. H. Choi, N. K. Kaushik, P. J. Stang and K. W. Chi, *Chem. Eur. J.*, 2014, **20**, 14410-14420.

201. Y. R. Zheng, K. Suntharalingam, P. M. Bruno, W. Lin, W. Wang, M. T. Hemann and S. J. Lippard, *Inorg. Chim. Acta.*, 2016, **452**, 125-129.

202. S. M. McNeill, D. Preston, J. E. Lewis, A. Robert, K. Knerr-Rupp, D. O. Graham, J. R. Wright, G. I. Giles and J. D. Crowley, *Dalton Trans.*, 2015, **44**, 11129-11136.

203. Z. Yue, H. Wang, Y. Li, Y. Qin, L. Xu, D. J. Bowers, M. Gangoda, X. Li, H. B. Yang and Y. R. Zheng, *Chem. Commun.*, 2018, **54**, 731-734.

204. J. M. Rademaker-Lakhai, D. van den Bongard, D. Pluim, H. Beijnen and J. H. M. Schellens, *Clin. Cancer Res.*, 2004, **10**, 3717-3727.

205. V. Vajpayee, Y. J. Yang, S. C. Kang, H. Kim, I. S. Kim, W. Ming, P. J. Stang and K. W. Chi, *Chem. Commun.*, 2011, **47**, 5184-5186.

206. H. S. Song, Y. H. Song, N. Singh, H. Kim, H. Jeon, I. Kim, S. C. Kang and K.-W. Chi, *Sci. Rep.*, 2019, **9**, 1-13.

207. H. Vardhan, A. Nafady, A. M. Al-Enizi, K. Khandker, H. M. El-Sagher, G. Verma, M. Acevedo-Duncan, T. M. Alotaibi and S. Ma, *Molecules*, 2019, **24**, 2284.

208. G. Gupta, A. Das, S. W. Lee, J. Y. Ryu, J. Lee, N. Nagesh, N. Mandal and C. Y. Lee, *J. Organomet. Chem.*, 2018, **868**, 86-94.

209. G. Gupta, A. Das, J. Lee, N. Mandal and C. Y. Lee, *ChemPlusChem*, 2018, **83**, 339-347.

210. G. Gupta, J. M. Kumar, A. Garci, N. Nagesh and B. Therrien, *Molecules*, 2014, **19**, 6031-6046.

211. H. Maeda, G. Y. Bharate and J. Daruwalla, *Eur. J. Pharm. Biopharm.*, 2009, **71**, 409-419.

212. D. F. Baban and L. W. Seymour, *Ad. Drug Deliv. Rev.*, 1998, **34**, 109–119.

CHAPTER 2

Synthesis and characterisation of a quinoline-containing ditopic ligand and the corresponding Ir(III) and Ru(II) binuclear complexes and metallarectangles

2.1 Introduction

The quinoline scaffold (Figure 2.1) is among the most widely researched and utilized pharmacophores within the field of drug design. As previously discussed, this pharmacophoric scaffold has been incorporated into the framework of several potential anticancer agents (Section 1.2.3.1), and more notably, has formed the foundation of some of the most successful antimalarials, including chloroquine and mefloquine (Section 1.1.3).[1,2] Unfortunately, the emergence of drug-resistant parasite strains and resistant cancer cell sub-types has rendered many of these chemotherapeutic agents ineffective.[3] Several attempts have thus been made to design new and/or modify existing quinoline-containing compounds.[1-4]

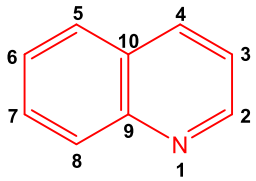

Figure 2.1: *Chemical structure of the quinoline scaffold.*

Metal incorporation, in particular, has proven invaluable, with the most notable discovery being cisplatin.[5,6] The success of this drug sparked a prolific increase in the use of metal-based compounds within the pharmaceutical industry. Not only does metal incorporation impose novel mechanisms of action, but it offers the opportunity to modulate and optimize the pharmacological properties of the organic drug.[3] A prime example of this is the metalloantimalarial ferroquine (Section 1.3.1), a structural derivative of chloroquine (CQ).[7,8] The incorporation of the ferrocene moiety enhanced the pharmacological activity of CQ by over 22-fold, while further imparting a new mechanism of action, due to the presence of the Fe metal centre. [9-11]

More recently, however, a specific class of metal-based compounds, SCCs, have been extensively evaluated for their anticancer activity. In most cases, these compounds have shown superior cytotoxicity and selectivity, relative to cisplatin, against a range of cancer cell lines.[12-14] Based on the EPR effect, the large and highly charged nature of these compounds make them suitable for cancer

treatment.[15,16] Furthermore, the additional intrinsic features of these compounds, as discussed in Section 1.5, make them attractive for biological applications. Interestingly, however, during this research project, no studies had reported on the potential antiplasmodial activity of SCCs.

Owing to the success of the well-established pharmacological efficacy of the quinoline scaffold, ligand **L** was designed (Figure 2.2). To elaborate on the quinoline scaffold, ligand **L** was designed to be structurally analogous to 4,4'-bipyridine, which was the principal ligand used in many of the early studies of SCCs.[17-19]

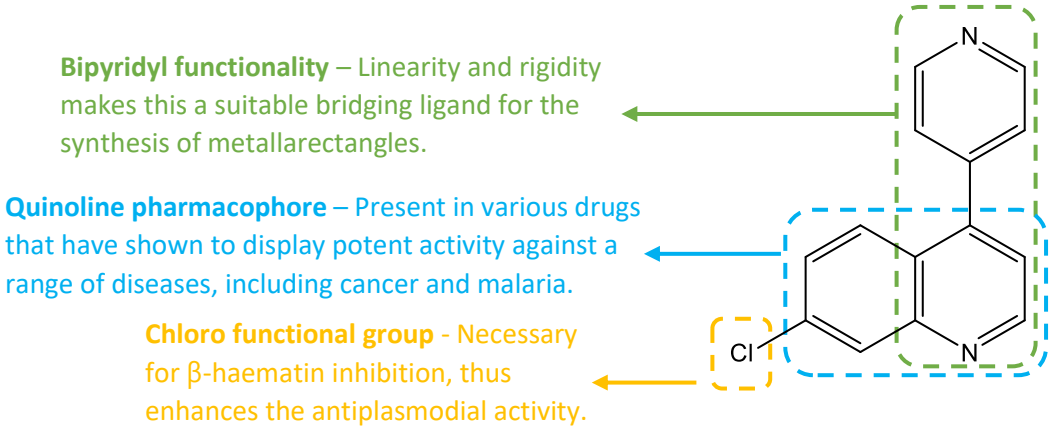

Figure 2.2: *Components of the desired quinoline-containing ditopic ligand* ***L****.*

Furthermore, this study aimed to exploit the favourable properties associated with SCCs (enhanced pharmacological activity and selectivity toward cancerous cells) and the pharmacological benefits of incorporating bioactive metals (e.g. ruthenium and iridium). With a desire to merge these properties, this chapter will focus on the coordination of the pharmacophoric quinoline ligand **L** to either iridium or ruthenium, to subsequently form supramolecular metallarectangles *via* coordination-driven self-assembly.

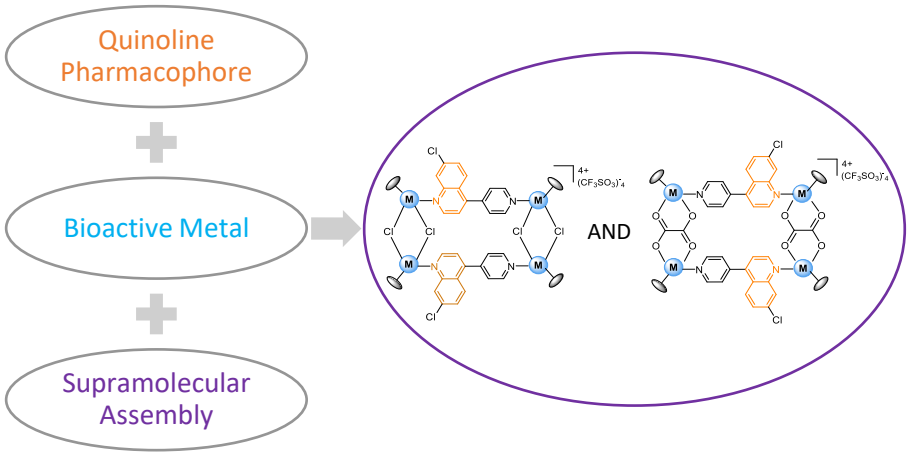

Scheme 2.1: *Components of the target metallarectangles with desirable properties.*

2.2 Synthesis of the 7-chloro-4-(pyridin-4-yl)quinoline ligand (L)

The synthesis of ligand **L** proceeded *via* a Suzuki cross-coupling reaction, following a modified literature procedure.[20] Suzuki cross-coupling reactions are a powerful tool for the formation of carbon-carbon bonds, in particular, the formation of biaryls.[20] Apart from the relatively low toxicity of boronic acids, these reactions have shown both air- and moisture-stability, and versatility, as a range of reaction conditions and catalysts can be used.[20,21] Unfortunately, nitrogen-containing heterocycles can lead to low reactivity within coupling reactions.[20] Kudo *et al*. subsequently discovered a set of reaction parameters that allowed for the successful coupling between an array of aryl halides and nitrogen-containing heteroaryl boronic acids.[20] Using a similar procedure, a mixture of 4-pyridinylboronic acid, 4,7-dichloroquinoline (4,7-DCQ), palladium(II) acetate ($Pd(OAc)_2$), and tricyclohexylphosphine (PCy_3) were refluxed for 18 hours in an aqueous solution of K_3PO_4 and 1,4-dioxane (Scheme 2.2). The obtained crude product was purified *via* column chromatography, yielding **L** as a white crystalline solid in a relatively poor yield of 42%.

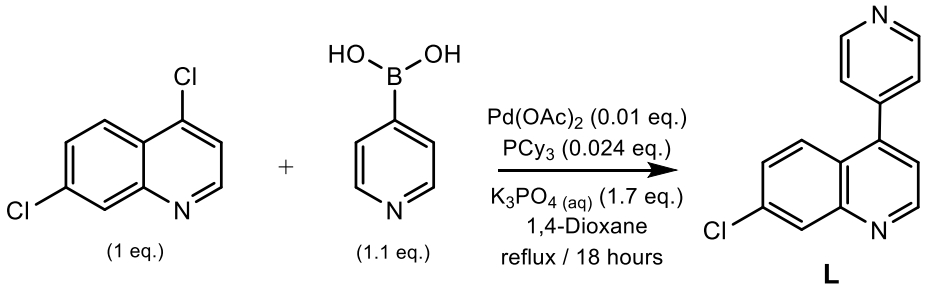

Scheme 2.2: *Synthesis of* ***L****.*

The generally accepted catalytic cycle for the Suzuki cross-coupling reaction involves three steps, namely; oxidative addition (OA), transmetalation, and reductive elimination (Scheme 2.3).[22-24] The first step involves activating the Pd(II) catalyst precursor ($Pd(OAc)_2$) by reducing it to Pd(0) (**I**).[22,24,25] It is suspected that the role of the PCy_3 is to bind to the palladium centre, stabilizing and/or activating it.[24-26] OA of the aryl halide to the active Pd(0) catalyst then affords the stable *trans*-Pd(II) complex (**II**).[23] This is considered the rate-determining step, with aryl chlorides often showing relatively poor reactivity unless activated in the presence of an electron-withdrawing group.[22-24] Based on resonance theory, the quinoline nitrogen can accept a lone pair of electrons, thus acting as an electron sink, increasing the reactivity of the chloride at the 4-position.[26] Furthermore, it has been suggested that the highly electron-donating nature of PCy_3 might further enhance the oxidative insertion of the Pd into the Ar-Cl bond.[26] Following OA, the aryl group attached to the boron atom displaces the chloride

in **II**, essentially transferring from one metal to another (transmetalation) (**III**).[24] Finally, for the organic partners to be eliminated they must undergo *cis-trans* isomerization, which is followed by reductive elimination, generating the desired biaryl species and regenerating the active catalyst (**I**).[22]

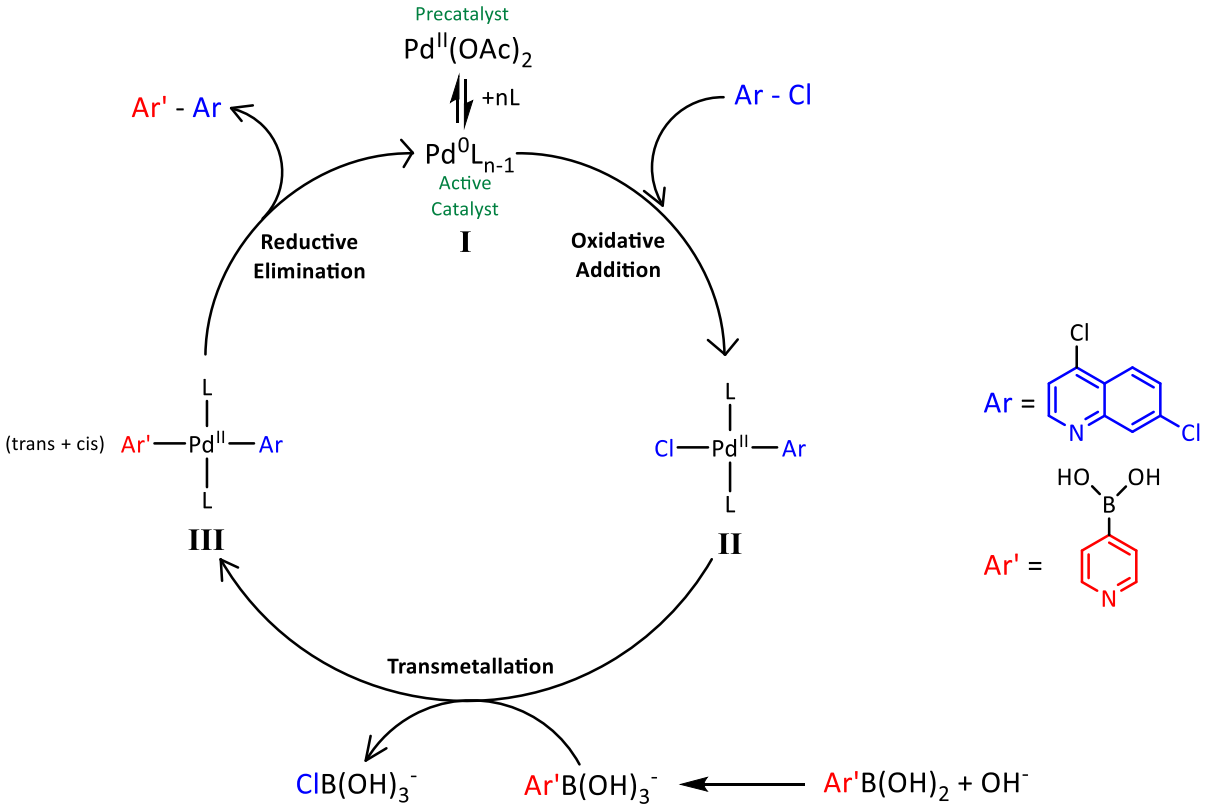

Scheme 2.3: *Suzuki cross-coupling catalytic cycle.*[22-24]

2.3 Characterisation of the 7-chloro-4-(pyridin-4-yl)quinoline ligand (L)

2.3.1 ^{1}H NMR spectroscopy

Upon analysis of the ^{1}H NMR spectrum of ligand **L** (Figure 2.3 - red), the most notable signals are the two doublets-of-doublets observed at δ_H = 8.79 and 7.60 ppm, each integrating for two protons. These signals are assigned to the α- and β-hydrogens of the pyridyl ring (H_f and H_g) respectively, and their presence supports the successful cross-coupling of the heteroaryl boronic acid to the aryl halide.

Although it is well known that the chloride *para* to the quinoline nitrogen is more reactive, the chloride at position 7 is known to be sufficiently reactive to potentially allow for the formation of a bis-substituted product.[27] However, the remaining five proton signals (H_{a-e}) each integrate for one proton, totalling the five protons on the quinoline ring, confirming the ratio of one quinoline moiety

to one pyridyl system. The doublet-of-doublets observed at δ_H = 7.67 ppm, which is characteristic of a 7-chloroquinoline system, is assigned to H_d and is a result of coupling to two chemically non-equivalent hydrogens (H_b and H_c). H_d is split into a doublet by H_b, with a large coupling constant of $^3J_{H\text{-}H}$ = 9.0 Hz, characteristic of *ortho*-coupling. Each peak is then further split into a doublet by coupling with H_c, with a much smaller coupling constant of $^4J_{H\text{-}H}$ = 2.2 Hz, which is typical of long-range coupling.

Despite the chloride at the *para* position being more reactive, shifts within the ^{1}H NMR spectrum further support substitution at position 4, as opposed to the substitution of the chloride at position 7 of the quinoline moiety. The signals corresponding to protons H_b, H_d, and H_e are all observed at lower chemical shifts in the spectrum of the ligand (**L**) compared to the spectrum of the precursor compound (Figure 2.3). This can be attributed to the increased electron density, experienced by these protons, due to their proximity to the pyridyl moiety at the 4-position.

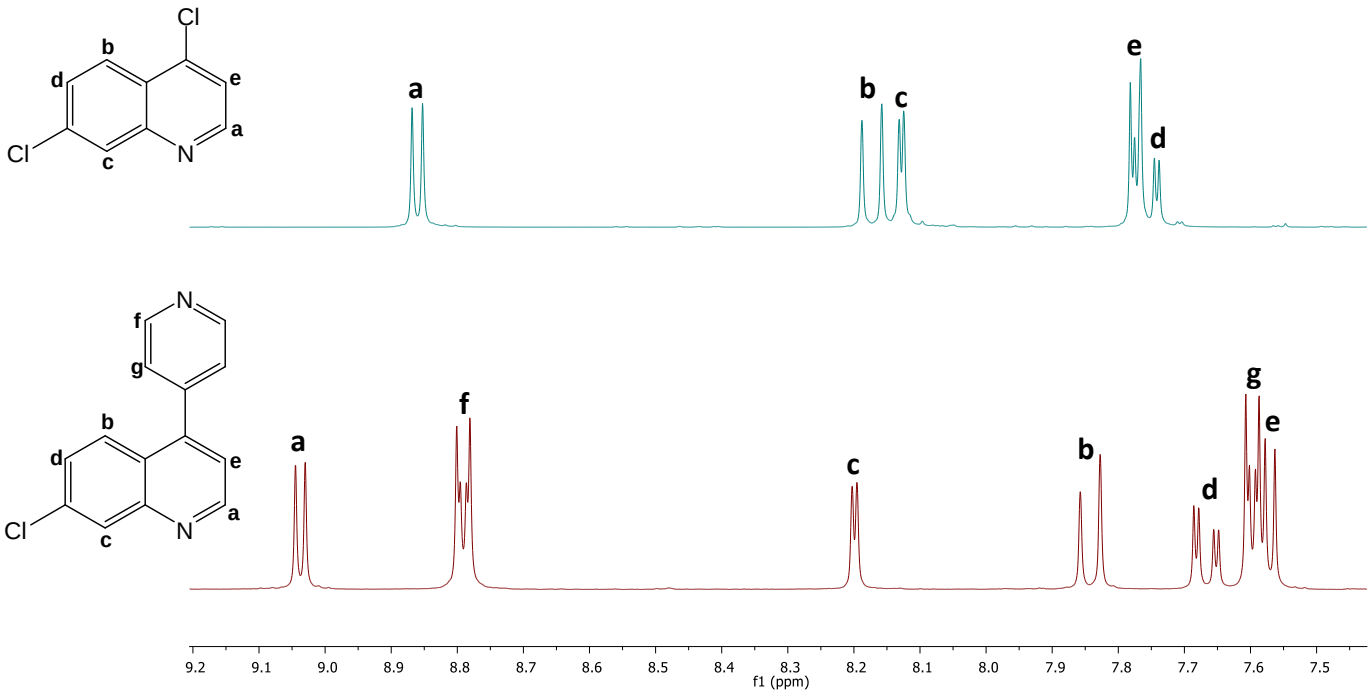

Figure 2.3: *Stacked ^{1}H NMR spectra showing the aromatic regions of the precursor 4,7-dichloroquinoline (top) and ligand **L** (bottom) in DMSO.*

2.3.2 Infrared spectroscopy

Infrared (IR) spectroscopy is a technique used to identify the various infrared-active (functional) groups within a molecule, based on the vibrations of the atoms within these groups upon interaction with infrared light. As expected, the infrared spectrum of ligand **L** displays two medium signals at 1604 and 1580 cm^{-1}. These signals are assigned to the two different C=N functional groups within the molecule, $C=N_{py}$ and $C=N_{quinoline}$ respectively, supporting the successful cross-coupling of the heteroaryl boronic acid to 4,7-dichloroquinoline.

2.3.3 Liquid chromatography-mass spectrometry

Ligand **L** was further evaluated using LC-MS to ascertain both the purity and molecular weight of the compound. Mass spectral data revealed a peak at 241.0 *m/z*, which corresponds to the protonated molecular ion, $[M+H]^+$, confirming the synthesis of the desired mono-substituted cross-coupled product. Furthermore, based on the peak area percentage of the isolated compound, the purity of the target compound was determined to be 100%.

2.4 Synthesis and characterisation of Ir(III) and Ru(II) dimer precursor complexes (1 and 2)

Before synthesizing the binuclear complexes, the iridium and ruthenium dimer precursors were synthesized following reported literature methods.[28,29] The synthesis of $[\{Ir(Cp^*)Cl\}_2(\mu\text{-}Cl)_2]$ (**1**) involved refluxing a solution of iridium(III) trichloride trihydrate and excess pentamethylcyclopentadiene in methanol for 72 hours. This yielded **1** as a bright orange powder in a relatively low yield of 26%. The ^1H NMR spectrum of this dimer reveals a single peak at δ_H = 1.59 ppm, in accordance with the literature,[28] which corresponds to the methyl groups of the two Cp* rings.

To synthesize the ruthenium dimer, $[\{Ru(p\text{-cymene})Cl\}_2(\mu\text{-}Cl)_2]$ (**2**), a solution of ruthenium(III) trichloride trihydrate and α-phellandrene in ethanol, was refluxed for 8.5 hours. This yielded complex **2** as a dark red powder in a moderate yield of 47%. Analysis of the ^1H NMR spectrum of complex **2**, which is in agreement with reported literature findings,[29] revealed two doublets at δ_H = 5.47 and 5.33 ppm, each integrating for four protons, which corresponds to the aromatic protons of the two *p*-cymene rings. Furthermore, signals at δ_H = 2.15 (s), 2.92 (hept), and 1.27 (d) ppm integrate for six, two, and twelve protons respectively. The two latter signals correspond to the ^{i}Pr protons on the *p*-cymene rings and the former signals, the methyl group *para* to the ^{i}Pr.

2.5 Synthesis of neutral Ir(III) and Ru(II) *μ-N,N'* bimetallic complexes (3 – 6)

The reaction of either [{Ir(Cp*)Cl}$_2$(μ-Cl)$_2$] (**1**) or [{Ru(*p*-cymene)Cl}$_2$(μ-Cl)$_2$] (**2**) with a suitable bipyridyl ligand, in a 1:1.2 molar ratio, yielded the appropriate binuclear complexes (**3** – **6**) in moderately high to excellent yields (74% – 96%) (Scheme 2.4). Their synthesis involved cleavage of the chloride bridges within the dimer complex, allowing for the "insertion" of the *N,N'*-ditopic ligand and thus coordination to both nitrogen donor atoms.

The resultant complexes were isolated as powders, ranging from bright yellow to orange, all of which display excellent solubility in dichloromethane (DCM) and are practically insoluble in a range of non-polar solvents, such as hexane, pentane, toluene, and diethyl ether (Et_2O). However, despite the low dipole moment of chloroform, which classifies it as a non-polar solvent, the aforementioned complexes have shown to be highly soluble in this organic solvent.

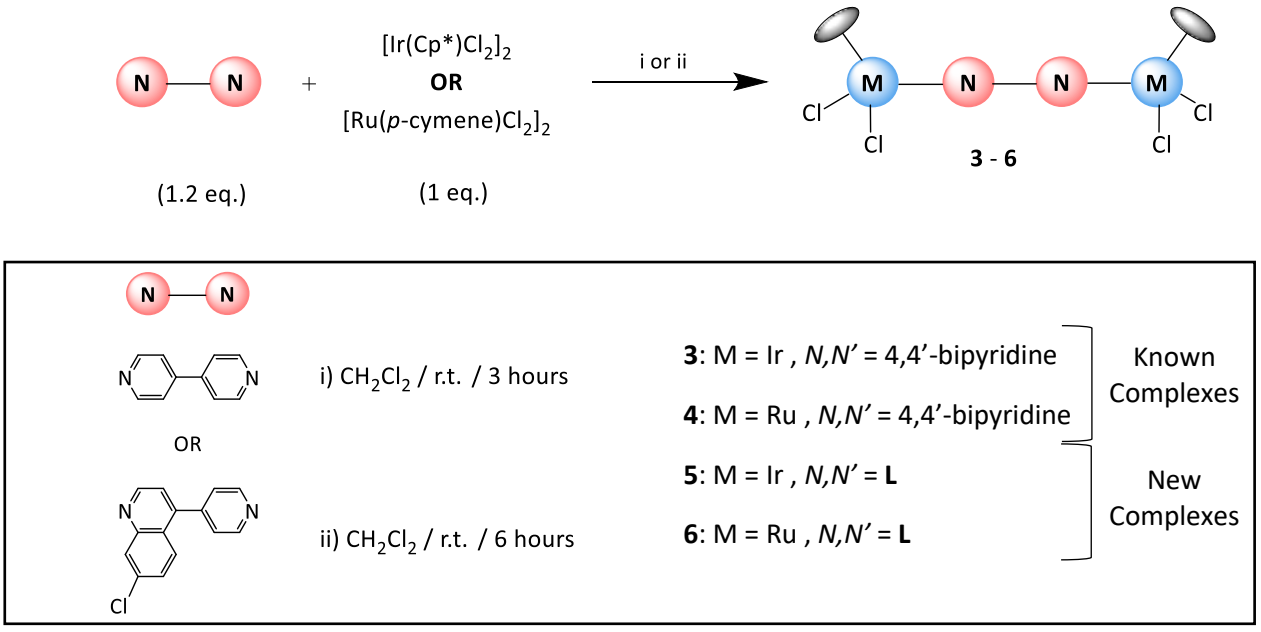

Scheme 2.4: *Synthesis of binuclear complexes* ***3 – 6****.*

2.6 Characterisation of neutral Ir(III) and Ru(II) *μ-N,N'* bimetallic complexes (3 – 6)

2.6.1 ^{1}H NMR spectroscopy

Analyses of the ^{1}H NMR spectra of complexes **3** and **4** (Figure 2.4) confirmed successful coordination to both nitrogen donor atoms of the 4,4'-bipyridyl ligand. In spectrum (a) of Figure 2.4, the broad signals at δ_H = 8.73 and 7.84 ppm, each integrating for four protons, are attributed to the α- and β-hydrogen atoms (H_a and H_b respectively), of the 4,4'-bipyridine ligand. Furthermore, the presence of a sharp singlet at δ_H = 1.63 ppm and a smaller signal at δ_H = 1.45 ppm, which collectively integrates for 30 protons, corresponds to the Cp* ligands and is evidence of metal coordination to two iridium metal centres.

In the ^{1}H NMR spectrum of complex **4** (Figure 2.4b), two sets of signals between δ_H = 9.09 – 8.72 ppm and δ_H = 8.19 – 7.82 ppm, each integrating for four protons, corresponds to protons H_a and H_b of the bipyridyl ligand respectively. The remaining signals, assigned to protons $H_{c\text{-}g}$, all integrate for the expected number of protons and supports the formation of a binuclear complex. The electron-donating effects of the isopropyl and methyl groups significantly shield the aromatic *p*-cymene protons, explaining their upfield appearance compared to the aromatic proton signals of the 4,4'-bipyridyl ligand.

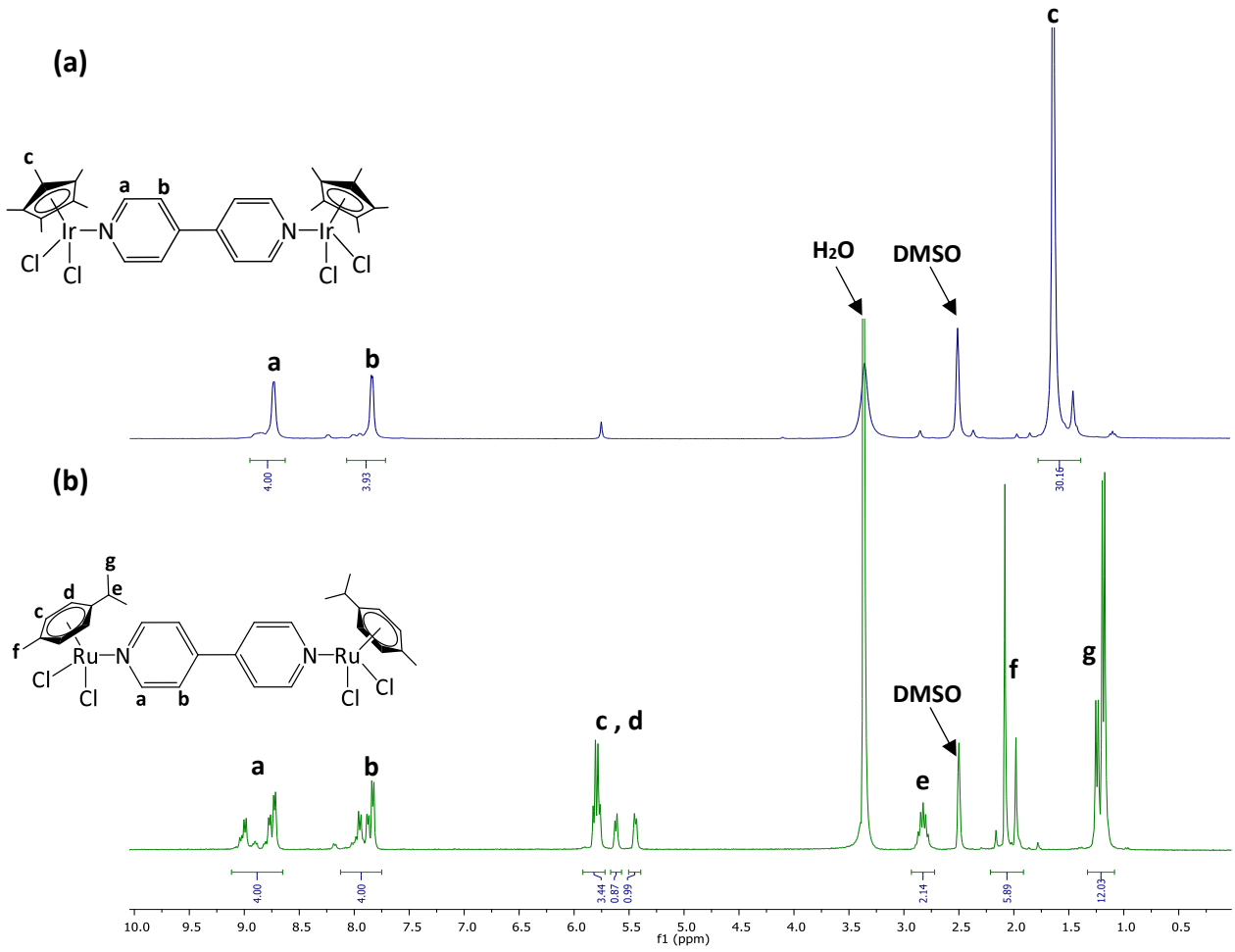

Figure 2.4: *Stacked ^{1}H NMR spectra of known binuclear complexes **3** and **4** in [D_6]-DMSO.*

Most notably in the above spectra, more than one signal is observed for a given proton. A dominant signal, along with one or more smaller signals are observed, which collectively integrate for the expected number of protons. For example, in spectrum (b) a doublet integrating for four protons was expected for proton signal H_a. However, a range of doublets, collectively integrating for four protons was observed. This phenomenon is similarly seen for all other proton signals within the spectra of complexes **3** and **4**, and due to the symmetrical nature of these complexes, this suggested the presence of conformational isomers (or rotamers) in solution. Consequently, the complexes were analysed using variable-temperature (VT) NMR studies to support this hypothesis.

Rotational isomerism in a molecule describes the phenomenon of rotation about a single bond and arises when rotation is hindered by a rotational energy barrier.[30] Displaying this pictorially, should a substituent be spherical (S), rotation around the C-S bond causes no isomers (Figure 2.5a).[30] However, as soon as the symmetry of substituent S is lowered, isomers (rotamers) may be formed

by mere rotation about the C-S bond (Figure 2.5b).[30] If there is free rotation about this C-S bond, the recognition of isomers, due to rotation, would not be possible, as the internal rotation requires no activation energy.[30] However, should rotamers be observed, it implies the presence of an energy barrier, required for rotation, which surpasses the given kinetic energy of the molecule.[30]

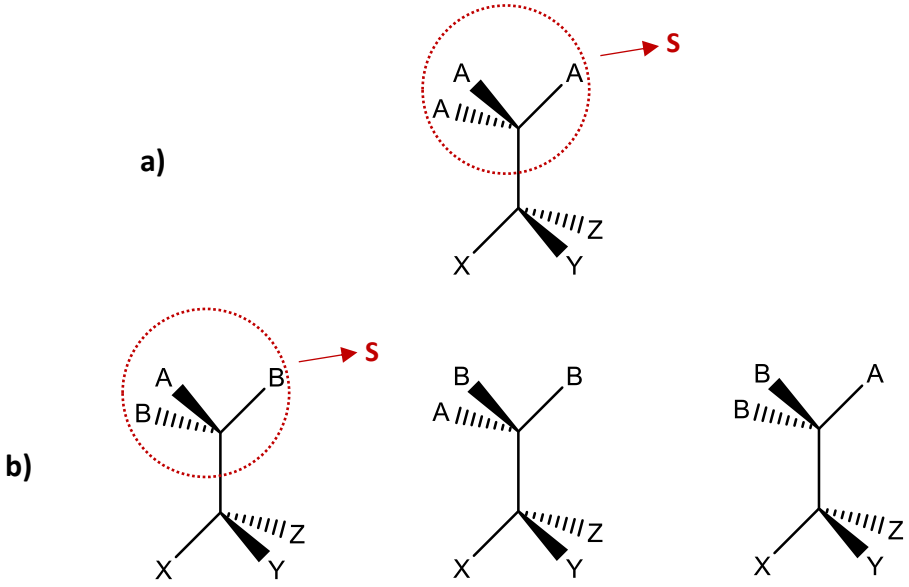

Figure 2.5: *Possible rotational isomers, depending on the nature of the substituent S.*

Within NMR spectroscopy, the time-scale is much slower, and sometimes rotational isomers do not rapidly equilibrate as rotation about a bond is slower than the NMR time-scale.[30] As a result, at room temperature, several isomers may exist, however, the most stable isomer would be the most dominant within the solution population, as noted by the intensity of the signal.[30] When increasing the temperature, the bond rotation on the NMR time scale is increased. Coalescence of a set of signals, as a result of changing temperature, can thus be attributed to a set of rotational isomers.[30]

A similar trend was observed for both complexes **3** and **4**, however, the spectra of complex **4** (Figure 2.6) serves as a representative example, as the coalescence of signals is more apparent. The proximity between the pyridyl and *p*-cymene protons may vary due to restricted rotation about the Ru-N bond, giving rise to rotamers. Upon observation of the spectra in Figure 2.6, it is apparent that as the temperature increases from 30°C (top) to 90°C (bottom), the signals seemingly converge, confirming the presence of rotational isomers.

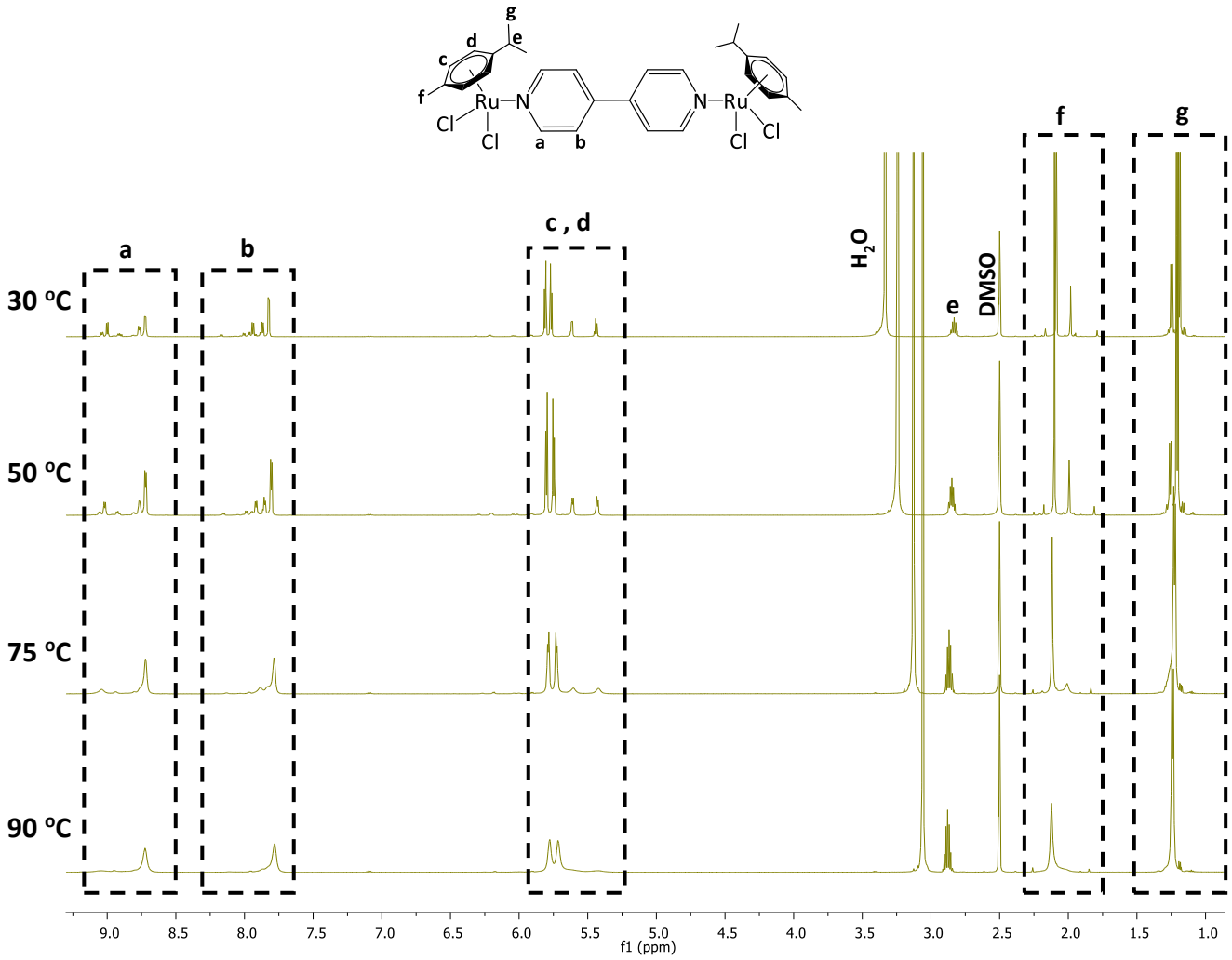

Figure 2.6: *Variable temperature ^{1}H NMR spectra of complex **4** in [D_6]-DMSO showing the coalescence of signals.*

Analysis of the ^{1}H NMR spectra of complexes **5** and **6** confirmed the successful coordination of ligand **L** to two metal centres. Figure 2.7 shows the ^{1}H NMR spectrum of the quinoline-containing iridium binuclear complex **5**. Evidence for coordination at both nitrogen donor atoms is provided by the presence of two sharp singlets at δ_H = 1.55 and 1.52 ppm, which collectively integrate for 30 protons, corresponding to the Cp* ligands. Compared to the single dominant signal observed in the ^{1}H NMR spectrum of the symmetrical complex **3** (Figure 2.4a), coordination to both nitrogen donor atoms of the asymmetric ligand **L** results in two signals with rather similar intensities and chemical shifts. Furthermore, the remaining signals ($H_{a\text{-}g}$) collectively integrate for the expected nine protons present on the ligand.

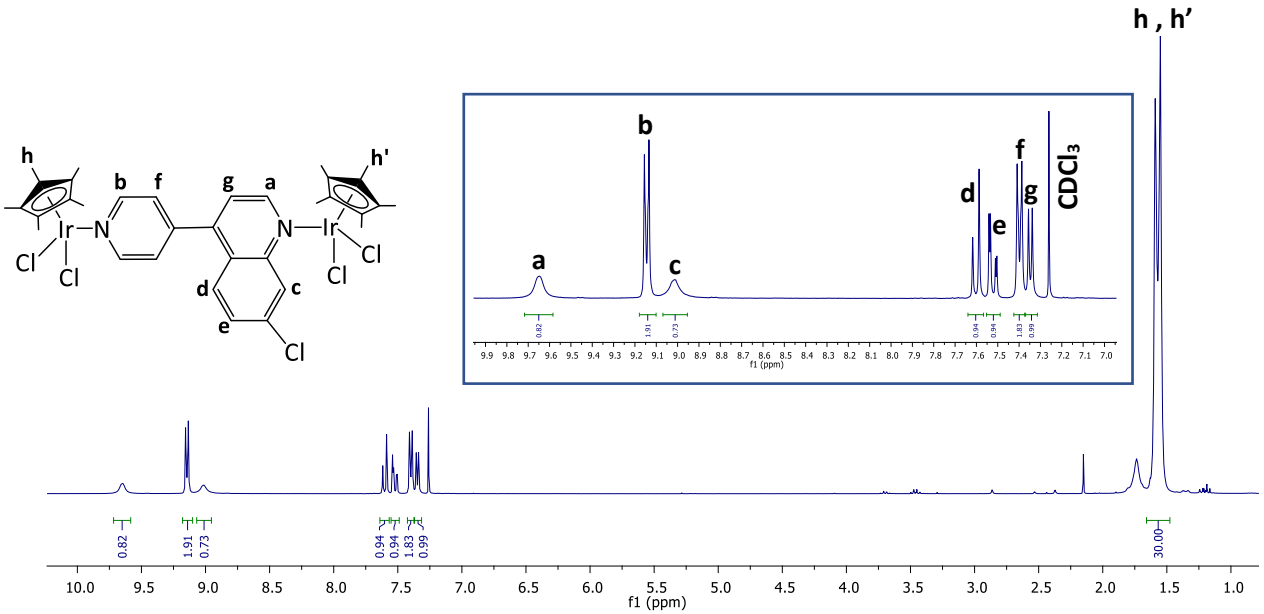

Figure 2.7: *The ^{1}H NMR spectrum of complex **5** in $CDCl_3$. The inset picture shows the aromatic signals of the complex and $CDCl_3$.*

When comparing the aromatic region of the ^{1}H NMR spectrum of complex **5**, with that of the corresponding uncoordinated ligand **L** (Figure 2.8), a general downfield shift is observed upon complexation, with the most notable shifts being those of proton signals H_a, H_b and H_c. This is expected as these protons are closest to the site of coordination and thus experience the electron-withdrawing effects of the electron-deficient iridium metal centre more strongly. Furthermore, the significant broadening and reduced intensity of proton signals H_a and H_c has been previously observed upon coordination to the quinoline nitrogen,[31] and may be due to long-range coupling with the Cp* ligand.

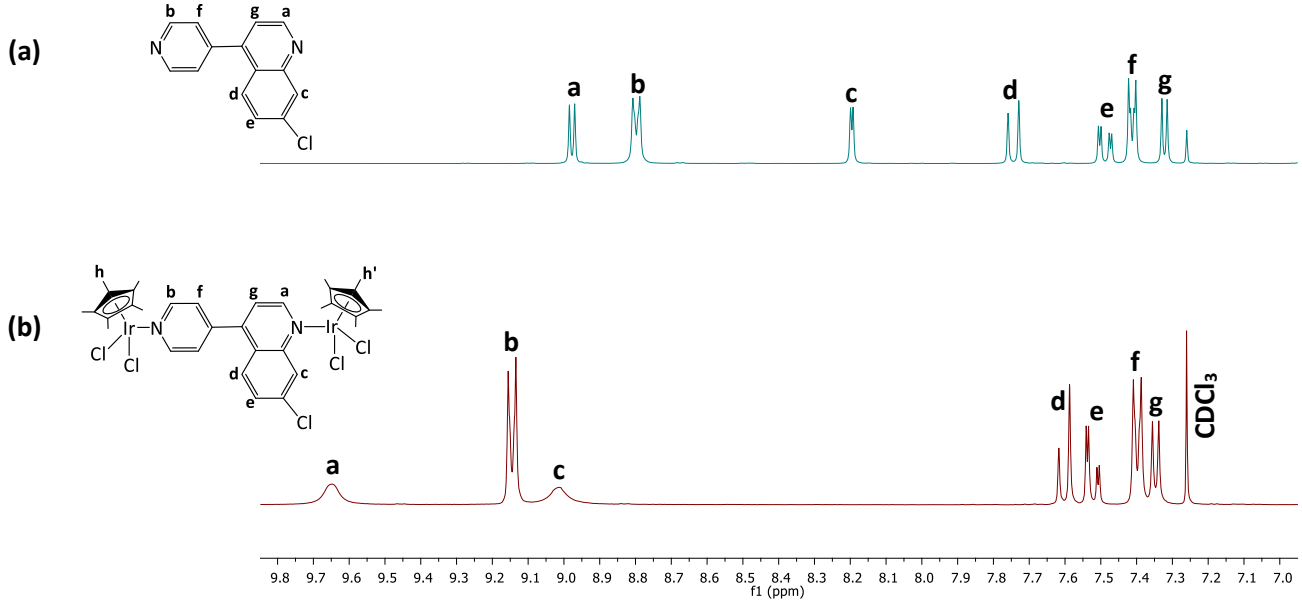

Figure 2.8: *Comparison between the aromatic regions of the ^{1}H NMR spectra of (a) **L** and (b) **5** in $CDCl_3$.*

Similarly, in the ^{1}H NMR spectrum of complex **6** (Figure 2.9), the signals assigned to protons H_a and H_c are significantly broadened. This observation was previously made in the ^{1}H NMR spectrum of the Ir(III) analogue (**5**) (Figure 2.8), suggesting that this is characteristic of coordination to a quinoline nitrogen. In addition to the signals assigned to the coordinated ligand **L**, which range between δ_H = 7.29 and 9.29 ppm, two singlets (H_k and $H_{k'}$), two doublets (H_l and $H_{l'}$), and two multiplets (H_j and $H_{j'}$) are noted in the aliphatic region, further attesting to the presence of the *p*-cymene ancillary ligands. Furthermore, the observed "doubling-up" of these signals points to the presence of two *p*-cymene ligands in slightly different chemical environments, and thus the successful coordination to both nitrogen donor atoms of the asymmetric ligand (**L**). Finally, the aromatic signals of the *p*-cymene ligands are present in the expected region (δ_H = 5.22 – 5.64 ppm) and collectively integrate for eight protons, further attesting to the formation of the bimetallic complex.

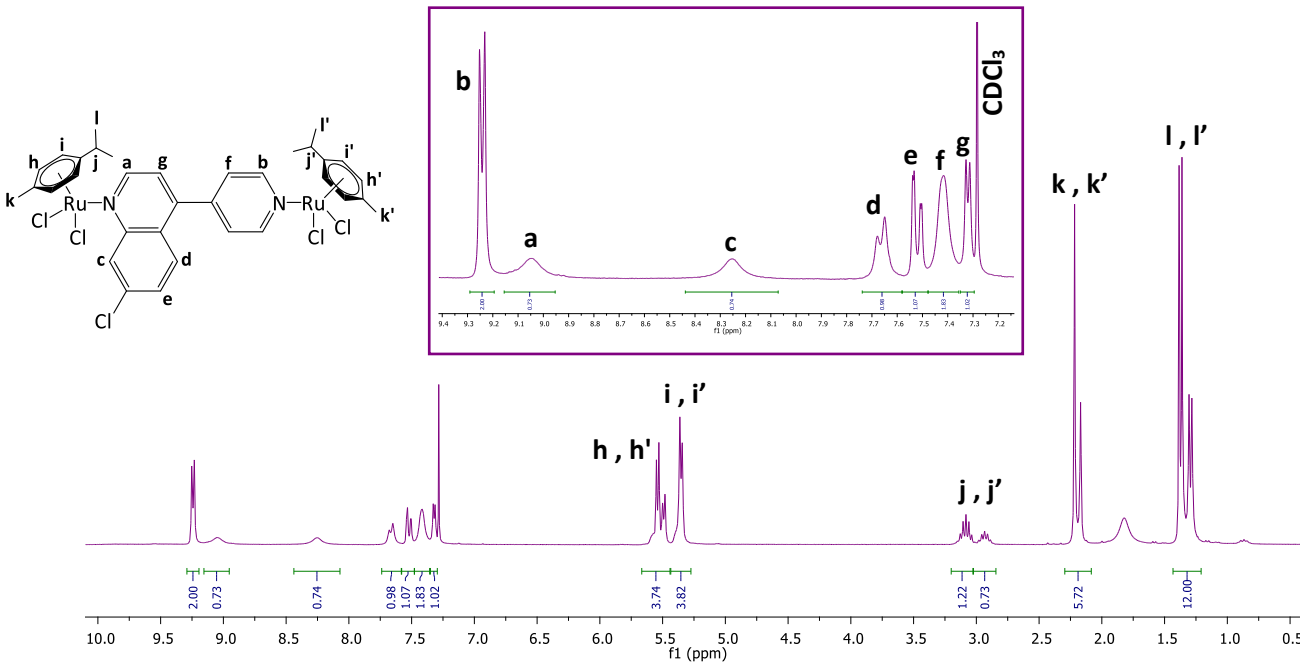

Figure 2.9: *^{1}H NMR spectrum of complex **6** in $CDCl_3$. The inset picture shows the signals attributed to the coordinated ligand **L** and $CDCl_3$.*

2.6.2 *Infrared spectroscopy*

Infrared spectroscopy was further used to verify the presence of the C=N functional groups within complexes **3** - **6**. In the IR spectra of complexes **3** and **4**, the $\nu(C=N)_{pyridyl}$ stretching vibrations are present at 1608 and 1610 cm^{-1} respectively, which agrees with reported literature values.[32] The $\nu(C=N)_{pyridyl}$ stretching frequency of both complexes is at a higher wavenumber than that of the uncoordinated ligand (4,4'-bipyridine), with $\nu(C=N)_{pyridyl}$ observed at 1596 cm^{-1}. The shift of the $\nu(C=N)$ absorption band in pyridyl moieties to a higher wavenumber upon complexation has been previously observed,[33,34] and supports metal coordination to the pyridyl nitrogen atoms.

Generally, upon coordination of a metal centre to an imine nitrogen, there is σ-donation of the lone pair from the sp^2 hybridized orbital on the nitrogen, into the vacant d-orbital on the metal, forming a σ-bond (Figure 2.10a – red arrow)[35]. There is subsequent backdonation of electron density from the filled d-orbitals on the metal, into the unoccupied π*-antibonding orbitals of the imine (Figure 2.10a – blue arrow).[35] This synergistic relationship causes the M-N bond to be strengthened,[35] and the bond order between the nitrogen and carbon to decrease (C=N bond weakened). As a result, the C=N absorption band within the infrared spectrum shifts to a lower wavenumber upon complexation. Coordination to a pyridine nitrogen, however, does not follow the same trend, with the $\nu(C=N)_{pyridine}$ absorption band shown to shift to a higher wavenumber.

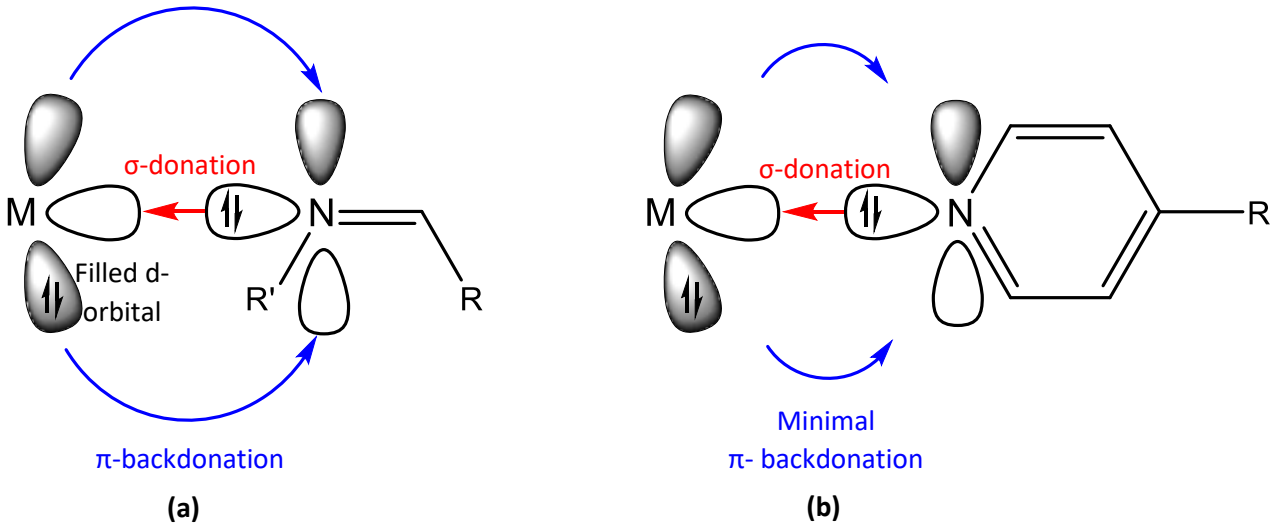

Figure 2.10: *(a) Molecular orbital diagram illustrating π-backbonding in an imine system, (b) Molecular orbital diagram illustrating possible π-backbonding in a pyridyl system.*

Only a slight shift of the $\nu(C=N)_{pyridine}$ absorption band to a higher wavenumber is observed upon complexation. This can be explained in part by the spectrochemical series of ligands. This series depicts pyridine as a moderately strong-field ligand and thus a strong σ-donor. Consequently, the strong electrostatic interaction between the lone pair on pyridine and the vacant d-orbitals of the metal results in a relatively strong metal-nitrogen bond. Similarly to an imine, σ-donation results in the formation of an M-N σ-bond (Figure 2.10b - red arrow). However, compared to ligands such as CO and CN^-, which have a small gap between their highest occupied molecular orbital (HOMO) and lowest unoccupied molecular orbital (LUMO), the LUMO of pyridine is higher in energy (these are the orbitals into which electron density is shifted from the metal).[36] As a result, this heterocyclic ligand acts as a weak(er) π-acceptor, minimising π-backdonation (Figure 2.10b – blue arrow).[36,37]

Extended delocalised π-systems have been shown to lower the energy of the LUMO, encouraging π-backdonation from the metal. As mentioned, pyridine is a strong σ-donor with rather weak π-acceptor abilities. Bipyridine is essentially a substituted pyridine, with the substituent being another pyridine. The extension of this delocalised π-system, in theory, should increase the π-acceptor character of the system. However, due to the shift of the C=N absorption bands in complexes **3** and **4** to a higher wavenumber, relative to the uncoordinated ligand, one can speculate that this increase in π-acceptor character does not result in a significant increase in π-backdonation. Instead, it is proposed that the extended delocalised system stabilises the electron-deficient nitrogen. The decreased synergic effect somewhat weakens the Ir-N bond, while subsequently strengthening the C=N bond, explaining the shift of the $\nu(C=N)_{pyridyl}$ absorption band to a higher wavenumber.

The infrared spectrum of the metal-free ligand **L** is shown in Figure 2.11, along with the spectra of complexes **5** and **6**, which are near identical to each other. Within the IR spectra of complexes **5** and **6**, each spectrum displays two ν(C=N) absorption bands, at 1607 and 1587 cm^{-1}, which are attributed to the two different C=N functionalities within the complex.

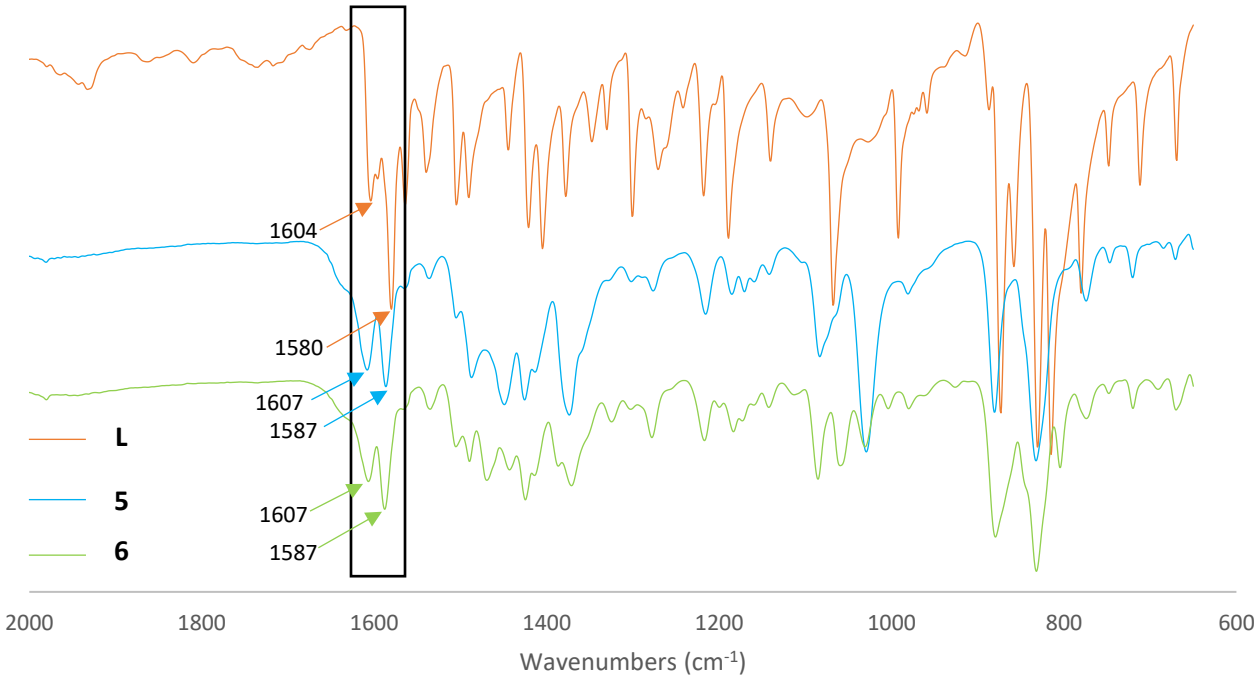

Figure 2.11: *Comparison between the IR spectra of ligand* ***L*** *and binuclear complexes* ***5*** *and* ***6****.*

Compared to the C=N absorption bands observed in the spectrum of the ligand **L** (ν(C=N) = 1604 and 1580 cm^{-1}), the corresponding absorption bands for the complexes (**5** and **6**) are observed at slightly higher wavenumbers (Figure 2.11). The observed shift upon complexation to a higher wavenumber was previously observed and discussed and supports metal coordination. Furthermore, the shift of both ν(C=N) absorption bands is evidence that coordination occurred at both the pyridyl and quinoline nitrogen atoms of the ligand.

2.6.3 High-resolution mass spectrometry

High-resolution electrospray ionisation mass spectrometry (ESI-MS), in the positive mode, was further used to confirm the structural integrity of the desired *N,N'*-binuclear complexes. The mass spectral data of all the aforementioned *N,N'*-binuclear complexes (**3** – **6**) shows a peak that corresponds to the molecular ion with the loss of two chloride ions, $[M\text{-}2Cl]^{2+}$. The observed *m/z* values are in agreement with the calculated values of the respective $[M\text{-}2Cl]^{2+}$ ions.

2.6.4 Single crystal X-ray diffraction

Suitable crystals of complex **5** were obtained by the slow evaporation of a saturated chloroform solution, at room temperature, and the molecular structure was elucidated by single-crystal X-ray diffraction (Figure 2.12). From the ORTEP diagram of complex **5**, the ditopic ligand **L** is observed to bridge two Ir(III) metal centres, with each Ir further coordinated by two chlorides and a η^5-pentamethylcyclopentadienyl (Cp*) ligand. It is also evident that one of the Cp* ligands are disordered, with refined site occupancy factors of 0.394(9) and 0.606(9) respectively. Cp* ligands occupy three coordination sites, and as a result, this complex adopts the well-known three-legged piano-stool conformation which is commonly observed in many other half-sandwich rhodium, iridium, and ruthenium complexes reported in the literature.[38-41] Furthermore, this complex has been shown to crystallize in a P-1 space group with a triclinic system, and a total of two molecules per unit cell was observed. Further crystallographic data and refinement parameters for complex **5** are summarised in Table 2.1 and selected bond lengths and angles are listed in Table 2.2.

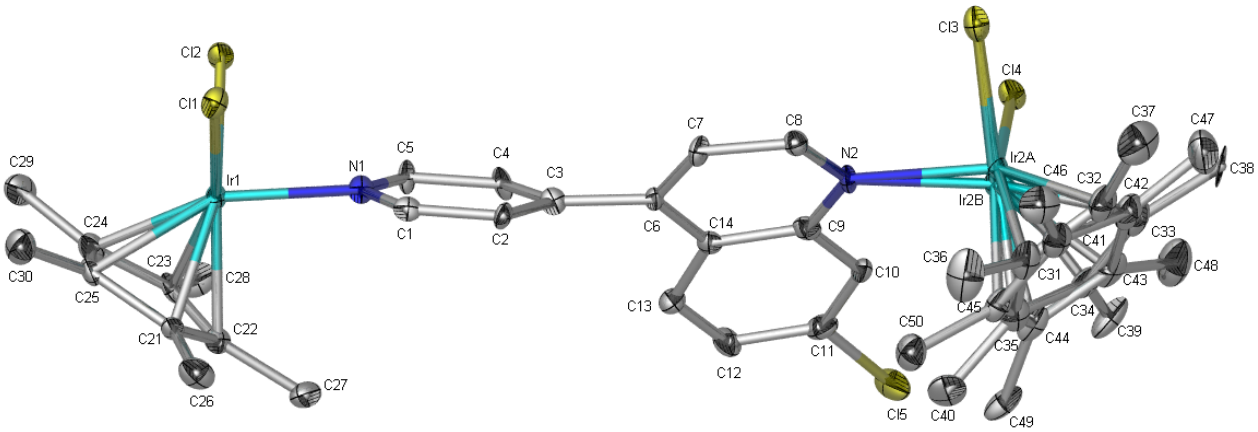

Figure 2.12: *Molecular structure of complex **5** with solvent molecules (five $CHCl_3$ molecules) and hydrogen atoms omitted for clarity. Ellipsoids are shown at 30% probability level.*

Table 2.1: *Crystallographic data and refinement parameters for complex* ***5*** *·* $5CHCl_3$.

Formula Unit	$C_{34}H_{39}Cl_5Ir_2N_2 \cdot 5(CHCl_3)$	***F(000)***	1572
Formula Weight	1634.20	***Crystal Size (mm)***	0.06 x 0.08 x 0.11
Crystal System	Triclinic	***Temperature (K)***	100
Space Group	P-1	***Scan Range (°)***	$1.6 < \theta < 28.3$
a, b, c (Å)	11.6063 (2), 16.2300 (3), 16.3533 (3)	***Unique Reflections***	13844
α, β, γ (°)	69.543 (3), 81.622 (3), 76.793 (4)	R_{int}	0.102
Volume (Å³)	2802.4 (9)	***Observed Data [I>2σ(I)]***	9029
Z	2	***R, wR2***	0.0548, 0.1271
$Density_{calc}$ ***(g/cm³)***	1.937	***Goodness-of-fit***	0.99
μ (mm⁻¹)	5.729	***Min, Max Δρ (e.Å⁻³)***	-1.75, 2.17

The data in Table 2.2 suggests that the geometry around the iridium metal centre is pseudo-tetrahedral, as the bond angles around the metal centre range between 83.0° and 90.4°. These angles are not the required 90° to be classified as square planar and are too low to be classified as tetrahedral. Furthermore, the Ir_1-N_1 bond length [2.113(6) Å] in complex **5** is comparable to related Ir(III)-pyridyl complexes,[18,40,42,43] however, the Ir_{2A}-N_2 and Ir_{2B}-N_2 bond lengths are slightly longer.[18,42,43] All of the metal-nitrogen bond lengths (Ir_1-N_1, Ir_{2A}-N_2, and Ir_{2B}-N_2) however are longer than reported metal-nitrogen bonds in imine complexes.[44] As previously discussed, upon complexation to an imine nitrogen, the ν(C=N) absorption band is observed at a lower wavenumber compared to the corresponding absorption band in the uncoordinated ligand. This shift is supported by analysing the metal-nitrogen bond lengths. Since the metal-nitrogen bonds in imine complexes are relatively shorter, this suggests that they are stronger and that increased backdonation results in a subsequent weakening of the C-N bond, causing the C=N absorption band to shift to a lower wavenumber. The opposite is true for metal-pyridyl/quinoline complexes, as the longer metal-nitrogen bond lengths (relative to metal-nitrogen imine complexes) supports the hypothesis that there is minimized back-donation, causing the ν(C=N) absorption band to shift to a higher wavenumber upon complexation, which has been observed for complexes **3** - **6**. Additionally, the quinoline and pyridyl ring systems are not coplanar, as expected, with a torsion angle of 44.3°.

Table 2.2: *Selected bond lengths (Å) and angles (°) for complex* ***5*** *· 5CHCl₃.*

Bond lengths (Å)					
$Ir_1 – N_1$	2.113 (6)	**$Ir_{2A} – N_2$**	2.203 (10)	**$Ir_{2B} – N_2$**	2.147 (13)
$Ir_1 – Cl_1$	2.401 (2)	**$Ir_{2A} – Cl_3$**	2.322 (7)	**$Ir_{2B} – Cl_3$**	2.562 (10)
$Ir_1 – Cl_2$	2.417 (2)	**$Ir_{2A} – Cl_4$**	2.408 (8)	**$Ir_{2B} – Cl_4$**	2.443 (11)
$Ir_1 – C_{21}$	2.132 (8)	**$Ir_{2A} – C_{31}$**	2.170 (2)	**$Ir_{2B} – C_{41}$**	2.140 (3)
$Ir_1 – C_{22}$	2.152 (8)	**$Ir_{2A} – C_{32}$**	2.218 (19)	**$Ir_{2B} – C_{42}$**	2.170 (3)
$Ir_1 – C_{23}$	2.141 (8)	**$Ir_{2A} – C_{33}$**	2.177 (19)	**$Ir_{2B} – C_{43}$**	2.130 (5)
$Ir_1 – C_{24}$	2.155 (8)	**$Ir_{2A} – C_{34}$**	2.170 (2)	**$Ir_{2B} – C_{44}$**	2.110 (3)
$Ir_1 – C_{25}$	2.173 (8)	**$Ir_{2A} – C_{35}$**	2.170 (2)	**$Ir_{2B} – C_{45}$**	2.080 (3)
Bond angles (°)					
$Cl_1 – Ir_1 – N_1$	87.27 (18)	***$Cl_3 – Ir_{2A} – N_2$***	90.4 (3)	***$Cl_3 – Ir_{2B} – N_2$***	85.5 (4)
$Cl_2 – Ir_1 – N_1$	86.9 (2)	***$Cl_4 – Ir_{2A} – N_2$***	88.7 (3)	***$Cl_4 – Ir_{2B} – N_2$***	89.0 (4)
$Cl_1 – Ir_1 – Cl_2$	87.64 (7)	***$Cl_3 – Ir_{2A} – Cl_4$***	89.1 (2)	***$Cl_3 – Ir_{2B} – Cl_4$***	83.0 (3)
Torsion angle (°)					
$C_2 – C_3 – C_6 – C_7$			44.3 (12)		

2.7 Synthesis of neutral Ir(III) and Ru(II) *O^O* bimetallic complexes (7 and 8)

A step-wise synthetic procedure is required to synthesize metallarectangles (Section 1.4.4). Consequently, directing ligands such as Cp* or *p*-cymene are used to generate a "preorganized" binuclear molecular clip. Incoming ligands are thus limited by the number of available coordination sites and their relative angularity, allowing for predictable coordination. This premise led to the subsequent synthesis of the known iridium and ruthenium binuclear molecular clips **7** and **8**, containing bridging oxalato ligands.

The synthesis of the Ir(III) and Ru(II) oxalato-chelating binuclear complexes, **7** and **8**, was achieved *via* a bridge-splitting reaction of either dimer **1** or **2**, and subsequent coordination of ammonium oxalate monohydrate in a bridging bidentate-fashion (Scheme 2.5). This yielded the corresponding binuclear complexes, **7** and **8**, as yellow and orange powders respectively, which is in agreement with reported literature.[19,43] Furthermore, these complexes were isolated in excellent yields, ranging between 74 - 89%.

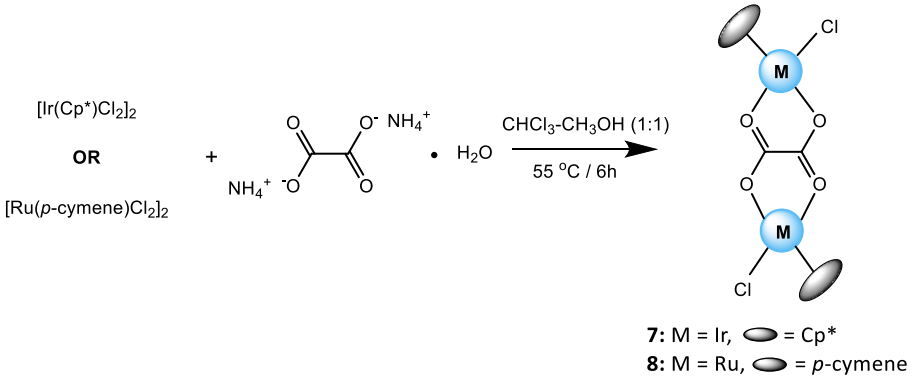

Scheme 2.5: *Synthesis of binuclear oxalate complexes,* ***7*** *and* ***8****.*

2.8 Characterisation of neutral Ir(III) and Ru(II) *O^O* bimetallic complexes (7 and 8)

2.8.1 ^{1}H NMR spectroscopy

Complexes **7** and **8** have both been previously synthesized and were thus only characterised using ^{1}H NMR and IR spectroscopy, and mass spectrometry, to confirm their synthesis. The ^{1}H NMR spectrum of complex **7** shows a single singlet at δ_H = 1.64 ppm, which is in agreement with reported literature,[43] and is assigned to the methyl groups of the two Cp* ligands. In the ^{1}H NMR spectrum of complex **8**, two doublets at δ_H = 5.56 and 5.33 ppm, each integrating for four protons, are attributed to the aromatic protons of the *p*-cymene moiety. Furthermore, a heptet (δ_H = 2.87 ppm), a singlet (δ_H = 2.21 ppm), and a doublet (δ_H = 1.30 ppm), integrating for 2, 6 and 12 protons respectively, are assigned to the aliphatic protons of the *p*-cymene functionality. All of the reported chemical shifts are in agreement with literature.[19]

2.8.2 Infrared spectroscopy

However, ^{1}H NMR spectroscopy alone could not be used to confirm successful synthesis. Since the coordinated oxalato ligand does not bear any additional protons, the spectra of the desired products are identical to that of the corresponding precursor dimers used. Consequently, the isolated

compounds were further analysed by IR spectroscopy (Figure 2.13). Most notably, the broad ν(OH) signal at approximately 3000 cm^{-1}, which is observed in the IR spectrum of the uncoordinated ligand (Figure 2.13 – purple), is not present in the spectra of the complexes. This not only confirms successful coordination to the oxygen donor atoms, but also the absence of any starting material in the isolated product. The spectra of complexes **7** and **8** are also dominated by strong absorption bands at 1618 and 1604 cm^{-1} respectively, as reported in literature,[19,43] and confirms the presence of the C=O functional groups within these complexes. Furthermore, the shift of the ν(C=O) absorption bands to a higher wavenumber than that of the ligand (1574 cm^{-1}) not only supports complexation but suggests minimized back donation and thus an increase in the bond order between the carbon and oxygen upon complexation.

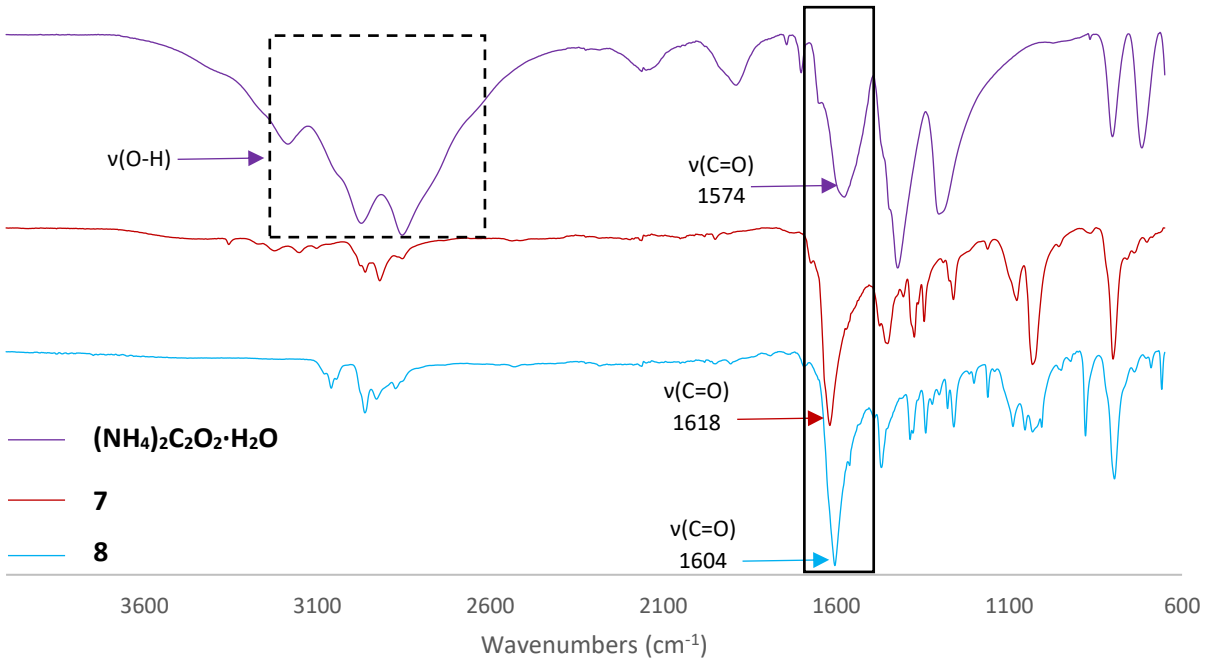

Figure 2.13: *IR spectra of ammonium oxalate monohydrate and complexes **7** and **8**.*

2.8.3 High-resolution mass spectrometry

The *O,O*-chelate binuclear molecular clips were further analysed using high-resolution ESI-MS. The mass spectrum of complex **7** yielded a peak at 371.060 *m/z*, which corresponds to the molecular ion with the loss of two chloride ions, $[M\text{-}2Cl]^{2+}$. In the spectral data of complex **8**, a fragment corresponding to $[M\text{-}2(p\text{-cymene})\text{-}Cl]^{+}$ was observed, with an *m/z* value of 325.0021.

2.9 Synthesis of cationic Ir(III) and Ru(II) metallarectangles containing *N,N'*-ditopic ligands and bridging chlorides (9 – 12)

As previously discussed in Section 1.4.4, a two-step synthetic procedure is required to synthesize a rectangular architecture. The first step involves synthesizing an appropriate precursor binuclear complex (Section 2.5). The subsequent step yields the desired metallarectangle, *via* coordination-driven self-assembly.

The synthesis of metallarectangles **9** – **12**, containing bridging chlorides, involved reacting the appropriate binuclear complex (**3** – **6**) with AgOTf, at room temperature (r.t.), for 24 hours (Scheme 2.6). The reaction with AgOTf resulted in chloride abstraction, which was confirmed by the formation of a silver salt (AgCl). The remaining chloride atoms bridged two metal centres, resulting in the self-assembly of two binuclear complexes to form the desired discrete metallarectangles (**9** – **12**).

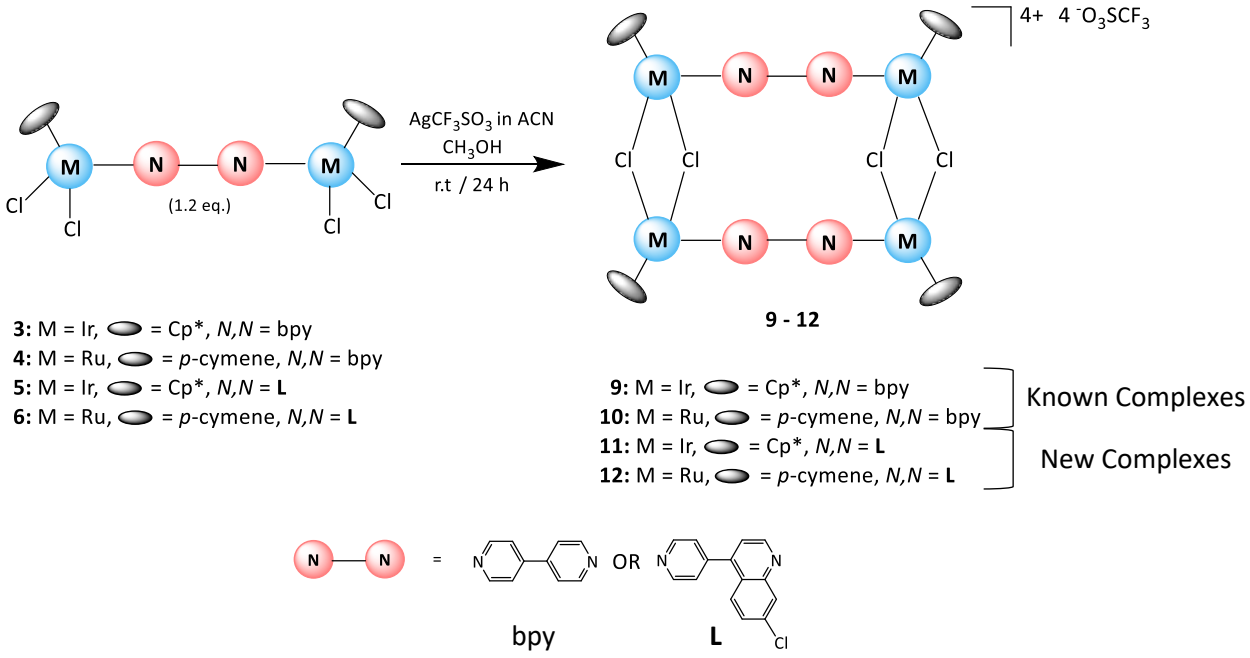

Scheme 2.6: *General method for the synthesis of metallarectangles* ***9*** *-* ***12****.*

All of the complexes were isolated as powders, ranging from pale yellow to bright orange. Metallarectangles **9** - **11** were isolated in moderately high yields (70 – 82%), however, complex **12** was isolated in a relatively low yield of 24%. Additionally, all of the aforementioned tetracationic metallarectangles displayed excellent solubility in DCM and DMSO and were practically insoluble in a range of non-polar organic solvents, including Et_2O, hexane, pentane, and toluene.

2.10 Characterisation of cationic Ir(III) and Ru(II) metallarectangles containing *N,N'*-ditopic ligands and bridging chlorides (9 – 12)

Metallarectangles **9** and **10**, containing the known 4,4'-bipyridine ligand, were only characterised using ^{1}H NMR and IR spectroscopy, and ESI mass spectrometry, to confirm their synthesis. Metallarectangles **11** and **12**, containing the newly designed ligand **L**, were fully characterised using ^{1}H, ^{13}C, and DOSY NMR and IR spectroscopy, and high-resolution ESI-MS.

2.10.1 ^{1}H NMR spectroscopy

In the ^{1}H NMR spectrum of the iridium metallarectangle **9** (Figure 2.14a), two signals at δ_H = 1.61 and 1.75 ppm, collectively integrating for 60 protons, are assigned to the four Cp* rings, confirming the presence of four Ir(III)Cp* moieties. Despite the symmetrical nature of the ligand (4,4'-bipyridine), the presence of two signals corresponding to the Cp* ligands has been observed in literature for both the iridium and analogous rhodium complexes,[45,46] and has been attributed to the presence of configurational isomers.[45] Furthermore, a dominant doublet and two smaller sets of doublets, present between δ_H = 8.80 - 9.02 ppm, collectively integrate for 8 protons, and correspond to the protons adjacent to the electronegative nitrogen atom of the pyridyl ring (α-protons). A similar set of signals are observed for the more shielded β-protons (H_b), which are observed between δ_H = 7.90 - 8.31 ppm, also collectively integrating for 8 protons. These respective integrations are in accordance with reported literature findings and support the formation of the desired tetranuclear system.[45]

Upon analysis of the ^{1}H NMR spectrum of the ruthenium analogue **10** (Figure 2.14b), a similar trend is observed, whereby a dominant signal is accompanied by a smaller set of signals. Interestingly, although VT-NMR analysis of the precursor complex **4** (Figure 2.6) confirmed the presence of rotamers, subsequent analysis of the corresponding metallarectangle (**10**) did not yield the same outcome, as the signals within this complex spectrum did not coalesce upon an increase in temperature.

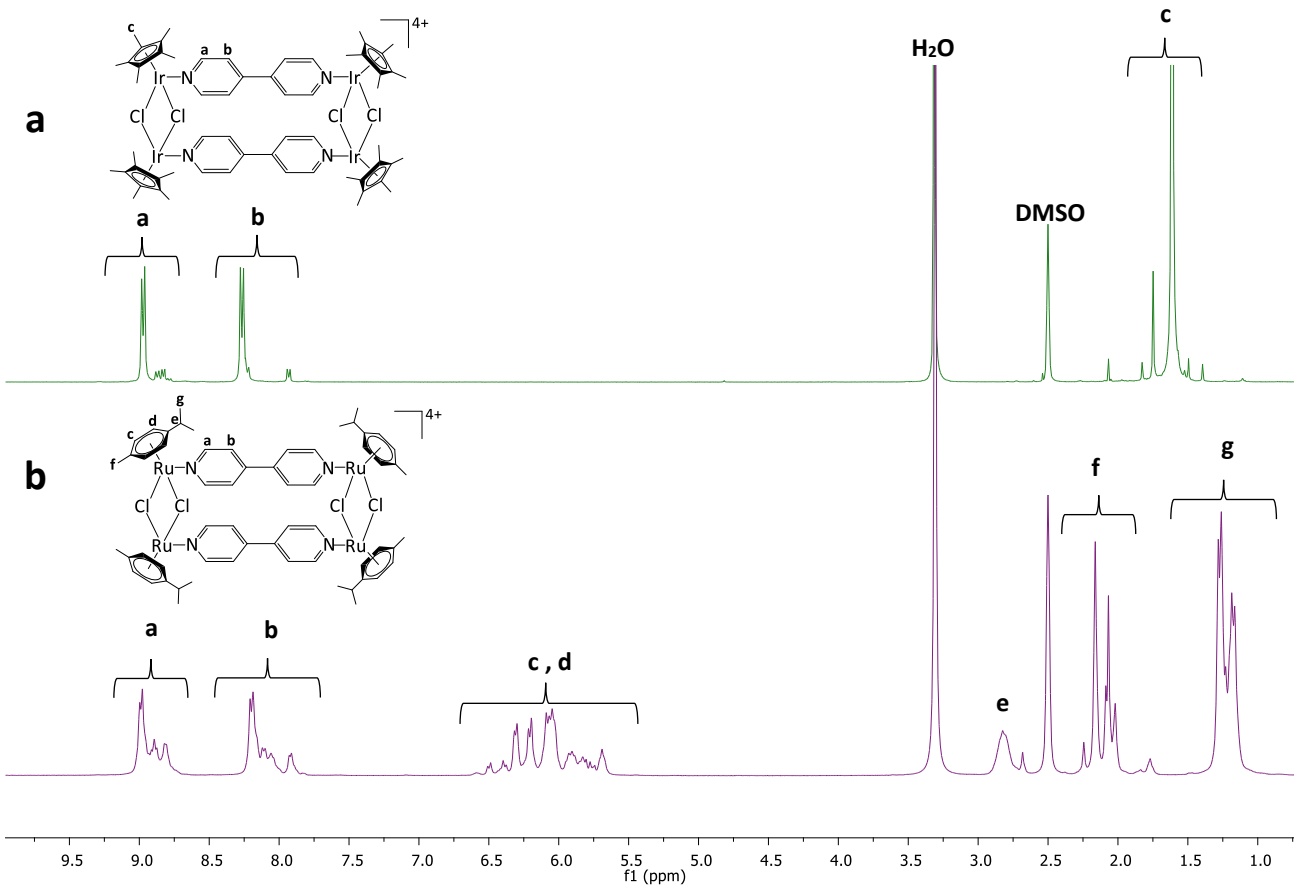

Figure 2.14: *^{1}H NMR spectra of complexes **9** and **10** in [D_6]-DMSO.*

It was initially assumed that the pyridyl rings of the 4,4'-bipyridine ligand would be co-planar, yielding a symmetrical system. And therefore, despite a possibly complex NMR spectrum, VT-NMR analysis would simplify the spectrum as the signals would coalesce due to the presence of rotational isomers. This, however, was not observed upon VT analysis of metallarectangle **10**. A paper reported by Yan *et al*.,[19] on a similar complex containing 4,4'-bipyridine, revealed a torsion angle between the two pyridyl rings upon the formation of the metallarectangle. The presence of this torsion angle, to possibly relieve steric strain, increases the possibility of atropisomers. Atropisomers are rotamers, however, compounds are termed atropisomers when the time scale for interconversion (between the different rotamers) is long enough to allow for the isolation of the individual rotamers. Such isomers are often observed for biphenyl systems and arise due to steric hinderance, which restricts rotation about the single bond between the two phenyl rings. Since the two pyridyl rings are possibly "locked" at a specific angle relative to each other, increasing the temperature and thus bond rotation would not necessarily yield an intermediate structure. Instead, several isomers would exist in solution, each giving rise to a set of signals on the NMR time-scale, contributing to the complexity of

the spectrum, with the most intense signals attributed to the dominant isomer. This is suspected to be the case for metallarectangle **10**.

Upon further inspection of the ^{1}H NMR spectrum of complex **10** (Figure 2.14), two sets of doublets between δ_H = 9.10 – 8.66 ppm and 8.30 – 7.79 ppm, each integrating for eight protons, are assigned to protons H_a and H_b of the bipyridyl ligands respectively. Furthermore, the proton signals between 6.65 – 5.60 ppm, integrating for 16 protons, are assigned to the aromatic protons of the four *p*-cymene ligands and thus confirm the presence of four metal centres. Finally, a broad signal at δ_H = 2.82 ppm, singlets between 2.29 – 1.95 ppm, and doublets between 1.37 – 1.07 ppm, are assigned to the aliphatic protons H_e, H_f, and H_g respectively.

Analysis of the ^{1}H NMR spectrum of the tetracationic iridium metallarectangle **11** (Figure 2.15), confirms coordination to both nitrogen atoms of the asymmetric ligand **L**. The two singlets at 1.74 and 1.64 ppm, which collectively integrate for 60 protons, are assigned to the methyl protons of the Cp* rings. Two Cp* signals are expected as two possible chemical environments exist for the Cp* ligands, due to the asymmetric nature of **L**. Furthermore, the remaining aromatic proton signals (H_{a-g}) collectively integrate for 18 protons, supporting the formation of a complex containing two **L** ligands. Additionally, a general downfield shift is observed for the aromatic proton signals H_c - H_g, compared to the corresponding signals in the spectrum of the precursor complex (Figure 2.7), further supporting the formation of a cationic (electron-deficient) compound. The slight upfield shift observed for the α-proton signals (H_a and H_b) has been described in other studies and has been attributed to the enhanced electron density at the metal centre, which has a greater influence on these protons.[47] It should also be noted that in the ^{1}H NMR spectrum of metallarectangle **11**, the signal corresponding to H_f is more deshielded than proton signals H_d and H_e. This was not observed in the ^{1}H NMR spectrum of the precursor iridium complex **5**, nor the spectrum of the uncoordinated ligand (Figure 2.8). Finally, the signal observed at 2.51 ppm is suspected to be encapsulated DMSO, which may further support the formation of a cavity-containing compound, which can encapsulate solvent molecules.

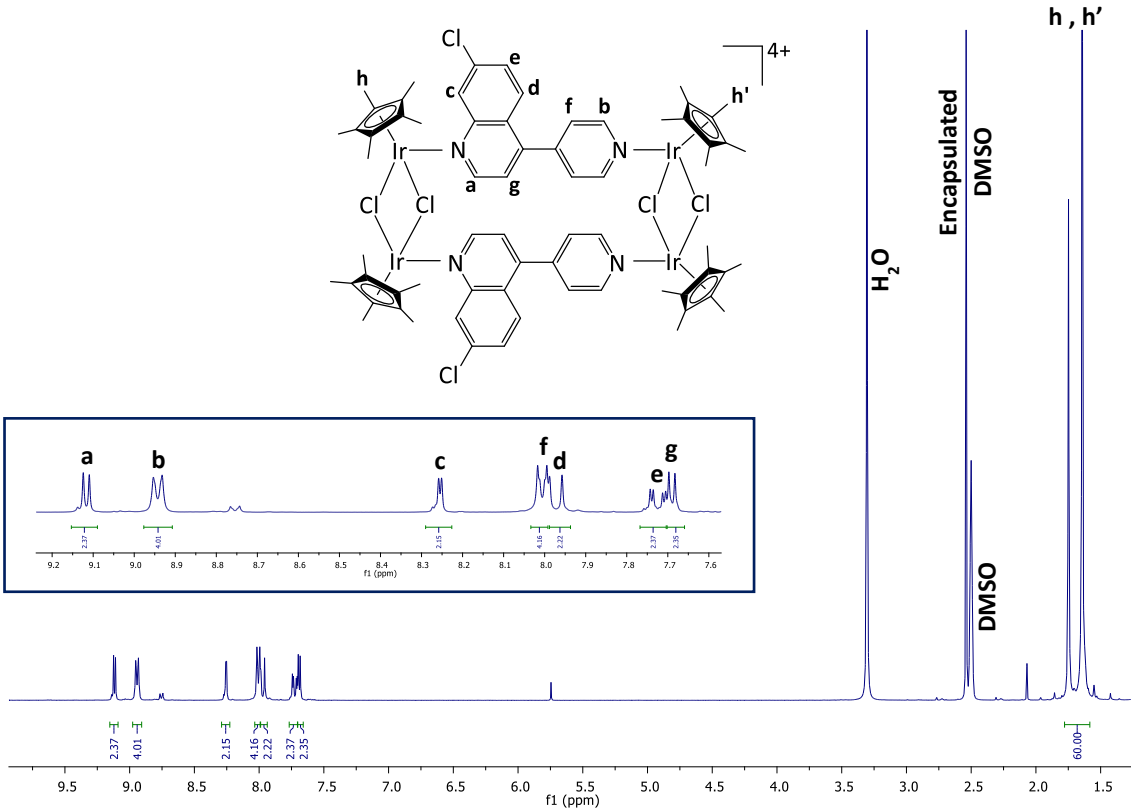

Figure 2.15: *^{1}H NMR spectrum of metallarectangle **11** in [D_6]-DMSO. The inset picture shows the aromatic region of the spectrum.*

It is important to note, however, that despite the NMR spectrum of compound **11** pointing to the formation of one pure complex, the exact configuration and conformation of this compound is unknown, as it could in fact be one of four possible isomers, as shown in Figure 2.16. As previously discussed, should more than one isomer be present in solution, each form (isomer) would be resolvable, contributing to the complexity of the spectrum. Should the sample contain a mixture of conformational isomers, VT-NMR analysis will result in the coalescence of signals. Based on the spectrum of complex **11**, one can deduce that a single, symmetrical isomer is favoured, and thus any of the pure compounds, **a** – **d** (Figure 2.16), could have formed. It is speculated that the absence of observable conformational isomers, or rotamers, may be due to a high barrier to rotation, resulting in restricted rotation. The reason for the selectivity toward a single constitutional isomer, however, is not entirely known, although steric strain may have a role to play.

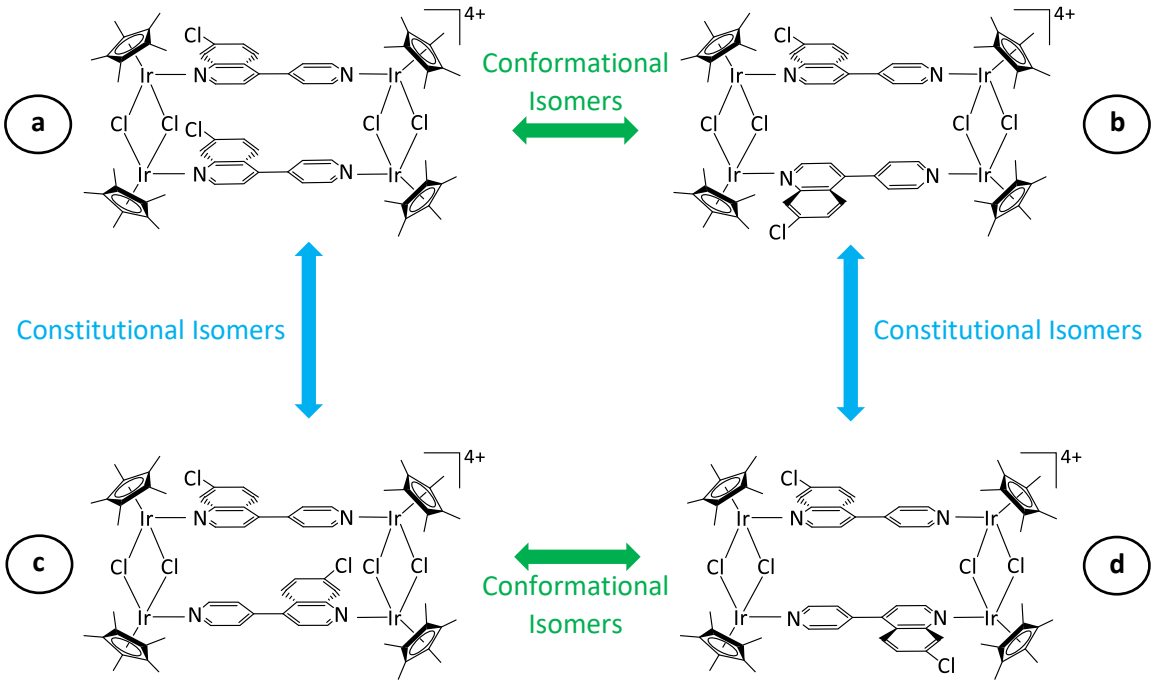

Figure 2.16: *Possible isomers of metallarectangle* ***11****.*

The ^{1}H NMR spectrum of the ruthenium metallarectangle **12**, containing **L** and bridging chloride ligands, is shown in Figure 2.17. Based on the structure alone, one would expect that similar to the iridium analogue (**11**), the *p*-cymene ligands can exist in one of two chemical environments, depending on which nitrogen atom (quinoline or pyridyl) the ruthenium metal centre is coordinated to. However, using protons H_k and $H_{k'}$ as an example, two singlets were expected, instead, four singlets are observed. This "doubling-up" is occurring with all proton signals (H_h – H_l) of the *p*-cymene ligand, suggesting that each of the four *p*-cymene ligands are in a unique chemical environment. The possible isomers shown in Figure 2.16 applies to all the metallarectangles containing **L**. However, this visual representation is rather simplified, as it does not highlight the possible atropisomers that may arise due to the torsion angle between the quinoline and pyridyl ring systems, which was observed in the crystal structure of complex **5** (Figure 2.12). It is speculated that this torsion angle can result in restricted rotation, causing each *p*-cymene moiety to be in a slightly different chemical environment, depending on its proximity to the different parts of **L**. However, despite the apparent "doubling-up" of the *p*-cymene signals, the integration of these signals ($H_{h\text{-}l}$), relative to that of the coordinated **L** ligands ($H_{a\text{-}g}$), suggests the presence of two *N,N'*-ditopic ligands and four *p*-cymene ligands. Moreover, as previously observed in the ^{1}H NMR spectrum of the iridium analogue (Figure 2.15), H_f is more deshielded than protons H_d and H_e.

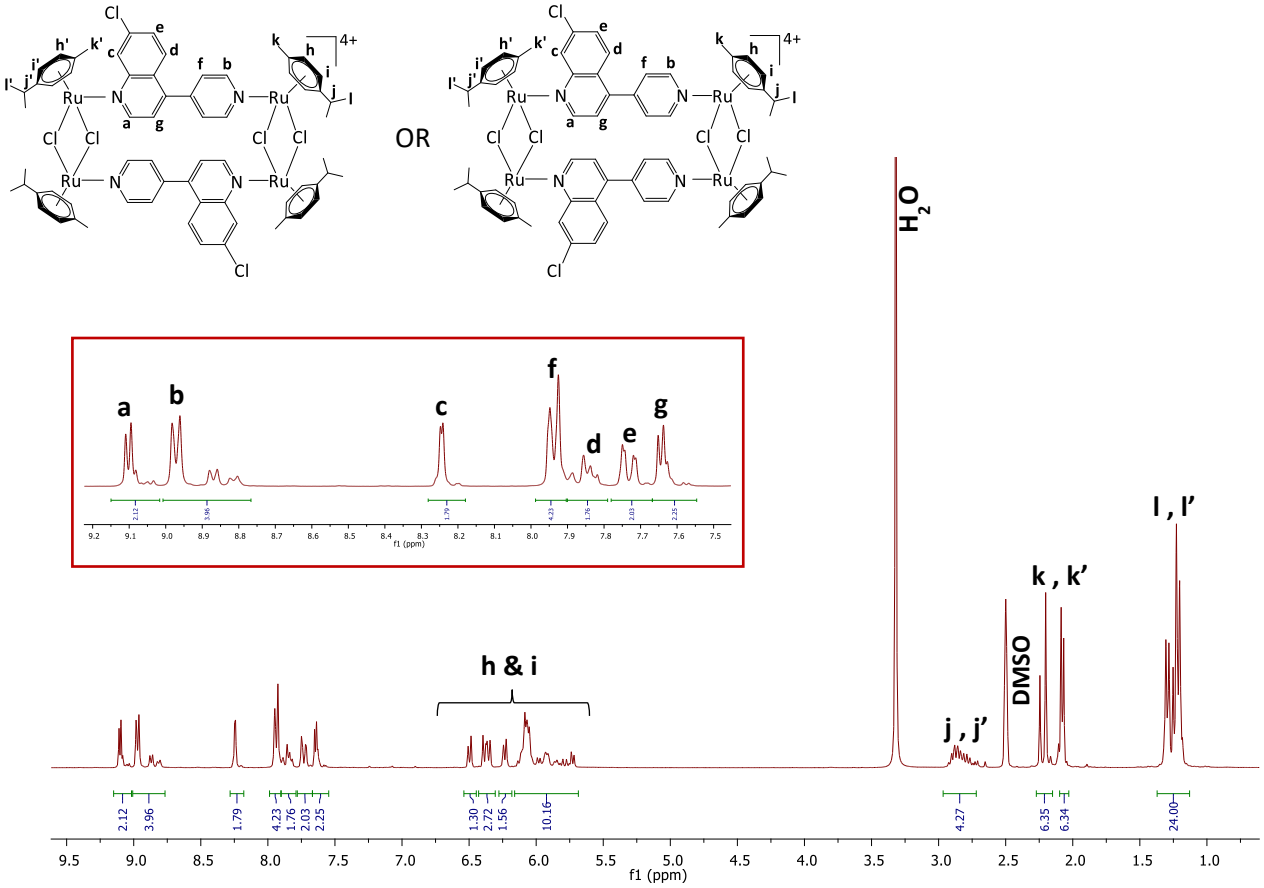

Figure 2.17: *^{1}H NMR spectrum of metallarectangle **12** $[D]_6$-DMSO. The inset picture shows the aromatic signals of the ligand **L**.*

2.10.2 Diffusion-ordered NMR spectroscopy

To confirm the presence of a single species in solution, the samples (**11** and **12**) were analysed using diffusion-ordered spectroscopy (DOSY). This technique is used to separate the NMR signals of different species in solution according to their diffusion coefficients. The diffusion coefficient of any given compound is directly related to both its size and shape, with bigger assemblies having a smaller diffusion coefficient. The spectrum of this diffusion NMR experiment allows one to identify the number of components present in a given sample. Consequently, this is a rather useful technique to corroborate the purity, as the ^{1}H NMR spectra of such complexes can often be quite complex, with smaller signals easily attributed to a contaminant. Furthermore, this technique also provides useful NMR information that can be used in the characterisation, assignment, and identification of the individual components.

When synthesizing supramolecular coordination complexes *via* self-assembly, depending on the nature of the ligands used (i.e. their flexibility), there is the possibility of forming a mixture of metallacycles, of varying sizes, as well as polymers. As a result, metallarectangles **11** and **12** were both analysed using DOSY spectroscopy to ensure the presence of a single assembly within the solution, confirmed by the presence of a single diffusion line. The DOSY NMR spectrum of complex **11**, shown in Figure 2.18, serves as a representative spectrum, as the spectra of both complexes reveal a single diffusion line. It should also be noted that the presence of a single diffusion line in the DOSY spectrum of the ruthenium analogue (**12**) provided evidence that the smaller signals observed within the ^{1}H NMR spectrum (Figure 2.17), are not the result of a separate compound, but possibly conformational isomers of the same compound. Furthermore, it is also important to note that this technique does not distinguish between the two isomeric metallarectangles (constitutional isomers) that may have formed, as these compounds, despite being chemically different, have the same molecular weight and shape, and would thus have the same diffusion coefficient.

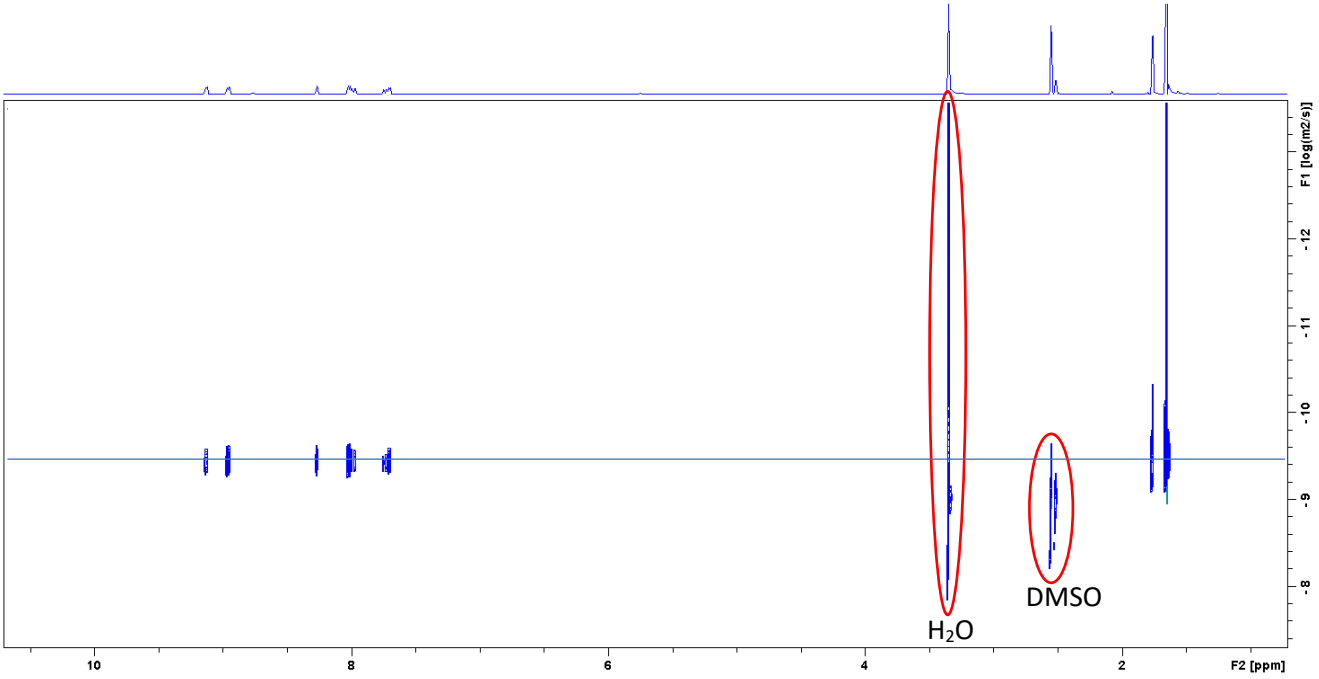

Figure 2.18: *DOSY spectrum of metallarectangle **11** in [D_6]-DMSO.*

2.10.3 Infrared spectroscopy

Infrared spectroscopy was then further used to verify the formation of the cationic metallarectangles. The IR spectra of the 4,4'-bipyridyl-containing metallarectangles, **9** and **10**, are quite similar and thus the spectrum of complex **9** serves as a representative example (Figure 2.19). The most notable signals in the IR spectrum of the metallarectangle (Figure 2.19 – blue), which are not present in the spectra of the precursor complex and uncoordinated ligand, are the strong absorption bands at 1248, 1224, 1149, and 1028 cm^{-1}. These signals are attributed to the triflate anions, with their assignments well-documented in literature,[48-50] and support the formation of the cationic metallarectangles as their triflate salts. Furthermore, it is evident that as the nuclearity of the system increases, the ν(C=N) absorption band shifts to a higher wavenumber. This was similarly observed within the IR spectrum of the ruthenium analogue (**10**) and is expected upon the formation of a cationic species. Due to this excess positive charge, there is decreased electron density on the metal centre, reducing backdonation. This decreased synergic effect thus explains the shift of the $\nu(C=N)_{pyridyl}$ absorption band to a higher wavenumber.

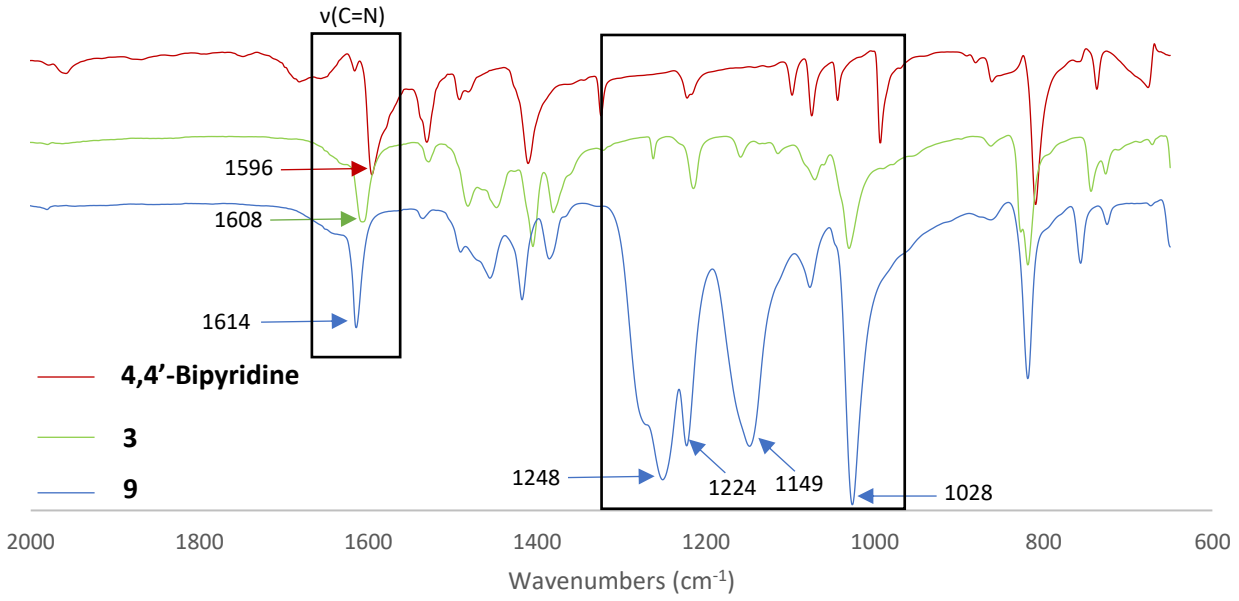

Figure 2.19: *IR spectra of 4,4'-bipyridine and complexes **3** and **9**.*

The IR spectra of metallarectangles **11** and **12**, containing ligand **L**, are almost identical to each other and thus a representative spectrum is shown in Figure 2.20. Similar to the IR spectrum of the metallarectangle containing 4,4'-bipyridine (Figure 2.19 - blue), sharp absorption bands are observed at 1258, 1124, 1150, and 1029 cm^{-1}, confirming the formation of a cationic species with triflate

counterions. However, unlike the spectrum of complex **9** (Figure 2.19), two absorption bands are observed at approximately 1600 cm^{-1}. These absorption bands, at 1609 and 1589 cm^{-1}, are assigned to the two different C=N functional groups within the asymmetric ligand **L**. The $\nu(C=N)_{quinoline}$ absorption band is present at a slightly lower wavenumber than that of the $\nu(C=N)_{pyridyl}$ absorption band, due to the extended delocalisation of the quinoline system. Furthermore, the shift of both ν(C=N) absorption bands supports the coordination to both nitrogen atoms of **L**, with the shift to a higher wavenumber providing further evidence for the formation of a cationic assembly.

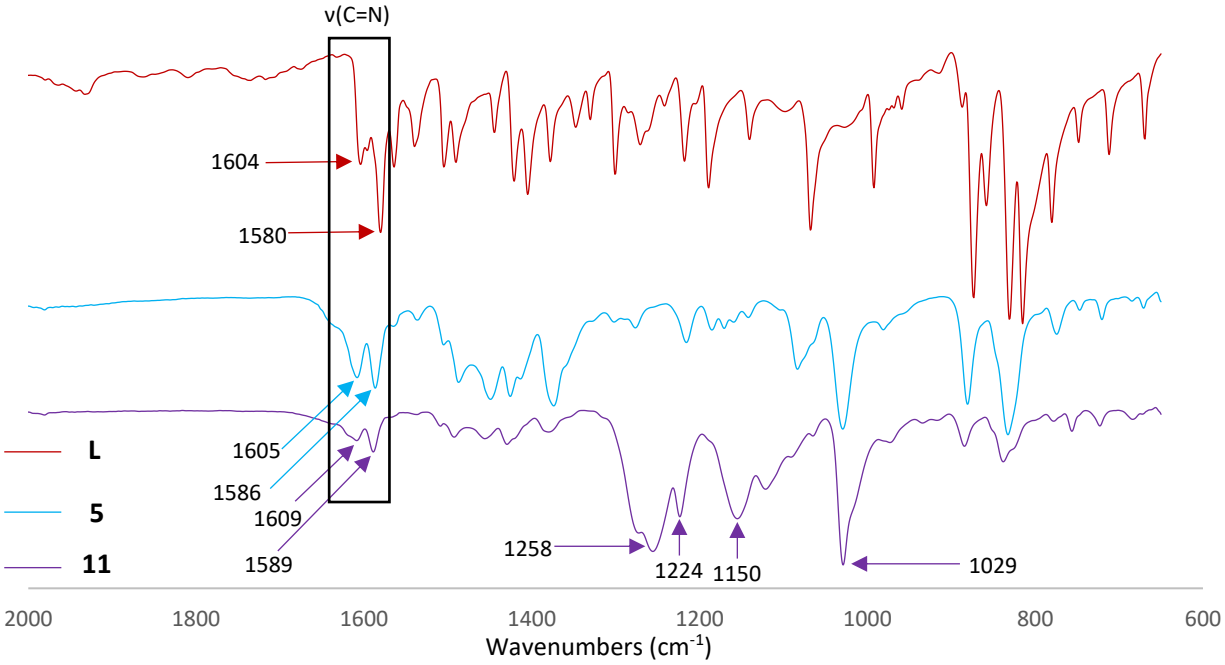

Figure 2.20: *Comparison between the IR spectra of ligand **L** and complexes **5** and **11**.*

2.10.4 High-resolution mass spectrometry

High-resolution ESI-MS was used to further support the structural integrity of the tetracationic metallarectangles **9** – **12**. The mass spectral data for the iridium metallarectangles, **9** and **11**, showed tetracationic peaks that correspond to the intact metallarectangles, with the loss of four triflate counterions, $[M\text{-}4(CF_3SO_3)]^{4+}$. This fragmentation is often observed for supramolecular rectangular architectures,[13,42,51,52] and agrees with the calculated values. Upon analysis of the mass spectral data for complexes **10** and **12**, peaks assigned to the molecular ion with the loss of two triflate ions, $[M\text{-}2OT_f]^{2+}$, was observed and agrees with the calculated values. Once again, this fragmentation is often observed for such systems, particularly for ruthenium metallarectangles.[14,51,53]

2.10.5 Powder X-ray diffraction

Unfortunately, to date, all attempts to grow single crystals of metallarectangles **11** and **12**, for X-ray structural analysis, were unsuccessful. The samples were thus analysed using powder X-ray diffraction (PXRD) to assess their level of crystallinity. PXRD measures the diffraction pattern of crystalline materials and is based on the principle that crystalline substances act as 3D diffraction gratings for X-ray wavelengths. Atoms in crystalline substances are arranged in a periodic array, and when X-rays are scattered from these atoms, a diffraction pattern is produced. In contrast, amorphous materials, such as glass, for example, do not produce sharp diffraction peaks as they do not have a periodic array of atoms with long-range order. Furthermore, a single crystal specimen would produce only one family of peaks within the diffraction pattern. Polycrystalline samples, however, contains thousands of crystallites that are randomly orientated. This constitutes the conditions for an ideal powder for PXRD analysis, which would allow all the possible diffraction peaks to be observed for a particular sample.

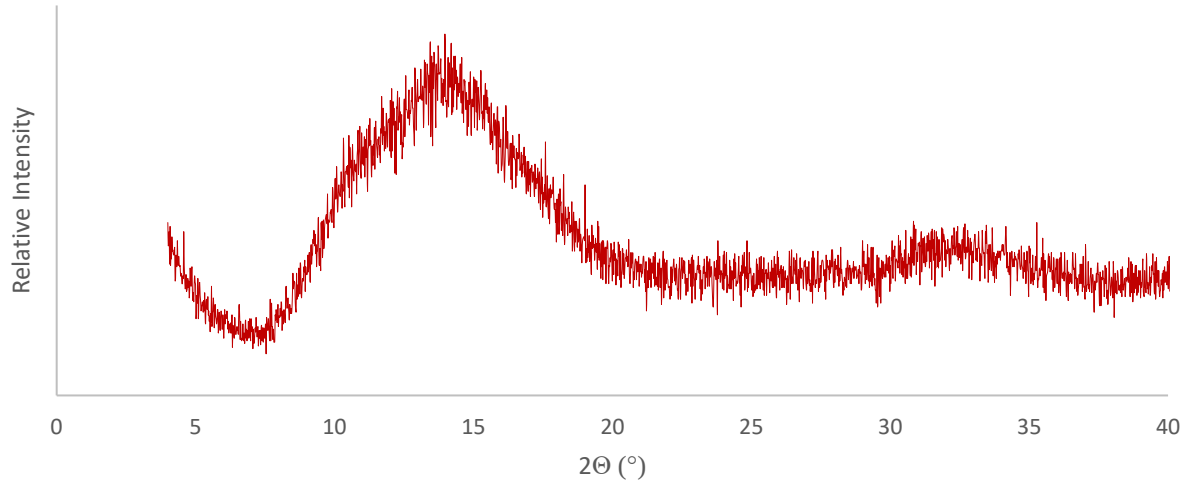

Figure 2.21: *PXRD of metallarectangle* ***11****.*

Based on the broad, humped peak, along with a very high signal to noise ratio as observed in Figure 2.21 for metallarectangle **11**, it can be postulated that the material is amorphous and therefore has no long-range atomic order. These broad, humped peaks are typical of amorphous materials. A similar spectrum (which was also characterised by a very broad, humped peak), was also observed for complex **12**, and consequently, this could explain the difficulty in growing single crystals of these compounds, as they both appear to be amorphous.

2.10.6 DFT calculations

Despite being unable to isolate a suitable crystal for analysis, a theoretical structure indicative of the 2D-rectangular nature of complex **11** is shown in Figure 2.22, as determined from a density functional theory (DFT) geometry optimization. As observed in the crystal structure of complex **5** (Figure 2.12), the optimized structures shown in Figure 2.22 also reveal a torsion angle between the pyridyl and quinoline ring systems of the ligand **L**. Within the *syn*-complex, the torsion angle in both ligands are near identical, with values of 41.48° and 41.43°. Within the *anti*-complex, the torsion angles are slightly smaller, with values of 33.33° and 34.70°. More notably, however, within a given isomer (*syn* or *anti*), the torsion angles of the two coordinated ligands are almost identical. This suggests that if the pyridyl ring of one ligand rotates, the pyridyl ring of the other ligand rotates in the same manner, possibly to relieve steric strain, a phenomenon which is supported in the literature.[54] Furthermore, analysis of these structures reveals that the geometry around the iridium metal centre is pseudo-tetrahedral, as the bond angles around the metal centre range between 81.00° and 94.55°.

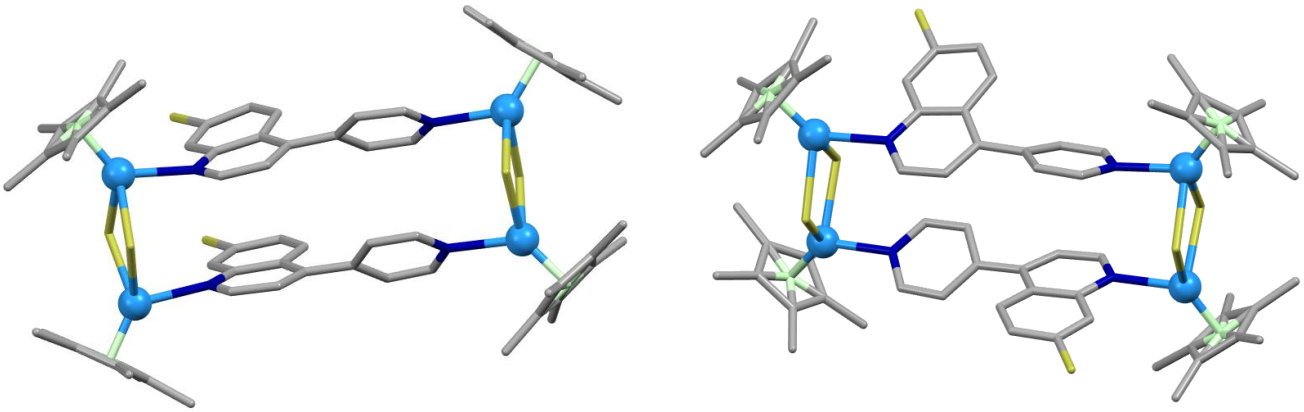

Figure 2.22: *DFT-optimized computational model of the syn- and anti-structures of complex* ***11****.*

2.11 Synthesis of cationic Ir(III) and Ru(II) metallarectangles containing *N,N'*-ditopic and bridging oxalato ligands (13 – 16)

Literature has shown that the final size of a metallarectangle can be easily controlled by adjusting the length of the precursor binuclear molecular clip used.[55,56] This led to the subsequent synthesis of metallarectangles **13** – **16**, containing the binuclear oxalato molecular clips discussed in Section 2.3.2.

The synthesis of metallarectangles **13** – **16**, containing chelating oxalato ligands, was achieved by reacting either complex **7** or **8** with 2.3 equivalents of $AgCF_3SO_3$, at r.t., for 3 hours. Not only does

this ensure complete abstraction of all the chlorides, but it has also been shown that the two chloro ligands in precursors **7** and **8** exist in a *trans* configuration relative to each other.[57] Addition of the $AgCF_3SO_3$ results in a fast equilibrium between the *cis* and *trans* geometries, with the *cis* geometry essential for the formation of the desired metallarectangle.[57] The successful abstraction of the chlorides was confirmed by the formation of AgCl, which was collected by filtration. Thereafter, the appropriate *N,N'*-ditopic ligand (bpy or **L**) was added, coordinating at the vacant parallel coordination sites on the metal centre (Scheme 2.7). The desired metallarectangles, formed *via* coordination-driven self-assembly, were isolated as powders, ranging from bright yellow to orange, in moderately good yields (67 – 88%).

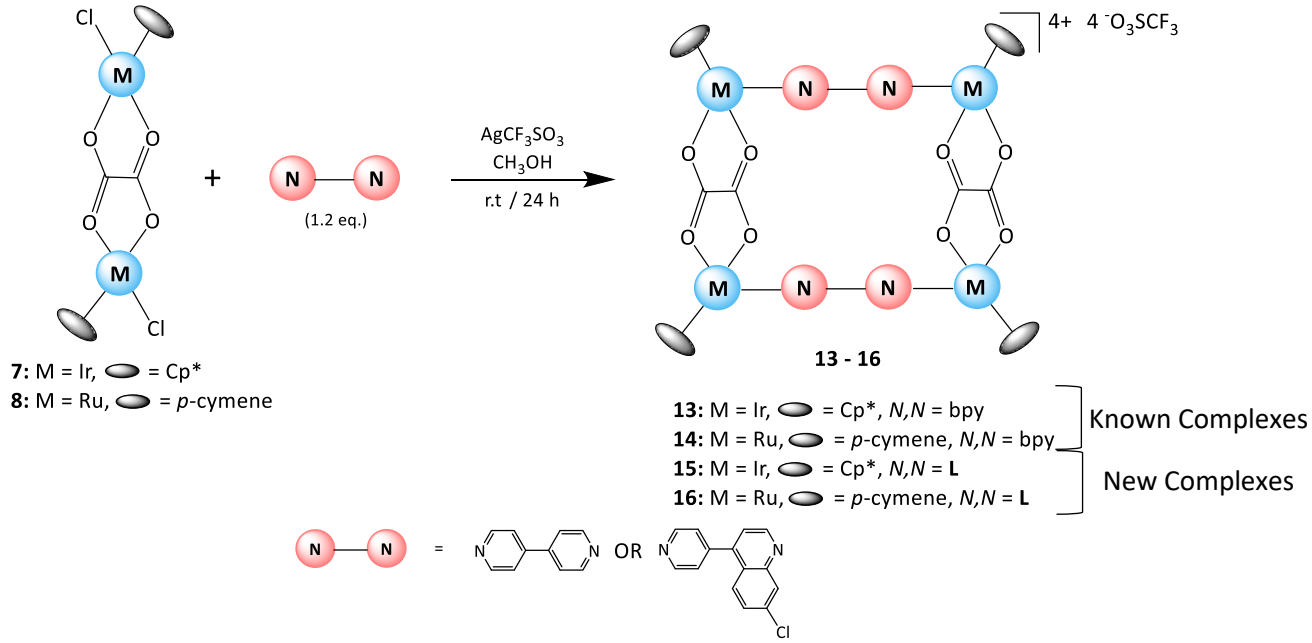

Scheme 2.7: *General method for the synthesis of metallarectangles* ***13*** *-* ***16****.*

2.12 Characterisation of cationic Ir(III) and Ru(II) metallarectangles containing *N,N'*-ditopic and bridging oxalato ligands (13 – 16)

The cationic metallarectangles, **13** – **16**, were characterised using various spectroscopic and analytical techniques. Metallarectangles **13** and **14** have been previously reported[19,43] and were thus only characterised using ^{1}H NMR and IR spectroscopy and mass spectrometry, to confirm their synthesis. The new metallarectangles, **15** and **16**, containing bridging **L** ligands, were characterized using, in addition to the aforementioned techniques, ^{13}C and DOSY NMR spectroscopy, to elucidate the structures of the proposed complexes.

2.12.1 ^{1}H NMR spectroscopy

The known metallarectangles **13** and **14** were first analysed using ^{1}H NMR spectroscopy. Analysis of the ^{1}H NMR spectrum of complex **13** in DMSO (Figure 2.23a), reveals two multiplets between 7.73 – 8.38 ppm and 8.50 – 9.08 ppm, each integrating for eight protons, with the most deshielded multiplet being assigned to the α-protons of the pyridyl ring (H_a). The appearance of multiplets for these protons, and their relative chemical shifts, are in accordance with the literature,[43] supporting the successful formation of this complex. Furthermore, the signals around 1.57 ppm were collectively assigned to the methyl protons of the Cp* rings, integrating for the expected 60 protons.

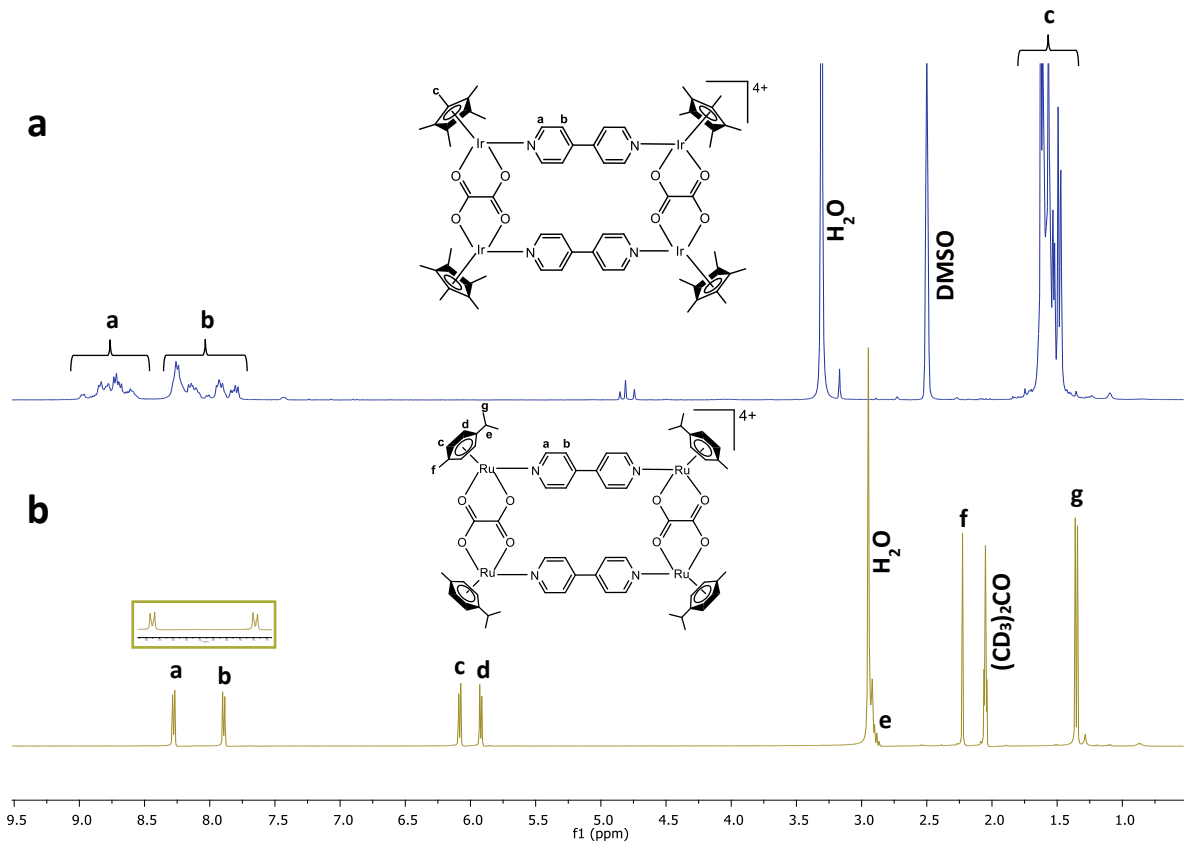

Figure 2.23: *Stacked ^{1}H NMR spectra of (a) metallarectangle **13** in [D_6]-DMSO and (b) metallarectangle **14** in [D_6]-(CD_3)$_2$CO.*

From the ^{1}H NMR spectrum of complex **14** (Figure 2.23b), it is evident that the signals are sharp and more defined, with distinct doublets present at δ_H = 8.28 and 7.89 ppm, which are assigned to protons H_a and H_b respectively. The observed multiplicity and chemical shifts of these signals are in accordance with reported literature values, along with the signals assigned to the *p*-cymene ligands (H_c – H_g).[19] At first, the poorly resolved signals in the spectrum of complex **13** (Figure 2.23a), were

postulated to be a result of the deuterated solvent used. However, analysis of the ^{1}H NMR spectra of compound **13** in various deuterated solvents (Figure 2.24) revealed no noticeable improvement in the resolution, and the signals were still observed to span over a range. It is thus speculated that this may be due to an intrinsic property of this complex.

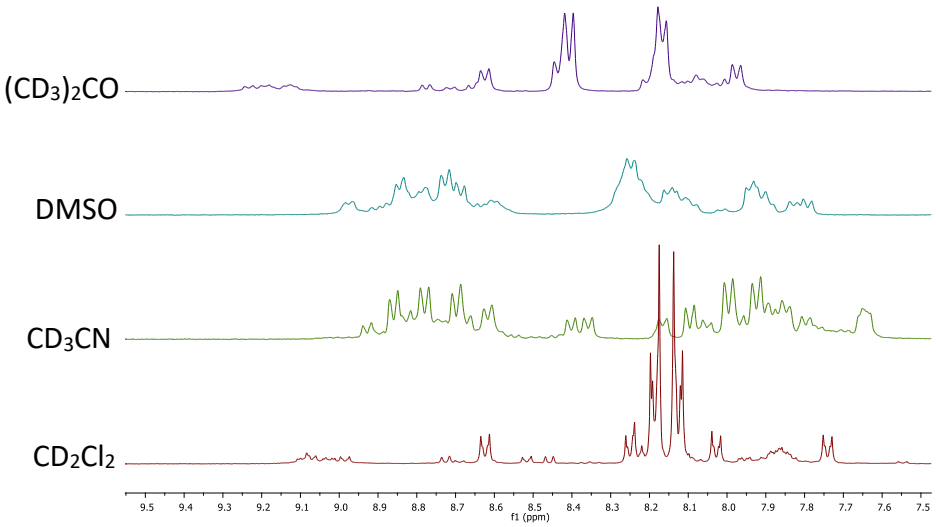

Figure 2.24: *Stacked ^{1}H NMR spectra of the aromatic region of complex **13** in $(CD_3)_2CO$, $[D_6]$-DMSO, CD_3CN and CD_2Cl_2.*

Upon analysis of the ^{1}H NMR spectrum of metallarectangle **15** (Figure 2.25), several singlets around δ_H = 1.50 ppm, collectively integrating for 60 protons, are assigned to the methyl groups of the four Cp* rings. More notably, however, the proton signals $H_{a\text{-}g}$ are not as well resolved as previously observed (Metallarectangle **11** - Figure 2.15). Instead, each dominant signal is accompanied by a smaller set of signals (*). Despite these "additional" signals, the integration of the aromatic proton signals collectively add up to 18 protons, confirming the presence of two **L** ligands.

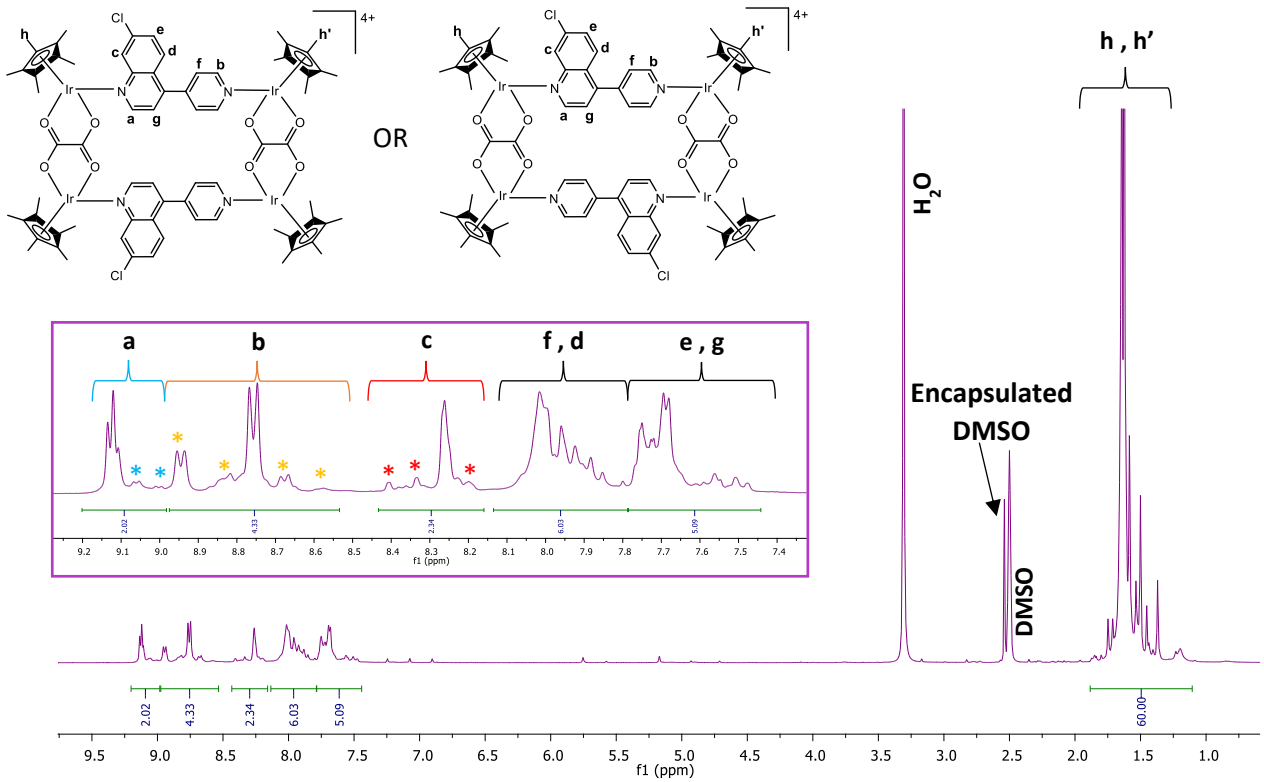

Figure 2.25: *^{1}H NMR spectrum of complex **15** in [D]$_6$-DMSO. The inset picture shows the proton signals of ligand **L**.*

To determine whether these smaller signals (*) are attributed to conformational isomers, as observed for complexes **3** and **4** (Section 2.6.1, Figure 2.6), or possible configurational isomers, as discussed for metallarectangles **9** and **10** (Section 2.10.1), the sample was analysed by VT-NMR. Unlike for metallarectangles **9** and **10**, VT-NMR analysis revealed the presence of conformational isomers, as the signals converged upon an increase in temperature. Furthermore, a general downfield shift of the dominant aromatic proton signals (H_a – H_g), compared to the uncoordinated ligand, suggests a loss of electron density, which is expected upon the formation of a cationic metallacycle.

Finally, compared to the ^{1}H NMR spectrum of the ruthenium metallarectangle **12** (Figure 2.17), the ^{1}H NMR spectrum of complex **16** (Figure 2.26) shows an apparent doubling-up of both the *p*-cymene and **L** signals. VT-NMR analysis confirmed that this is not due to rotational isomers, instead, it is suspected that the sample contains a mixture of two constitutional isomers. The presence of two sets of signals corresponding to **L**, in a 1:1 ratio, points to a mixture of two metallarectangles. Based on the premise that if one ring is twisted about an M-N bond, steric constraints can cause the other rings to twist in the same manner,[54] it is likely that the two **L** ligands are parallel to each other, despite a possible torsion angle between the pyridyl and quinoline ring systems. Moreover, the integrations of the *p*-cymene signals ($H_{h\text{-}l}$) also support the presence of two metallarectangles.

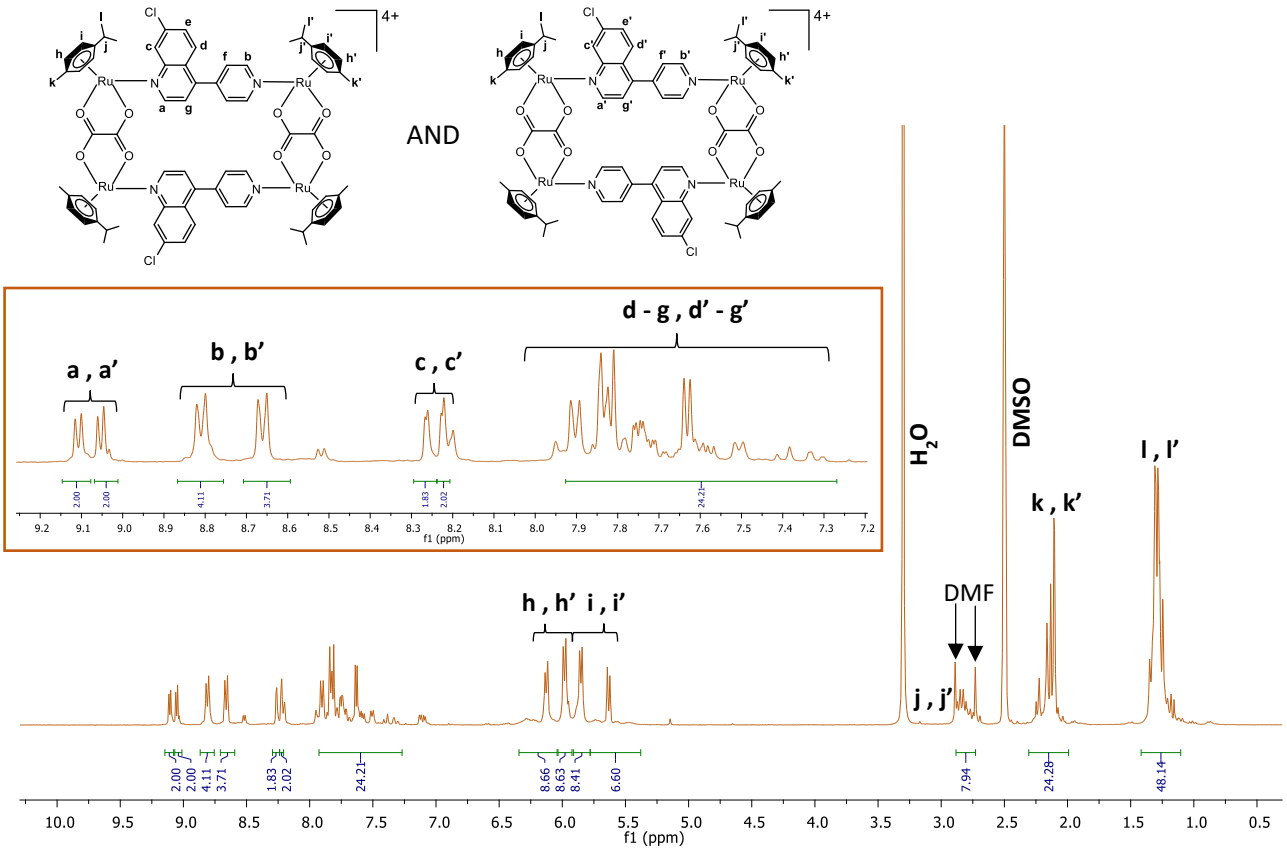

Figure 2.26: *^{1}H NMR spectrum of complex **16** in [D]$_6$-DMSO. The inset picture shows the proton signals of ligand **L**.*

The selectivity toward a dominant isomer, which was observed for metallarectangles **11**, **12**, and **15**, is rather interesting. However, the reason for that selectivity, or lack thereof, in the case of metallarectangle **16**, warrants further exploration.

2.12.2 Diffusion-ordered NMR spectroscopy

To confirm the presence of a single compound in solution, the new metallarectangles **15** and **16** were further analysed using DOSY NMR experiments. The DOSY spectrum of complex **15** is shown in Figure 2.27 and serves as a representative example, as the spectra of both compounds (**15** and **16**) display a single vertical trace. This spectrum suggests the formation of one product and provides further evidence that the smaller signals observed in the ^{1}H NMR spectrum of complex **15** (Figure 2.25), are due to conformational isomers of the same compound rather than contaminants. It should also be noted that although the ^{1}H NMR spectrum of complex **16** (Figure 2.26) reveals a mixture of two constitutional isomers, the DOSY NMR spectrum still only reveals a single vertical trace, as the two compounds, despite being chemically different, have the same molecular weight and shape.

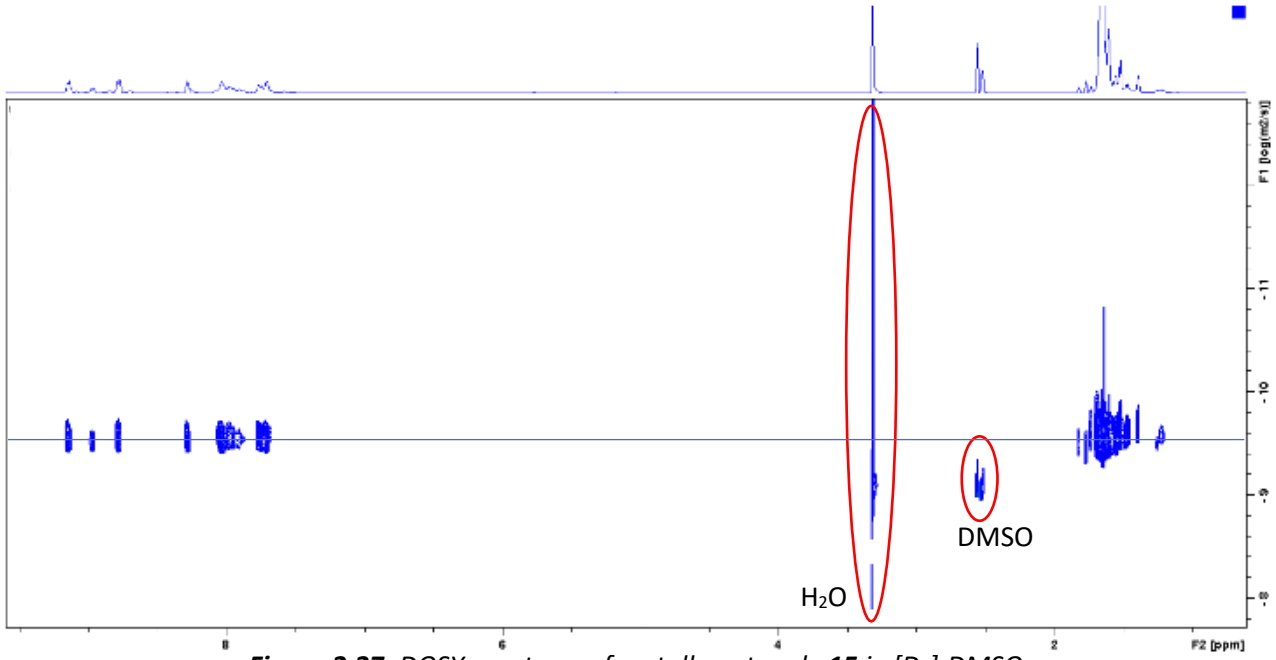

Figure 2.27: *DOSY spectrum of metallarectangle **15** in [D_6]-DMSO.*

2.12.3 Infrared spectroscopy

IR spectroscopy was used as another tool for the elucidation of the chemical structures. The infrared spectra of metallarectangles **13** – **16** are almost identical to each other, displaying characteristic absorption bands at very similar wavenumbers. The IR spectra of the precursor complex **7** and metallarectangle **15** can be seen in Figure 2.28 and serves as a representative example. In the IR spectrum of complex **15**, the characteristic ν(C=O) stretching frequency is present at approximately 1626 cm^{-1}, which is higher than the wavenumber of the corresponding absorption band in the

precursor complex, observed at 1618 cm^{-1}. This is due to the reduced electron density upon the formation of the cationic species. The backdonation of electrons into the empty π*-antibonding orbitals of the ligand is reduced, strengthening the C=O bond, causing the absorption band to shift to a higher frequency. No C=N absorption bands are observed due to overlap by the intense C=O absorption band. Furthermore, similarly to the previously discussed metallarectangles, the spectrum of complex **15** is dominated by strong absorption bands at 1250, 1222, 1155, and 1019 cm^{-1}, which are a result of the triflate counter ions, further supporting the formation of the cationic metallarectangle.

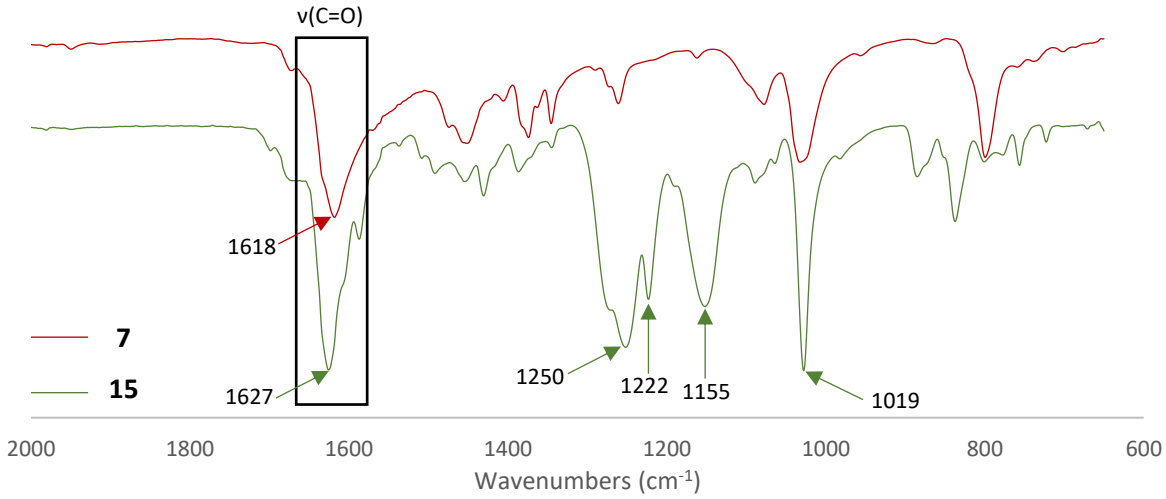

Figure 2.28: *Comparison between the IR spectra of the precursor binuclear complex **7** and metallarectangle **15**.*

2.12.4 High-resolution mass spectrometry

Finally, high-resolution ESI-MS was used to support the structural integrity of metallarectangles **13** – **16**. The mass spectral data of all the aforementioned complexes reveal an *m/z* value corresponding to the molecular ion with the loss of four triflate counter ions, $[M\text{-}OTf]^{4+}$. These observed tetracationic peaks correspond to the intact metallarectangles and agree with the calculated values.

2.13 Summary

A new quinoline containing *N,N'* ditopic ligand (**L**) was successfully synthesized *via* a Suzuki cross-coupling reaction and isolated in a relatively low yield of 42%. Furthermore, a series of ruthenium and iridium precursor binuclear complexes (**3** – **6**) were synthesized. The complexes contained either the known 4,4'-bipyridine (complexes **3** and **4**) or the new quinoline-containing ligand **L** (complexes **5** and **6**). All of the aforementioned complexes were synthesized *via* a bridge splitting reaction of the chlorides, within the dimer, and isolated as powders in moderately high to excellent yields (74 – 96%). Finally, the corresponding metallarectangles (**9** – **16**) were synthesized *via* coordination-driven self-assembly and isolated as their triflate salts. Generally, the metallarectangles were isolated in moderate to excellent yields (67 – 88%), apart from metallarectangle **12** which was isolated in a relatively low yield of 24%.

The known metallarectangles containing 4,4'-bipyridine were only characterized using ^{1}H NMR and IR spectroscopy, and high-resolution mass spectrometry, to ensure their successful synthesis. The new ligand **L**, and all complexes containing **L** (**5**, **6**, **11**, **12**, **15**, and **16**), were fully characterized using various spectroscopic and analytical techniques, including ^{1}H and ^{13}C NMR spectroscopy, infrared spectroscopy, and LC-MS or high-resolution ESI-MS. For metallarectangles **11**, **12**, **15**, and **16**, these techniques, in conjunction with DOSY NMR experiments, were collectively used to elucidate the structures of the rectangular architectures. Finally, single crystal X-ray analysis of the binuclear iridium complex **5** confirmed coordination of the iridium metal center to both nitrogen donor atoms of ligand **L** and provided evidence that the pyridyl and quinoline ring systems of the ligand are not co-planar.

Analyses of the ^{1}H NMR spectra of the new metallarectangles (**11**, **12**, **15**, and **16**) revealed rather interesting results. The ^{1}H NMR spectrum of the iridium metallarectangle **11** pointed toward the selective formation of a single symmetrical isomer. However, the spectra of complexes **12** and **15**, despite showing selectivity toward a dominant isomer, revealed the presence of conformational isomers within solution. Finally, the ^{1}H NMR spectrum of metallarectangle **16** suggests a lack of selectivity, as two sets of signals, assigned to ligand **L**, are observed in a 1:1 ratio. These signals do not coalesce upon analysis by VT-NMR, suggesting a mixture of two constitutional isomers in solution.

2.14 References

1. M. Foley and L. Tilley, *Pharmacol. Ther.*, 1998, **79**, 55–87.
2. K. Yearick, K. Ekoue-Kovi, D. P. Iwaniuk, J. K. Natarajan, J. Alumasa, A. C. d. Dios, P. D. Roepe and C. Wolf, *J. Med. Chem.*, 2008, **51**, 1995 - 1998.
3. M. Mushtaque and Shahjahan, *Eur. J. Med. Chem.*, 2015, **90**, 280-295.
4. G. R. Pereira, G. C. Brandao, L. M. Arantes, H. A. de Oliveira, Jr., R. C. de Paula, M. F. do Nascimento, F. M. dos Santos, R. K. da Rocha, J. C. Lopes and A. B. de Oliveira, *Eur. J. Med. Chem.*, 2014, **73**, 295-309.
5. Z. Guo and P. J. Sadler, *Angew. Chem. Int. Ed.*, 1999, **38**, 1512-1531.
6. L. Kelland, *Nat. Rev. Cancer*, 2007, **7**, 573-584.
7. O. Domarle, G. Blampain, H. Agnaniet, T. Nzadiyabi, J. Lebibi, J. S. Brocard, L. A. Maciejewski, C. Biot, A. J. Georges and P. Millet, *Antimicrob. Agents. Chemother.*, 1998, **42**, 540–544.
8. C. Biot, G. Glorian, L. A. Maciejewski and J. S. Brocard, *J. Med. Chem.*, 1997, **40**, 3715-3718.
9. M. Navarro, C. Gabbiani, L. Messori and D. Gambino, *Drug Discov. Today*, 2010, **15**, 1070-1078.
10. R. A. Jones, S. S. Panda and C. D. Hall, *Eur. J. Med. Chem.*, 2015, **97**, 335-355.
11. F. Dubar, C. Slomianny, J. Khalife, D. Dive, H. Kalamou, Y. Guerardel, P. Grellier and C. Biot, *Angew. Chem. Int. Ed.*, 2013, **52**, 7690-7693.
12. G. Gupta, B. S. Murray, P. J. Dyson and B. Therrien, *Materials*, 2013, **6**, 5352-5366.
13. G. Gupta, A. Das, J. Lee, N. Mandal and C. Y. Lee, *ChemPlusChem*, 2018, **83**, 339-347.
14. Y. Zhao, L. Zhang, X. Li, Y. Shi, R. Ding, M. Teng, P. Zhang, C. Cao and P. J. Stang, *PNAS*, 2019, **116**, 4090-4098.
15. H. Maeda, G. Y. Bharate and J. Daruwalla, *Eur. J. Pharm. Biopharm.*, 2009, **71**, 409-419.
16. D. F. Baban and L. W. Seymour, *Ad. Drug Deliv. Rev.*, 1998, **34**, 109–119.
17. M. Fujita, J. Yazaki and K. Ogura, *J. Am. Chem. Soc.*, 1990, **112**, 5645-5647.
18. G. L. Wang, Y. J. Lin and G. X. Jin, *J. Organomet. Chem.*, 2010, **695**, 1225-1230.
19. H. Yan, G. Süss-Fink, A. Neels and H. Stoeckli-Evans, *Dalton Trans.*, 1997, 4345-4350.
20. N. Kudo, M. Perseghini and G. C. Fu, *Angew. Chem. Int. Ed.*, 2006, **45**, 1282-1284.
21. N. E. Leadbeater, *Chem. Commun.*, 2005, 2881–2902.
22. N. Miyaura and A. Suzuki, *Chem. Rev.*, 1995, **95**, 2457-2483.
23. A. Suzuki, *J. Organomet. Chem.*, 1999, **576**, 147–168.
24. N. Miyaura, in *Advances in Metal-Organic Chemistry*, JAI Press Inc., 1998, vol. 6, pp. 187-243.
25. B. Tao and D. W. Boykin, *J. Org. Chem.*, 2004, **69**, 4330-4335.
26. W. Shen, *Tetrahedron Lett.*, 1997, **38**, 5575 – 5578.
27. R. W. Friesen and L. A. Trimble, *Can. J. Chem.*, 2004, **82**, 206-214.

28. C. White, A. Yates and P. M. Maitlis, in *Inorganic Syntheses*, ed. D. M. Heinekey, John Wiley & Sons Inc., 1992, vol. 29, ch. 53, pp. 228-234.
29. M. A. Bennet, T.-N. Huang, T. W. Matheson and A. K. Smith, in *Inorganic Syntheses*, eds. S. Ittel and W. Nickerson, John Wiley & Sons Inc., 1982, vol. XXI, ch. 16, pp. 75-78.
30. M. Oki, in *The Chemistry of Rotational Isomers*, eds. K. Hafner, J.-M. Lehn, C. W. Rees, P. v. R. Schleyer, B. M. Trost and R. Zahradnik, Springer-Verlag, 1993, vol. 30.
31. D. Melis, MSc Thesis, University of Cape Town, 2020.
32. A. Bacchi, G. Cantoni, P. Pelagatti and S. Rizzato, *J. Organomet. Chem.*, 2012, **714**, 81-87.
33. R. Payne, P. Govender, B. Therrien, C. M. Clavel, P. J. Dyson and G. S. Smith, *J. Organomet. Chem.*, 2013, **729**, 20-27.
34. J. G. Małecki and A. Maroń, *Transition Met. Chem.*, 2011, **36**, 297-305.
35. R. J. Lundgren and M. Stradiotto, in *Ligand Design in Metal Chemistry: Reactivity and Catalysis*, eds. M. Stradiotto and R. J. Lundgren, John Wiley & Sons, Ltd., 1st edn., 2016, pp. 1-14.
36. T. Leyssens, D. Peeters, A. G. Orpen and J. N. Harvey, *Organometallics*, 2007, **26**, 2637-2645.
37. L. Palacios, A. D. Giuseppe, R. Castarlenas, F. J. Lahoz, J. J. PérezTorrente and L. A. Oro, *Dalton Trans.*, 2015, **44**, 5777-5789.
38. B. Therrien, *Coord. Chem. Rev.*, 2009, **253**, 493-519.
39. E. Ekengard, K. Kumar, T. Fogeron, C. de Kock, P. J. Smith, M. Haukka, M. Monarid and E. Nordlander, *Dalton Trans.*, 2016, **45**, 3905-3917.
40. P. Chellan, K. M. Land, A. Shokar, A. Au, S. H. An, D. Taylor, P. J. Smith, K. Chibale and G. S. Smith, *Organometallics*, 2013, **32**, 4793-4804.
41. K.-G. Liu, X.-Q. Cai, X.-C. Li, D.-A. Qin and M.-L. Hu, *Inorg. Chim. Acta*, 2012, **388**, 78-83.
42. G. Gupta, A. Das, S. W. Lee, J. Y. Ryu, J. Lee, N. Nagesh, N. Mandal and C. Y. Lee, *J. Organomet. Chem.*, 2018, **868**, 86-94.
43. Y.-F. Han, Y.-J. Lin, W.-G. Jia, L.-H. Weng and G.-X. Jin, *Organometallics*, 2007, **26**, 5848-5853.
44. L. Rylands, A. Welsh, K. Maepa, T. Stringer, D. Taylor, K. Chibale and G. S. Smith, *Eur. J. Med. Chem.*, 2019, **161**, 11-21.
45. Y. Yamamotoa, H. Suzuki, N. Tajima and K. Tatsumi, *Chem. Eur. J.*, 2002, **8**, 372-379.
46. L. Lin, Y. J. Lin and G. X. Jin, *Appl. Organomet. Chem.*, 2019, **33**, 1-10.
47. A. Mishra, H. Jung, J. W. Park, H. K. Kim, H. Kim, P. J. Stang and K. W. Chi, *Organometallics*, 2012, **31**, 3519-3526.
48. P. Govindaswamy, G. Süss-Fink and B. Therrien, *Organometallics*, 2007, **26**, 915-924.
49. E. H. Wi, J. Y. Ryu, S. G. Lee, U. Farwa, M. Pait, S. Lee, S. Cho and J. Lee, *Inorg. Chem.*, 2019, **58**, 11493-11499.

50. P. Govindaswamy, G. Süss-Fink and B. Therrien, *Inorg. Chem. Commun.*, 2007, **10**, 1489-1492.
51. H. Vardhan, A. Nafady, A. M. Al-Enizi, K. Khandker, H. M. El-Sagher, G. Verma, M. Acevedo-Duncan, T. M. Alotaibi and S. Ma, *Molecules*, 2019, **24**, 2284.
52. A. Dubey, J. W. Min, H. J. Koo, H. Kim, T. R. Cook, S. C. Kang, P. J. Stang and K. W. Chi, *Chem. Eur. J.*, 2013, **19**, 11622-11628.
53. P. Li, Y.-M. Xu, W. Deng and Z.-J. Yao, *J. Organomet. Chem.*, 2019, **884**.
54. D. C. Caskey, T. Yamamoto, C. Addicott, R. K. Shoemaker, J. Vacek, A. M. Hawkridge, D. C. Muddiman, G. S. Kottas, J. Michl and P. J. Stang, *J. Am. Chem. Soc.*, 2008, **130**, 7620–7628.
55. L. L. Ma, J. Q. Han, W. G. Jia and Y. F. Han, *Beilstein J. Org. Chem.*, 2018, **14**, 2027-2034.
56. Y. Han and G. Jin, *Acc. Chem. Res.*, 2014, **47**, 3571-3579.
57. P. Govindaswamy, D. Linder, J. Lacour, G. Suss-Fink and B. Therrien, *Dalton Trans.*, 2007, 4457-4463.

CHAPTER 3

In vitro antiplasmodial and anticancer evaluation of the quinoline-containing ditopic ligand and the corresponding Ir(III) and Ru(II) binuclear complexes and metallarectangles

3.1 Introduction

The use of metal-based compounds, as chemotherapeutic agents, has revolutionized the field of drug discovery. This was prompted by the discovery of cisplatin,[1,2] and although its anticancer properties were discovered in the 1960s, to this day it continues to be one of the most widely used metal-based anticancer drugs.[1,3] Unfortunately, the lack of specificity within cancer chemotherapeutic agents leads to severe side-effects during treatment, with cisplatin in particular known to be notoriously toxic to the gastrointestinal tract and kidneys.[4,5] Furthermore, the development of resistance by various cancers, to known clinical drugs, is a growing concern, as platinum drugs constitute the majority of chemotherapeutic regimens.[6,7] Consequently, researchers have directed their focus toward alternative platinum group metals (PGMs), such as ruthenium and iridium, in the hope to not only combat the emerging resistance but reduce the inherent side-effects associated with many platinum-based compounds.

A new class of metal-based compounds that have been extensively studied for their anticancer activity is supramolecular coordination complexes (SCCs).[8-17] One example is a ruthenium pyridyl-amide metallarectangle (Figure 3.1), synthesized by Vardhan *et al.*, that displayed activity superior to cisplatin (IC_{50} >100 μM), with IC_{50} values of 3.3 and 4.0 μM in CAKI-1 (kidney) and A549 (lung) metastatic cancer cell lines, respectively.[11] At 5 μM, this compound reduced the cell proliferation of CAKI-1 and A549 cells by 63 and 58%, respectively.[11] However, at the same concentration, there was practically no reduction in normal Human Embryonic Kidney cells (HEK 293), suggesting that this compound is non-cytotoxic toward normal cells, and thus displays increased specificity toward cancerous cells.[11] Another example is a series of ruthenium metallarectangles, of the general formula $[(\eta^6\text{-}p\text{-cymene})_4Ru_4(OO\cap OO)_2(N\cap N)_2]^{4+}$ and $[(\eta^6\text{-}p\text{-cymene})_4Ru_4(NO\cap NO)_2(N\cap N)_2]^{4+}$, synthesized by Barry *et al.*, which were evaluated for their *in vitro* cytotoxicity against A2780 and A2780cisR ovarian cancer cell lines.[18] All of the complexes exhibited moderate to excellent activity in both the cisplatin-

resistant and -sensitive cells, with some complexes more active in the cisplatin-resistant cancer cell line, suggesting a mode of action different from cisplatin.[18]

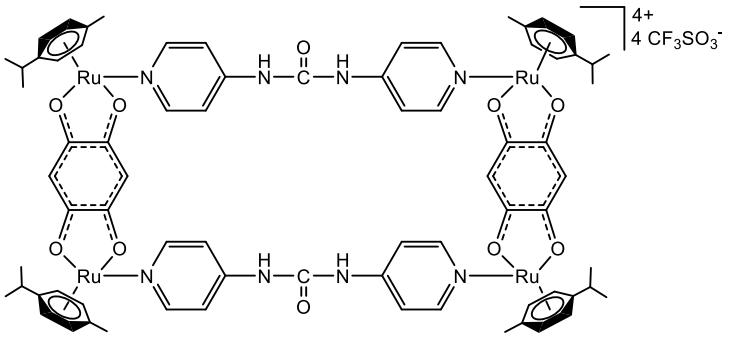

Figure 3.1: *Structure of a ruthenium bis-pyridyl amide metallarectangle, synthesized by Vardhan et al.*[11]

The enhanced potency of these multinuclear macromolecular systems may be attributed to the Enhanced Permeability and Retention (EPR) effect.[19,20] The EPR effect is based on the premise that low molecular weight compounds inherently freely traverse, in a non-selective manner, in and out of blood vessels.[19] Consequently, the undesirable indiscriminatory distribution of these compounds in normal tissue and their inability to accumulate selectively in tumour tissues, can cause severe systemic side-effects, most commonly observed upon treatment with anticancer agents.[19] The EPR-effect is the phenomenon of preferential accumulation and retention of macromolecular compounds in solid tumours, over normal tissue, thus enhancing the therapeutic efficacy of the drug while minimizing adverse side-effects.[19,20]

Moreover, metal incorporation has also exerted its influence on antimalarial agents, with the most notable example being FQ (Figure 3.2). Introduction of the ferrocene moiety, into the CQ scaffold, enhanced the antimalarial activity of CQ by over 22-fold in CQ-resistant strains of *P. falciparum*.[21] This approach thus offers an opportunity to combat the intrinsic and emerging resistance to known antimalarials.[22] Since then, several metal-based compounds have shown promise as potential antimalarial agents, with the metal imperative to the enhanced antiplasmodial activity observed, possibly due to the introduction of potentially new mode(s) of action.[23-25]

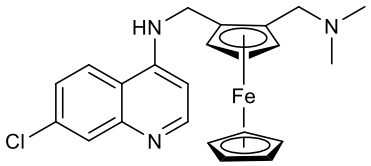

Figure 3.2: *Structure of FQ.*

A plethora of research has been done on the anticancer activity of SCCs, however, no studies have reported on their potential as antiplasmodial agents. Consequently, this chapter focuses on the biological activity of the synthesized compounds (**L**, **3** – **6**, **9** – **11**, and **13** – **16**), with a particular interest in the biological activity of the metallarectangles (**9** – **16**). The anticancer activity of the new quinoline-containing compounds was investigated in the MCF-7 and MDA-MB-231 cancer cell lines and selected complexes were also tested against the non-tumorigenic MCF-12A cell line. Furthermore, the antimalarial activity of all the synthesized compounds was explored in chloroquine-sensitive (NF54) and chloroquine-resistant (K1) strains of *P. falciparum*, shedding light on this less investigated area and providing some insight into the ability of SCCs to potentially act as antimalarials. Finally, to gain further insight into a possible mechanism of action of these compounds, a β-haematin inhibition assay was performed on selected compounds.

3.2 *In vitro* antiplasmodial evaluation against *P. falciparum* strains

As previously discussed (Section 1.3), a plethora of studies have reported on the pharmacological benefits of metal incorporation, which has shown, in many cases, to enhance the antiplasmodial activity of the parental organic ligand.[21,24,26-28] Interestingly, however, during this research study, there were no reports on the antiplasmodial activity of SCCs.

Consequently, all of the synthesized compounds, both known and new, were evaluated for their *in vitro* antiplasmodial activity, using a *Plasmodium* lactate dehydrogenase (*p*LDH) assay. During the asexual intraerythrocytic cycle *Plasmodium* parasites rely on anaerobic metabolism for the generation of energy.[29,30] During the glycolytic pathway, *p*LDH, which is the terminal enzyme in this pathway, catalyzes the conversion of lactate to pyruvate, using cofactor NADH.[30] The *p*LDH assay utilizes this intracellular catalytic process to specifically detect the *p*LDH enzyme, taking into account that this parasitic lactate dehydrogenase enzyme is 300 times more active toward $APAD^+$, an analogue of NAD^+, than human lactate dehydrogenase (*h*LDH). To exploit this kinetic difference, Makler *et al*. developed the Malstat assay,[31] for the specific detection of *p*LDH over *h*LDH activity. In this assay, the *p*LDH enzyme, present within parasite-infected lysed red blood cells, oxidizes lactate to pyruvate and in doing so, reduces cofactor $APAD^+$ (found within the Malstat™ reagent) to APADH (Scheme 3.1). The APADH subsequently reduces nitroblue tetrazolium (NBT), a yellow tetrazolium dye, with the assistance of phenazine ethosulfate (PES), to a blue diformazan compound, which is indicative of parasitic viability.[29]

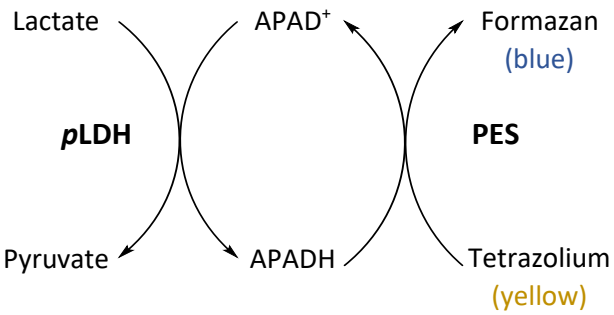

Scheme 3.1: *Principle of the pLDH Malstat™ assay for the detection of parasitic viability.*[31]

3.2.1 Antiplasmodial evaluation against the chloroquine-sensitive NF54 strain

The absence of research into the antimalarial activity of SCCs prompted an investigation into the potential antiplasmodial activity of the synthesized compounds, with a particular interest in the ruthenium(II) and iridium(III) metallarectangles. Consequently, the well-known 4,4'-bipyridine ligand, which was used in the prototypical metallarectangle,[32] the quinoline-containing ligand **L**, that was designed to be analogous to 4,4'-bipyridine while containing a pharmacophoric scaffold, as well as the corresponding binuclear complexes (**3** – **6**) and metallarectangles (**9** – **16**) were evaluated for their *in vitro* antiplasmodial activity against the chloroquine-sensitive (CQS) NF54 strain of *P. falciparum*. The IC_{50} values of the synthesized compounds were determined using the *p*LDH assay, with the IC_{50} value of a drug defined as the concentration at which 50% of the parasitic growth is inhibited.

The IC_{50} values of the ligands and corresponding complexes are summarised in Table 3.1, with chloroquine diphosphate (CQDP) used as the positive control. Most notably, the antiplasmodial results show that the quinoline-analogues (both the ligand and complexes) generally exhibit antiplasmodial activity superior to their corresponding 4,4'-bipyridyl counterparts. The activity of the quinoline-containing ligand **L**, with an IC_{50} value of 50.88 µM, outperforms 4,4'-bipyridine ($p = 0.03$) by almost 10-fold, pointing to the pharmacological benefits of incorporating a pharmacophoric quinoline scaffold into the framework of a potential drug candidate, as is evidenced in many antimalarial drugs.[33-35]

Table 3.1: *In vitro antiplasmodial data of 4,4'-bipyridine and* ***L****, and the corresponding binuclear complexes (****3*** *–* ***6****) and metallarectangles (****9*** *–* ***16****), against the chloroquine-sensitive NF54 strain of P. falciparum.*

Bipyridyl-analogues		***Quinoline-analogues***	
Compound	**IC_{50} (µM) ± SE NF54**	**Compound**	**IC_{50} (µM) ± SE NF54**
Ligands			
4,4'-bipyridine	500.50 ± 35.01	**L**	50.88 ± 7.34
Binuclear Complexes			
3	90.66 ± 50.58	**5**	46.26 ± 28.18
4	13.33 ± 4.21	**6**	14.75 ± 1.05
Metallarectangles			
9	19.40 ± 0.73	**11**	9.28 ± 0.75
10	9.41 ± 2.82	**12**	n/d[a]
13	26.25 ± 5.98	**15**	20.55 ± 5.60
14	1.08 ± 0.53	**16**	9.82 ± 0.89
Positive Control			
CQDP	0.0134 ± 0.0096		

[a] Not determined

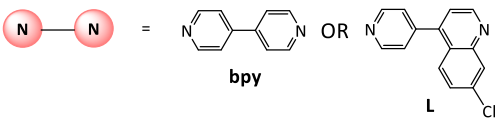

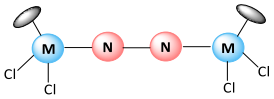

3: M = Ir, ⬭ = Cp*, *N,N* = bpy
4: M = Ru, ⬭ = *p*-cymene, *N,N* = bpy
5: M = Ir, ⬭ = Cp*, *N,N* = **L**
6: M = Ru, ⬭ = *p*-cymene, *N,N* = **L**

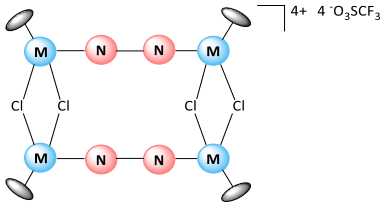

9: M = Ir, ⬭ = Cp*, *N,N* = bpy
10: M = Ru, ⬭ = *p*-cymene, *N,N* = bpy
11: M = Ir, ⬭ = Cp*, *N,N* = **L**
12: M = Ru, ⬭ = *p*-cymene, *N,N* = **L**

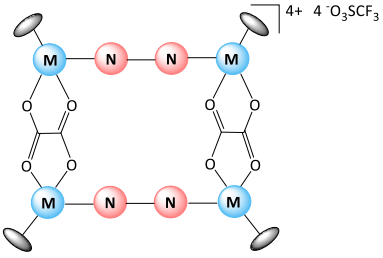

13: M = Ir, ⬭ = Cp*, *N,N* = bpy
14: M = Ru, ⬭ = *p*-cymene, *N,N* = bpy
15: M = Ir, ⬭ = Cp*, *N,N* = **L**
16: M = Ru, ⬭ = *p*-cymene, *N,N* = **L**

Furthermore, the activity of both ligands is generally enhanced upon metal complexation (statistically significant, $p < 0.05$), with either metal, with most complexes approximately five-times more active than their respective ligands. Interestingly, the antiplasmodial activity further increases upon an increase in the nuclearity of the system. For example, the IC_{50} value of 4,4'-bipyridine is 500.50 µM, however, upon complexation to form a binuclear complex e.g. the iridium complex **3**, the activity

increases 5-fold. Formation of the corresponding iridium tetranuclear metallarectangles (**9** or **13**) results in a further 4-fold increase in activity. This trend was similarly observed for the ruthenium-bipyridyl analogues, as well as the quinoline-analogues, further contributing to the plethora of studies that emphasize the advantages of metal incorporation on the pharmacological activity of organic compounds.[24,26-28] The enhanced activity observed upon the formation of the supramolecular metallarectangles demonstrates the potential of such multinuclear, highly charged systems, to act as antiplasmodial agents.

The increased antiplasmodial activity observed upon complexation suggests that the metal centre is crucial to the reduction in parasitic viability, by possible interaction with target compounds, although the exact mechanism is still unknown. Upon further analysis of the data, it was observed that in all cases the ruthenium analogues (**4**, **6**, **10**, **14**, and **16**) are more active than their corresponding iridium counterparts (**3**, **5**, **9**, **13**, and **15**), by at least two-fold. The most active of the synthesized compounds is the ruthenium metallarectangle containing 4,4'-bipyridine and bridging oxalato ligands (**14**), which has an IC_{50} value (1.08 µM) in the low micromolar range. The stability of the synthesized complexes (**3** – **6**, **9** – **11**, and **13** – **16**), in DMSO, were studied over 48 hours using ^{1}H NMR spectroscopy. Upon investigation into the stability of these complexes, stability studies of metallarectangle **14** revealed that it is unstable in DMSO. It is thus unlikely that the observed pharmacological activity is due to the intact metallarectangle, but rather a possible decomposition product. The most active complexes containing ligand **L** were metallarectangles **11** and **16**, which displayed comparable activity, with IC_{50} values of 9.28 and 9.82 µM, respectively. However, the activity of the synthesized compounds do not compare favourably to CQDP, which has an IC_{50} value of 0.0134 µM in the NF54 strain.

Despite no research studies investigating the antiplasmodial activity of SCCs, more specifically metallarectangles, it is interesting to note that these complexes can impede parasitic growth. Although their activity is not comparable to CQ, this data attests to the potential of such complexes to act as antiplasmodial agents. The reason for the limited antiplasmodial activity warrants further exploration, and investigations into further fine-tuning and possible ligand modifications could enhance the antimalarial efficacy of these complexes.

3.2.2 Antiplasmodial evaluation against the chloroquine-resistant K1 strain

To determine whether the ligands and corresponding synthesized complexes display activity toward resistant strains of the *Plasmodium* parasite, the compounds were tested for their *in vitro* antiplasmodial activity against the multidrug-resistant *P. falciparum* K1 strain (Table 3.2).

Table 3.2: *In vitro antiplasmodial data of 4,4'-bipyridine and* ***L****, and the corresponding binuclear complexes (****3*** *–* ***6****) and metallarectangles (****9*** *–* ***16****), against the chloroquine-resistant K1 strain of P. falciparum.*

Bipyridyl-analogues		***Quinoline-analogues***	
Compound	**IC_{50} (µM) ± SE K1**	**Compound**	**IC_{50} (µM) ± SE K1**
Ligands			
4,4'-bipyridine	778.76 ± 12.68	**L**	118.31 ± 59.17
Binuclear Complexes			
3	211.97 ± 19.99	**5**	50.24 ± 0.16
4	15.54 ± 0.46	**6**	17.39 ± 1.92
Metallarectangles			
9	17.14 ± 7.43	**11**	15.30 ± 2.60
10	19.76 ± 12.91	**12**	n/d[a]
13	70.32 ± 1.26	**15**	22.69 ± 5.38
14	2.25 ± 0.82	**16**	7.65 ± 0.77
Positive Control			
CQDP	0.296 ± 0.0283		

[a] Not determined

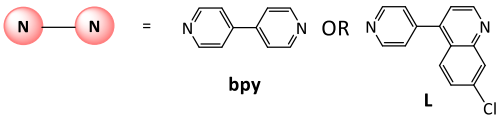

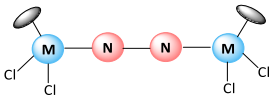

3: M = Ir, ⬭ = Cp*, *N,N* = bpy
4: M = Ru, ⬭ = *p*-cymene, *N,N* = bpy
5: M = Ir, ⬭ = Cp*, *N,N* = **L**
6: M = Ru, ⬭ = *p*-cymene, *N,N* = **L**

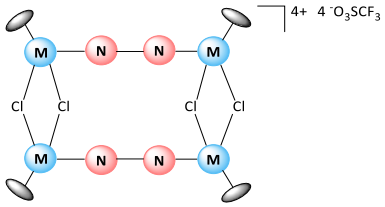

9: M = Ir, ⬭ = Cp*, *N,N* = bpy
10: M = Ru, ⬭ = *p*-cymene, *N,N* = bpy
11: M = Ir, ⬭ = Cp*, *N,N* = **L**
12: M = Ru, ⬭ = *p*-cymene, *N,N* = **L**

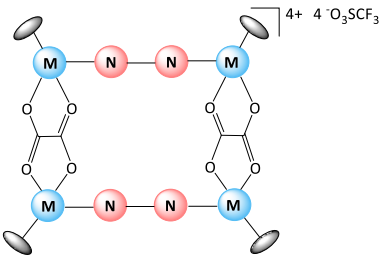

13: M = Ir, ⬭ = Cp*, *N,N* = bpy
14: M = Ru, ⬭ = *p*-cymene, *N,N* = bpy
15: M = Ir, ⬭ = Cp*, *N,N* = **L**
16: M = Ru, ⬭ = *p*-cymene, *N,N* = **L**

The inhibitory data of these compounds somewhat resemble the trend observed in the NF54 strain. The quinoline-containing ligand **L** was observed to be approximately seven-times more active than 4,4'-bipyridine, reiterating the importance of the quinoline scaffold for antiplasmodial activity. Furthermore, as previously observed in Table 3.1, the antiplasmodial data for the resistant strain similarly reveals that complexation enhances the pharmacological activity of the uncoordinated ligand, with the activity further increased upon an increase in the nuclearity of the system. Metallarectangle **16** (IC_{50} = 7.65 µM) is over two-times more active than the precursor binuclear complex **6** (IC_{50} = 17.39 µM), which further outperforms ligand **L** (IC_{50} = 118.31 µM) by approximately 15-fold.

Once again, complex **14** was observed to be the most active, however, as previously mentioned, the poor stability of this compound in DMSO suggests that the observed activity may not be a result of the intact metallarectangle. Of the quinoline-containing compounds, complex **16** showed the greatest activity, with an IC_{50} value in the low-micromolar range. Despite none of the synthesized compounds displaying activity greater than or comparable to CQ, the observed antiplasmodial data is still promising, as it points to a potentially new class of metal-based antiplasmodial agents.

To draw conclusions about the difference in activity of the compounds, across the two strains, the resistance index (RI) for each compound was calculated, with the values shown in Table 3.3. The RI of a compound is defined as the quotient of the IC_{50} value obtained in the resistant strain and the IC_{50} value obtained in the sensitive strain and is an important implement in the analysis of potential drug candidates. These indices provide valuable information on the ability of a compound to retain its activity in resistant parasitic strains, with a smaller RI value (RI ≤ 1) desired, which is indicative of a compound being more or equally active against the resistant parasitic strain relative to the sensitive strain. Complex **16** has the lowest RI value (0.8), suggesting that this complex is slightly more active in the resistant parasitic strain. The remaining complexes containing ligand **L** (**5**, **6**, **11**, and **15**) have RI values only slightly greater than 1, suggesting that these complexes largely retain their activity in the resistant K1 strain, experiencing only mild cross-resistance, however, not to the extent of CQ, which has an RI value of 22.1. It should also be noted that the RI values of the quinoline-containing complexes (**5**, **6**, **11**, **15**, and **16)**, which range between 0.8 – 1.6, are lower than the 2.3 RI value calculated for the uncoordinated ligand **L**. This suggests that metal incorporation imposed a potentially new mechanism of action, that is not subject to the same resistance mechanism experienced by the uncoordinated ligand, thus minimizing cross-resistance.

Table 3.3: *Resistance indices for the synthesized compounds.*

Bipyridyl-analogues		***Quinoline-analogues***	
Compound	**Resistance Index (RI)[a]**	**Compound**	**Resistance Index (RI)[a]**
Ligands			
4,4'-bipyridine	1.6	**L**	2.3
Binuclear Complexes			
3	2.3	**5**	1.1
4	1.2	**6**	1.2
Metallarectangles			
9	0.9	**11**	1.6
10	2.1	**12**	n/d[b]
13	2.7	**15**	1.1
14	2.1	**16**	0.8
Positive Control			
CQDP	22.1		

[a] IC_{50} K1 / IC_{50} NF54
[b] Not determined

3.3 β-Haematin inhibition studies

Haemozoin formation is an important target within antiplasmodial drug development.[26,36] During the intraerythrocytic stage of the parasites' life cycle, the parasite degrades haemoglobin (Hb) found within the infected red blood cells of the host.[37-39] This process provides the parasite with essential amino acids and nutrients and is thus crucial for its maturation and survival.[37,38] A side product of this Hb digestion is the production of haem, which is toxic to the parasite. To circumvent these effects, the parasite initiates a detoxification mechanism, converting the free haem into inert crystalline haemozoin (Figure 1.3), which is non-toxic to the parasite,[38] although when leaked from ruptured erythrocytes is toxic to humans, causing a high fever in patients.[40]

Many researchers have thus exploited this process by developing antimalarials that interfere with this haem detoxification method, the most promising of which has been CQ.[40,41] Upon entry into the digestive vacuole (DV), CQ inhibits haemozoin formation by forming a dimeric hematin complex, through π-π interactions, which leads to a build-up of free haem and subsequent death of the

parasite (Figure 1.5).[40] The target for many quinoline-based compounds is suggested to be haemozoin formation.[25,39,42] Consequently, the presence of the quinoline scaffold in ligand **L**, and the corresponding complexes, prompted investigation into the β-haematin (synthetic haemozoin) inhibition ability of selected compounds, as a potential mechanism of action. The ability of a potential drug candidate to inhibit haemozoin formation can be measured using the NP40-mediated β-haematin inhibition assay.[36,43] This assay seeks to mimic the conditions in the acidic DV of the parasite to better measure haemozoin formation.[36,43]

From the compounds screened for their *in vitro* antiplasmodial activity, complex **16**, which displayed the most promising activity across both strains, complex **15**, the analogous iridium complex, and ligand **L**, were assayed for β-haematin inhibition (Figure 3.3). Surprisingly, the quinoline-containing ligand **L** did not show any β-haematin inhibitory activity. Complexes **15** and **16** however, were found to inhibit β-haematin formation to almost the same extent as CQ, as indicated by their characteristic log-based sigmoidal curves (Figure 3.3), with the IC_{50} values represented graphically in Figure 3.4.

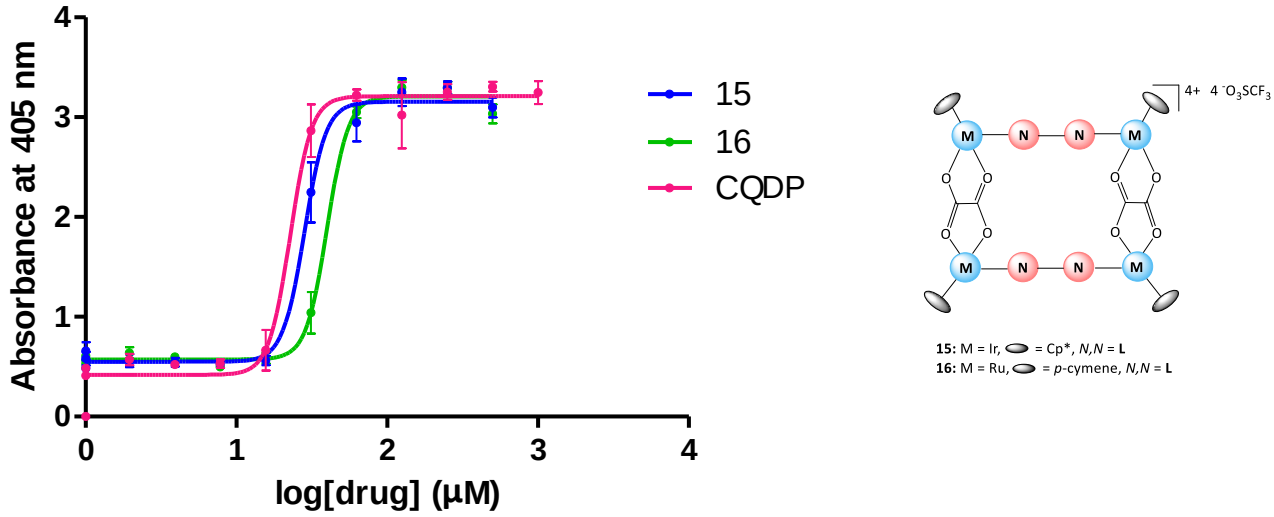

Figure 3.3: *Dose-response curves obtained for compounds **15** and **16**, as well as CQDP, using the NP-40 detergent-mediated β-haematin inhibition assay.*

The β-haematin inhibition activity of complexes **15** and **16** was unexpected since ligand **L** did not demonstrate any β-haematin inhibitory activity. Metal incorporation and the formation of these supramolecular assemblies (**15** and **16**) thus imposed this mechanism of action. This further supports the enhanced antiplasmodial activity observed for these complexes, in both strains, compared to the antiplasmodial activity of the uncoordinated ligand **L** (Tables 3.1 and 3.2). Interestingly, however, neither complexes **15** nor **16** had antiplasmodial activity near comparable to CQ. However, the IC_{50}

value of complex **15** (IC_{50} = 28.29 µM), obtained from the β-haematin inhibition assay, is comparable to CQ (IC_{50} = 22.75 µM). This suggests that complex **15** is inhibiting β-haematin to almost the same extent as CQ, however, the observed antiplasmodial activities do not corroborate this finding. This suggests that other factors are contributing to the limited antiplasmodial activity observed for this complex. One possibility is that entry into and/or accumulation in the parasitic DV, where haemozoin crystallization takes place, is limited, possibly due to the size and/or highly charged nature of this complex, as it has a very good cell-free β-haematin inhibitory activity but poor *in vitro* antiplasmodial activity.

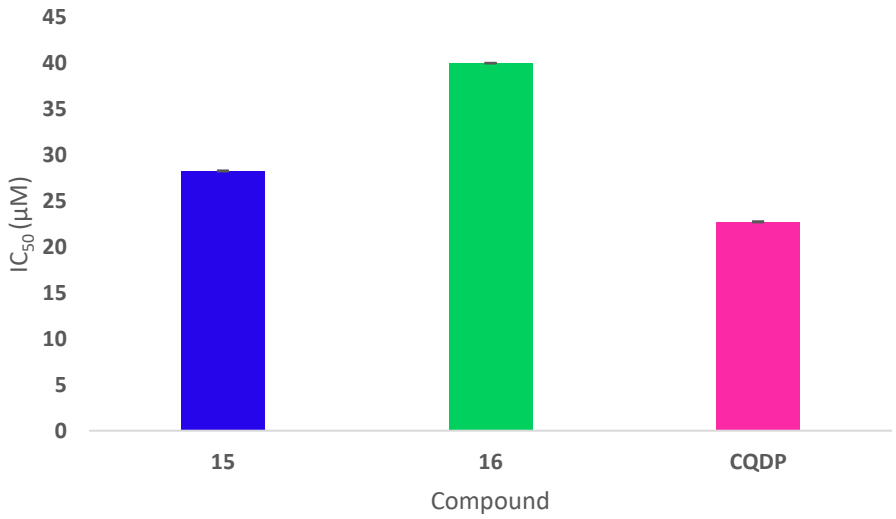

Figure 3.4: *IC_{50} values obtained from the* β*-haematin inhibition studies for compounds **15** and **16**, as well as CQDP.*

Finally, the polyaryl nature of these complexes (**15** and **16**) suggests that they are capable of intermolecular π-π interactions and it is thus possible that these complexes inhibit β-haematin formation through π-π stacking with haematin.

3.4 *In vitro* anticancer single dose pre-screening

The known anticancer activity of quinoline-containing compounds[44-47] and the extensive research into the anticancer activity of SCCs,[8,48-51] prompted investigations into the anticancer activity of the new quinoline-based compounds (**L**, **5**, **6**, **11**, **15**, and **16**). To identify compounds with potential anticancer activity, ligand **L** and the corresponding iridium(III) and ruthenium(II) complexes were pre-screened for their *in vitro* cytotoxicity, against the MCF-7 and MDA-MB-231 breast cancer cell lines, using the 3-(4,5-dimethylthiazol-2-yl)-2,5 diphenyltetrazolium bromide (MTT) assay. In viable cells,

MTT, a yellow tetrazolium salt, is reduced by dehydrogenase enzymes to water-insoluble formazan crystals (purple), using NADH/NAPDH co-substrates (Scheme 3.2).[52] This assay is thus a measure of cellular viability as the solubilization of the formazan crystals allows the number of cells to quantified colorimetrically, by measuring the absorption at 600 nm.[52]

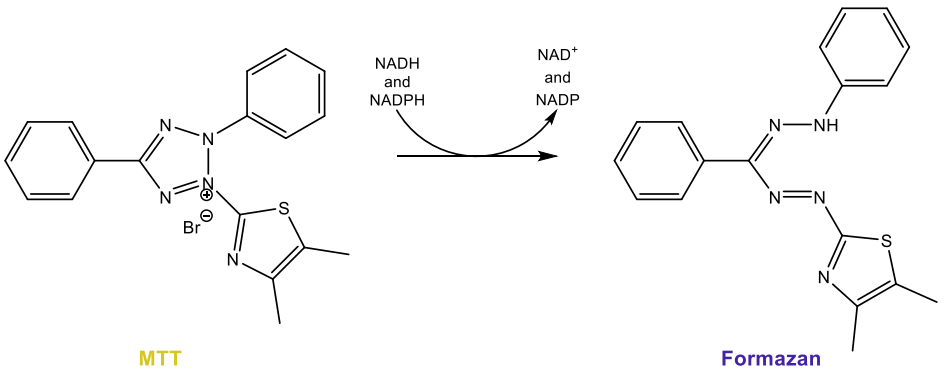

Scheme 3.2: *Principle of the MTT assay for the evaluation of cellular viability.*[52]

The compounds were first tested for their cytotoxicity at 10 µM. This was chosen as the starting concentration based on the approach by the National Cancer Institute (NCI), which conducts pre-screens at 10 µM for putative anticancer agents.[53]

3.4.1 In vitro cytotoxicity against the MCF-7 breast cancer cell line

The data obtained from the *in vitro* anticancer evaluation of ligand **L**, the corresponding iridium and ruthenium binuclear complexes (**5** and **6**), and metallarectangles **11**, **15**, and **16**, against the MCF-7 cell line, is summarized in Figure 3.3. At 10 µM, the quinoline-containing ligand **L** showed the greatest activity of the synthesized compounds ($p < 0.03$), reducing the cancer cell viability by almost 33%. This exceeds the 11% reduction observed for cisplatin at the same concentration. Complex **11** also showed increased efficacy compared to cisplatin, reducing the cell viability by 22%. The ruthenium complexes (**6** and **16**) showed no activity at the tested concentration, while the corresponding iridium complexes (**5** and **15**) displayed activity comparable to cisplatin, reducing the percentage cell viability by 12 and 16%, respectively.

Similar to the data obtained at 10 µM, upon doubling the concentration to 20 µM, ligand **L** and the iridium metallarectangle **11** showed the greatest activity. Most notably, metallarectangle **11** was the most potent, reducing the percentage cell viability by almost 60%, far exceeding that of cisplatin which was observed to impede the MCF-7 cell viability by only 20% at 20 µM. Ligand **L** also showed activity that exceeds cisplatin, reducing the cell viability by approximately 50%. Binuclear complexes

5 and **6**, and metallarectangle **16**, displayed activity comparable to cisplatin, reducing the cell viability by between 17 and 26%. The asterisks within the graph denote a significant difference in activity ($p < 0.05$) upon doubling the concentration.

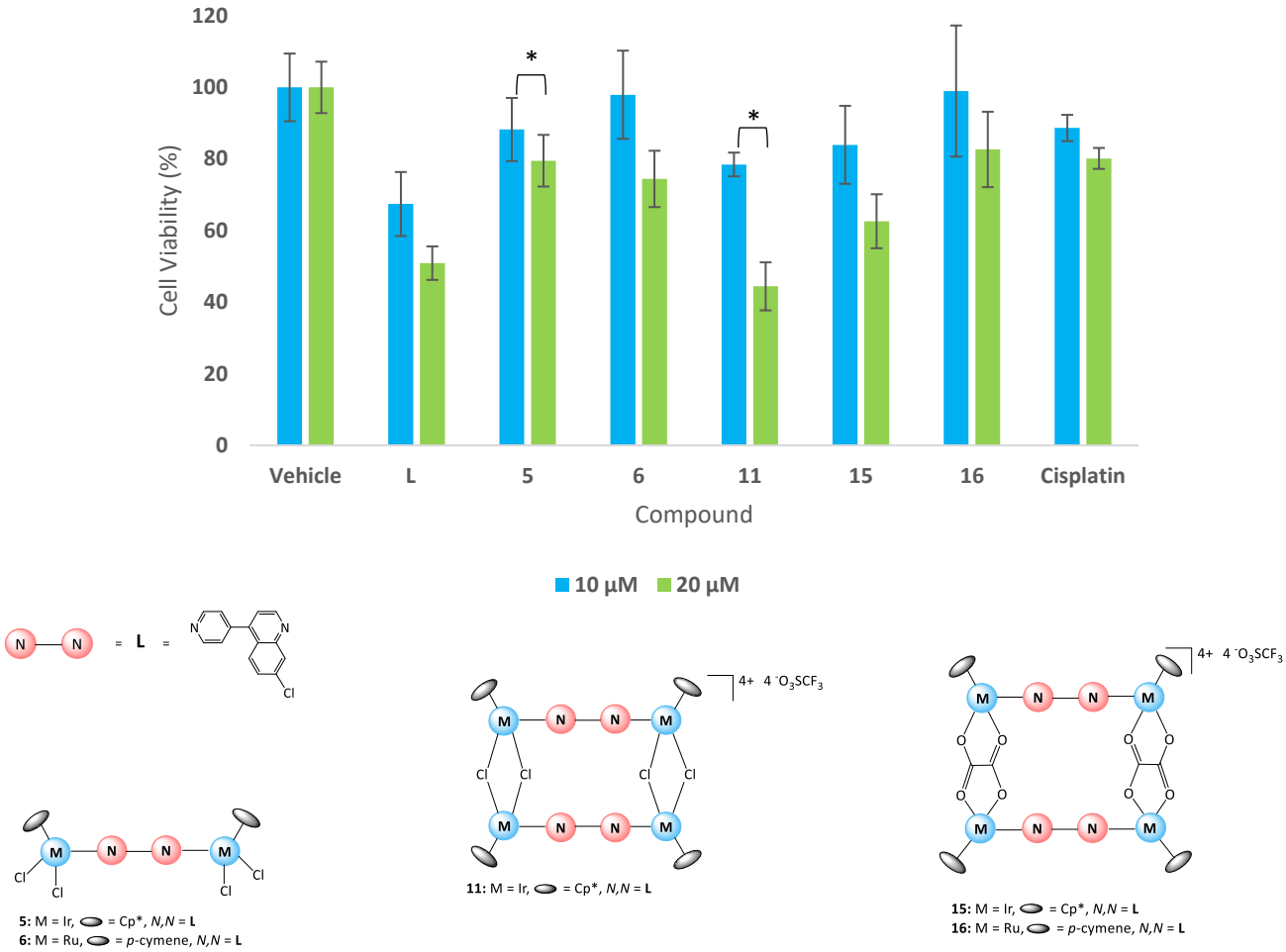

Figure 3.3: *The percentage cell viability as measured by MTT assays in MCF-7 breast cancer cells exposed to either the vehicle (0.1% DMSO) or the synthesized quinoline-containing compounds, at 10 and 20 µM concentrations, for 48 hours. Cisplatin was included as a positive control.*

3.4.2 In vitro cytotoxicity against the MDA-MB-231 breast cancer cell line

Due to the promising cytotoxic activity observed for the quinoline-containing compounds in the MCF-7 cell line, the same compounds were further evaluated for their *in vitro* cytotoxicity against the MDA-MB-231 breast cancer cell line. This cell line is notoriously difficult to treat,[54] as it is a triple-negative (i.e. immunohistochemically negative for the oestrogen receptor (ER) and progesterone

receptor (PgR) and lacking over-expression and amplification of the HER2 gene) and highly invasive cancer cell type.[55,56]

The *in vitro* pre-screen data obtained for ligand **L** and the corresponding complexes, against the MDA-MB-231 cell line, are summarized in Figure 3.4. Once again, the compounds were first screened for their cytotoxicity at 10 µM. At 10 µM, metallarectangle **16** showed the greatest activity ($p < 0.05$), reducing the percentage cell viability of this triple-negative cell line by approximately 58%. Most notably, however, the cytotoxicity of compound **16** at 10 µM exceeded that of cisplatin at 20 µM, which caused a 45% reduction in cell viability. Doubling the concentration of complex **16** resulted in a further 5% reduction in cell viability. The observed activity of this complex was unexpected, as it is largely inactive in the MCF-7 cell line, suggesting increased selectivity toward this triple-negative MDA-MB-231 cancer cell type.

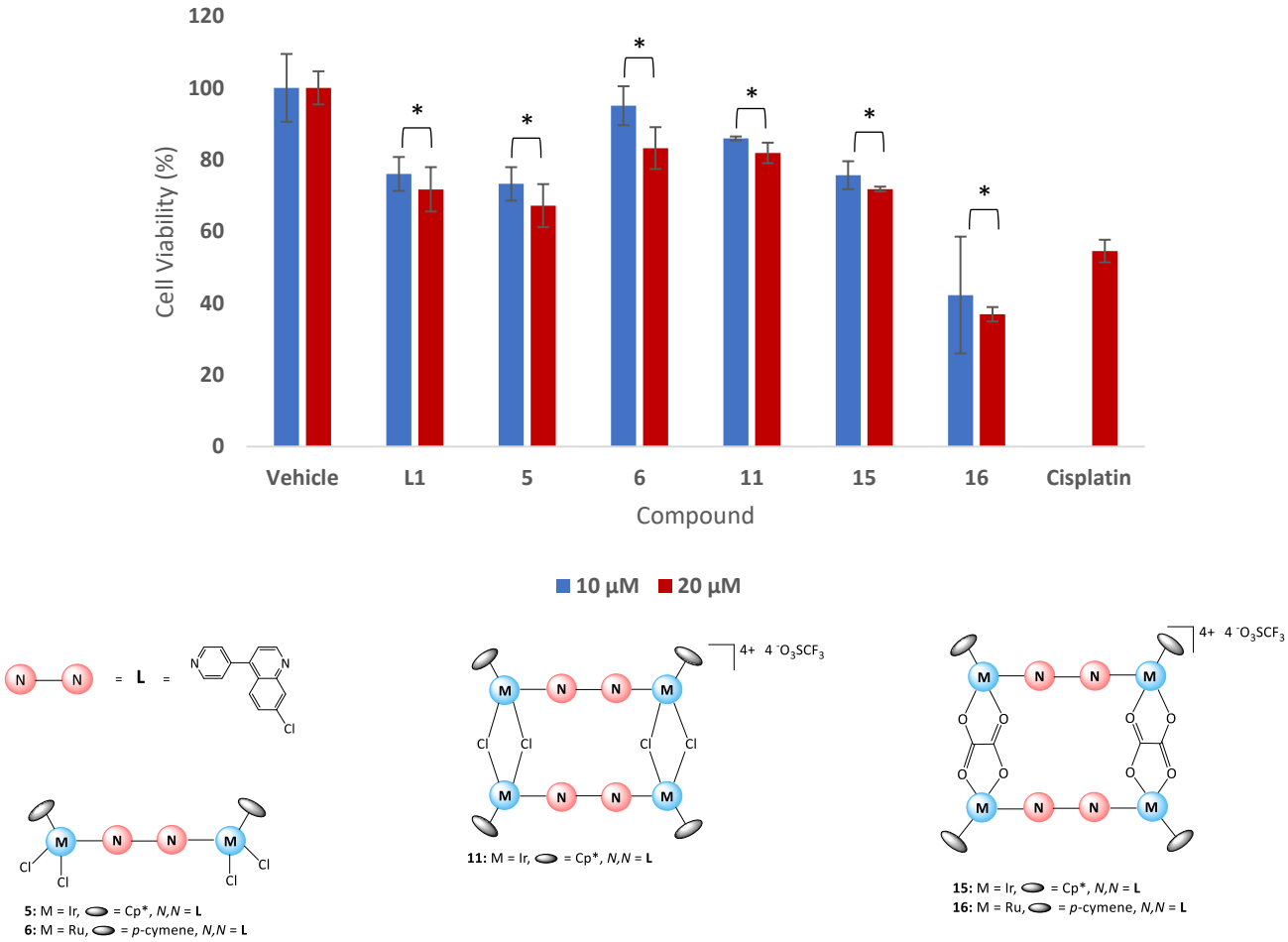

Figure 3.4: *The percentage cell viability as measured by MTT assays in MDA-MB-231 breast cancer cells exposed to either the vehicle (0.1% DMSO) or the synthesized quinoline-containing compounds, at 10 and 20 µM concentrations, for 48 hours. Cisplatin was included as a positive control.*

For compounds **L**, **5**, **6**, **11**, and **15**, doubling the concentration to 20 µM resulted in a further reduction in cell viability of between 4 and 12%. However, none of the aforementioned compounds displayed activity comparable to cisplatin at 20 µM, causing only a 16 – 33% reduction in cell viability. The asterisks, once again, denotes a significant difference in activity ($p < 0.05$) between the two concentrations.

3.5 *In vitro* multidose screening

Based on the promising results obtained from the pre-screen data, the IC_{50} values of selected compounds were determined. The IC_{50} values of ligand **L** and metallarectangle **11** were determined in the MCF-7 breast cancer cell line since these compounds demonstrated the greatest activity against this cancer cell type. Furthermore, the IC_{50} value of metallarectangle **16** was determined in the MDA-MB-231 cancer cell line, as this complex was highly efficacious, displaying a potency that exceeded that of cisplatin. Within these experiments, the cancer cells were treated with the test compounds at concentrations ranging from 5 to 20 µM.

3.5.1 In vitro multidose screening in the MCF-7 breast cancer cell line

The dose-response data obtained from the multidose screen in the MCF-7 cell line, as well as the IC_{50} values for the selected compounds, are summarized in Figure 3.5. Ligand **L** and complex **11** demonstrated comparable (statistically insignificant, $p > 0.05$) activity, with IC_{50} values of 19.45 and 17.38 µM, respectively. Most notably, however, these compounds display activity superior to cisplatin, which has an IC_{50} value of 36 µM[57] in the MCF-7 cell line.

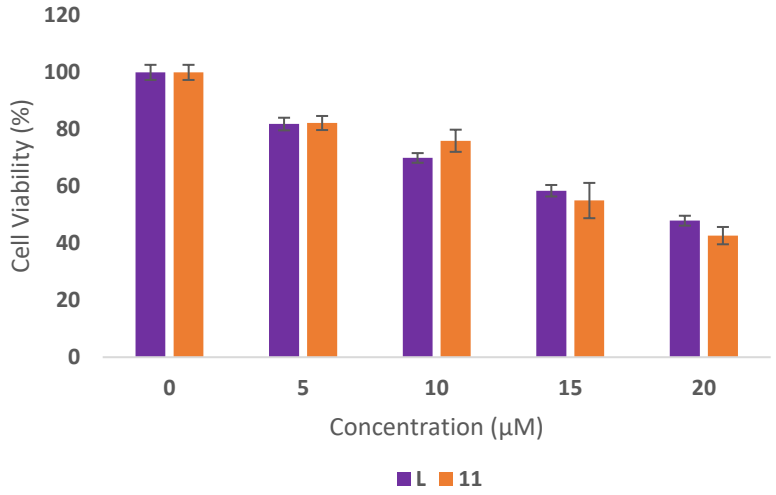

Compound	IC_{50} (μM) ± SE
L	19.45 ± 0.03
11	17.38 ± 0.05
Cisplatin	36[57]

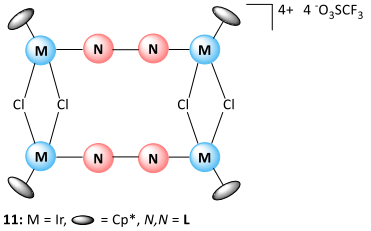

Figure 3.5: *The percentage cell viability, as measured by MTT assays, in MCF-7 breast cancer cells treated with increasing concentrations of* ***L*** *or metallarectangle* ***11****, for 48 hours. The table shows the* IC_{50} *values of the tested compounds (****L*** *and* ***11****) and cisplatin,*[57] *in the MCF-7 breast cancer cell line.*

Based on research done during this study, no metallarectangles containing bridging chlorides were evaluated for their anticancer activity. Consequently, comparisons were made with alternative supramolecular macrocycles tested against the MCF-7 breast cancer cell line. The observed IC_{50} value for metallarectangle **11** is lower than reported literature values for imidazole-based ruthenium metallarectangles containing bridging oxalato- and 2,5-dihydroxy-1,4-benzoquinone (dhbq) ligands, which displayed IC_{50} values greater than 50 μM.[8] Furthermore, metallarectangle **11** also displayed cytotoxicity that exceeded heterometallic platinum and palladium BODIPY-based metallasquares, synthesized by Gupta *et al*., which exhibited IC_{50} values ranging between 19.80 and 53.86 μM.[51]

3.5.2 In vitro multidose screening in the MDA-MB-231 breast cancer cell line

Only metallarectangle **16** was evaluated against the more aggressive MDA-MB-231 cancer cell line, as it showed the most promise during the pre-screen evaluation. This complex showed excellent cytotoxic activity, with an IC_{50} value of 10.05 μM, which is over two-fold greater than that of cisplatin (IC_{50} = 23 μM[58]) (Figure 3.6). The obtained results are promising as the MDA-MB-231 cell line is known to be resistant to an array of chemotherapeutic agents, emphasizing the possibility of such complexes (SSCs) to act as a potentially new class of anticancer chemotherapeutic agents to target this highly invasive triple-negative cancer sub-type.

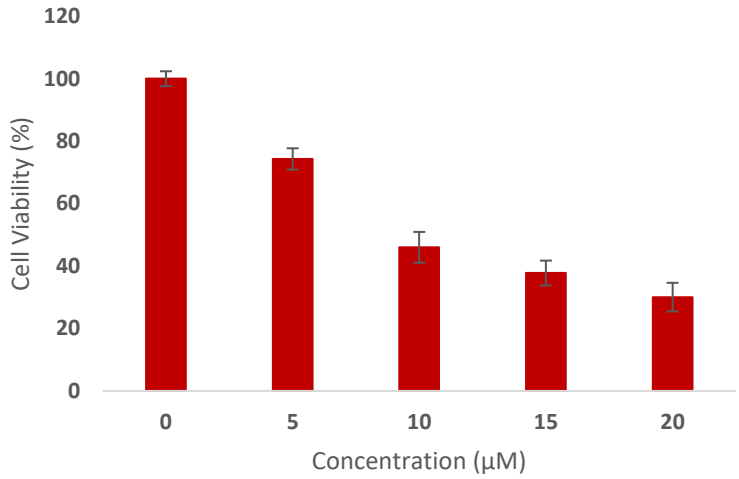

Compound	IC_{50} (μM) ± SE
16	10.05 ± 0.04
Cisplatin	23[58]

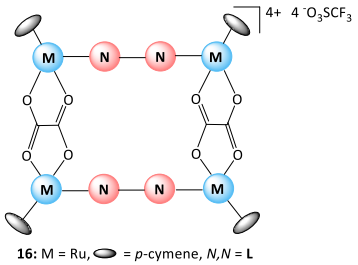

Figure 3.6: *The percentage cell viability, as measured by MTT assays, in MDA-MB-231 breast cancer cells treated with increasing concentrations of metallarectangle* ***16****, for 48 hours. The table shows the* IC_{50} *values of the tested compound (****16****) and cisplatin[58], in the MDA-MB-231 breast cancer cell line.*

The IC_{50} value of metallarectangle **16**, containing bridging oxalato ligands, is greater than that of analogous ruthenium metallarectangles containing bridging oxalato and imidazole-based ligands, as reported by Zhao *et al*., with IC_{50} values greater than 35 μM in the MDA-MB-231 cell line.[8] Furthermore, complex **16** was also more potent than ruthenium metallarectangles containing bridging oxalato and amide ligands synthesized by Vajpayee *et al*., with IC_{50} values exceeding 200 μM.[48] However, an analogous ruthenium metallarectangle, containing 5,8-dihydroxy-1,4-naphthoquinonato (dhnq) bridging ligands (IC_{50} = 2.8 μM), was over three-times more active than complex **16** (IC_{50} = 10.05 μM).[48] This dhnq ligand has however been shown to increase the pharmacological activity of SCCs compared to other *O,O*-chelating ligands.[8,48-50] Finally, metallarectangle **16** was approximately 20-fold more efficacious than a ruthenium hexanuclear metallacage containing bridging oxalato-ligands, against the MDA-MB-231 cell line.[50] The cancer cells in the given examples, however, were only exposed to the test compounds for 24 hours. [44-46]

3.5.3 In vitro cytotoxicity studies in the MCF-12A non-tumorigenic breast epithelial cell line

One of the biggest challenges faced with current anticancer chemotherapeutic agents is their poor specificity, which results in unfavourable side-effects (Section 1.2.3). A prime example of this is cisplatin, which results in severe dose-dependent toxic side-effects.[59] Despite this, cisplatin continues to be one of the most sought-after chemotherapeutic agents.[59] Consequently, developing anticancer agents with minimal unwanted side-effects is imperative within drug-discovery.

Ligand **L** and metallarectangles **11** and **16** were thus evaluated for their cytotoxicity against non-tumorigenic MCF-12A breast epithelial cells. These cells were treated with varying concentrations (5 – 20 µM) of the test compounds for 48 hours. Thereafter, the cell viability was assessed using the MTT assay, with the results summarized in Figure 3.7.

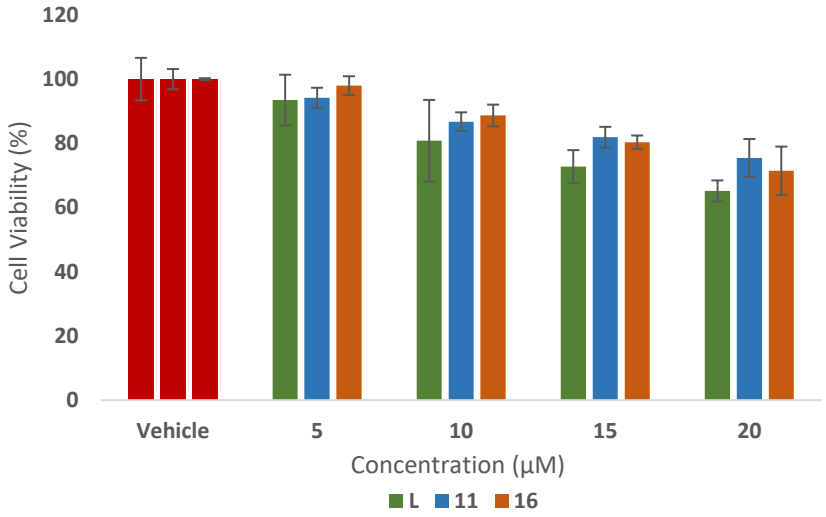

Compound	IC_{50} (µM) ± SE
L	31.48 ± 0.05
11	53.49 ± 0.12
16	33.24 ± 0.02
Cisplatin	36.32 ± 1.09

Figure 3.7: *The percentage cell viability, as measured by MTT assays, of non-tumorigenic MCF-12A breast epithelial cells treated with increasing concentrations of compound* ***L*** *and metallarectangles* ***11*** *and* ***16****, for 48 hours. Vehicle (0.1% DMSO) treated cells included as a control.*

From the results obtained, it is evident that ligand **L** and metallarectangle **16** show comparable cytotoxicity to each other (not statistically significant, $p > 0.05$) and cisplatin, in the MCF-12A breast epithelial cell line, with IC_{50} values of 31.48 and 33.24 µM, respectively. Complex **11**, however, showed less cytotoxic activity toward the non-tumorigenic cell line, with an IC_{50} value of 53.49 µM.

The selectivity indices (SI) of the tested compounds (**L**, **11,** and **16**) were then calculated by dividing the IC_{50} values obtained in the non-tumorigenic MCF-12A cell line by the IC_{50} values obtained in the

respective breast cancer cell lines, and are summarized in Table 3.4. The SI of a compound is a useful indicator of the selectivity of a potential anticancer chemotherapeutic agent. A larger SI value is desired, which is indicative of a compound showing increased cytotoxicity toward cancerous cells over non-tumorigenic healthy cells.

Table 3.4: *Summary of the IC_{50} values and selectivity indices of compounds **L**, **11** and **16**, in the various cell lines.*

Compound	**IC_{50} (µM) ± SE**			**Selectivity Index (SI)**
	MCF-7	*MDA-MB-231*	*MCF-12A*	
L	19.45 ± 0.03	n/d[a]	31.48 ± 0.05	1.62[b]
11	17.38 ± 0.05	n/d[a]	53.49 ± 0.12	3.08[b]
16	n/d[a]	10.05 ± 0.04	33.24 ± 0.02	3.31[c]
Cisplatin	36[57]	23[58]	36.32 ± 1.09	1.01[b] 1.58[c]

[a] Not determined
[b] IC_{50} MCF-12A / IC_{50} MCF-7
[c] IC_{50} MCF-12A / IC_{50} MDA-MB-231

Despite compounds **L** and **16** displaying IC_{50} values comparable to cisplatin (Figure 3.7) in the MCF-12A cell line, the SI values of these compounds are higher than the SI values obtained for cisplatin. This points to the increased selectivity of these compounds towards cancerous cells over non-tumorigenic healthy cells. Ligand **L** is more selective toward the MCF-7 cell line (SI = 1.62) relative to cisplatin (SI = 1.01). Similarly, complex **16** displays increased selectivity toward the MDA-MB-231 cell line (SI = 3.31) compared to cisplatin (SI = 1.58). Finally, complex **11** displayed an SI value (3.08) three-times greater than cisplatin, suggesting that it is not only more cytotoxic (Figure 3.5) but selective (Table 3.4) toward the MCF-7 breast cancer cells than cisplatin. Furthermore, the larger SI values of the metallarectangles (**11** and **16**) in particular, suggests that these compounds are preferentially cytotoxic toward cancerous cells over healthy cells. Consequently, these compounds may display minimal side-effects relative to cisplatin.

3.6 Summary

The known 4,4'-bipyridine-containing compounds (bpy, **3**, **4**, **9**, **10**, **13**, and **14**) and the new quinoline-containing compounds (**L**, **5**, **6**, **11**, **15**, and **16**) were all evaluated for their *in vitro* antiplasmodial activity against the CQ-sensitive NF54 strain of *P. falciparum*. Upon evaluation of the effects of incorporating a quinoline scaffold into the framework, it was observed that the quinoline-based ligand **L** displayed antiplasmodial activity approximately 10-fold greater than 4,4'-bipyridine. Upon complexation, the activity of both ligands (4,4'-bipyridine and **L**) were significantly enhanced, with most complexes over five-times more active than their respective ligands, demonstrating the advantages of metal incorporation on the pharmacological activity of organic compounds. The ruthenium analogues were, however, found to be at least two-fold more active than their corresponding iridium congeners. Furthermore, an increase in the nuclearity of the system correlated with an increase in the antiplasmodial activity, suggesting that supramolecular metallarectangles have the potential to act as antiplasmodial agents. Finally, of the newly synthesized quinoline-based compounds, metallarectangles **11** and **16** displayed superior activity, having IC_{50} values of 9.28 and 9.82 µM, respectively.

All of the aforementioned compounds were further evaluated for their *in vitro* antiplasmodial activity against the multidrug-resistant K1 strain of *P. falciparum*. Complexation was again observed to significantly enhance the antiplasmodial activity, with some complexes at least ten-times more active than their respective ligands. Additionally, an increase in the nuclearity of the system, to form the tetranuclear metallarectangles, resulted in a further increase in the antiplasmodial activity of the compound. Metallarectangle **16** was once again the most active quinoline-based compound, with an IC_{50} value of 7.65 µM.

None of the compounds displayed activity comparable to CQ, however, the RI values of the quinoline-containing compounds, which are all approximately equal to 1, suggests that these compounds display minimal cross-resistance compared to CQ (RI = 22.1), and thus largely retain their activity in the resistant strain of the parasite.

Due to the presence of the quinoline scaffold and to gain some insight into a possible mechanism of action, selected compounds (**L**, **15**, and **16**) were screened for their β-haematin inhibition ability. Despite the limited antiplasmodial activity observed for metallarectangles **15** and **16**, relative to CQ, these complexes displayed rather good β-haematin inhibitory activity. The IC_{50} value of complex **15**

(IC_{50} = 28.29 µM) is near comparable to CQ (IC_{50} = 22.75 µM), suggesting that it inhibits β-haematin formation to almost the same extent. Since the β-haematin inhibition assay is performed in a cell-free environment, this suggests that the limited *in vitro* antiplasmodial activity observed for metallarectangle **15** may be due to limited entry and/or accumulation in the cell. It is important to note, however, that this is but one possible mechanism of action, and further in-depth studies are required to identify alternative mechanisms that may be at play.

Furthermore, the cytotoxicity of the new quinoline-containing compounds (**L**, **5**, **6**, **11**, **15**, and **16**) were evaluated in pre-screen experiments against the MCF-7 breast cancer cell line, at 10 and 20 µM. Ligand **L** and iridium metallarectangle **11** showed the greatest activity, reducing the percentage cell viability at 20 µM by 50 and 60% respectively, exceeding the 20% reduction observed for cisplatin at the same concentration.

The promising activity observed for the aforementioned quinoline-based compounds prompted the investigation into the chemotherapeutic activity of these compounds against the triple-negative MDA-MB-231 cell line. Complex **16** displayed superior activity, far exceeding that of cisplatin, reducing the percentage cell viability by 58 and 63%, at 10 and 20 µM respectively. The activity of this compound however was unexpected, as it was inactive against the MCF-7 cell line at the tested concentrations, suggesting increased selectivity toward the triple-negative cell line. Compounds **L** and **11**, conversely, showed enhanced activity in the MCF-7 cell line and were less potent in the MDA-MB-231 cell line, pointing to increased selectivity toward the MCF-7 cell type.

The IC_{50} values of selected compounds (**L**, **11**, and **16**) were then determined. Ligand **L** and metallarectangle **11** showed comparable activity against the MCF-7 breast cancer cell line, with IC_{50} values of 19.45 and 17.38 µM, respectively, both of which exceed that of cisplatin. The IC_{50} value of complex **16** (IC_{50} = 10.05 µM) was determined in the MDA-MB-231 cell line and was over two-fold greater than cisplatin (IC_{50} = 23 µM). Through these assays, it is evident that compounds **L**, **11**, and **16** are capable of acting as anticancer agents, as their potency exceeds cisplatin in the respective cell lines. Furthermore, the aforementioned compounds were also investigated for their cytotoxicity toward non-tumorigenic MCF-12A epithelial cells. The SI values of **L**, **11** and **16** exceeded cisplatin, suggesting that these compounds show increased selectivity toward cancerous cells over healthy cells.

3.7 References

1. Z. Guo and P. J. Sadler, *Angew. Chem. Int. Ed.*, 1999, **38**, 1512-1531.
2. L. Kelland, *Nat. Rev. Cancer*, 2007, **7**, 573-584.
3. C. S. Allardyce and P. J. Dyson, *Platinum Metals Rev.*, 2001, **45**, 62-69.
4. R. C. DeConti, B. R. Toftness, R. C. Lange and W. A. Creasey, *Cancer Res.*, 1973, **33**, 1310-1315.
5. R. Wilkinson, P. J. Cox, M. Jones and K. R. Harrap, *Biochimie*, 1978, **60**, 851-857.
6. D. W. Shen, L. M. Pouliot, M. D. Hall and M. M. Gottesman, *Pharmacol. Rev.*, 2012, **64**, 706-721.
7. Z. Ai, Y. Lu, S. Qiu and Z. Fan, *Cancer Lett.*, 2016, **373**, 36-44.
8. Y. Zhao, L. Zhang, X. Li, Y. Shi, R. Ding, M. Teng, P. Zhang, C. Cao and P. J. Stang, *PNAS*, 2019, **116**, 4090-4098.
9. X. Zhang, D. Liu, F. Lv, B. Yu, Y. Shen and H. Cong, *Colloids Surf. B. Biointerfaces*, 2019, **182**, 1-9.
10. B. Woods, D. Dollerer, B. Aikman, M. N. Wenzel, E. J. Sayers, F. E. Kuhn, A. T. Jones and A. Casini, *J. Inorg. Biochem.*, 2019, **199**, 1-7.
11. H. Vardhan, A. Nafady, A. M. Al-Enizi, K. Khandker, H. M. El-Sagher, G. Verma, M. Acevedo-Duncan, T. M. Alotaibi and S. Ma, *Molecules*, 2019, **24**, 2284.
12. B. Therrien, G. Süss-Fink, P. Govindaswamy, A. K. Renfrew and P. J. Dyson, *Angew. Chem. Int. Ed.*, 2008, **47**, 3773-3776.
13. H. Sepehrpour, W. Fu, Y. Sun and P. J. Stang, *J. Am. Chem. Soc.*, 2019, **141**, 14005-14020.
14. J. Mattsson, P. Govindaswamy, A. K. Renfrew, P. J. Dyson, P. Stepnicka, B. Suss-Fink and B. Therrien, *Organometallics*, 2009, **28**, 4350-4357.
15. G. Gupta, J. M. Kumar, A. Garci, N. Nagesh and B. Therrien, *Molecules*, 2014, **19**, 6031-6046.
16. G. Gupta, A. Das, S. W. Lee, J. Y. Ryu, J. Lee, N. Nagesh, N. Mandal and C. Y. Lee, *J. Organomet. Chem.*, 2018, **868**, 86-94.
17. G. Gupta, A. Das, J. Lee, N. Mandal and C. Y. Lee, *ChemPlusChem*, 2018, **83**, 339-347.
18. N. P. Barry, F. Edafe and B. Therrien, *Dalton Trans.*, 2011, **40**, 7172-7180.
19. H. Maeda, G. Y. Bharate and J. Daruwalla, *Eur. J. Pharm. Biopharm.*, 2009, **71**, 409-419.
20. D. F. Baban and L. W. Seymour, *Ad. Drug Deliv. Rev.*, 1998, **34**, 109–119.
21. C. Biot, G. Glorian, L. A. Maciejewski and J. S. Brocard, *J. Med. Chem.*, 1997, **40**, 3715-3718.
22. B. Hanboonkunupakarn and N. J. White, *Trop. Dis. Travel Med. Vaccines*, 2016, **2**, 1-5.
23. B. S. Sekhon and N. Bimal, *J. Pharm. Educ. Res.*, 2012, **3**, 52-63.
24. R. A. Sánchez-Delgado, M. Navarro, H. Pérez and J. A. Urbina, *J. Med. Chem.*, 1996, **39**, 1095-1099.
25. P. F. Salas, C. Herrmann and C. Orvig, *Chem. Rev.*, 2013, **113**, 3450-3492.
26. P. Chellan, K. M. Land, A. Shokar, A. Au, S. H. An, D. Taylor, P. J. Smith, K. Chibale and G. S. Smith, *Organometallics*, 2013, **32**, 4793-4804.

27. C. S. K. Rajapakse, A. Martínez, B. Naoulou, A. A. Jarzecki, L. Suárez, C. Deregnaucourt, V. Sinou, j. Schrével, E. Musi, G. Ambrosini, G. K. Schwartz and R. A. Sánchez-Delgado, *Inorg. Chem.*, 2009, **48**, 1122-1131.
28. D. R. Melis, C. B. Barnett, L. Wiesner, E. Nordlander and G. S. Smith, *Dalton Trans.*, 2020, **49**, 11543-11555.
29. C. F. Markwalter, K. M. Davis and D. W. Wright, *Anal. Biochem.*, 2016, **493**, 30-34.
30. L. K. Basco, F. Marquet, M. M. Makler and J. Lebras, *Exp. Parasitol.*, 1995, **80**, 260 -271.
31. M. T. Makler and D. J. Hinrichs, *Am. J. Trop. Med. Hyg.*, 1993, **48**, 205-210.
32. M. Fujita, J. Yazaki and K. Ogura, *J. Am. Chem. Soc.*, 1990, **112**, 5645-5647.
33. R. A. Jones, S. S. Panda and C. D. Hall, *Eur. J. Med. Chem.*, 2015, **97**, 335-355.
34. L. Tilley, P. Loria and M. Foley, in *Antimalarial Chemotherapy*, ed. P. J. Rosenthal, Humana Press Inc., Totowa, NJ, 2001, pp. 87-121.
35. S. K. Singh and S. Singh, *Int. J. Pharm. Sci. Rev. Res.*, 2014, **25**, 295-302.
36. R. D. Sandlin, M. D. Carter, P. J. Lee, J. M. Auschwitz, S. E. Leed, J. D. Johnson and D. W. Wright, *Antimicrob. Agents Chemother.*, 2011, **55**, 3363-3369.
37. D. E. Goldberg, A. F. G. Slater, A. Cerami and G. B. Henderson, *Proc. Natl. Acad. Sci.*, 1990, **87**, 2931-2935.
38. S. E. Francis, J. David J. Sullivan and D. E. Goldberg, *Annu. Rev. Microbiol.*, 1997, **51**, 97–123.
39. M. Navarro, W. Castro and C. Biot, *Organometallics*, 2012, **31**, 5715-5727.
40. M. Mushtaque and Shahjahan, *Eur. J. Med. Chem.*, 2015, **90**, 280-295.
41. L. Tilley, P. Loria and M. Foley, *Antimalarial Chemotherapy*, Humana Press Inc., Totowa, New Jersey, 2001.
42. M. Foley and L. Tilley, *Pharmacol. Ther.*, 1998, **79**, 55–87.
43. M. D. Carter, V. V. Phelan, R. D. Sandlin, B. O. Bachmann and D. W. Wright, *Comb. Chem. High Throughput Screen.*, 2010, **13**, 285-292.
44. W. Kemnitzer, J. Kuemmerle, S. Jiang, H. Z. Zhang, N. Sirisoma, S. Kasibhatla, C. Crogan-Grundy, B. Tseng, J. Drewe and S. X. Cai, *Bioorg. Med. Chem. Lett.*, 2008, **18**, 6259-6264.
45. L. K. Kohn, C. H. Pavam, D. Veronese, F. Coelho, J. E. De Carvalho and W. P. Almeida, *Eur. J. Med. Chem.*, 2006, **41**, 738-744.
46. Y. Mikata, M. Yokoyama, S.-i. Ogura, I. Okura, M. Kawasaki, M. Maeda and S. Yano, *Bioorg. Med. Chem. Lett.*, 1998, **8**, 1243-1248.
47. D. Sharples, G. Spengler, J. Molnar, Z. Antal, A. Molnar, J. T. Kiss, J. A. Szabo, A. Hilgeroth, S. Gallo, A. Mahamoud and J. Barbe, *Eur. J. Med. Chem.*, 2005, **40**, 195-202.

48. V. Vajpayee, Y. H. Song, Y. J. Yang, S. C. Kang, H. Kim, I. S. Kim, M. Wang, P. J. Stang and K. W. Chi, *Organometallics*, 2011, **30**, 3242-3245.
49. A. Dubey, J. W. Min, H. J. Koo, H. Kim, T. R. Cook, S. C. Kang, P. J. Stang and K. W. Chi, *Chem. Eur. J.*, 2013, **19**, 11622-11628.
50. V. Vajpayee, Y. J. Yang, S. C. Kang, H. Kim, I. S. Kim, W. Ming, P. J. Stang and K. W. Chi, *Chem. Commun.*, 2011, **47**, 5184-5186.
51. G. Gupta, Y. You, R. Hadiputra, J. Jung, D. K. Kang and C. Y. Lee, *ACS Omega*, 2019, **4**, 13200-13208.
52. K. Präbst, H. Engelhardt, S. Ringgeler and H. Hübner, in *Cell Viability Assays: Methods and Protocols*, eds. D. F. Gilbert and O. Friedrich, Humana Press, New York, 2017, ch. 1, pp. 1 - 19.
53. M. A. Rudek, C. H. Chau, W. D. Figg, H. L. McLeod and (Eds.), *Handbook of Anticancer Pharmacokinetics and Pharmacodynamics*, Humana Press, 2nd edn., 2014.
54. L. K. Diaz, V. L. Cryns, W. F. Symmans and N. Sneige, *Adv. Anat. Pathol.*, 2007, **14**.
55. G. Viale and L. Bottiglieri, *Eur. J. Cancer*, 2009, **45**, 5 - 10.
56. D. L. Holliday and V. Speirs, *Breast Cancer Res.*, 2011, **13**, 215 - 222.
57. Y. Mizumura, Y. Matsumura, T. Hamaguchi, N. Nishiyama, K. Kataoka, T. Kawaguchi, W. J. M. Hrushesky, F. Moriyasu and T. Kakizoe, *Jpn. J. Cancer Res.*, 2001, **92**, 328–336.
58. A. Z. Pauzi, S. K. Yeap, N. Abu, K. L. Lim, A. R. Omar, S. A. Aziz, A. L. Chow, T. Subramani, S. G. Tan and N. B. Alitheen, *Chin. Med.*, 2016, **11**, 46.
59. L. Qi, Q. Luo, Y. Zhang, F. Jia, Y. Zhao and F. Wang, *Chem. Res. Toxicol.*, 2019, **32**, 1469-1486.

CHAPTER 4

Conclusions and future outlook

4.1 Overall summary and conclusions

The overall aim of this project was to incorporate the pharmacophoric quinoline scaffold into the framework of a series of supramolecular metallarectangles and evaluate these compounds for their antiplasmodial and anticancer activity. Initially, a new quinoline-containing ditopic ligand (**L**) was prepared by a Suzuki cross-coupling reaction. The quinoline scaffold was successfully incorporated and the desired ligand **L** mimicked the principal ligand (4,4'-bipyridine) used in the synthesis of metallarectangles. Ligand **L** was reacted with either $[IrCl(\mu\text{-}Cl)(Cp^*)]_2$ (**1**) or $[RuCl(\mu\text{-}Cl)(p\text{-cymene})]_2$ (**2**) to afford the precursor iridium(III) and ruthenium(II) binuclear complexes (**5** and **6**), in high yields. The binuclear complexes (**5** and **6**) were further reacted with silver triflate and *via* coordination-driven self-assembly formed metallarectangles **11** and **12**, containing bridging chlorides. Alternatively, ligand **L** was reacted with either precursor complex **7** or **8**, in the presence of silver triflate, to form metallarectangles **15** and **16**, containing bridging oxalato ligands. Thus, two types of metallarectangles were prepared, of varying sizes, all of which were isolated as their triflate salts in moderate to excellent yields. It is thus possible to incorporate a quinoline pharmacophore as part of a metallarectangle scaffold, with the evidence obtained discussed comprehensively in Chapter 2.

The aforementioned compounds were fully characterised using an array of spectroscopic (^1H, $^{13}C\{^1H\}$, and FT-IR spectroscopy) and analytical (mass spectrometry and melting point analysis) techniques. Single-crystal X-ray diffraction confirmed the molecular structure of the precursor binuclear complex **5** and inevitably corroborated the structure of the quinoline-containing ligand **L**. Due to the asymmetrical nature of the ligand, upon the formation of the metallarectangles, there is the possibility of forming constitutional isomers. Interestingly, however, the ^1H NMR spectra of metallarectangles **11**, **12**, and **15**, reveals only one dominant isomer in solution, suggesting increased selectivity toward a preferred configuration. The ^1H NMR spectrum of ruthenium metallarectangle **16**, however, suggests a mixture of two metallarectangles (constitutional isomers) in solution. The metallarectangles (**11**, **12**, **15**, and **16**) were further evaluated using diffusion-ordered spectroscopy (DOSY). Due to the inherently complex spectra of such compounds, this technique was used to

confirm the existence of only a single species in solution, which was confirmed for all metallarectangles by the presence of a single diffusion line.

To the best of our knowledge, the antiplasmodial activity of supramolecular coordination complexes has not been reported in literature. Consequently, the new ligand (**L**), the precursor complexes (**5** and **6**), the metallarectangles (**11**, **15**, and **16**), as well as the corresponding 4,4'-bipyridine analogues were initially evaluated for their *in vitro* antiplasmodial activity in the chloroquine-sensitive NF54 strain of *P. falciparum*. The presence of the pharmacophoric quinoline scaffold significantly enhanced the antiplasmodial activity, with an approximately 100-fold difference in activity observed between 4,4'-bipyridine and the structurally analogous ligand **L**. This denotes the importance of the quinoline pharmacophore for antiplasmodial activity. Metal complexation resulted in a further increase in activity of up to 50-fold, compared to the activity of the uncoordinated ligand. Upon evaluating the activity of the ligand, the corresponding binuclear complexes, and the corresponding metallarectangles, the activity was observed to increase upon an increase in the nuclearity of the compound. The synthesized compounds were further evaluated for their antiplasmodial activity against the multidrug-resistant K1 strain of *P. falciparum*. Similar trends in activity were observed in the resistant strain and, in general, the quinoline-containing complexes displayed only a slight decrease in activity compared to the activity observed in the sensitive strain. The calculated resistance indices further suggest that the compounds may experience mild cross-resistance, however, not to the extent of CQ. Despite not being effective antimalarial agents, the metallarectangles can inhibit antiplasmodial activity. A reason for the limited activity may be the size and/or highly charged nature of these supramolecular coordination complexes, which may impede their uptake and/or accumulation in the parasite, although further in-depth studies are required to verify this hypothesis.

Haemozoin inhibition is a well-known target of quinoline-containing compounds and, therefore, to gain insight into a potential mechanism of action, the quinoline-containing ligand **L** and selected metallarectangles (**15** and **16**) were tested for their ability to inhibit β-haematin (synthetic haemozoin) formation. Both metallarectangles **15** and **16** displayed β-haematin inhibitory activity, with the iridium metallarectangle (**15**) having an IC_{50} value (28.29 μM) near comparable to CQ (IC_{50} = 22.75 μM). The superior cell-free β-haematin inhibitory activity of metallarectangle **15**, but limited *in vitro* antiplasmodial activity, further supports the hypothesis that the entry of this large, highly charged compound into the digestive vacuole of the parasite is hindered, as entry into the cell will

make this compound a likely candidate for haemozoin inhibition, and thus a promising antimalarial agent.

The quinoline-containing ligand **L** and the corresponding complexes (**5**, **6**, **11**, **15**, and **16**) were also pre-screened for their anticancer activity in the MCF-7 breast cancer cell line, at 10 and 20 μM. The pre-screen studies revealed no discernible trends in activity, however, ligand **L** and iridium metallarectangle **11** displayed the greatest activity, which exceeded that of cisplatin at both the tested concentrations. These promising results prompted further investigation into the anticancer activity of the aforementioned compounds (**L**, **5**, **6**, **11**, **15**, and **16**) against the triple-negative MDA-MB-231 breast cancer cell line. Surprisingly, despite being inactive in the MCF-7 cell line, ruthenium metallarectangle **16** displayed superior activity, inhibiting the percentage cell viability of the MDA-MB-231 cell line by 58% at 10 μM, compared to the 45% reduction observed for cisplatin at the same concentration.

Based on the promising results obtained during the pre-screen evaluation, selected compounds (**L**, **11,** and **16**) were investigated in a multidose experiment. Both ligand **L** and metallarectangle **11** were found to be approximately two-times more potent than cisplatin (IC_{50} = 36 μM) in the MCF-7 cancer cell line, with IC_{50} values of 19.45 μM and 17.38 μM, respectively. Furthermore, since showing the greatest activity in the MDA-MB-231 cell line during the pre-screen evaluation, the IC_{50} value of compound **16** (IC_{50} = 10.05 μM) was determined and found to be over two-fold greater than that of cisplatin. Compounds **L**, **11**, and **16** all demonstrated activity greater than cisplatin in their respective tested cancer cell lines, and are thus able to act as anticancer agents.

Furthermore, to investigate the possible cytotoxicity and thus gain insight into the selectivity of these compounds, compounds **L**, **11**, and **16** were evaluated for their cytotoxic activity toward the MCF-12A non-tumorigenic breast epithelial cells. Ligand **L** and ruthenium metallarectangle **16** displayed cytotoxicity comparable to cisplatin (IC_{50} = 36.32) in the MCF-12A cell line, while metallarectangle **15** was noted to be less cytotoxic than cisplatin, with an IC_{50} value of 53.49 μM. Upon evaluation of the selectivity indices, compounds **L** and **11** were shown to display increased selectivity toward the MCF-7 cell line relative to cisplatin. Moreover, the ruthenium metallarectangle **16** displayed enhanced selectivity toward the triple-negative cell line, with a selectivity index over two-times greater than that of cisplatin. The increased selectivity of the metallarectangles in particular, toward cancer cells,

is in accordance with several studies[1-3] and further promotes the use of supramolecular coordination complexes as anticancer agents.

4.2 Future outlook

Based on the antiplasmodial results of this study, the supramolecular coordination complexes (metallarectangles) do exhibit antiplasmodial activity. However, further studies are required to gain insight into the possible limitations (e.g. size and/or charge) of such complexes to permeate the parasitic membrane, which may impede their activity. Improvements could be made, perhaps *via* structural modifications, to enhance permeability and activity. Furthermore, the anticancer studies suggest that the metallarectangles display promising antiproliferative activity and therefore mechanistic studies are required to identify the mechanism(s) of action at play for such complexes to elicit this activity. Additionally, structural modifications could be made to further fine-tune the activity of these compounds.

4.2.1 Mechanistic studies

4.2.1.1 Malaria

Based on the potential of the selected metallarectangles to inhibit β-haematin formation, it would be interesting to identify alternative mechanisms by which these compounds may act. One approach would be to investigate the ability of the metallarectangles to produce reactive oxygen species (ROS) and thus cause oxidative stress. This could be determined by incubating the compound with an antioxidant such as *N*-acetylcysteine (NAC), which would lower the antiplasmodial activity of the compound should it cause oxidative damage as a result of ROS formation.[4] Furthermore, considering that PGM complexes have shown to be effective transfer hydrogenation catalysts,[5-7] the iridium and ruthenium metallarectangles can be investigated for their ability to reduce NAD^+ to NADH in a cell-free environment. Based on a modified procedure of the *p*LDH assay, the cell-free catalytic ability of the metallarectangles can be investigated by incubating the selected complexes with NAD^+ and sodium formate.[7] Should the complexes facilitate the reduction of NAD^+ to NADH, the NADH will result in the subsequent reduction of NBT (yellow) to formazan (dark blue), from which one can infer the transfer hydrogenation catalytic ability.[7]

4.2.1.2 Cancer

DNA is regarded as a well-known potential target for metal complexes used in the treatment of cancer. The most widely known example is cisplatin, whose cytotoxic activity is mediated by its interaction with DNA, forming primarily intra-strand crosslink adducts.[8,9] A simple model used to study possible nucleotide interactions is Guanosine 5'-monophosphate disodium (5'-GMP). The most active metallarectangles could be studied for their interaction with 5'-GMP using ^{1}H NMR spectroscopy. Furthermore, to confirm if genomic DNA is the main cellular target, immunoblotting analysis can be conducted to monitor any changes in expression of biomarkers (e.g. γH2AX, p53, P-p53, and p21) related to DNA damage pathways.[10] Western blot analysis can also be conducted to investigate potential protein targets. Furthermore, the metallarectangles could be evaluated for their anticancer activity against additional cell lines, such as ovarian (A2780 and A2780cisR), colon (HCT15 and HCT15/CLO2), and cervical (HeLa) cancer cell lines, to provide additional information about their biological profile. Further investigations into the stability of such compounds, under physiological conditions, will also be beneficial in designing more potent anticancer and antimalarial agents for therapeutic use.

4.2.2 Structural modifications

Although the metallarectangles displayed promising anticancer and potential antiplasmodial activity, structural modifications could further enhance their potency. Some of the suggested structural modifications include using 5,8-dihydroxy-1,4-naphthoquinone (dhnq) (Figure 4.1), as opposed to ammonium oxalate, as dhnq has been shown to significantly enhance the pharmacological activity compared to other *O*,*O*-chelating ligands.[1,11-13]

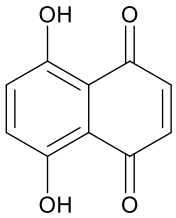

Figure 4.1: *Structure of 5,8-dihydroxy-1,4-naphthoquinone.*

Due to the pharmacophoric nature of the quinoline scaffold, and its ability to inhibit β-haematin formation, it should still be incorporated into the framework, upon the design of new anticancer and antimalarial agents. However, perhaps an additional quinoline or benzimidazole scaffold, which is also a well-known pharmacophore,[14-18] could be incorporated, to further enhance the efficacy of

these compounds. Examples of alternative pharmacophoric-containing *N*,*N*'-ditopic ligands that can be synthesized and incorporated into the framework of the metallarectangle is shown in Figure 4.2. Furthermore, the incorporation of additional basic nitrogen atoms can aid in pH trapping, enhancing the accumulation of the drug within the digestive vacuole of the parasite and thus the activity.[19]

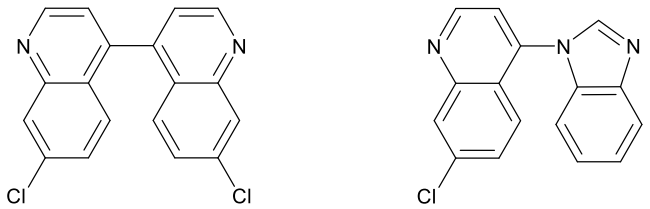

Figure 4.2: *Structures of alternative ligands that can be used in the framework of the metallarectangles.*

As previously mentioned, one of the main challenges within cancer chemotherapy is the development of selective chemotherapeutic agents, in order to reduce the overall toxicity and subsequent side-effects. An avenue that may prove fruitful is the use of large carrier compounds (i.e. cavity-containing supramolecular complexes) containing encapsulated drugs that are released once inside cancer cells.[20] Cisplatin is an example of a compound that has been encapsulated within a supramolecular assembly.[21] This approach can thus be further used to enhance (perhaps synergistically) not only the anticancer activity, but also the antiplasmodial activity of the metallarectangles, depending on the nature of the encapsulated compound.

4.3 References

1. Y. Zhao, L. Zhang, X. Li, Y. Shi, R. Ding, M. Teng, P. Zhang, C. Cao and P. J. Stang, *PNAS*, 2019, **116**, 4090-4098.
2. H. Vardhan, A. Nafady, A. M. Al-Enizi, K. Khandker, H. M. El-Sagher, G. Verma, M. Acevedo-Duncan, T. M. Alotaibi and S. Ma, *Molecules*, 2019, **24**, 2284.
3. A. Mishra, S. C. Lee, N. Kaushik, T. R. Cook, E. H. Choi, N. K. Kaushik, P. J. Stang and K. W. Chi, *Chem. Eur. J.*, 2014, **20**, 14410-14420.
4. P. Arreesrisom, A. M. Dondorp, S. Looareesuwan and R. Udomsangpetch, *Parasitol. Int.*, 2007, **56**, 221-226.
5. X. Wu, C. Wang and J. Xiao, *Platinum Metals Rev.*, 2010, **54**, 3-19.
6. G. Chelucci, S. Baldino and W. Baratta, *Acc. Chem. Res.*, 2015, **48**, 363-379.
7. T. Stringer, D. R. Melis and G. S. Smith, *Dalton Trans.*, 2019, **48**, 13143-13148.
8. Z. H. Siddik, *Oncogene*, 2003, **22**, 7265-7279.
9. P. M. Takahara, A. C. Rosenzweig, C. A. Frederick and S. J. Lippard, *Nature*, 1995, **377**, 649-652.

10. Y. R. Zheng, K. Suntharalingam, P. M. Bruno, W. Lin, W. Wang, M. T. Hemann and S. J. Lippard, *Inorg. Chim. Acta.*, 2016, **452**, 125-129.
11. V. Vajpayee, Y. H. Song, Y. J. Yang, S. C. Kang, H. Kim, I. S. Kim, M. Wang, P. J. Stang and K. W. Chi, *Organometallics*, 2011, **30**, 3242-3245.
12. V. Vajpayee, Y. J. Yang, S. C. Kang, H. Kim, I. S. Kim, W. Ming, P. J. Stang and K. W. Chi, *Chem. Commun.*, 2011, **47**, 5184-5186.
13. A. Dubey, J. W. Min, H. J. Koo, H. Kim, T. R. Cook, S. C. Kang, P. J. Stang and K. W. Chi, *Chem. Eur. J.*, 2013, **19**, 11622-11628.
14. V. Vajpayee, S. M. Lee, J. W. Park, A. Dubey, H. Kim, T. R. Cook, P. J. Stang and K. W. Chi, *Organometallics*, 2013, **32**, 1563-1566.
15. L. Rylands, A. Welsh, K. Maepa, T. Stringer, D. Taylor, K. Chibale and G. S. Smith, *Eur. J. Med. Chem.*, 2019, **161**, 11-21.
16. B. D. Palmer, J. B. Smaill, M. Boyd, D. H. Boschelli, A. M. Doherty, J. M. Hamby, S. S. Khatana, J. B. Kramer, A. J. Kraker, R. L. Panek, G. H. Lu, T. K. Dahring, R. T. Winters, H. D. H. Showalter and W. A. Denny, *J. Med. Chem.*, 1998, **41**, 5457-5465.
17. G. Gupta, A. Das, S. W. Lee, J. Y. Ryu, J. Lee, N. Nagesh, N. Mandal and C. Y. Lee, *J. Organomet. Chem.*, 2018, **868**, 86-94.
18. A. Beloqui, in *Chemistry and Applications of Benzimidazole and its Derivatives*, ed. M. Marinescu, IntechOpen, London, United Kingdom, 2019, ch. 11, p. 203.
19. T. J. Egan, R. Hunter, C. H. Kaschula, H. M. Marques, A. Misplon and J. Walden, *J. Med. Chem.*, 2000, **43**, 283-291.
20. B. Therrien, G. Süss-Fink, P. Govindaswamy, A. K. Renfrew and P. J. Dyson, *Angew. Chem. Int. Ed.*, 2008, **47**, 3773-3776.
21. B. Woods, M. N. Wenzel, T. Williams, S. R. Thomas, R. L. Jenkins and A. Casini, *Front. Chem.*, 2019, **7**, 1-6.

CHAPTER 5

Experimental

5.1 Chemicals and general methods

All solvents and reagents were obtained from commercial sources (Sigma-Aldrich and Merck) and, unless otherwise stated, were used without any further purification. All manipulations were performed using standard Schlenk techniques under an atmosphere of argon. Reactions were monitored by thin-layer chromatography (TLC) using aluminium-backed Merck precoated silica-gel 60 F_{254} plates and compounds were visualised by ultraviolet light. Column chromatography was performed using 60 Å silica gel (7-230 mesh).

5.2 Spectroscopic and analytical techniques

Nuclear Magnetic Resonance (NMR) spectra were recorded using either a Bruker XR600 MHz spectrometer (^{1}H at 599.95 MHz and $^{13}C\{^{1}H\}$ at 151.0 MHz), a Varian Mercury XR300 MHz (^{1}H at 299.95 MHz), or a Bruker XR400 MHz spectrometer (^{1}H at 399.95 MHz and $^{13}C\{^{1}H\}$ at 100.58 MHz), with tetramethylsilane (TMS) as the internal standard. Chemical shifts (δ) and *J*-coupling values are reported in units of ppm and Hz respectively.

All DOSY NMR spectra were recorded using a Bruker 400 MHz spectrometer, equipped with a pulse gradient unit capable of producing magnetic field pulse gradients in the z-direction. All spectra were acquired using a 5mm broad-band multinuclear (PABBO) probe at 303K in 5mm tubes. DOSY experiments were performed using the 2D Stimulated Echo experiment using bipolar gradients (stebpgp1s pulse sequence). The diffusion time (d20) was 0.1 sec and the relaxation delay (d1) was set to 21.24 sec. The gradient pulse(p30) was 1800 µs with a spoil gradient (p19) of 600 µs with 17:13% ratio. The pulse gradients were incremented from 2% to 95% of the maximum gradient strength, in a linear ramp.

Infrared (IR) spectroscopic analysis was done using a Perkin-Elmer Spectrum 100 FT-IR spectrometer using Attenuated Total Reflectance (ATR) with vibrations measured in units of cm^{-1}.

Melting points were obtained using a Büchi Melting Point Apparatus B-540 and are uncorrected.

Powder X-ray diffraction (PXRD) analysis was performed using a D8 Advance diffractometer, using CuKα_1 radiation (λ = 1.5406 Å), at room temperature, with an X-ray generator set at 30 kV and 40 mA. Sample preparation involved grinding the material into a very fine powder in order to minimise the possible effects of preferred orientation. The sample was subsequently placed onto a silicon zero background sample holder and the scanning range was 4° – 40° 2θ with a step size of 0.0164° and a primary beam path slit of 0.6 mm.

5.3 Synthesis of ligand (L)

*5.3.1 7-Chloro-4-(pyridin-4-yl)quinoline, (**L**)*

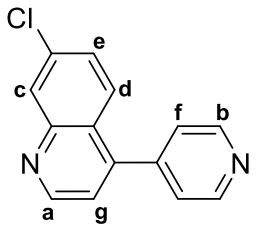

A mixture of 4,7-dichloroquinoline (2.00 g, 0.0101 mol), 4-pyridinylboronic acid (1.37 g, 0.0111 mol), PCy_3 (0.0680 g, 0.242 mmol) and $Pd(OAc)_2$ (0.0232 g, 0.103 mmol) were placed in a Schlenk flask, which was evacuated and filled with argon three times. An aqueous K_3PO_4 solution (1.27 M, 13.5 mL, 0.0172 mol) was added, followed by 1,4-dioxane (29.6 mL), and the reaction mixture refluxed at 100°C for 21 hours. The mixture was filtered through a pad of silica gel, the filtrate concentrated under reduced pressure and the aqueous residue extracted with EtOAc (3 x 30.0 mL). The organic layers were combined, dried over anhydrous $MgSO_4$, filtered and the crude product purified *via* column chromatography, using hexane:ethyl acetate as the eluent. This yielded compound **L** as a white crystalline solid. **Yield**: 42% (1.02 g, 4.25 mmol); **R_f**: 0.36 (100% EtOAc); **LC-MS**: (*m/z*) = 241.0 (100% purity, M+1); **^{1}H NMR (300 MHz, [D$_6$]-DMSO)**: δ(ppm) = 9.04 (d, 1H, H_a, $^3J_{H\text{-}H}$ = 4.4 Hz), 8.79 (dd, 2H, H_b, *J* = 4.4, 1.6 Hz), 8.20 (d, 1H, H_c, $^4J_{H\text{-}H}$ = 2.2 Hz), 7.84 (d, 1H, H_d, $^3J_{H\text{-}H}$ = 9.0 Hz), 7.67 (dd, 1H, H_e, $^3J_{H\text{-}H}$ = 9.0 Hz, $^4J_{H\text{-}H}$ = 2.2 Hz), 7.60 (dd, 2H, H_f, *J* = 4.4, 1.6 Hz), 7.57 (d, 1H, H_g, $^3J_{H\text{-}H}$ = 4.4 Hz); **^{13}C{^{1}H} NMR (100 MHz, [D$_6$]DMSO)**: δ (ppm) = 151.2, 150.0, 148.4, 145.0, 144.3, 134.4, 128.1, 128.0, 127.1, 124.2, 123.8, 121.7; **IR (ATR)** (ν_{max}/cm^{-1}): 1604, 1580 (C=N); **M.P.** (°C): 156.5 – 157.1.

5.4 Synthesis of Ir(III) and Ru(II) dimers (1 – 2)

*5.4.1 $[IrCl_2(Cp^*)]_2$, (**1**)* [1]

Pentamethylcyclopentadiene (0.947 mL, 5.99 mmol) was added to a stirring solution of $IrCl_3 \cdot 3H_2O$ (1.06 g, 3.00 mmol) in CH_3OH (65.0 mL). The dark brown reaction mixture was refluxed at 65 °C for 72 hours. The solvent was then reduced to promote the precipitation of an orange solid. The precipitate was filtered, washed with cold diethyl ether and dried *in vacuo* to yield **1** as a bright orange powder. **Yield**: 26% (0.631 g, 0.792 mmol); **^{1}H NMR (300 MHz, $CDCl_3$)**: δ(ppm) = 1.59 (s, 30H, H_{CH3}).

*5.4.2 $[RuCl_2(p\text{-cymene})]_2$, (**2**)* [2]

$RuCl_3 \cdot 3H_2O$ (1.10 g, 4.21 mmol) was dissolved in EtOH (100 mL) and stirred for *c.a.* 5 minutes at room temperature. α-Phellandrene (4.62 mL, 29.5 mmol) was then added to the reaction flask and the mixture refluxed at 80 °C for 8.5 hours. The solvent was then reduced and cooled on ice to promote precipitation. The precipitate was then filtered and washed with cold diethyl ether, yielding **2** as a dark red powder. **Yield**: 45% (1.16 g, 1.89 mmol); **^{1}H NMR (300 MHz, [D_6]-DMSO)**: δ(ppm) = 5.47 (d, 4H, $H_{Ph\text{-}CH}$, $^3J_{H\text{-}H}$ = 6.0 Hz), 5.33 (d, 4H, $H_{Ph\text{-}CH}$, $^3J_{H\text{-}H}$ = 6.0 Hz), 2.92 (hept, 2H, $H_{iso\text{-}CH}$, $^3J_{H\text{-}H}$ = 6.9 Hz), 2.15 (s, 6H, H_{CH3}), 1.27 (d, 12H, $H_{iso\text{-}CH3}$, $^3J_{H\text{-}H}$ = 6.9 Hz).

5.5 Synthesis of neutral Ir(III) and Ru(II) bimetallic complexes (3 – 8)

*5.5.1 General method for complexes **3** and **4**:*

4,4'-Bipyridine (1.2 eq.) was added to a stirring solution of the appropriate dimer (either **1** or **2**) (1.0 eq.) in CH_2Cl_2 (15.0 mL). An immediate colour change and the formation of a precipitate was observed, however, the mixture was stirred at r.t. for 3 hours to ensure completion of the reaction, as confirmed by TLC analysis, and to maximise the yield. The resulting precipitate was filtered and washed with cold Et_2O, to give the corresponding binuclear complexes in relatively high yields.

5.5.1.1 [{$IrCl_2(Cp^*)\}_2(\mu$-bpy)], (**3**) [3]

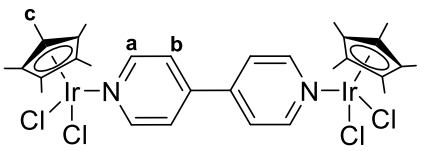

4,4'-Bipyridine (0.0225 g, 0.144 mmol) and $[Ir(Cp^*)Cl_2]_2$ (**1**) (0.100 g, 0.126 mmol) yielded **3** as a bright yellow powder. **Yield**: 78% (0.0929 g, 0.0975 mmol); **^{1}H NMR (300 MHz, [D_6]-DMSO)**: δ(ppm) = 8.73 (br, 4H, H_a), 7.84 (br, 4H, H_b), 1.63 (s, 30H, H_c); **IR (ATR)** (ν_{max}/cm^{-1}): 1608 (C=N); **M.P.** (°C): Onset of decomp. with melting = 397.3; **HR-MS** (ESI (+), *m/z*): Found = 441.0610 (10%, $[M\text{-}2Cl]^{2+}$), Calculated = 440.9970.

5.5.1.2 [{$RuCl_2$(*p*-cymene)}$_2$(μ-bpy)], (**4**) [4]

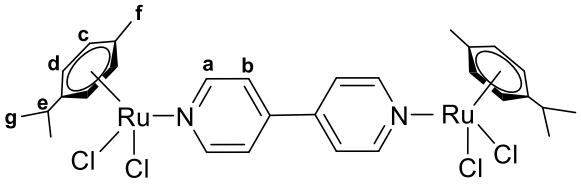

A mixture of 4,4'-bipyridine (0.0798 g, 0.511 mmol) and [Ru(*p*-cymene)$Cl_2]_2$ (**2**) (0.300 g, 0.490 mmol) yielded **4** as a bright orange powder. **Yield**: 96% (0.362 g, 0.472 mmol); **^{1}H NMR (300 MHz, [D_6]-DMSO)**: δ(ppm) = 8.72 (d, 4H, H_a, $^3J_{H\text{-}H}$ = 5.5 Hz), 7.83 (d, 4H, H_b, $^3J_{H\text{-}H}$ = 5.9 Hz), 5.94 – 5.39 (m, 8H, $H_{c,d}$), 2.82 (hept, 2H, H_e, $^3J_{H\text{-}H}$ = 6.9 Hz), 2.08 (s, 6H, H_f), 1.18 (d, 12H, H_g, $^3J_{H\text{-}H}$ = 6.9 Hz); **IR (ATR)** (ν_{max}/cm^{-1}): 1610 (C=N); **M.P.** (°C): Onset of decomp. without melting = 273.3; **HR-MS** (ESI (+), *m/z*): Found = 281.0122 (38%, $[M\text{-}(p\text{-cymene})\text{-}2Cl]^{2+}$), Calculated = 281.7280, Found = 348.9967 (9%, $[M\text{-}2Cl]^{2+}$), Calculated = 348.8390.

*5.5.2 General method for complexes **5** and **6**:*

Ligand **L** (1.2 eq.) and the appropriate dimer (either **1** or **2**) (1 eq.) were stirred in CH_2Cl_2 (15.0 mL) at r.t. for 6 hours. An evident colour change was observed following completion of the reaction. The solution was then concentrated and added to excess cold Et_2O. This resulted in the precipitation of the corresponding binuclear complex, which was filtered and washed with copious amounts of cold Et_2O.

5.5.2.1 [{$IrCl_2(Cp^*)\}_2(\mu$-**L**)], (**5**)

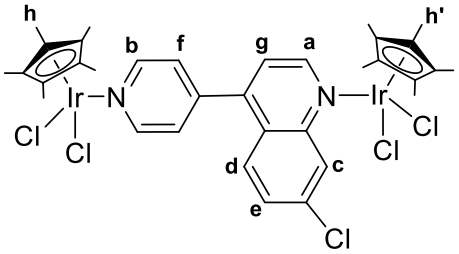

$[Ir(Cp^*)Cl_2]_2$ (**1**) (0.100 g, 0.126 mmol) was reacted with **L** (0.0350 g, 0.146 mmol), yielding **5** as a bright yellow powder. **Yield**: 76% (0.0985 g, 0.0949 mmol); **^{1}H NMR (300 MHz, $CDCl_3$)**: δ(ppm) = 9.65 (br, 1H, H_a), 9.15 (d, 2H, H_b, $^3J_{H\text{-}H}$ = 6.6 Hz), 9.01 (br, 1H, H_c), 7.60 (d, 1H, H_d, $^3J_{H\text{-}H}$ = 9.0 Hz), 7.52 (dd, 1H, H_e, $^3J_{H\text{-}H}$ = 9.0 Hz, $^4J_{H\text{-}H}$ = 2.0 Hz), 7.40 (d, 2H, H_f, $^3J_{H\text{-}H}$ = 6.6 Hz), 7.35 (d, 1H, H_g, $^3J_{H\text{-}H}$ = 5.2 Hz), 1.59 (s, 15H, $H_{h'/h}$), 1.55 (s, 15H, $H_{h'/h'}$); **^{13}C{^{1}H} NMR (100 MHz, $CDCl_3$)**: δ(ppm) = 154.08, 148.47, 146.57, 145.60, 137.18, 131.19, 129.52, 126.52, 125.85, 125.03, 121.83, 86.57, 86.23, 9.22, 8.84; **IR (ATR)** (ν_{max}/cm^{-1}): 1607 (C=N_{py}), 1587 (C=N_{quin}); **M.P.** (°C): Onset of decomp. with melting = 286.4; **HR-MS** (ESI (+), *m/z*): Found = 483.1130 (17%, $[M\text{-}2Cl]^{2+}$), Calculated = 483.2480.

5.5.2.2 [{$RuCl_2$(*p*-cymene)$_2(\mu$-**L**)], (**6**)

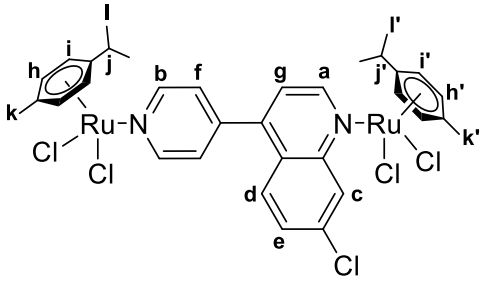

Ligand **L** (0.0449 g, 0.187 mmol) and [Ru(*p*-cymene)$Cl_2]_2$ (**2**) (0.102 g, 0.167 mmol) yielded **6** as a mustard powder. **Yield**: 74% (0.105 g, 0.123 mmol); **^{1}H NMR (300 MHz, $CDCl_3$)**: δ(ppm) = 9.24 (d, 2H, H_b, $^3J_{H\text{-}H}$ = 6.2 Hz), 9.05 (br, 1H, H_a), 8.25 (br, 1H, H_c), 7.66 (d, 1H, H_d, $^3J_{H\text{-}H}$ = 8.6 Hz), 7.52 (dd, 1H, H_e, $^3J_{H\text{-}H}$ = 9.0 Hz, $^4J_{H\text{-}H}$ = 1.7 Hz), 7.42 (br, 2H, H_f), 7.32 (d, 1H, H_g, $^3J_{H\text{-}H}$ = 4.5 Hz), 5.54 (d, 2H, $H_{h/h'}$, $^3J_{H\text{-}H}$ = 5.7 Hz), 5.49 (d, 2H, $H_{h/h'}$, $^3J_{H\text{-}H}$ = 5.5 Hz), 5.35 (d, 4H, $H_{i,i'}$, $^3J_{H\text{-}H}$ = 5.5 Hz), 3.18 – 3.02 (m, 1H, $H_{j/j'}$), 3.01 – 2.85 (m, 1H $H_{j/j'}$), 2.22 (s, 3H, $H_{k/k'}$), 2.17 (s, 3H, $H_{k/k'}$), 1.37 (d, 6H, $H_{l/l'}$, $^3J_{H\text{-}H}$ = 6.9 Hz), 1.29 (d, 6H, $H_{l/l'}$, $^3J_{H\text{-}H}$ = 6.9 Hz); **^{13}C{^{1}H} NMR (100 MHz, $CDCl_3$)**: 155.42, 151.05, 149.02, 147.17, 144.01, 136.36, 129.20, 128.85, 126.17, 124.94, 123.78, 121.25, 104.16, 101.37, 97.40, 96.83, 82.77, 82.64, 81.40, 80.65, 30.88, 30.78, 22.45, 22.27, 19.03, 18.50; **IR (ATR)** (ν_{max}/cm^{-1}): 1608 (C=N_{py}), 1587 (C=N_{quin}); **M.P.** (°C): Onset of decomp. with melting = 155.5; **HR-MS** (ESI (+), *m/z*): Found = 390.9359 (19%, [M-

2Cl]$^{2+}$), Calculated = 391.0900, Found = 324.0395 (17%, [M-(*p*-cymene)-2Cl]$^{2+}$), Calculated = 323.9790.

*5.5.3 General method for complexes **7** and **8**:*

$(NH_4)_2C_2O_4{\cdot}H_2O$ (1 eq.) was added to a solution of the appropriate dimer (either **1** or **2**) (1 eq.) in $CHCl_3$-CH_3OH (1:1 v/v ratio) and the mixture refluxed at 55°C for between 5 and 6 hours. The solvent was then evaporated to dryness, the remaining residue dissolved in CH_2Cl_2 and filtered to remove the insoluble salts. The solvent was then removed to give the corresponding oxygen-chelate binuclear complexes in high yields.

5.5.3.1 [{IrCl(Cp*)}$_2$(μ-η^2-η^2-C_2O_4)], (**7**) [5]

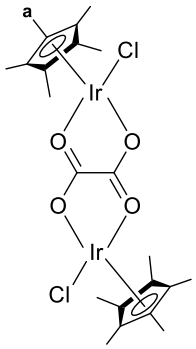

$(NH_4)_2C_2O_4{\cdot}H_2O$ (0.0178 g, 0.126 mmol) was reacted with [Ir(Cp*)Cl$_2$]$_2$ (**1**) (0.100 g, 0.126 mmol), yielding **7** as a yellow powder. **Yield**: 74% (0.0754 g, 0.0926 mmol); **^{1}H NMR (300 MHz, $CDCl_3$)**: δ(ppm) = 1.64 (s, 30H, H_a); **IR (ATR)** (ν_{max}/cm^{-1}): 1618 (C=O); **M.P.** (°C): Onset of decomp. with melting = 309.8; **HR-MS** (ESI (+), *m/z*): Found = 371.060 (20%, [M-2Cl]$^{2+}$), Calculated = 371.461.

5.5.3.2 [{RuCl(*p*-cymene)}$_2$(μ-η^2-η^2-C_2O_4)], (**8**) [6]

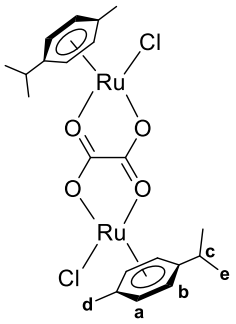

$(NH_4)_2C_2O_4{\cdot}H_2O$ (0.0232 g, 0.163 mmol) was reacted with [Ru(*p*-cymene)Cl$_2$]$_2$ (**2**) (0.100 g, 0.163 mmol) to give **8** as an orange powder. **Yield**: 89% (0.0914 g, 0.145 mmol); **^{1}H NMR (300 MHz, $CDCl_3$)**: δ(ppm) = 5.56 (d, 4H, H_a, $^3J_{H\text{-}H}$ = 6.1 Hz), 5.33 (d, 4H, H_b, $^3J_{H\text{-}H}$ = 6.1 Hz), 2.87 (hept, 2H, H_c), 2.22 (s, 6H,

H_d), 1.31 (d, 12H, H_e, $^3J_{H\text{-}H}$ = 6.9 Hz); **IR (ATR)** (ν_{max}/cm^{-1}): 1602 (C=O); **M.P.** (°C): Onset of decomp. without melting = 265; **HR-MS** (ESI (+), *m/z*): Found = 325.0021 (21%, [M-2(*p*-cymene)-Cl]$^+$, Calculated = 325.6120.

5.6 Synthesis of cationic Ir(III) and Ru(II) metallarectangles (9 – 16)

*5.6.1 General method for complexes **9** - **12***

$Ag(CF_3SO_3)$ (2.1 eq.), in anhydrous acetonitrile, was added to a stirring solution of the appropriate *N*,*N*'-binuclear complex (**3** – **6**) (1 eq.) in dry CH_2Cl_2. The mixture was shielded from light and stirred at r.t. for 24 hours. The solvent was then removed under reduced pressure, CH_2Cl_2 added to the remaining residue, and the solution filtered to remove the insoluble salts (AgCl). The filtrate was concentrated and added to excess cold Et_2O, resulting in the precipitation of the corresponding metallarectangle, as its triflate salt.

5.6.1.1 [{Ir(μ-Cl)(Cp*)}$_4$(μ-bpy)$_2$](CF$_3$SO$_3$)$_4$, (**9**).[3]

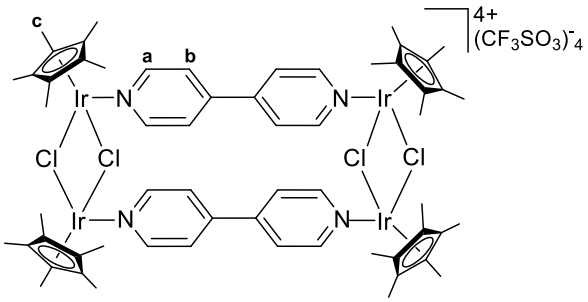

$Ag(CF_3SO_3)$ (0.0398 g, 0.155 mmol) in anhydrous acetonitrile (10.0 mL) was added to a solution of **3** (0.0713 g, 0.0748 mmol) in dry CH_2Cl_2 (10.0 mL), yielding **9** as a bright yellow powder. **Yield:** 70% (0.0622 g, 0.0263 mmol); **^{1}H NMR (300 MHz, [D$_6$]-DMSO)**: δ(ppm) = 8.97 (d, 7H, H_a, $^3J_{H\text{-}H}$ = 6.5 Hz), 8.85 (dd, 1H, H_a, $J_{H\text{-}H}$ = 12.9 Hz and 6.3 Hz), 8.27 (d, 7H, H_b, $^3J_{H\text{-}H}$ = 6.8 Hz), 7.93 (d, 1H, H_b, $^3J_{H\text{-}H}$ = 6.2 Hz), 1.75 (s, 2H, H_c), 1.61 (s, 58H, H_c); **IR (ATR)** (ν_{max}/cm^{-1}): 1615 (C=N), 1250 ($CF_{3\ sym}$), 1222 ($SO_{3\ asym}$), 1147 ($CF_{3\ asym}$), 1027($SO_{3\ sym}$); **HR-MS** (ESI (+), *m/z*): Found = 441.0624 (100%, [M]$^{4+}$), Calculated = 440.9980.

5.6.1.2 [{Ru(μ-Cl)(*p*-cymene)}$_4$(μ-bpy)$_2$](CF$_3$SO$_3$)$_4$, (**10**).[4]

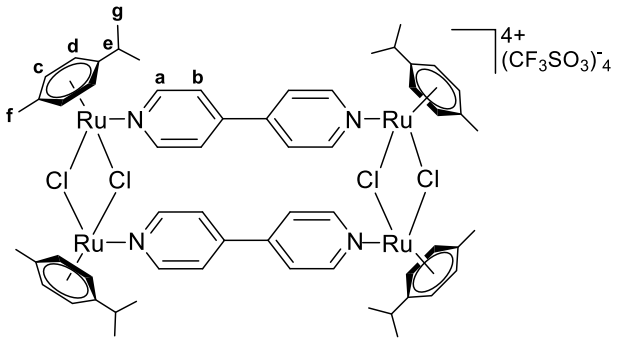

Ag(CF$_3$SO$_3$) (0.0735 g, 0.286 mmol) in anhydrous acetonitrile (10.0 mL) was added to a suspension of **4** (0.110 g, 0.143 mmol) in dry CH_2Cl_2 (10.0 mL), resulting in the formation **10** as an orange powder. **Yield:** 82% (0.117 g, 0.0587 mmol); **^{1}H NMR (300 MHz, [D$_6$]-DMSO)**: δ(ppm) = 9.04 – 8.72 (m, 8H, H$_a$), 8.24 – 7.82 (m, 8H, H$_b$), 6.54 – 5.65 (m, 16H, H$_{c,d}$), 2.91 – 2.73 (m, 4H, H$_e$), 2.20 – 1.98 (m, 12H, H$_f$), 1.37 – 1.07 (m, 24H, H$_g$); **IR (ATR)** (ν_{max}/cm^{-1}): 1613 (C=N), 1247 (CF$_3$ $_{sym}$), 1223 (SO$_3$ $_{asym}$), 1152 (CF$_3$ $_{asym}$), 1027 (SO$_3$ $_{sym}$); **HR-MS** (ESI (+), *m/z*): Found = 846.1074 (10%, [M-2OTf]$^{2+}$), Calculated = 846.7440, Found = 405.0733 (9%, [M-2OTf-2Cl]$^{4+}$), Calculated = 405.6470.

5.6.1.3 [{Ir(μ-Cl)(Cp*)}$_4$(μ-**L**)$_2$](CF$_3$SO$_3$)$_4$, (**11**).

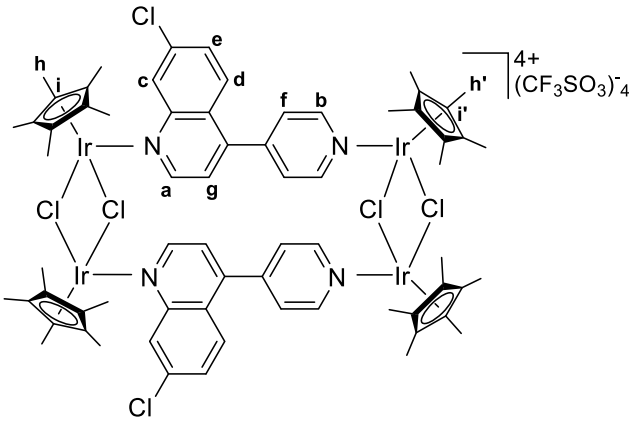

Ag(CF$_3$SO$_3$) (0.0219 g, 0.0852 mmol) in anhydrous acetonitrile (10.0 mL) was added to a solution of **5** (0.0419 g, 0.0404 mmol) in dry CH_2Cl_2 (10.0 mL), yielding **11** as a pale yellow powder. **Yield:** 71% (0.0365g, 0.0144 mmol); **^{1}H NMR (300 MHz, [D$_6$]-DMSO)**: δ(ppm) = 9.12 (d, 2H, H$_a$, $^3J_{H\text{-}H}$ = 4.4 Hz), 8.94 (d, 4H, H$_b$, $^3J_{H\text{-}H}$ = 6.4 Hz), 8.25 (d, 2H, H$_c$, $^4J_{H\text{-}H}$ = 2.1 Hz), 8.01 (d, 4H, H$_f$, $^3J_{H\text{-}H}$ = 6.7 Hz), 7.97 (d, 2H, H$_d$, $^3J_{H\text{-}H}$ = 9.1 Hz), 7.72 (dd, 2H, H$_e$, $^3J_{H\text{-}H}$ = 9.0 Hz, $^4J_{H\text{-}H}$ = 2.2 Hz), 7.69 (d, 2H, H$_g$, $^3J_{H\text{-}H}$ = 4.4 Hz), 1.75 (s, 20H, H$_{h/h'}$), 1.64 (s, 40H, H$_{h/h'}$); **^{13}C{^{1}H} NMR (100 MHz, [D$_6$]-DMSO)**: δ (ppm) = 153.92, 151.57, 148.41, 142.79, 134.73, 128.57, 128.33, 127.11, 123.13, 122.21, 121.73, 119.59, 100.39, 94.50, 8.58, 7.96; **IR (ATR)** (ν_{max}/cm^{-1}): 1609 (C=N$_{py}$), 1589 (C=N$_{quin}$), 1252 (CF$_3$ $_{sym}$), 1222 (SO$_3$ $_{asym}$), 1159 (CF$_3$ $_{asym}$),

1029 ($SO_{3\ sym}$); **M.P.** (°C): Onset of decomp. without melting = 242.5; **HR-MS** (ESI (+), *m/z*): Found = 483.1129 (48%, $[M]^{4+}$), Calculated = 483.2490.

5.6.1.4 [{Ru(μ-Cl)(*p*-cymene)}$_4$(μ-**L**)$_2$](CF$_3$SO$_3$)$_4$, (**12**).

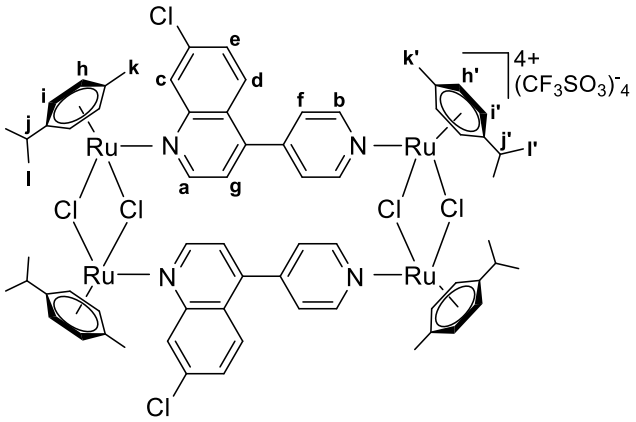

Ag(CF_3SO_3) (0.0500 g, 0.195 mmol) in anhydrous acetonitrile (3.00 mL) was added to a solution of **6** (0.0721 g, 0.0845 mmol) in dry CH_2Cl_2 (5.00 mL), yielding **12** as an orange powder. **Yield:** 24% (0.0218g, 0.0101 mmol); **^{1}H NMR (300 MHz, [D$_6$]-DMSO)**: δ(ppm) = 9.10 (d, 2H, H_a, $^3J_{H\text{-}H}$ = 4.3 Hz), 8.97 (d, 4H, H_b, $^3J_{H\text{-}H}$ = 6.4 Hz), 8.24 (d, 2H, H_c, $^4J_{H\text{-}H}$ = 2.0 Hz), 7.94 (d, 4H, H_f, $^3J_{H\text{-}H}$ = 7.0 Hz), 7.89 – 7.79 (m, 2H, H_d), 7.73 (dd, 2H, H_e, $^3J_{H\text{-}H}$ = 9.0 Hz, $^4J_{H\text{-}H}$ = 1.9 Hz,), 7.76 (d, 2H, H_g, $^3J_{H\text{-}H}$ = 4.3 Hz); **^{13}C{^{1}H} NMR (100 MHz, [D$_6$]-DMSO)**: δ (ppm) = 153.90, 151.53, 148.42, 148.37, 142.79, 134.73, 128.54, 128.31, 127.07, 123.12, 122.25, 122.17, 119.05, 100.39, 94.49, 40.43, 8.56, 8.26, 7.94; **IR (ATR)** (ν_{max}/cm^{-1}): 1611 ($C{=}N_{py}$), 1589 ($C{=}N_{quin}$), 1244 ($CF_{3\ sym}$), 1223 ($SO_{3\ asym}$), 1156 ($CF_{3\ asym}$), 1027 ($SO_{3\ sym}$); **M.P.** (°C): Onset of decomp. with melting = 120.4; **HR-MS** (ESI (+), *m/z*): Found = 931.9568 (28%, $[M\text{-}2OTf]^{2+}$), Calculated = 931.2460.

*5.6.2 General method for complexes **13** - **16***

Ag(CF_3SO_3) (2.3 eq.) was added to a solution of either binuclear complex **7** or **8** (1 eq.), in anhydrous CH_3OH (10.0 mL), and the mixture stirred at r.t. for approximately 3 hours, ensuring complete abstraction of the chlorides. The AgCl was then filtered by gravity and washed with anhydrous CH_3OH. The appropriate *N*,*N*'-ligand (4,4'-bipyridine or **L**) (1 eq.) was then added to the filtrate and the mixture stirred for a final 24 hours. The solvent was then removed under reduced pressure, the residue suspended in CH_2Cl_2 and the insoluble materials filtered. The filtrate was concentrated and added to excess cold Et_2O resulting in the precipitation the corresponding metallarectangles, as its triflate salt, in moderate yields.

5.6.2.1 [{Ir(Cp*)}$_4$(μ-η^2-η^2-C_2O_4)(μ-bpy)$_2$](CF_3SO_3)$_4$, (**13**).[5]

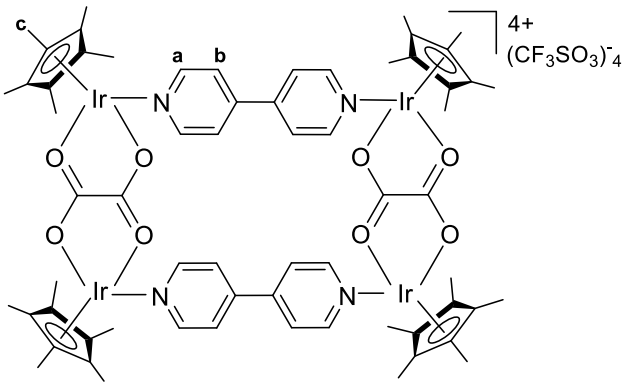

Complex **7** (0.0600 g, 0.0737 mmol) was reacted with $Ag(CF_3SO_3)$ (0.0436 g, 0.170 mmol) followed by 4,4'-bipyridine (0.0115 g, 0.0737 mmol), resulting in the formation of **13** as a yellow solid. **Yield:** 67% (0.0594 g, 0.0248 mmol); **^{1}H NMR (300 MHz, [D$_6$]-DMSO)**: δ(ppm) = 8.50 – 9.08 (m, 8H, H_a), 7.73 – 8.38 (m, 8H, H_b), 1.41 – 1.73 (m, 60H, H_c); **IR (ATR)** (ν_{max}/cm^{-1}): 1624 (C=O), 1250 (CF_3 $_{sym}$), 1222 (SO_3 $_{asym}$), 1151 (CF_3 $_{asym}$), 1028 (SO_3 $_{sym}$); **M.P.** (°C): Onset of decomp. without melting = 311.9; **HR-MS** (ESI (+), *m/z*): Found = 449.1031 (33%, [M-4OTf]$^{4+}$), Calculated = 448.5450.

5.6.2.2 [{Ru(*p*-cymene)}$_4$(μ-η^2-η^2-C_2O_4)(μ-bpy)$_2$](CF_3SO_3)$_4$, (**14**).[6]

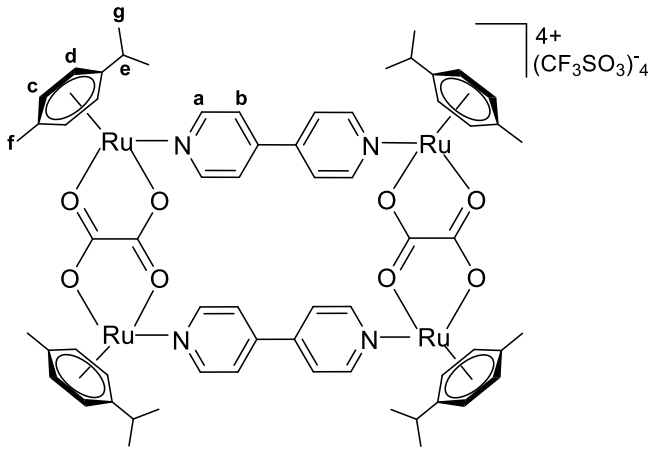

$Ag(CF_3SO_3)$ (0.0535 g, 0.208 mmol), complex **8** (0.0570 g, 0.0905 mmol) and 4,4'-bipyridine (0.0141 g, 0.0903 mmol) yielded metallarectangle **14** as a bright orange powder. **Yield:** 88% (0.130 g, 0.0641 mmol); **^{1}H NMR (300 MHz, [D$_6$]-(CD$_3$)$_2$CO)**: δ(ppm) = 8.28 (dd, 8H, H_a, $^3J_{H\text{-}H}$ = 5.4 Hz, $^4J_{H\text{-}H}$ = 1.3 Hz), 7.89 (dd, 8H, H_b, $^3J_{H\text{-}H}$ = 5.4 Hz, $^4J_{H\text{-}H}$ = 1.4 Hz), 6.08 (d, 8H, H_c, $^3J_{H\text{-}H}$ = 6.3 Hz), 5.92 (d, 8H, H_d, $^3J_{H\text{-}H}$ = 6.3 Hz), 2.92 (br, 4H, H_e), 2.23 (s, 12H, H_f), 1.35 (d, 24H, H_g, $^3J_{H\text{-}H}$ = 6.9 Hz); **IR (ATR)** (ν_{max}/cm^{-1}): 1627 (C=O), 1276 (CF_3 $_{sym}$), 1220 (SO_3 $_{asym}$), 1153 (CF_3 $_{asym}$), 1021 (SO_3 $_{sym}$); **M.P.** (°C): Onset of decomp.

without melting = 223.4; **HR-MS** (ESI (+), *m/z*): Found = 357.5395 (42%, $[M\text{-}4OTf]^{4+}$), Calculated = 357.3950.

5.6.2.3 $[\{Ir(Cp^*)\}_4(\mu\text{-}\eta^2\text{-}\eta^2\text{-}C_2O_4)(\mu\text{-}\mathbf{L})_2](CF_3SO_3)_4$, (**15**).

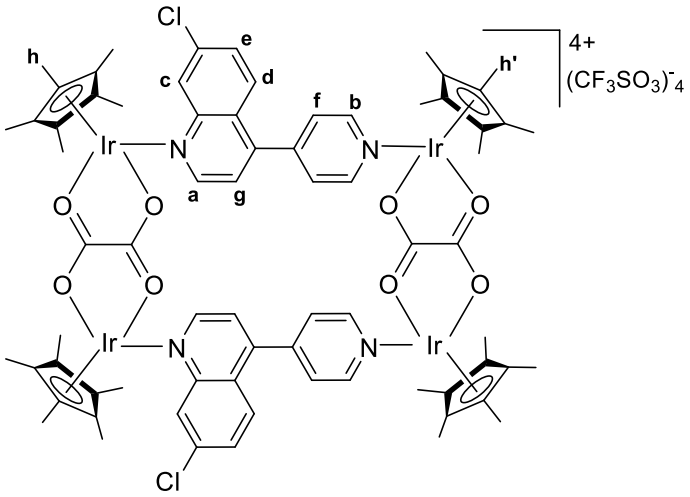

Complex **7** (0.0500 g, 0.0614 mmol) was reacted with $Ag(CF_3SO_3)$ (0.0387 g, 0.151 mmol), followed by **L** (0.0148 g, 0.0614 mmol), yielding **15** as a mustard-yellow solid. **Yield**: 74% (0.0586 g, 0.0229 mmol); **^{1}H NMR (300 MHz, [D$_6$]-DMSO)**: δ(ppm) = 9.19 – 8.99 (m, 2H, H_a), 8.8 – 8.53 (m, 4H, H_b), 8.45 – 8.16 (m, 2H, H_c), 8.12 – 7.79 (m, 6H, $H_{f,d}$), 7.78 – 7.45 (m, 4H, $H_{e,g}$), 1.91 – 1.05 (m, 60H, $H_{h,h'}$); **^{13}C{^{1}H} NMR (100 MHz, [D$_6$]-DMSO)**: δ (ppm) = 165.01, 164.12, 152.22, 151.64, 148.44, 142.71, 134.79, 128.38, 127.00, 123.19, 122.27, 119.08, 115.87, 94.53, 93.90, 93.47, 90.85, 83.87, 8.31, 7.94; **IR (ATR)** (ν_{max}/cm^{-1}): 1627 (C=O), 1250 ($CF_{3\ sym}$), 1222 ($SO_{3\ asym}$), 1155 ($CF_{3\ asym}$), 1019 ($SO_{3\ sym}$); **M.P.** (°C): Onset of decomp. without melting = 271.8; **HR-MS** (ESI (+), *m/z*): Found = 492.0915 (32%, $[M\text{-}4OTf]^{4+}$), Calculated = 491.8040, Found = 1133.1420 (53%, $[M\text{-}2OTf]^{2+}$), Calculated = 1132.6840.

5.6.2.4 [{Ru(*p*-cymene)}$_4$(μ-η^2-η^2-C_2O_4)(μ-**L**)$_2$](CF$_3$SO$_3$)$_4$, (**16**).

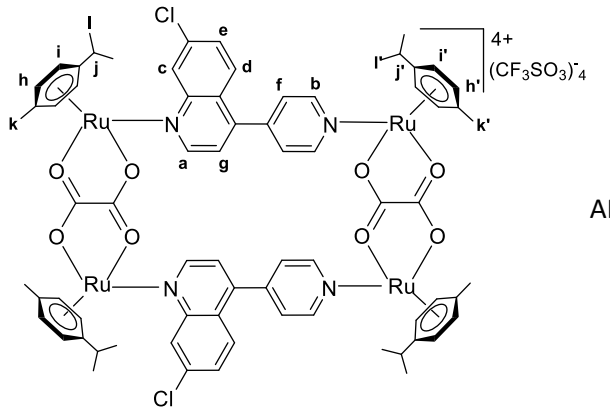

AND

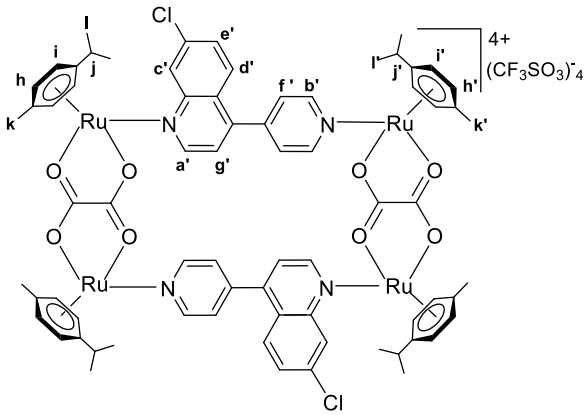

AgOTf (0.0685 g, 0.267 mmol), complex **8** (0.0700 g, 0.111 mmol) and **L** (0.0268 g, 0.111 mmol) yielded **16** as a yellow solid. **Yield**: 71% (0.0867 g, 0.0395 mmol); **^{1}H NMR (300 MHz, [D$_6$]-DMSO)**: δ(ppm) = 9.11 (d, 2H, H$_{a/a'}$, $^3J_{H\text{-}H}$ = 4.4 Hz), 9.05 (d, 2H, H$_{a/a'}$, $^3J_{H\text{-}H}$ = 4.3 Hz), 8.81 (d, 4H, H$_{b/b'}$, $^3J_{H\text{-}H}$ = 6.3 Hz), 8.66 (d, 4H, H$_{b/b'}$, $^3J_{H\text{-}H}$ = 6.3 Hz), 8.26 (d, 2H, H$_{c/c'}$, $^3J_{H\text{-}H}$ = 1.8 Hz), 8.22 (d, 2H, H$_{c/c'}$, $^3J_{H\text{-}H}$ = 2.0 Hz), 7.90 (d, 4H, H$_{f/f'}$, $^3J_{H\text{-}H}$ = 6.4 Hz), 7.83 (d, 4H, H$_{f/f'}$, $^3J_{H\text{-}H}$ = 6.5 Hz), 7.77 – 7.67 (m, 4H, H$_{e,e'}$), 7.67 – 7.28 (m, 8H, H$_{d,d',\,g,g'}$), 6.12 (d, 8H, H$_{h/h'}$, $^3J_{H\text{-}H}$ = 6.1 Hz), 5.98 (d, 8H, H$_{h/h'}$, $^3J_{H\text{-}H}$ = 6.1 Hz), 5.85 (d, 8H, H$_{i/i'}$, $^3J_{H\text{-}H}$ = 5.9 Hz), 5.63 (d, 8H, H$_{i/i'}$, $^3J_{H\text{-}H}$ = 6.0 Hz), 2.92 – 2.69 (m, 8H, H$_{j,j'}$), 2.30 – 1.99 (m, 24H, H$_{k,k'}$), 1.44 – 1.09 (m, 48H, H$_{l,l'}$); **^{13}C{^{1}H} NMR (100 MHz, [D$_6$]-DMSO)**: δ (ppm) = 172.42, 166.35, 164.38, 152.99, 151.61, 150.07, 148.42, 145.30, 144.99, 144.48, 143.15, 134.55, 128.80, 128.21, 128.03, 127.19, 126.08, 124.28, 123.79, 123.34, 121.79, 119.07, 102.72, 96.82, 80.43, 79.99, 32.98, 23.98, 21.86, 20.56; **IR (ATR)** (ν_{max}/cm^{-1}): 1627 (C=O), 1251 (CF$_{3\ sym}$), 1224 (SO$_{3\ asym}$), 1152 (CF$_{3\ asym}$), 1028 (SO$_{3\ sym}$); **M.P.** (°C): Onset of decomp. without melting = 188.0; **HR-MS** (ESI (+), *m/z*): Found = 400.0251 (9%, [M-4OTf]$^{4+}$), Calculated = 399.6440, Found = 949.0110 (43%, [M-2OTf]$^{2+}$), Calculated = 948.3640.

5.7 Single crystal X-ray crystallography

Single-crystal X-ray diffraction data were collected on a Bruker KAPPA APEX II DUO diffractometer using graphite-monochromated Mo-Kα radiation (χ = 0.71073 Å). Data collection was carried out at 100 (2) K. Temperature was controlled by an Oxford Cryostream cooling system (Oxford Cryostat). Cell refinement and data reduction were performed using the program SAINT.[7] The data were scaled and absorption correction performed using SADABS.[8]

The structure was solved by direct methods using SHELXS-97[8] and refined by full-matrix least-squares methods based on F^2 using SHELXL-2018[8] and using the graphics interface program X-Seed[9,10]. The programs X-Seed and POV-Ray[11] were used to prepare molecular graphic images.

All non-hydrogen atoms were refined anisotropically. All hydrogen atoms were placed in idealised positions and refined in riding models with U_{iso} assigned 1.2 or 1.5 times U_{eq} of their parent atoms and the bond distances were constrained to 0.95 Å, 0.98 Å and 1.00 Å for different types of C-H.

5.8 DFT calculations

The structure of the model of the metallarectangle was predicted by density functional theory (DFT) calculations, using the DMol^3 interface in BIOVIA Materials Studio 2017 (v. 17.1.0.48, 2016, Dassault Systèmes, Vélizy-Villacoublay Cedex, France).[12-14] The molecular structure was optimized at the DFT level of theory, using the GGA-PBE density functional (i.e. generalized gradient approximation with Perdew–Burke-Ernzerhof exchange energies) and DND basis set (i.e. double numerical basis set with *d*-polarization functions (DND), file 4.4).[15] The quantum contributions of all electrons in the system were taken into consideration in the calculation. For quality of the calculation, the integration accuracy was set to coarse, with a SCF tolerance of 1.0 x 10^{-4} and a maximum number of 50 cycles. The spin polarization was restricted and a global orbital cut off set at 3.40 Å, with no solvation model, as the calculation was done *in vacuo*.

5.9 *In vitro* antiplasmodial studies

The test samples were evaluated in triplicate, on two or three separate occasions, against both the CQ-sensitive (NF54) and CQ-resistant (K1) strains of the malaria parasite *P. falciparum*. Continuous i*n vitro* cultures of asexual erythrocyte stages of the parasite were maintained using a modified literature method of Trager and Jensen.[16] Quantitative assessment of the *in vitro* antiplasmodial

activity was determined using the parasitic lactate dehydrogenase (pLDH) assay.[17] Stock solutions of the test samples were prepared to 20 mg/mL in 100% DMSO and the solutions stored at -20 °C. Further dilutions were prepared on the day of the assay. Test samples were tested at a starting concentration of 100 µg/mL, which was serially diluted 2-fold in complete growth medium until a concentration of 0.2 µg/mL was obtained. The same dilution technique was used for all samples to give 10 concentrations. CQDP was used as the reference drug for all experiments. A full dose-response was performed for all compounds to determine the concentration inhibiting 50% of parasite growth (IC_{50} value). The IC_{50} values of all the compounds were obtained using a sigmoidal dose-response curve generated using GraphPad Prism v.5.0 software.

5.10 NP-40 detergent-mediated β-hematin inhibition assay

The β-hematin inhibition assay was modified from the method reported by Sandlin *et al*.[18,19] Stock solutions (20 mM or 10 mM) of the respective test compounds were prepared in 100% DMSO with the exception of CQDP, which was prepared in MilliQ water. The compounds were dispensed into a 96-well plate in triplicate and were tested over a concentration range of 0 – 1000 µM or 0 – 500 µM (final well concentration). A 100 µL solution of MilliQ water/NP-40/ DMSO in a v/v ratio of 7:2:1 was added to all wells in columns 1 – 11. MilliQ water (140 µL) and NP-40 (305.5 µM, 40.0 µL) was added to column 12. NP-40 is a detergent used to mediate the formation of β-haematin. The respective test compounds (20.0 µL) were then added to column 12 and serially diluted two-fold to give a total of 11 concentrations. Column 1 thus served as a blank containing no test compound. Since the compounds were coloured, the plates were pre-read at 405 nm. A 25 mM stock solution of haematin was then prepared by dissolving haemin in DMSO and sonicating for 1 minute. A 178.8 µL aliquot of this haematin stock solution was suspended in acetate buffer (20.0 mL, 1 M, pH 4.8) and 100 µL of this suspension added to each well. The plates were covered and incubated at 37 °C for 6 hours in an incubator. The assay was analysed using the pyridine-ferrochrome method developed by Egan and co-workers.[20] A solution of pyridine/MilliQ water/acetone/HEPES(2 M, pH 7.4) in a v/v ratio of 5:2:2:1 respectively, was prepared, and 32.0 µL of this solution added to each well, followed by acetone (60.0 µL) and mixed. The absorption was recorded using a Thermo Scientific Multiscan GO plate reader at 405 nm. The IC_{50} values were obtained using a sigmoidal dose-response curves generated using Graph Pad Prism v.5.0 software.

5.11 *In vitro* cytotoxicity studies

Compounds were tested for their *in vitro* cytotoxicity against the human breast adenocarcinoma MCF-7 (oestrogen-receptor positive, ER+) cell line, the triple-negative MDA-MB-231 (oestrogen-receptor negative (ER-), progesterone-receptor negative (PgR-) and lacking overexpression of the HER2 gene) cell line and the non-tumorigenic human breast epithelial MCF-12A cell line, using the 3-(4,5-dimethylthiazol-2-yl)-2,5-diphenyltetrazoliumbromide (MTT) assay. The MTT assay is used as a colorimetric assay for cellular growth and survival and compares well with other available assays.[21,22]

The MCF-7 and MDA-MB-231 cell lines were maintained in Roswell Park Memorial Institute (RPMI) 1640 medium (Sigma Aldrich, USA) and Dulbecco's Modified Eagle's Medium (DMEM) (Sigma Aldrich, USA), respectively. All culture media were supplemented with 10% heat-inactivated foetal bovine serum (FBS), 100 U/mL penicillin and 100 µg/mL streptomycin. The MCF-12A cells were maintained in complete medium consisting of DMEM and HAMS F-12, supplemented with 10% heat-inactivated FBS, 100 U/mL penicillin, 100 µg/mL streptomycin, 0.1 µg/mL cholera toxin (Sigma, St. Louis, MO, USA), 0.5 µg/mL hydrocortisone (Calbiochem, Billerica, MA), 20 ng/mL epidermal growth factor (Gibco, Life Technologies, Carlsbad, CA), 10 µg/mL insulin (Novorapid; Novo Nordisk, Copenhagen, Denmark), and 5% horse serum (Highveld Biological, Lyndhurst, South Africa). The cells were maintained in an environment of 5% CO_2, at 37 °C.

The cells (MCF-7, MDA-MB-231, and MCF-12A) were seeded in a 96-well flat-bottomed plate at a density of 4500 cells/well, 3000 cells/well, and 6000 cells/well respectively, and incubated at 37 °C for 24 or 48 hours to allow adhesion. Thereafter, the cells were treated with either the vehicle (0.1% DMSO) or 10 or 20 µM of the test compounds, for 48 hours. After 48 hours of incubation, an aliquot of MTT (10 µL) solution was added to each well and the plates incubated at 37°C for 4 hours. The MTT crystals were then solubilized using 100 µL solubilizing solution (10% SDS in 0.01M HCl). The absorption at 600 nm was then determined for each well using a GloMax® Explorer Multimode Microplate Reader GM3500. To determine the IC_{50} values, cells with treated with selected compounds with concentrations ranging between 5 to 20 µM. These samples were tested in triplicate on two separate occasions and the IC_{50} values obtained using Graph Pad Prism v.5.0 software.

5.12 References

1. C. White, A. Yates and P. M. Maitlis, in *Inorganic Syntheses*, ed. D. M. Heinekey, John Wiley & Sons Inc., 1992, vol. 29, ch. 53, pp. 228-234.
2. M. A. Bennet, T.-N. Huang, T. W. Matheson and A. K. Smith, in *Inorganic Syntheses*, eds. S. Ittel and W. Nickerson, John Wiley & Sons Inc., 1982, vol. XXI, ch. 16, pp. 75-78.
3. Y. Yamamotoa, H. Suzuki, N. Tajima and K. Tatsumi, *Chem. Eur. J.*, 2002, **8**, 372-379.
4. A. Bacchi, G. Cantoni, P. Pelagatti and S. Rizzato, *J. Organomet. Chem.*, 2012, **714**, 81-87.
5. Y.-F. Han, Y.-J. Lin, W.-G. Jia, L.-H. Weng and G.-X. Jin, *Organometallics*, 2007, **26**, 5848-5853.
6. H. Yan, G. Süss-Fink, A. Neels and H. Stoeckli-Evans, *Dalton Trans.*, 1997, 4345-4350.
7. SAINT, Version 7.60a Bruker AXS Inc., Madison, WI, USA, 2006.
8. G. M. Sheldrick, SHELXS-97, SHELXL-2018/3 and SADABS version 2.05, University of Göttingen, Germany, 1997.
9. L. J. Barbour, *J. Supramol. Chem.*, 2001, **1**, 189-191.
10. J. L. Atwood and L. J. Barbour, *Cryst. Growth Des.*, 2003, **3**, 3 - 8.
11. http://www.povray.org.
12. B. Delley, *J. Chem. Phys.*, 1990, **92**, 508 - 517.
13. B. Delley, *J. Chem. Phys.*, 2000, **113**, 7756 - 7764.
14. *BIOVIA Materials Studio*, https://www.materials-studio.com/products/collaborative-science/biovia-materials-studio, Accessed: 07 Dec 2020.
15. J. P. Perdew, J. A. Chevary, S. H. Vosko, K. A. Jackson, M. R. Pederson, D. J. Singh and C. Fiolhais, *Phys. Rev. B*, 1992, **46**, 6671-6687.
16. W. Trager and J. Jensen, *Science*, 1976, **193**, 673-675.
17. M. T. Makler and D. J. Hinrichs, *Am. J. Trop. Med. Hyg.*, 1993, **48**, 205-210.
18. R. D. Sandlin, M. D. Carter, P. J. Lee, J. M. Auschwitz, S. E. Leed, J. D. Johnson and D. W. Wright, *Antimicrob. Agents Chemother.*, 2011, **55**, 3363-3369.
19. M. D. Carter, V. V. Phelan, R. D. Sandlin, B. O. Bachmann and D. W. Wright, *Comb. Chem. High Throughput Screen.*, 2010, **13**, 285-292.
20. K. K. Ncokazi and T. J. Egan, *Anal. Biochem.*, 2005, **338**, 306-319.
21. T. Mosmann, *J. Immunol. Methods*, 1983, **65**, 55-63.
22. L. V. Rubinstein, R. H. Shoemaker, K. D. Paull, R. M. Simon, S. Tosini, P. Skehan, D. A. Scudiero, A. Monks and M. R. Boyd, *J. Natl. Cancer Inst.*, 1990, **82**, 1113-1118.